Optical MEMS Switches: Theory, Design, and Fabrication of a New Architecture

by

Mohamed A. Basha

A thesis
presented to the University of Waterloo
in fulfillment of the
thesis requirement for the degree of
Doctor of Philosophy
in
Electrical and Computer Engineering

Waterloo, Ontario, Canada, 2007

I hereby declare that I am the sole author of this thesis. This is a true copy of the thesis, including any required final revisions, as accepted by my examiners. I Understand that my thesis may be made electronically available to the public.

Mohamed A. Basha

Abstract

The scalability and cost of microelectromechanical systems (MEMS) optical switches are now the important factors driving the development of MEMS optical switches technology. The employment of MEMS in the design and fabrication of optical switches through the use of micromachining fabricated micromirrors expands the capability and integrity of optical backbone networks. The focus of this dissertation is on the design, fabrication, and implementation of a new type of MEMS optical switch that combines the advantages of both 2-D and 3-D MEMS switch architectures.

This research presents a new digital MEMS switch architecture for $1 \times N$ and $N \times N$ optical switches. The architecture is based on a new microassembled smart 3-D rotating inclined micromirror ($3DRIM$). The $3DRIM$ is the key device in the new switch architectures.

The $3DRIM$ was constructed through a microassembly process using a passive microgripper, key, and inter-lock (PMKIL) assembly system. An electrostatic micromotor was chosen as the actuator for the $3DRIM$ since it offers continuous rotation as well as small, precise step motions with excellent repeatability that can achieve repeatable alignment with minimum optical insertion loss between the input and output ports of the switch. In the first $3DRIM$ prototype, a 200×280 μm micromirror was assembled on the top of the electrostatic micromotor and was supported through two vertical *supportposts*. The assembly technique was then modified so that the second prototype can support micromirrors with dimensions up to 400×400 μm. Both prototypes of the $3DRIM$ are rigid and stable during operation. Also, rotor pole shaping (RPS) design technique was introduced to optimally reshape the physical dimensions of the rotor pole in order to maximize the generated motive torque of the micromotor and minimize the required driving voltage signal. The targeted performance of the $3DRIM$ was achieved after several PolyMUMPs fabrication runs.

The new switch architecture is neither 2-D nor 3-D. Since it is composed of two layers, it can be considered 2.5-D. The new switch overcomes many of the limitations of current traditional 2-D MEMS switches, such as limited scalability and large variations in the insertion loss across output ports. The $1 \times N$ MEMS switch fabric has the advantage of being digitally operated. It uses only one $3DRIM$ to switch the light signal from the input port to any output port. The symmetry employed in the switch design gives it the ability to incorporate a large number of output ports with uniform insertion losses over all output channels, which is not possible with any available

2-D or 3-D MEMS switch architectures. The second switch that employs the $3DRIM$ is an $N \times N$ optical cross-connect (OXC) switch. The design of an $N \times N$ OXC uses only $2N$ of the $3DRIM$, which is significantly smaller than the N^2 switching micromirrors used in 2-D MEMS architecture. The new $N \times N$ architecture is useful for a medium-sized OXC and is simpler than 3-D architecture.

A natural extension of the $3DRIM$ will be to extend its application into more complex optical signal processing, i.e., wavelength-selective switch. A grating structures have been selected to explore the selectivity of the switch. For this reason, we proposed that the surface of the micromirror being replaced by a suitable gratings instead of the flat reflective surface. Thus, this research has developed a rigorous formulation of the electromagnetic scattered near-field from a general-shaped finite gratings in a perfect conducting plane. The formulation utilizes a Fourier-transform representation of the scattered field for the rapid convergence in the upper half-space and the staircase approximation to represent the field in the general-shaped groove. This method provides a solution for the scattered near-field from the groove and hence is considered an essential design tool for near-field manipulation in optical devices. Furthermore, it is applicable for multiple grooves with different profiles and different spacings. Each groove can be filled with an arbitrary material and can take any cross-sectional profile, yet the solution is rigorous because of the rigorous formulations of the fields in the upper-half space and the groove reigns. The efficient formulation of the coefficient matrix results in a banded-matrix form for an efficient and time-saving solution.

Acknowledgements

First, I am grateful to God Almighty for giving me the soul support to continue my graduate studies and to complete this dissertation with all kind of pressure and difficulties I faced throughout my doctoral studies.

To the memory of my father Ali Basha who always wanted me to be the best among all human. I am really missing his warm appreciation and encouragement that I always wanted to hear from him after each achievements. He always inspired me to advance without limits.

I would like to express my deep grateful to my supervisors at the University of Waterloo, Prof. Saffeddin Safavi-Naeini and Prof. Sujeet K. Chaudhuri for providing me the true guidance, inspiration, and endless support throughout my doctoral studies. I really consider my relationship with my supervisors as one of the most achievements and significant contribution while in Waterloo. Indeed, my gratitude to them can not be expressed in a few words.

I extend my sincere gratitude to other committee members, Prof. Khalil Najafi from the University of Michigan, Prof. Rafaat Mansour, Prof. Manoj Sachdev, and Prof. Eihab Abdel-Rahman all from the University of Waterloo for reading my thesis and invaluable feedback.

Sincere thanks goes to Nikolai Dechev at the University of Victoria. The first time I met him was through a CMC MEMS workshop. Later on and after two years, we started to work with each other. Then, it end up with a strong and nice friendship. I still remember all days and nights we spent at the mechanical lab in the University of Toronto trying the assembly techniques and facing all kind of challenges. I still remember when we almost finished assembling one of the 3DRIM and I destroyed it after that because of one wrong command of the assembly station. Nick came back and started to laugh when he saw the situation. He said: I did that several times and when you remember that later on, you will Lough, which is the case.

My thanks to the staff of the Department of Electrical and Computer Engineering of University of Waterloo for having been helpful and supportive. Special thanks to Wendy Bole where I still remember her first letter of acceptance. She is remarkably organized and supportive at all time. Another remarkable person to thank is Anne Jenson for really managing my last-minute purchase orders.

I would also like to thank the Natural Sciences and Engineering Research Council (NSERC) and Research in Motion (RIM) for the financial support of this work. Thanks to CMC for the

support, chip fabrication, training courses, and MEMS workshops they provide throughout my doctoral study.

I am at a loss of words to express my gratitude to my wife Sally, who always provide me with the encouragement and emotional support to continue and finish my doctoral degree. She always prayed for me to be the best.

Thanks to Barbara Trotter for editing my thesis, which I believe makes a big difference.

To my Parents and my darling wife Sally

Contents

List of Figures

List of Tables

Table of Abreviations

OEC	Optical-to-Electronic Converters
EOC	Electronic-to-Optical Converters
OXC	Optical Cross-Connects
MEMS	Micro-Electro-Mechanical Systems
2-D	Two Dimensional
3-D	Three Dimensional
OPL	Optical Path Length
3DRIM	3-D Rotating Inclined Micromirror
PMKIL	Passive Microassembly and Key Inter-Lock microassembly system
RPS	Rotor-Poles-Shaping
SDA	Scratch Drive Actuator
DRIE	Deep Reactive Ion Etching
SOI	Silicon-on-Insulator
DWDM	Dense Wave Division Multiplexing
GE-OSAN	Gigabit Ethernet Optical Switched Access network
SEM	Scanning Electron Micrograph
PDMA	Plastic Deformation Magnetic Assembly
TPDA	Thermal Plastic Deformation Assembly
SCS	Single Crystal Silicon
λ	Operating Wavelengths
FEM	Finite Element Method
HS	High Sector
LS	Low Sector
PPBC	Potential Periodic Boundary Condition
ZIF	Zero-Insertion-Force
RPM	Rotation Per Minute
BEM	Boundary Element Method
IRT	Isosceles Right Triangle

Chapter 1

Introduction

1.1 Motivation and Problem Statement

Optical networks have been able to alleviate the strong growth in data communications because of the immense bandwidth they can support. The communication bandwidth is expected to increase even further in coming years. The bottleneck for optical networks is the electronic processing of the data flow, which currently uses high-speed electronic circuits involving optical-to-electronic (OEC) and electronic-to-optical (EOC) converters. However, electronic devices have reached their modulation limits, and high-speed equipment is becoming increasingly complex. Hence, moving towards all-optical components, which enable the maximum use of bandwidth, is becoming very appealing. To maintain the integrity and reliability of an optical network, reconfiguration of the network is achieved through devices such as OXCs, add/drop multiplexers, wavelength routing and selection devices, wavelength converters, and optical tunable filters. Such devices are critical components of next-generation high-performance optical networks.

Because it integrate optical, mechanical, and electronic components, MEMS technology shows great potential for providing these reliable, cost-effective, and compact optical components for next-generation optical networks. Replacement of electronic components with MEMS-based optical components in the backbone of optical networks, that operate independently of the wavelength, polarization of the light signal, and type of fiber used, will increase the reliability, flexibility, link capacity, and wavelength reuse of the network. The integration of MEMS technology in the physical layer of the optical network fabric can increase the speed of transmission and management

of data.

Two types of MEMS switch architectures are currently used for the implementation of optical switches: the two-dimensional (2-D) and three dimensional (3-D). In 2-D MEMS switches, the micromirrors, input, and output ports are located in the same plane [1, 3, 4, 6, 37, 38, 39, 40, 41]. The 2-D switching micromirrors have limited functionality, since they are in either the ON or OFF position. The number of switching micromirrorss employed in a 2-D switch is N^2. The switch packaging and fabrication are considered simple when compared to the 3-D MEMS optical switches [8, 42, 43, 44, 45, 46, 47, 48, 49, 50]. In this switch configuration, a maximum of 16×16 [40] strictly nonblocking switches have been achieved with acceptable coupling loss between the input and output ports.

3-D MEMS switches consist of two sets of micromirrors with two sets of lens matrices for coupling between the input and output ports. The micromirrors used in this switch architecture scan a cone in free space. Compared to the 2-D MEMS switches, 3-D MEMS switch architectures can provide a large scalable switch fabric with small coupling loss. However, the 3-D switch architecture needs a complex control circuit for the actuation of the micromirrors plus complex packaging, which leads to higher costs than for 2-D switches.

One of the interesting optical MEMS switch fabrics is the $1 \times N$ optical switch. The switch provides a switching of optical signal from the input port to one of the N output ports. This type of optical switch is important for many applications such as network monitoring and maintenance, and a Gigabit Ethernet optical switched access network (GE-OSAN), which is considered a key network element [51].

Scalability and actuator design and reliability are critical factors that significantly affect the performance of these types of MEMS switches. Scalability is considered the most critical factor that could compromise the use of MEMS switches for optical applications. 3-D MEMS switches offer significant scalability compared to 2-D switches. Mechanical alignment is also considered a critical factor that affects optical performance in MEMS switches, especially for 3-D MEMS switch architecture, in which the optical path length (OPL) is large and the insertion loss is significant. A robust and reliable design for the actuator and control circuit for the switching micromirrors is essential for accurate alignment and repeatably low optical coupling loss.

The inherent variations in the free-space OPLs among output ports when they are switching

cause variations in optical loss which results in a non-uniform coupling loss across output ports. These significant variations in the output signals require an optical equalizer in order to achieve a uniform output signal. This requirement adds cost and complexity to the switch and is considered one of the drawback of MEMS switch architectures.

1.2 Significant Research Contributions

This dissertation introduces a new MEMS switch architecture for both a $1 \times N$ optical switch and an $N \times N$ strictly nonblocking OXC. The new architecture combines the simplicity and low cost of the 2-D architecture and the flexibility of the 3-D.

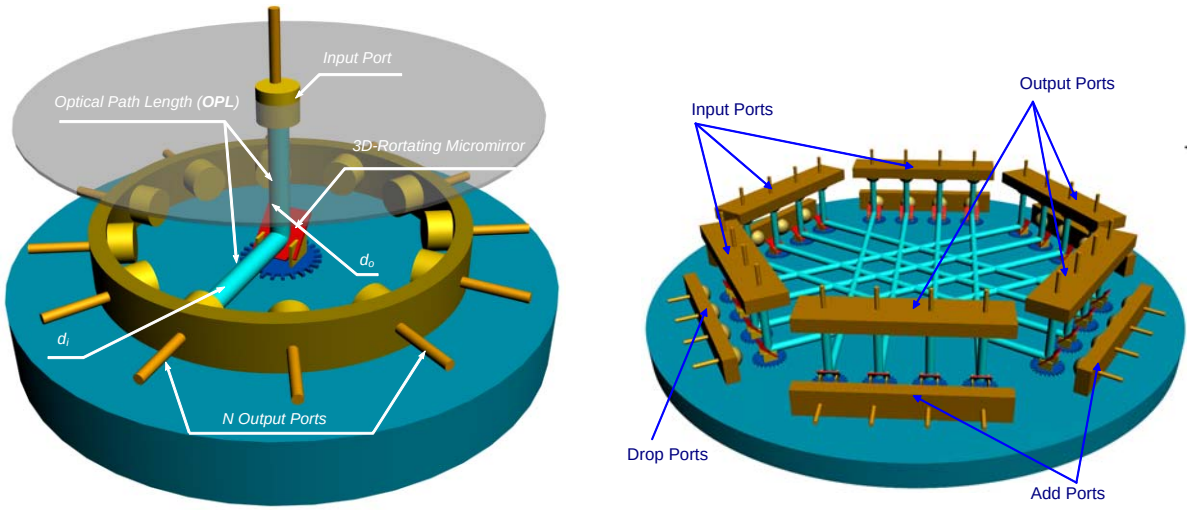

(a) (b)

Figure 1.1: A schematic diagram of the proposed MEMS switch architectures for (a) a $1 \times N$ optical switch and (b) an $N \times N$ OXC.

This research introduces novel design architecture for an optical MEMS $1 \times N$ switch and an $N \times N$ OXC as shown in Fig. 1.1(a) and (b), respectively. The design of the new $1 \times N$ MEMS switch architecture utilizes only one smart rotating micromirror and is capable of handling a large number of output ports and providing significant scalability. The new switch fabric avoids all the drawbacks of previous MEMS switches. Scalability to incorporate a large number of output ports, low and uniform coupling loss across all output ports, the simplicity and low cost of 2-D

MEMS switches and the versatility of 3-D MEMS switches are advantages of the new switch architecture. The switch utilizes a new design of a 3-D rotating inclined micromirror ($3DRIM$) that is digitally operated, Fig. 1.2. The $3DRIM$ is assembled through a microassembly process [52] on a newly redesigned micromotor that operates at low voltage. The $3DRIM$ was designed to meet the following design requirements

1. The micromirror surface must have high reflectivity and flatness.
2. The rotary platform, on which the micromirror is supported, must be free to rotate 360 degrees with a precise step size of 0.75 degree or less.
3. The micromirrors plane must be precisely at 45 degrees to the substrate.
4. The structure of the $3DRIM$ must be rigid.
5. The $3DRIM$ structure must be compatible with the rotary platform design.
6. The constituent micromirrors micro-parts must be able to be handled and joined by the passive microassembly and key inter-lock (PMKIL) microassembly system [32].

The PMKIL microassembly technique used in constructing the $3DRIM$ from planner parts, fabricated using the PolyMUMPs [53] fabrication process, is essential for achieving scalability and high level of performance. Higher electrostatic torque is required in order to account for the extra weight of the assembled microparts (micromirror and its support structure) on top of the micromotor. A new design technique called rotor-poles-shaping (RPS) [54] has been introduced to optimize the physical dimensions of the rotor poles in order to achieve higher driving torque. The new design of the electrostatic micromotors offers higher driving torque for the same driving voltage [55]. A driving voltage for the electrostatic micromotors of 16V was the lowest value achieved using the RPS technique. The $3DRIM$ is capable of achieving precisely 480 steps per full revolution for switching and alignment purposes with a minimum operating voltage of 40V, which is still relatively low.

A new $N \times N$ OXC architecture that require only $2N$ micromirrors was introduced. Input and output ports are located in the same layer while all the $3DRIMs$ are in a second layer and match the same pattern as of the input and output ports in the first layer. A modified assembly

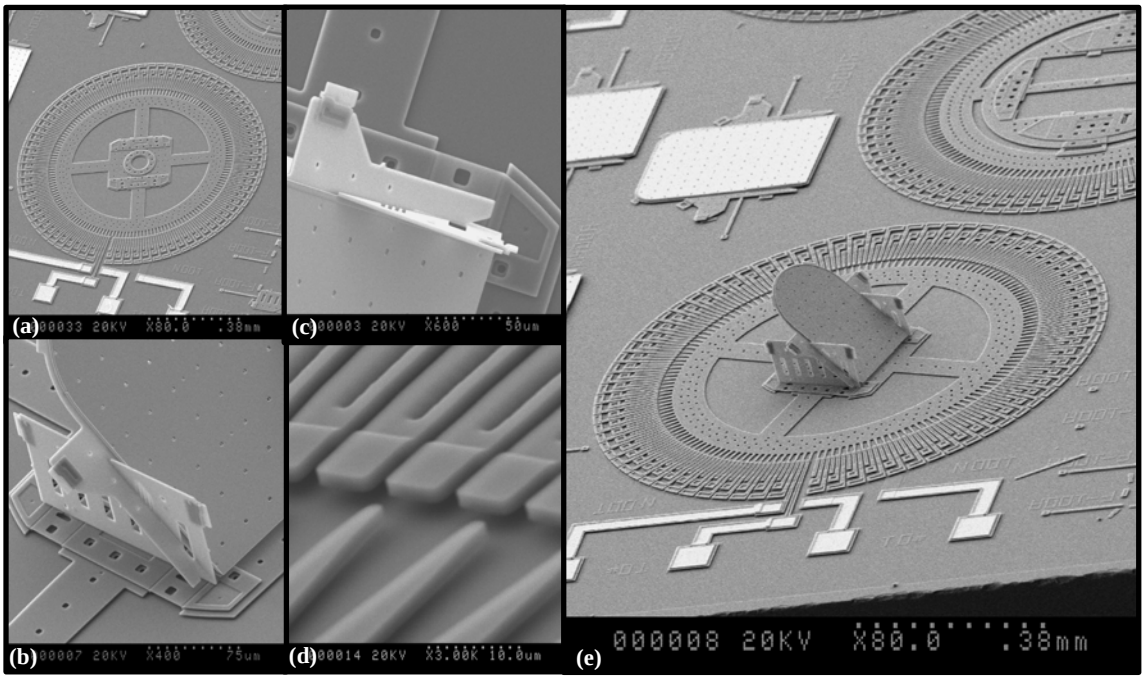

Figure 1.2: SEM images of the first assembled prototype of the $3DRIM$.

technique was developed in order to be able to assemble micromirrors with large dimensions (see Fig. 1.3).

Fast and accurate computational methods are essential for design optimization of such complex components. These methods should be able to include all of the relevant geometrical and physical parameters of the structure. A previously developed hybrid method based on rigorous analytical formulations was used to decide on the optimum collimating optical components to achieve the largest number of output ports in the switch.

A more complex optical signal processing such as wavelength-selection for a switched optical signal is targeted as an additional capability of the $3DRIM$. In order to achieve the switch ability to perform such a complex processing of optical signal in the physical layer, grating structures are to be integrated in the $3DRIM$. A good design of the grating is allow for a high efficiency of coupling into a specific diffracted order. Fully numerical methods are required for a finite arbitrary grating structure. These numerical methods are computationally expensive because of the simulation time and computational resources required. Rigorous analytical methods are available only to analyze finite rectangular grooves. The author has developed, to the best of his

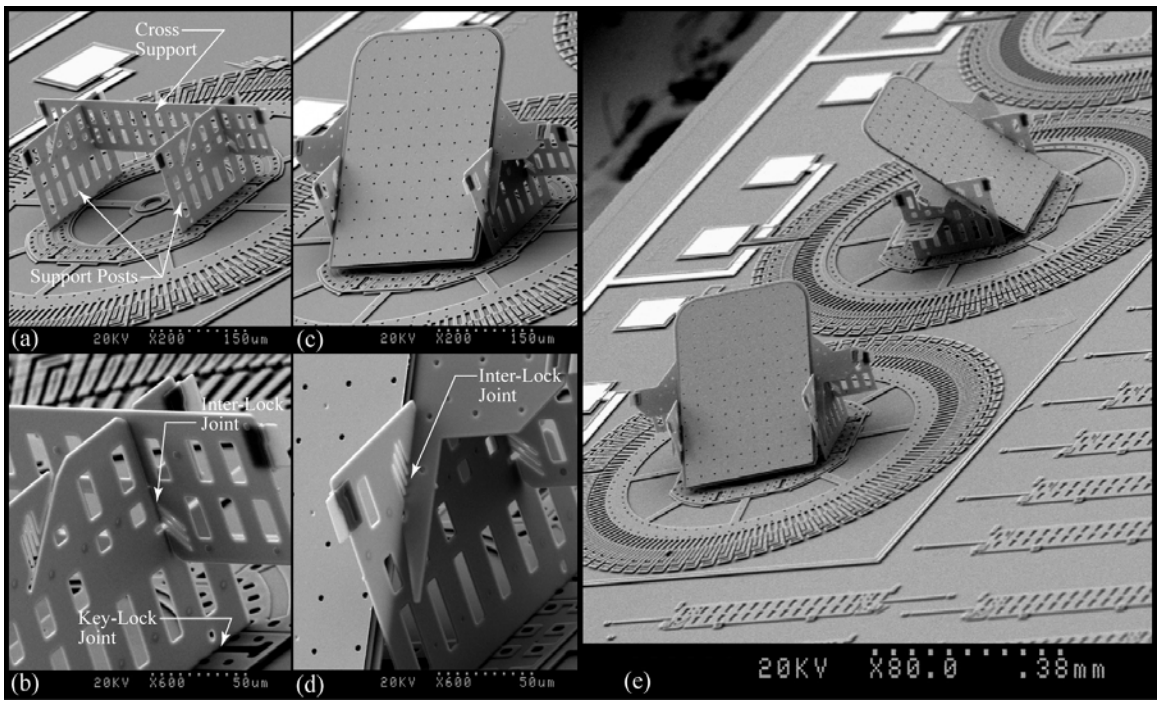

Figure 1.3: SEM images of the assembly of the second prototype of the $3DRIM$. (a) Support posts assembled onto the micromotor rotor. (b) Close-up of key-lock joint and inter-lock joints on the support posts. (c) The assembled 3-D micromirrors/micromotor. (d) Close-up of the micromirrors micro-part inter-lock joint. (e) A pair of $3DRIMs$ ready for the optical cross-connect test.

knowledge for the first time, a rigorous electromagnetic analytical method for analyzing a finite grating in a perfect conducting plane with an arbitrary groove profile. The new method makes use of the Fourier-transform to represent the fields in the upper half-space of the grating. To avoid any instability in the calculation, an adaptive method was introduced to express the fields in the groove region. The method arcuately calculates the near- and far-fields and will open a window in the future for near-field analysis and manipulation using smart MEMS micromirrors.

1.3 Thesis Outline

This Ph.D. thesis is organized into six chapters. The first chapter states the research motivation and summarizes the significant research contributions. In Chapter 2, the current state of the

technology of micromirror design and fabrications are reviewed for the latest optical switching technology.

Chapter 3 introduces the new architectures for the $1 \times N$ optical MEMS switch and the $N \times N$ cross-connect. The design of the physical layout of the $1 \times N$ MEMS optical switch is presented. The chapter describes simulations of the insertion loss between the input port and any of the output ports using a gradient-index (GRIN) lens to collimate the optics. The scalability of the switch is addressed based on extensive simulations to achieve the maximum possible number of outports for a predefined insertion loss and cross-talk level. The design of the electrostatic micromotors using the RPS technique is also discussed.

In Chapter 4, the fabrication of the $3DRIM$ using the PolyMUMPs fabrication process is discussed as is the microassembly process of the first prototype of the assembled $3DRIM$. A modified assembly structures are introduced for the efficient and rigid construction of larger micromirrors.

Chapter 5 presents the development of the rigorous analytical modeling of a finite grating in a perfect conducting plane with an arbitrary profile. First, a single groove is formulated, followed by the formulation of a finite grating, based on the single groove. The method was improved so that it can model a finite asymmetric grating with different periods, i.e., relaxing any constraints on the shape and periodicity of the grating that lead to a grating-like rough surface.

Finally, Chapter 6 summarizes the significant contributions of this research and explores the potential future work leading to the combining of the ideas presented.

Chapter 2

Current State of The Technology

Optical switches are considered important components in the next-generation of all-optical backbone networks. Reconfiguration of optical network is achieved through optical switches to maintain the integrity and reliability of the network. To maintain the integrity and reliability, optical networks can be reconfigured through Optical switches. Because of the integration of microelectromechanical system (MEMS) and optical components, the performance of optical switches has almost no dependence on the operating wavelength, polarization of the light signal, and type of fiber used.

This chapter reviews the currently available optical MEMS architectures for implementing $1 \times N$ optical switches and $N \times M$ OXCs. The scalability of each MEMS switch architecture is discussed.

2.1 Optical MEMS Switch Architectures

The architectures of optical MEMS switches are divided into two main categories: 2-D and 3-D MEMS-based switch architectures. The first MEMS based switch architecture to appear was a 2-D switch. Due to its limitations, 3-D switch architectures were developed mainly to increase switch scalability to incorporate large port counts. Each architecture has advantages and disadvantages. The main advantage of a 2-D switch is the low cost compared to that of a 3-D one. On the other hand, 3-D switch architecture's main advantage is its large port count with low insertion loss. Micromirrors are the key elements in both switch architectures with

a more complex design employed in switches. Mechanical alignment, stability, reliability, and repeatability are considered critical factors that affect optical performance in MEMS switches. A robust and reliable design of the actuator and control circuit for the switching micromirrors is essential for accurate alignment and repeatably low optical coupling loss. The next sections present the already developed architecture and the required micromirror functionally.

2.1.1 2-D MEMS $N \times N$ Optical Cross-Connects

A 2-D $N \times N$ MEMS optical switch has N input ports and N output ports, and employs N^2 MEMS switching micromirrors. All switch components are placed in the same plane. The switch architecture is realized by N^2 2-D planar micromirrors arranged in a matrix. Fig. 2.1 shows a schematic diagram of a 2-D MEMS switch architecture. The MEMS switching micromirrors have limited functionality, since they are either in the NO state in which they reflect an incoming optical beam from an input port to an output port or in the OFF state in which they bypass it to a drop port. Thus, it is appropriate to describe the micromirror functionality in a 2-D MEMS switch as a digital micromirror that exhibit an ON or OFF state. For each input port, there is an array of N output micromirrors that corresponds to the same number of output ports. The same condition applies for all output ports. After fabrication, all micromirrors have the same ON or OFF state depending on the operation of the micromirror. In most 2-D switches, the micromirrors are in the OFF state. Only one micromirror in a column or row can be activated in the ON state to switch the incoming optical beam from an input port to a specific output port. This operation is considered an advantage for this type of micromirror since it does not need a complex control circuit, but only a simple circuit to drive and control the micromirror between the ON and OFF states. Several 2-D MEMS switches based on electrostatic [1, 3, 37, 41, 56] and magnetic [4, 6, 38, 39] actuation have been reported. Optical collimating lenses are required in order to collimate the optical beams and minimize the coupling loss between the input and output ports for switches larger than 2×2. Some of the 2×2 switches were realized without optical coupling lenses through the use of a simple switch architecture [4, 57]. Surface and bulk micromachining were the main fabrication processes used to produce most of the previous micromirrors.

The first 2×2 MEMS 2-D optical switch, reported in [1], uses electrostatic torsion micromir-

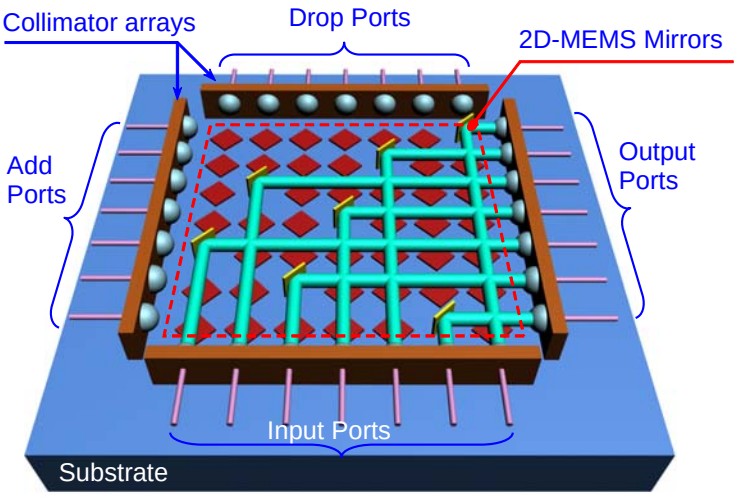

Figure 2.1: Schematic diagram of a 2-D MEMS optical switch architecture.

rors. For collimation, the switch uses ball lenses pig-tailed to single-mode fibers as shown in Fig. 2.2. The micromirror rotate in and out of the free-space OPLs to reflect or bypass optical beams through electrostatic actuation. The performance of the switch is as follows: actuation voltage = 100-150V, micromirror holding voltage = 50V, insertion loss = 7.66 dB, and cross-talk = -60 dB.

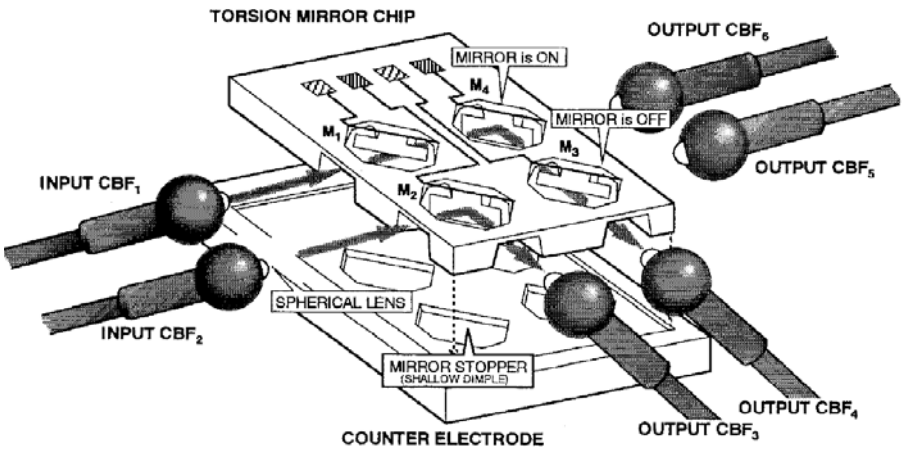

Figure 2.2: diagram of free space 2-D MEMS optical switch using electrostatic torsion micromirrors [1].

To switch the micromirror from one state to another (i.e from OFF to ON), two main approach were used. In the first approach, the micromirror is initially parallel to the substrate (OFF state). An actuator is used to rotate the micromirror out of the plane (ON state). Electrostatic [1, 56] and magnetic [39] actuators were used to realize this type of micromirror operation. One method of rotating the micromirror out of the plane is to use a scratch drive actuator (SDA) [18, 19, 58]. An array of SDAs [2, 40, 56, 59] was used to rotate the micromirror from the substrate level to the vertical position, as show, in Fig. 2.3. The micromirror is attached to the substrate through a set of microhinges [60]. A 4×4 switch [56] was fabricated and uses integrated binary-amplitude Fresnel lenses for the input/output coupling. The switch offers a very good switching time of $700\mu sec$, an insertion loss of 19.9 dB, and cross-talk of less than -60 dB. An 8×8 bidirectional switch [40] employing fiber collimators shows an insertion loss of 3.5 dB. A 16×16 version of the switch was also developed using four self-aligned 1 cm^2 polysilicon interchip bridging latches with a 2.9 dB loss for the longest path. The main problem of the micromirror is the reliability of the SDA, although it offers a large force/unit area compared to other many actuators.

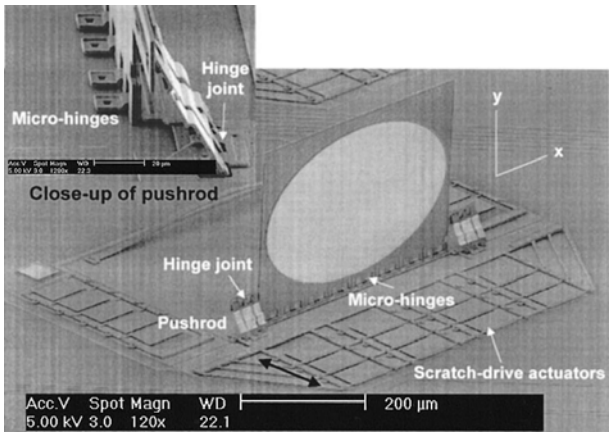

Figure 2.3: SEM of free-rotating micromirror using an array of SDAs for out-of-plane rotation [2].

In the second approach, a vertical micromirror is placed in the free space OPL to reflect or bypass an incoming optical beam to an output port. To switch the micromirror from one state to another, electrostatic [3, 37, 41] or magnetic [4, 6, 38] actuators are also used to rotate or translate it in order to bypass or reflect the optical beam. The micromirror maintains its

verticality to the substrate with the actuator in either state. A comb-drive actuator is used to move the micromirror in and out of the free-space optical path as shown in Fig. 2.4(a). This type of micromirror is fabricated with deep reactive ion etching (DRIE) and plasma-etched silicon micromirror techniques [3, 57]. The main advantages of this type of switch are the simple switch structure and the one-step fabrication process. The switch achieves good mechanical and optical performance without optical coupling lenses as shown in Fig. 2.4(a). Tapered bar-fibers are used directly for the input and output ports. A double-sided coated micromirror is used. A low insertion loss of 0.6 dB and sub-millisecond switching times are achieved. However, the limitations imposed by the switch structure (no collimating optical lenses are used) restrict the switch scalability to 2×2. This type of micromirror is best for 2×2 switches, unless optical coupling lenses are used, and can not be expanded to a large switch matrix without difficulty. A 4×4 version of the switch [61] using a weakly guiding and strip-loaded integrated optical waveguide [62] was fabricated, but it resulted in significantly high insertion loss.

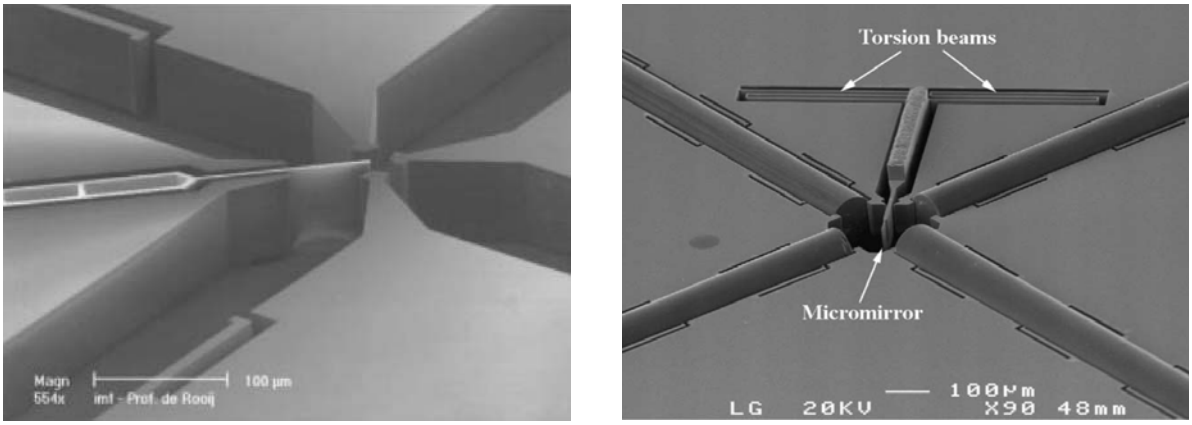

(a) (b)

Figure 2.4: (a) SEM of a micromirror fabricated by DRIE and actuated by a comb-drive [3]. (b) SEM of a magnetically actuated micromirror for the same switch architecture [4].

A similar switch that uses a magnetically actuated micromirror [4] is shown in Fig. 2.4(b). The micromirror is connected to the substrate by means of a torsion spring. A soft electroplated nickel as magnetic material on top of the actuator and vertical magnetic field induced by an external electromagnet were used to actuate the micromirror. The micromirror can be rotated

both upward and downward from its initial state if the direction of the magnetic field is changed by altering the input current to the coil. The torsion springs are used to return the micromirror back in its original position once the current is removed. The switch exhibits a 1 ms switching time, a 0.8 dB insertion loss, -60 dB cross-talk, and a power consumption of 223 mW.

Another micromirror-switching mechanism uses stress-induced bending bimorph beams (due to residual stresses in materials with different thermal coefficients of expansion resulting from different deposition temperatures) [5, 41]. The residual stresses cause the beam to curl up in the initial state. The height of the beam tip depends on the residual stress between the two layers as well as on the beam length. The larger residual stress in long beams provides a good vertical distance for bypassing optical beams in such switches. A vertical micromirror is assembled on the beam normal to the substrate as shown in Fig. 2.5(a). The switch is activated by electrostatic forces with a low operating voltage of 18V [41]. The micromirror is used to form a large switch matrix of 10×10 [5]. A 2×2 switch has a $600\mu s$ switching time and a 0.7 dB insertion loss. A similar micromirror is actuated using magnetic force to move the beam-carrying micromirror in and out of the optical path, as shown in Fig. 2.5(b) [6].

2.1.2 3-D MEMS $N \times N$ Optical Cross-Connect

The development of a 3-D MEMS optical cross-connect followed the 2-D MEMS switch to increase the switch scalability, which was needed because of the explosion of data transmission on the internet. The development of a 3-D MEMS switch emphasized a large port number, low uniform insertion loss, low power, low cost, and a small footprint. A 3-D MEMS-based transparent OXC with a large port count was realized using the two main architectures illustrated in Fig.3.12. Optical cross-connects with port counts from 64×64 to 1296×1296 were realized using the two architectures shown in Fig.3.12 [8, 42, 44, 45, 43, 46, 47, 48, 49, 50]. Because of the rapid proliferation of new network services, especially those involving mobile access applications, the most recent system focuses on access to metropolitan area networks which need fast cross-connect optical switches of the 100×100 class for practical deployment [8, 42, 43]. 3-D switch architecture offers low and uniform insertion loss compared to 2-D switch architecture. The number of micromirrors scales linearly with the number of input ports, which is in contrast to the scalability of system used in the 2-D switch.

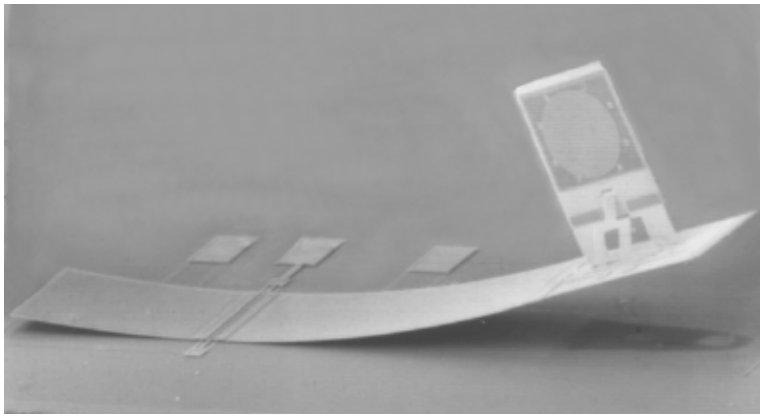

(a)

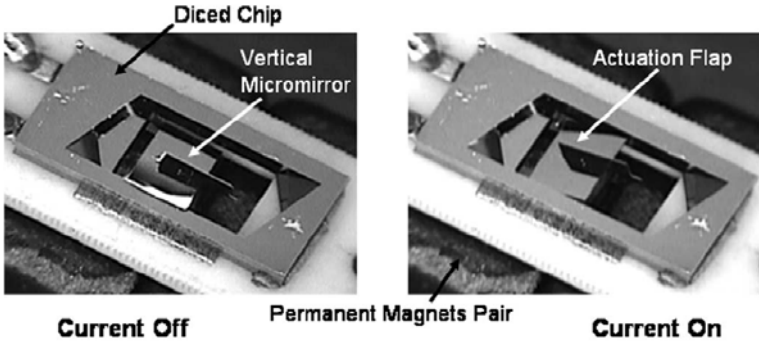

(b)

Figure 2.5: (a) SEM of a stress-induced beam-carrying micromirror [5]. (b) SEM of magnetically actuated micromirror [6] using an idea similar to that in (a).

Two 3-D MEMS switch architecture have been developed. The first consists of two identical sets of components called input and output components. Each component set consists of a 2-D array of fibers, lens collimators, and 2-D array of steering micromirrors as shown in Fig. 3.12(a). The input fibers are arranged in matrix-like form and are attached to the same arrangement of lenses for collimation. The optical beams are steered in three dimensions by two stages of dual-axis micromirrors, directing them toward the desired output port. The second switch architecture [8], illustrated in Fig. 3.12(b), uses the same components as the previous architecture,with the addition of a roof-type micromirror. The arrangement of the switch components is different and provides efficient way to downsize the switch. The input and output 2-D arrays of fibers are located in the same plane. Same configuration applies to the 2-D arrays of steering micromirrors.

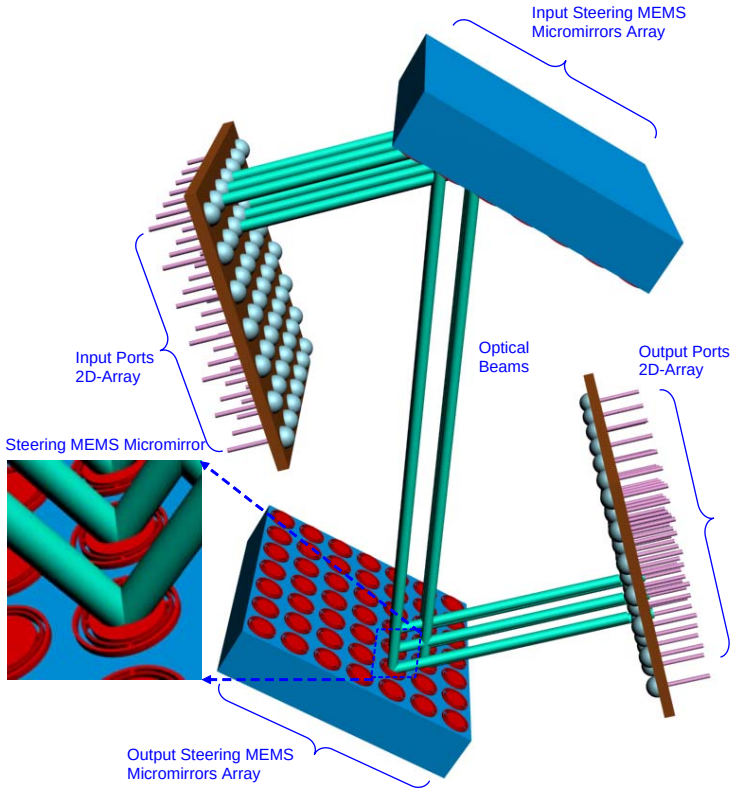

(a)

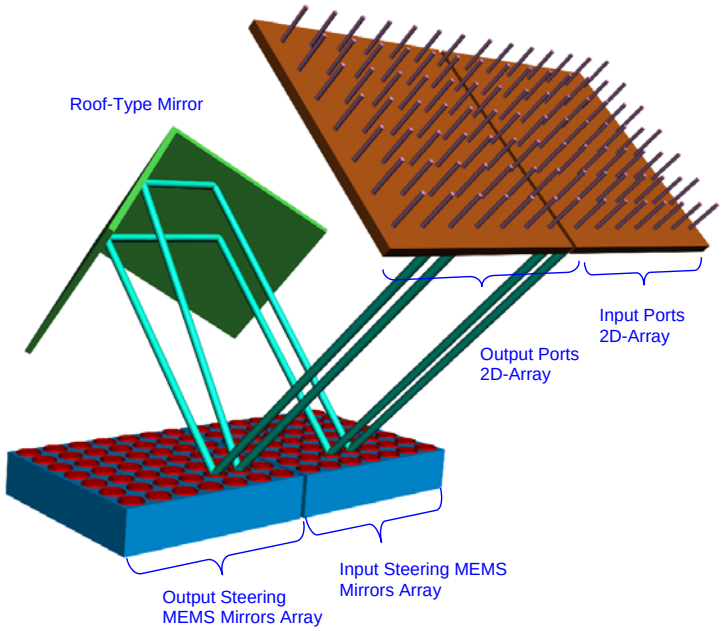

(b)

Figure 2.6: Schematic drawing of 3-D MEMS optical cross-connect architectures. (a) The first introduced switch architecture [7], and (b) The second switch architecture [8].

This configuration provides better and easier alignment of the switch components. In addition, one 2-D array of fiber and steering micromirrors can be used for both the input and output stages. The second 3-D OXC architecture requires a micromirror with a smaller steering angle in order to achieve output to the same number ports as the first architecture.

The array of two-axis steering micromirrors is considered the key to enabling the 3-D MEMS switch to operate. Important design parameters include the size, maximum tilt angle, flatness, fill factor, and resonant frequency of the micromirror. The stability of the micromirror also plays a critical role in the complexity of the control circuit.

Some of the problems associated with this type of micromirror are the micromirror residual stress that limits its size (mainly in surface micromachining fabrications), and the difference between the thermal expansion coefficient of the micromirror and that of the metal coating that causes the micromirror's curvature to change with temperature. Surface [7, 11] and bulk micromachining fabrication processes [9, 63, 64] or a combination [65] are used to fabricate the steering micromirrors. Bulk-micromachined SOI micromirrors are often and shows better micromirror surface quality in larger micromirror sizes. The actuation of such micromirrors commonly uses electrostatic forces, which provide low power consumption, a major advantage of this class of actuators. A gimbal-type structure [7, 9, 11, 64, 65] is often used to operate the steering micromirrors. Other techniques are also used [12, 66]. Parallel-plate and comb-drive actuators are the most common type for 2-D steering micromirrors. Magnetic actuators are also used to fabricate two-axis micromirrors [10].

Fig. 2.7 shows several types of steering micromirrors. The micromirror in Fig. 2.7(a) was fabricated using a surface micromachining fabrication process [7] similar to that of PolyMUMPs [53]. A self-assembly technique using the residual internal-stress between the polysilicon and the deposited metal such as nickel was used to assemble the micromirror into a 3-D structure. A modified version of this micromirror fabricated by DRIE of silicon-on-insulator (SOI) wafers [9] is shown in Fig 2.7(b). The design of both micromirrors uses the gimbal technique to achieve the required scanning angles. A similar micromirror that uses magnetic actuation [10] is shown in Fig. 2.7(c). Four springs with magnetic material deposited on them are used to actuate the micromirror for the 2-D scanning. Vertical comb-drive actuators arranged in a gimbal-type structure are used as an actuator for the steering micromirror, which is mounted on a pedestal

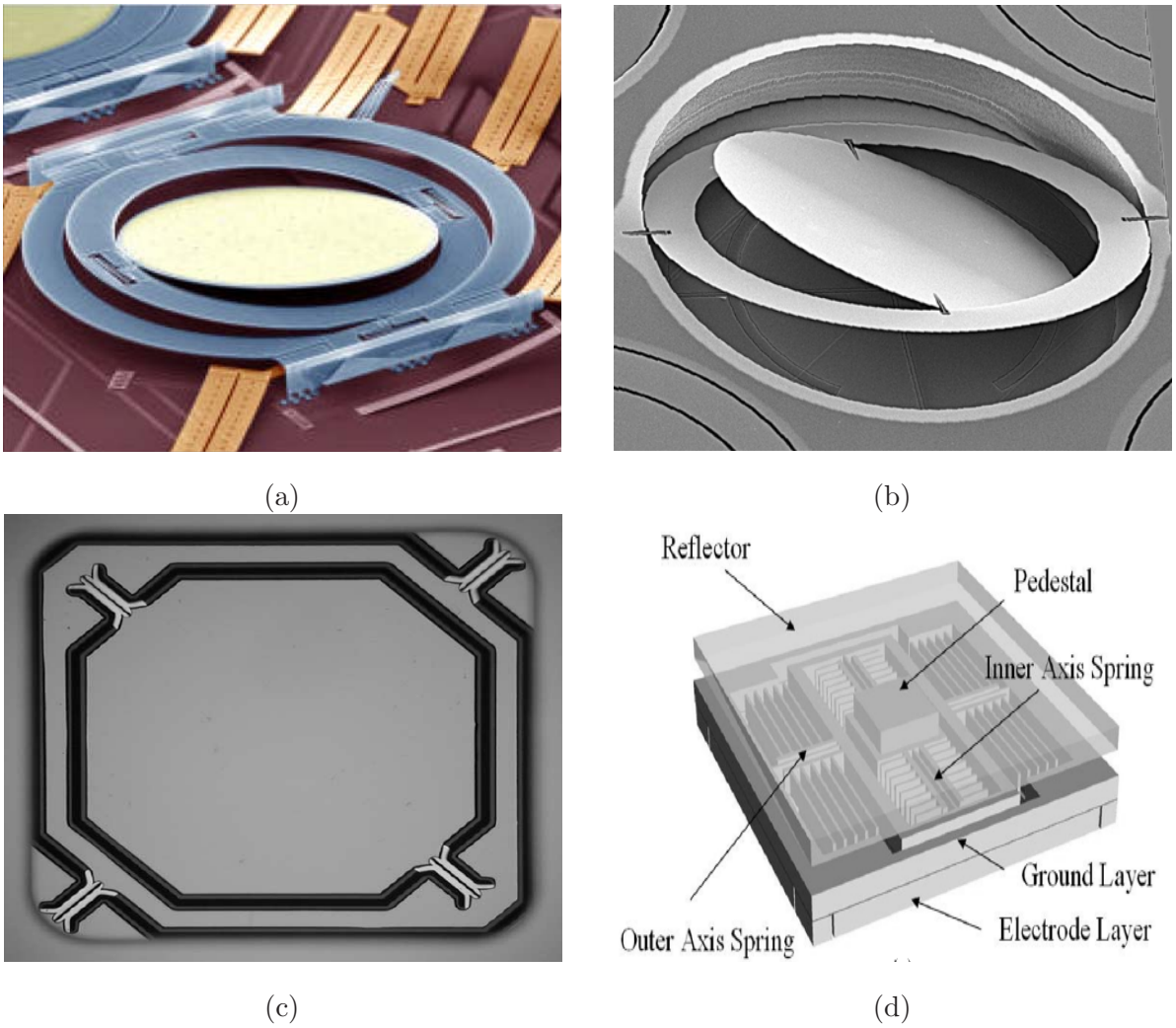

Figure 2.7: SEM pictures of 2-D steering micromirrors fabricated by surface or bulk micromachining technology using the gimbal technique. (a) A surface-micromachining self-assembled micromirror [7]. (b) A bulk micromachining version of the micromirror in (a) [9]. (c) A magnetically actuated micromirror [10]. (d) A comb-drive actuated micromirror [11].

[67]. The comb-drive actuators are best fabricated with bulk micromachining since it offers a high aspect ratio for the comb fingers.

A gimbal-less micromirror is shown in Fig. 2.8(a) [66]. The micromirror is fabricated using the SUMMiT V fabrication process [68] provided by Sandia National lab. The process involves four releasable structural layers. The micromirror is supported by two springs: a lower and upper spring perpendicular to each other. The micromirror is electrostatically actuated through four electrodes beneath it. A second type of gimbal-less steering micromirror uses four sets of angular actuators connected to the micromirror through four 2-D joints (Fig. 2.8(b)) [12]. The steering micromirror can also have a piston motion. Thermal actuators [13, 14] are also used to fabricate steering micromirrors to be used in different applications, as shown in Fig. 2.8(c) and (d). The advantage of thermal actuators is that their driving voltages are low compared to the high voltage sources required by the electrostatic ones. However, their power consumption is significantly higher than that of the electrostatic ones.

Research has been undertaken to achieve a larger scanning angle beyond the pull-in angle of the steering micromirrors [69]. This large angle, in turn, provides greater scalability of switch arrays and an increased dynamic range for the optical attenuator. Closed loop control of a double-gimbal micromirror is used to enhance the switching time and stability and to increase the tilt angle [70].

2.1.3 $1 \times N$ Optical MEMS Switch

One of the interesting optical switch fabrics is the $1 \times N$ optical switch. The switch provides switching between one common port and N output ports. This type of optical switch is important for many applications, including channel monitoring within DWDM networks; wavelength optical add/drop multiplexer; and gigabit ethernet optical switched access network (GE-OSAN) [51], which are considered a key component in next-generation optical networks.

Several switch architectures were previously used to implement a $1 \times N$ optical MEMS switch. Depending on the number of output ports, some switch designs are more desirable than others in terms of cost. The two most common switch architectures are shown in Fig. 2.9. The first architecture uses a 1-D array of N aligned micromirrors on the same substrate, as shown in Fig. 2.9(a). The number of output ports is the same as the number of micromirrors in the 1-D array.

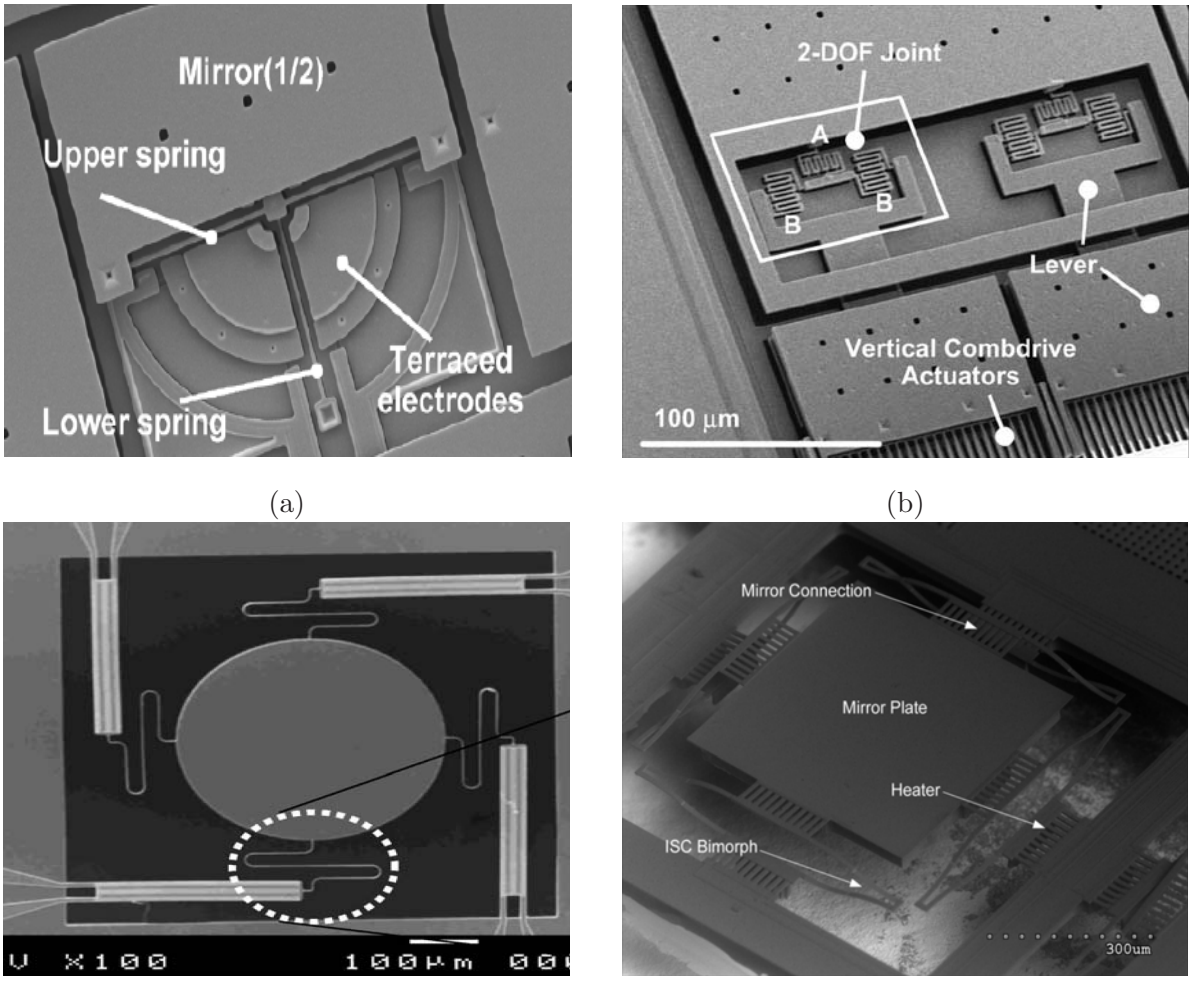

Figure 2.8: SEM pictures of gimbal-less steering micromirrors fabricated by surface- or bulk micromachining. (a) A surface-micromachining gimbal-less micromirror [11]. (b) A comb-drive and micromirror connected by 2-D joints [12]. (c) A thermally actuated micromirror [13]. (d) A thermally actuade micromirrors fabricated by a post-process of CMOS [14].

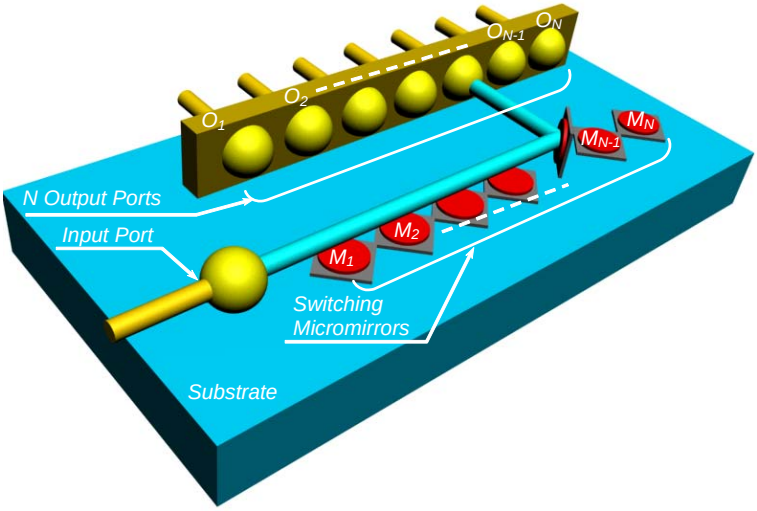

(a)

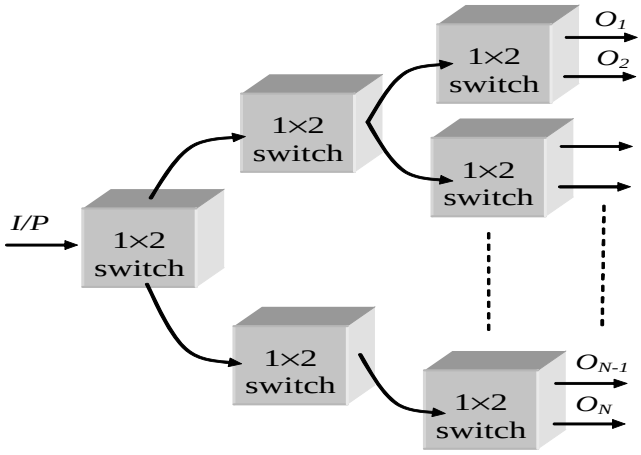

(b)

Figure 2.9: Conventional 2-D $1 \times N$ MEMS switch architectures. (a) The switch architecture uses N ON/OFF micromirrors on the same substrate. (b) The switch architecture uses several 1×2 cascaded switches to achieve the desired number of output ports.

Each outport is aligned with one micromirror. The input port is aligned perpendicularly to the output ports. The light beam coming from the input port is reflected to the desired output port when the corresponding micromirror is actuated to the ON state and all other micromirrors are left in the OFF state. The inherent variations in the propagation paths generate a non-uniform coupling loss across the output ports. Because of the significant variation differences across the output ports, an optical equalizer is required in order to achieve a uniform output signal. This requirement adds cost and complexity to the switch and is considered one of the drawbacks of this switch architecture. Most of the micromirrors used in the 2-D MEMS switch are suitable for this type of architecture.

The second architecture is shown in Fig. 2.9(b). Cascading several 1×2 MEMS optical switches achieves the desired number of output ports. The number of 1×2 switches required to build a $1 \times N$ switch using this architecture is $N-1$ placed in $log_2 N$ stages. The micromicromirror used in each individual 1×2 switch configuration is either in the ON or OFF positions to reflect or bypass the light beam to either of the two output ports. The OPLs for all output ports are the same. However, each light beam does not experience the same number of reflections. This switch configuration still causes variations in the insertion loss across output ports. In addition, the insertion loss increases as more 2-D 1×2 MEMS switches are cascaded to increase the number of output ports. Both switch architectures have limited scalability for a large number of output ports mainly because of the significant increase in the insertion loss. The maximum number of output ports reported is 32 [71].

Another technique for constructing a $1 \times N$ cost-effective optical switch is to use a high force actuator to directly align the input fiber with any of the output fibers. The most commonly used actuators for this type of switch are thermal [72, 73] and magnetic [74] actuators, which are able to produce the necessary high force. In this switch configuration, all output fibers are fixed in position, and the input fiber is attached directly to the high force actuator and faces the output fibers. Schematic diagrams of this type of switch are shown in Fig. 2.10. The output fibers are arranged in either a linear 1-D or a 2-D planar array. In the first configuration in Fig. 2.10(a), an input fiber is attached to a linear actuator that moves in plane, parallel to the substrate. The travel distance required in this case is long and is equal to twice the pitch of a bar fiber (a bar fiber has a cladding diameter of 125 μm). The second switch configuration, shown in Fig.

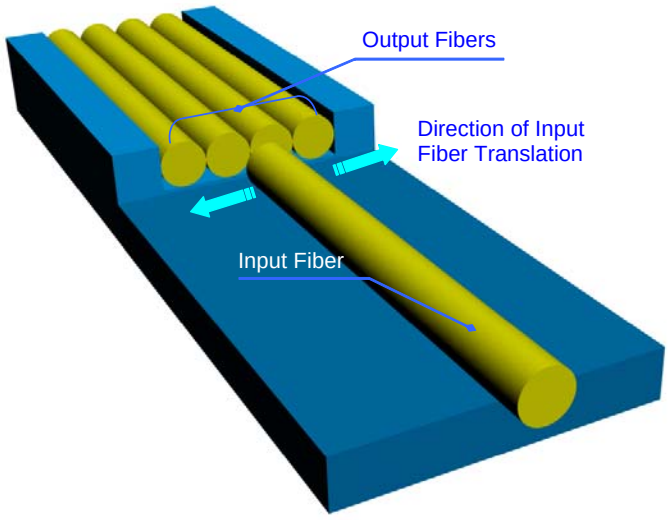

(a)

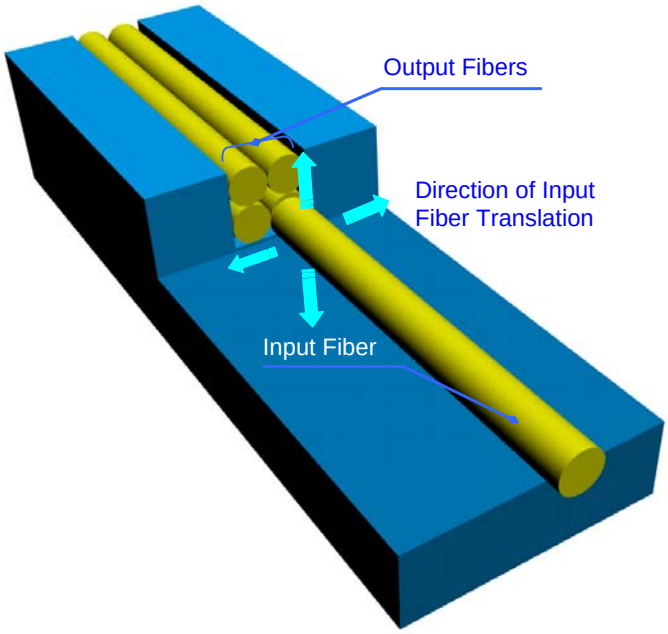

(b)

Figure 2.10: Schematic drawings of 1×4 MEMS switch architectures using a high-force actuator for direct fiber alignment with the output fibers. (b) A 1-D linear array arrangement of the output fibers. (b) A matrix-type output fiber arrangement.

2.10(b), uses an actuator that can move in 2-D space. The input fiber is placed at the center between the 2×2 output fiber arrangement. When no actuation occurs, the input fiber is not aligned with any output fibers. The input fiber has to be actuated in both x and y directions in order for it to align with any output fiber. This switch design has the advantage of low cost since neither micromirrors nor optical collimating lenses are used. However, the scalability of this type of switch architecture is limited due to the long travel distance the input fiber has to move in order to align with any output fiber. Only 1×2 [75, 76] and 1×4 [77] switches have been reported.

An efficient method of achieving a scalable $1 \times N$ MEMS optical switch is to use a smart micromirror capable of switching the input optical beam to any of the output ports in the switch. Yassen et al. designed and fabricated a 1×8 MEMS optical switch using a micromirror assembled on top of a micromotor [15] as shown in Fig. 2.11. the insertion loss is not uniform across all output fibers because of different incident angles. Output fibers can not be placed along the entire premier of the circle since an incident angle greater than 60 degrees causes significant insertion loss. This restriction means that the input and output ports can occupy only a total angle of 240 degrees and that other third of the premier of the circle is not used.

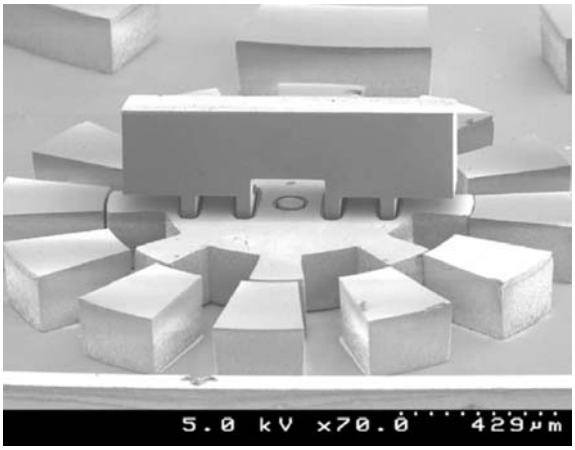

(a)

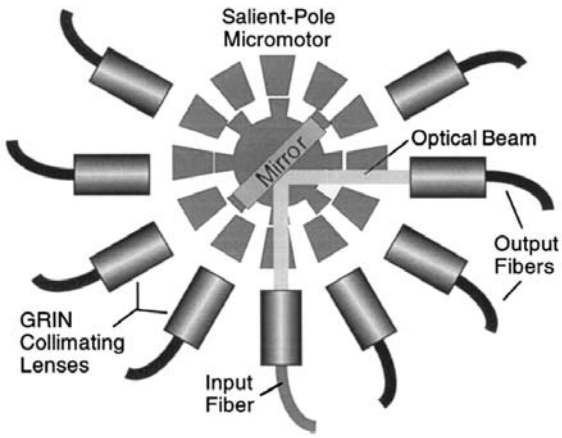

(b)

Figure 2.11: (a) SEM of a rotating micromirror [15]. (b) Schematic drawing of a 1×8 MEMS switch using the rotating micromirror.

2.2 Micromotors

To implement the rotating micromirror shown in Fig. 2.11, a rotary platform plus a microassembly technique that can assemble a micromirror on top of a rotary platform are essential. A rotary platform can be implemented using several types of actuators. Ultrasonic [78, 79], magnetic [80, 81], piezoelectric [78], electrostatic [22, 26, 82], and thermally actuated [16, 17] micromotors have been designed and fabricated in the last two decades. The small size of micromotors has made them an effective candidate for several emerging applications, such as precision surgical and medical applications [83, 84], optical scanners [24, 85], optical switching and routing of wavelengths in optical backbone networks [15, 33, 86] high-density data storage [87], and the construction of micro-robots [88, 89].

Electrostatic forces are not significant at the macro scale and are not comparable to magnetic forces. When motors are resized down to microscale, electrostatic forces become significant, more powerful, and capable of driving and actuating micromotors. Because of their small size and the fact that they can be produced through standardized fabrication processes, electrostatic micromotors are more advantageous than other types of micromotors. The next section review electro-thermal and electrostatic rotary platforms because their simple fabrication and design made them a candidate for rotating micromirrors.

LIGA [25] and DRIE of SOI wafers [24] are the two main fabrication methods for micromotors with a high aspect-ratio rotor. The surface micromachining fabrication process with two structural layers [53] has been used successfully to fabricate planar micromotors with rotor diameters ranging from 100 to 1200 μm for different applications [22, 26, 55, 82].

2.2.1 Electro-thermally Actuated Micromotors

Thermal actuators are one of the popular candidates for MEMS devices. They are simple in their fabrication and operation and can provide linear in-plane [90, 91, 92, 93] or out-of-plane [94, 95] actuation. The rectilinear stroke of an actuator can be converted into the rotary motion of a gear by means of the orthogonal arrangement of two linear actuators acting in tandem. The time-sequenced operation of this mechanism provides the motion necessary to rotate a rotary platform [17]. The main advantages of a thermal actuator are

1. Large static deflection
2. Low deriving voltage compatible with standard CMOS circuitry
3. Easy and reliable design and fabrication
4. Provision of an easy mechanism for combining the forces of an array of actuators to provide a larger force

The two types of thermal actuator suitable for driving a rotary platform are the U-shaped thermal actuator and the bent-beam thermal actuator.

U-Shaped Thermal Actuator

As its name implies, the U-shaped thermal actuator has a U-shape, as shown in Fig. 2.12(a). The narrower arm is called the hot arm and the wider arm is called the cold arm. This method relies on the difference in the expansion coefficient of the the cold and hot arms that causes the tip to bend in plane (parallel to the substrate). This type of thermal actuator can be fabricated by any MEMS fabrication process that has one releasable structural layer. Another type of thermal actuator uses three beams:two hot and one cold [96].

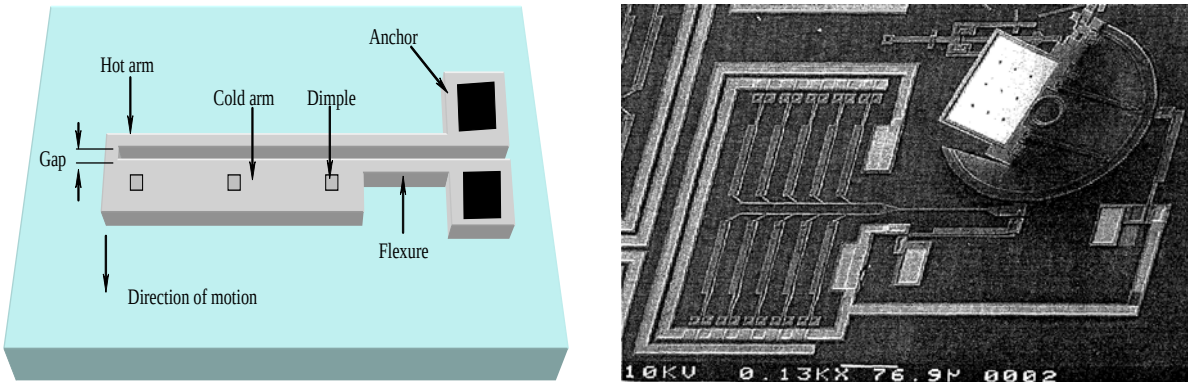

(a) (b)

Figure 2.12: (a) Schematic drawing of a U-shaped thermal actuator (b) SEM of two arrays of U-shaped thermal actuators for rotating a micromirror [16].

To operate the actuator, a voltage difference is applied between the two anchors. A current

passes through the hot and cold arms. Since the hot arm has a smaller cross section than the cold one, the current density through the hot arm is larger than through the cold arm, causing it to expand more. Since both arms are joined at the free end, the actuator tip is constrained to move laterally in an arcing motion toward the cold arm side. The resulting force and deflection of the flexure depends on the dimensions of the hot and cold arms, the gap, and the length of the flexure. The force delivered by a single thermal actuator is often insufficient to drive a microstructure to overcome friction. More often, an array arrangement is used. Fig. 2.12(b) shows SEM picture of a rotating micromirror driven by thermal actuators [16]. The micromirror can perform only half of a full rotation. Moreover, the exact angular location can not be expected or calculated. This type of micromirror is good for continuous rotation rather than for the stepwise motion required for optical switching.

Bent-Beam Thermal Actuators

The bent-beam thermal actuator is composed of two beams connected in a V-shape and anchored at both ends [91, 92, 93], as shown in Fig. 2.13(a). When voltage is applied between the two anchors, an electric current passes through the V-shaped beams. Both beams expand because of the joule heating and push the apex outward, causing in-plane rectilinear movements. The beam is designed in a V-shape so that buckling has an affinity for movement in-plane. The resistivity of the polysilicon allows the actuator to operate at low voltages and currents compatible with standard CMOS integrated circuits. It also can be fabricated using any MEMS fabrication process that has at least one releasable structural layer.

This type of thermal actuator can produce a larger force than the U-shaped thermal actuator, and the generated force per area is much better [93]. The generated force and deflection of the actuator depends on the physical dimensions of the actuator as well as on the thermal expansion of its materials. Fig. 2.13(b) shows a bent-beam thermal actuator that can rotate a rotary platform [17].

2.2.2 Scratch-Drive Actuated Micromotors

A scratch-drive actuator (SDA) is an electrostatic actuator able to offer a high force, long range, and nanometer-precision placement of $\simeq$20 nm [58]. The actuator consists of a polysilicon plate,

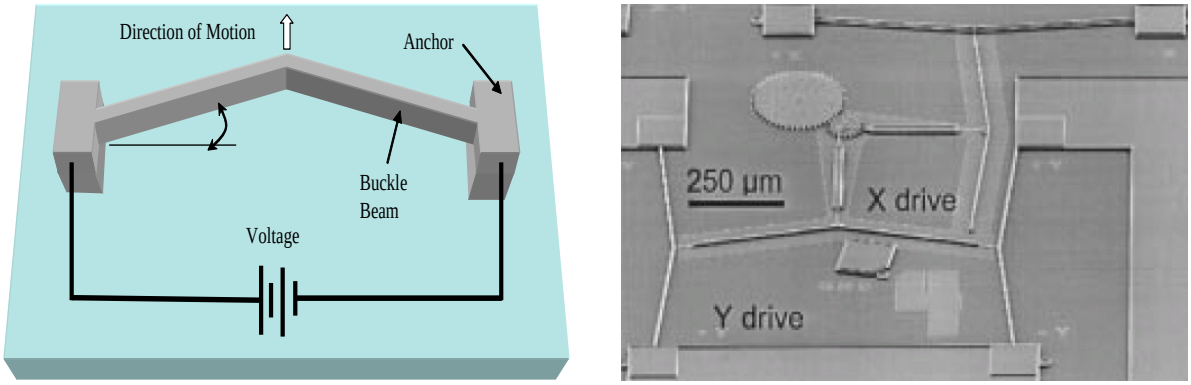

(a) (b)

Figure 2.13: (a) Schematic drawing of a bent-beam thermal actuator (b) SEM of a bent-beam thermal actuator for operating a rotary platform [17].

bushing, and supporting arms. The plate and bushing are isolated from the silicon wafer by a thin film of silicon nitride insulator as shown in Fig. 2.14. The plate and the substrate act as a capacitor. The actuator's operation depends on the electrostatic force that can be generated by applying a voltage difference between the substrate and the plate. The step motion of an SDA depends on the plate dimensions and bushing height as well as on the applied voltage amplitude. The speed of the SDA hence depends on the step motion and frequency of the applied voltage. Since each step needs one complete cycle, the simple relationship between the SDA speed and the step motion can be shown to be [58]

$$v = \Delta x \times f \tag{2.1}$$

where v is the SDA's velocity, Δx is the step motion, and f is the frequency of the applied voltage. The step motion of the SDA increases as a function of the voltage amplitudes up to a specific limit [18, 19]. Increasing the operating frequency will also increase the speed of an SDA. A speed of $500\mu m$/sec has been reached for a high frequency with a precision step of $20 \sim 30nm$.

A rotary SDA motor is shown in Fig. 2.15(b). The SDA motor produces a cyclic stepping motion from the electrostatic loading with a sinusoidal voltage signal. Depending on the signal's voltage, its frequency, and the SDA's physical dimensions, different speeds can be achieved. However, the step motion can not be accurately controlled so that it will stop at specific angular

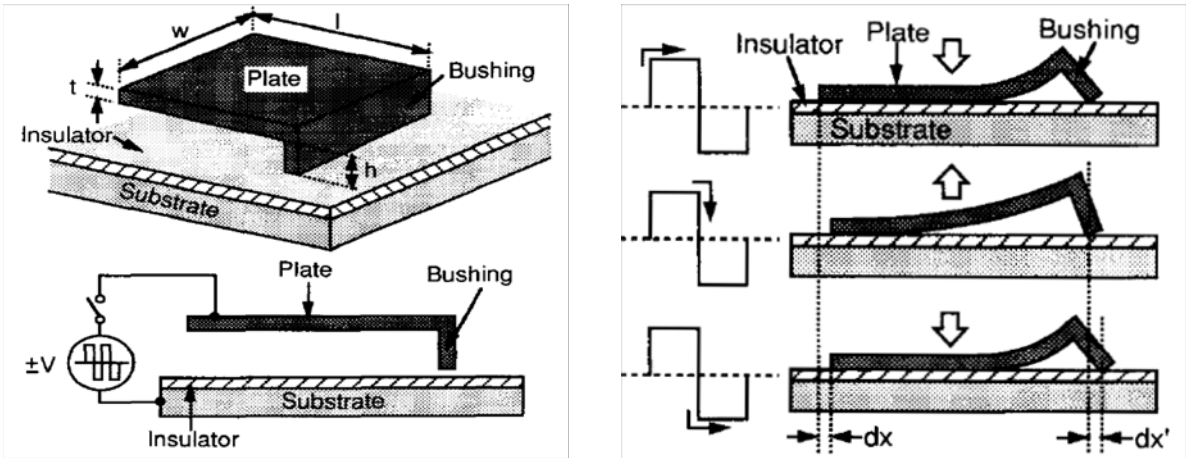

(a) (b)

Figure 2.14: (a) A schematic diagram and cross-section view of an SDA. (b) The step-motion operation of an SDA [18].

positions. In addition, since the SDA is electrically connected to the rotor, a problem will arise because of the attractive force between the rotor and the substrate.

2.2.3 Rotary Comb-Drive Actuator

A comb drive is an electrostatic actuator that consists of a stationary and a moving poles. Both poles can be arranged to provide either translational or angular movements [20, 97, 98, 99]. To achieve angular rotation, the fingers of the comb-drive should have an angular shape. Fig. 2.16(a) shows an angular comb-drive actuator fabricated by DRIE of SOI wafers [20]. A micromirror has been assembled in a vertical position to provide a reflective surface for the optical beams [97]. The angular comb drive rotates by ±6 degrees. A second micromirror has been self-assembled on top of the angular comb-drive [21]. Two wafers have been bonded using wafer-bonding techniques. The first wafer is etched to form the vertical micromirror. Then the second wafer is etched to form the angular comb-drive. A release process follows the two etching processes. The dimensions of the micromirror are $100 \times 300 \mu m$, which is considered small for optical switching. Moreover, the micromirror is able to rotate only 1.6 degrees maximum at 150 V.

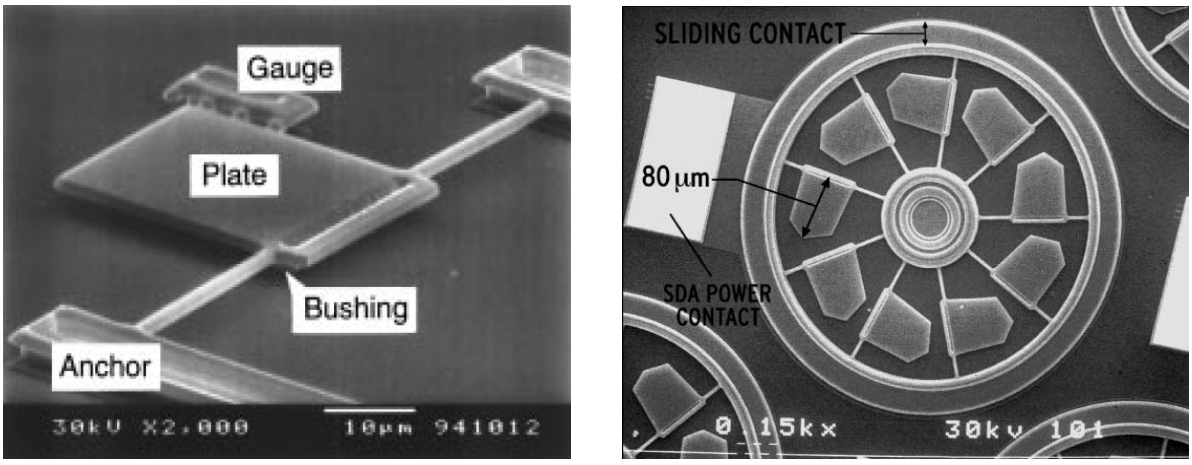

(a) (b)

Figure 2.15: (a) SEM of the first fabricated SDA actuator. (b) SEM of the SDA actuator for implementing a rotary platform [19].

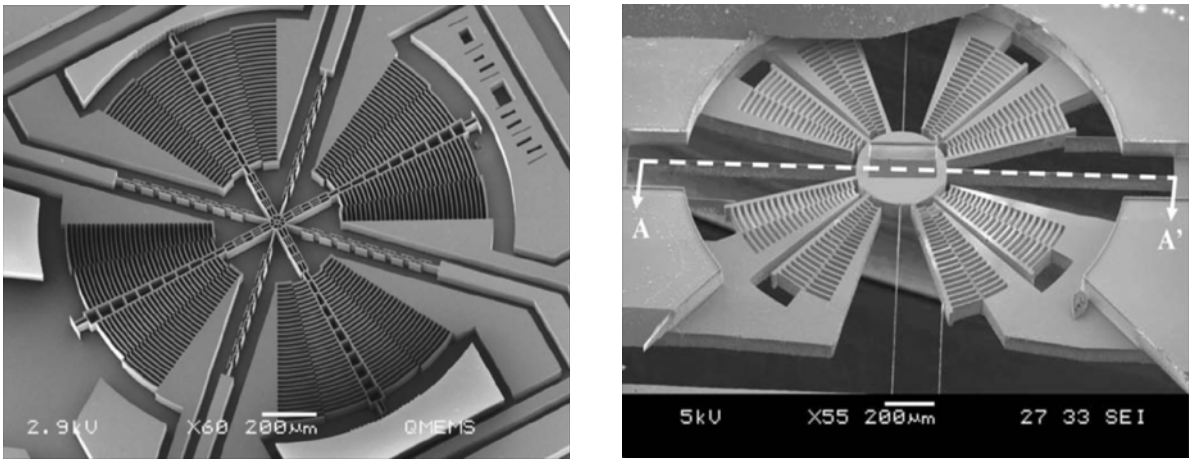

(a) (b)

Figure 2.16: (a) SEM image of a rotary comb-drive actuator [20]. (b) SEM image of a rotary comb-drive actuator with a self-assembled micromirror [21].

2.2.4 Electrostatic Micromotors

Several types of electrostatic micromotors exist, depending on the rotor and stator arrangement [82]. Side-drive, top-drive, and harmonic micromotors have been designed and fabricated. Fig. 2.17 shows different types of electrostatic micromotors with both large and small dimensions fabricated with surface and bulk micromachining techniques. The most interesting one for optical switching is the side-drive micromotor since it can provide a precise, stable, and repeatable step motion.

The first design of a functional electrostatic micromotor at Berkeley [22] was fabricated using a surface micromachining process. The electrostatic excitation of the micromotor is achieved through a sequence of high voltage pulses ($100V - 400V$) supplied to different stator poles depending on the configuration of the stator and rotor poles.

Electrostatic side-drive micromotors are variable capacitance micromotors. Basically, these micromotors consist of a number of rotating poles, which are the rotor, and a number of fixed poles that constitute the stator, as shown in Fig. 2.18. They form variable capacitors that are able to store the electrical energy. In this structure of micromotors, the ratio of rotor to stator poles is 2:3. The rotor and stator should be electrically isolated and their materials should be electrically conductive. When a voltage is applied between a set of rotor poles and stator poles, the electrical energy is converted to mechanical energy that causes the rotor to rotate around the bearing by means of torque. A micromotor with this structure operates in a stepwise or a continuous rotation. Because of the stepwise operation of electrostatic micromotors, they are attractive rotary actuators for optical switches and cross-connects since they provide precise and repeatable movement steps. The assembly of the micromirror on top of a micromotor produces a smart rotating micromirror [33, 52]. Adding extra microstructures on top of the micromotor increases the friction between the rotor bushing and the substrate This friction, in turn, increases the driving voltage required to rotate the micromotor rotor. This progression pushes the edges of the required driving voltage to the breakdown voltage in the rotor-stator air gap. The principle of operation can be summarized as follows:

1. the rotor and stator poles are divided into three sets of poles: A, B, and C, as shown in Fig. 2.18.

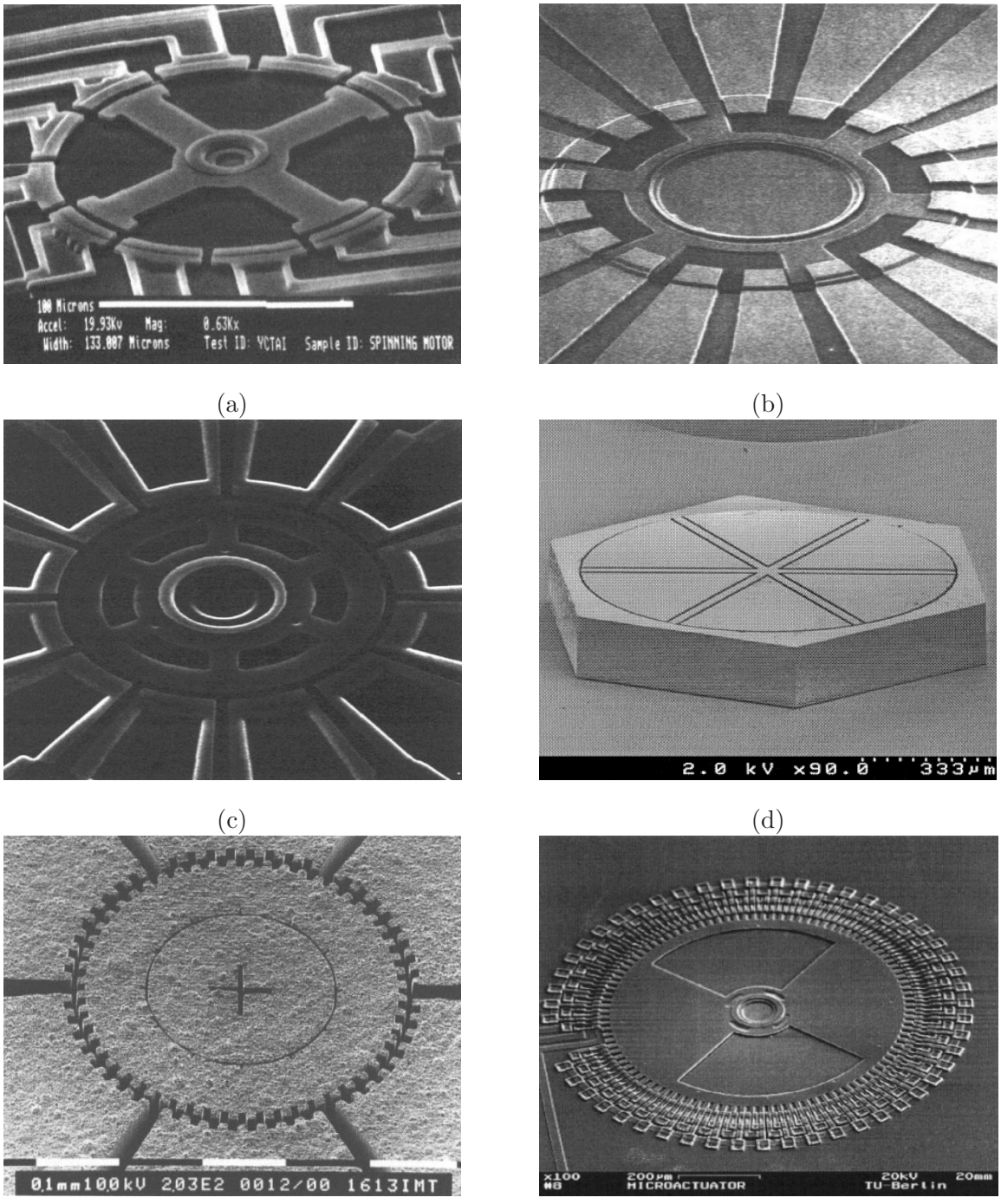

Figure 2.17: SEM pictures of several electrostatic micromotors. (a) The first-fabricated electrostatic side-drive micromotor using surface micromachining [22]. (b) An electrostatic top-drive micromotor [23]. (c) An electrostatic harmonic micromotor [23]. (d) A high aspect-ratio electrostatic harmonic micromotor [24]. (e) A LIGA-fabricated electrostatic micromotor [25]. (f) A micromotor with large dimensions fabricated by a surface-micromachining process [26].

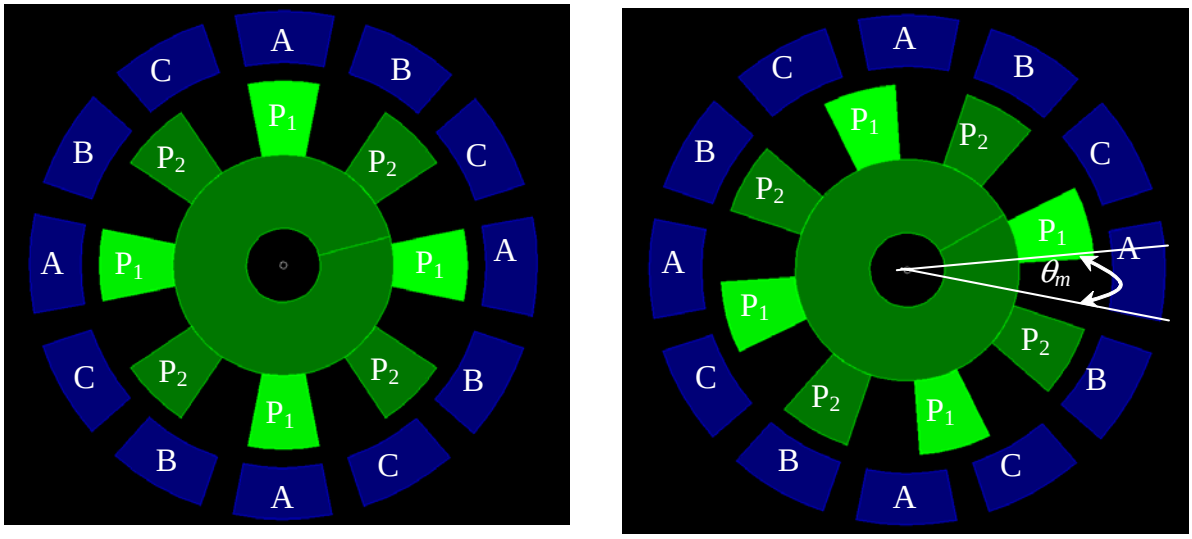

(a) (b)

Figure 2.18: Schematic diagram of the micromotor operation (a) before and (b) after actuation.

2. Applying a voltage to set A of the stator poles causes the rotor poles to align with the excited stator poles.

3. Removing the voltage from set A of the stator poles and applying it to set B produces a torque from the capacitance between set B of the stator pole and the rotor poles P_2. This torque causes the rotor to rotate clockwise by an angle equal to $\theta_m = 360/(2N_s)$, where N_s is the number of stator poles. Then the rotor poles are aligned with the new set B of the stator poles.

4. If the voltage is applied to set C of the, the rotor will rotate counterclockwise by the same angle.

5. The angle of rotation θ_m is controlled by the number of rotor and stator poles.

2.3 Microassembly of 3-D Micromirrors

In order to achieve a true 3-D structures, a microassembly is necessary to achieve the required functionality of the proposed device. Surface micromachining fabrication processes create only planar structures. Bulk micromachining of Silicon-On-Insulator (SOI) wafers are able to fabricate

structures with a high aspect-ratio, though not a true 3-D structures. Hinge-based structures [60] consists of a fixed staple and a movable pin were assembled manually using probes [100] or through the use of actuators [90, 101]. The microhinge method was among the first attempts to create 3-D structures. Self-assembly techniques and and assembly using grasping tools like microgripper or microtweezer are the most common methods to construct 3-D MEMS structures.

2.3.1 Self-Assembly Techniques

Self-microassembly techniques include plastic deformation magnetic assembly (PDMA) [30], polyimide joint technology [27], solder self-assembly [102], surface tension self assembly technique [28, 103], and thermal plastic deformation assembly (TPDA) [29], which use heat to drive the self-assembly process to create microstructures that fold out-of-plane. In this approach, a self-assembly system is designed whereby constituent microparts will assemble themselves while under the influence of an external force. Self-assembly methods are attractive because of the high yield they can provide and the nature of the process it self of being parallel assembly process to achieve as many 3-D devices assembled at one step. However, each has its advantages and drawbacks.

In all self-assembly techniques, the accuracy of the constructed 3-D structures is questionable. The sensitivity of the final rotation angle of structures is sensitive to the parameters of fabrication process. Additionally, a mechanism is required to control the final position of the assembled 3-D structures in order to ensure the required accuracy. This is considered an additional complexity added to the structures. Each self-assembly technique requires an extra customized fabrication steps in order to complete the self-assembly.

The polyimide joint process consists of a series of V-grooves etched in silicon layer of a SOI wafer. The V-grooves are then filled with a polymide material. To complete the assembly process, a temperature up to 400 C^o is required to activate the assembly process. Application of heat will results in a thermal shrinkage of polyimide material in the V-grooves. This process resulted in bending 3-D structures out-of-plane. the bending involves flexing of the structure into curved , rather than pivoting one part with respect to another. The static bending angle for the permanent out-of-plane rotated structure is controlled by the applied temperature (relatively high up to 400 C^o) and the number of V-grooves. For different static angle, different temperature is required. The application of temperature to a structures having micromirrors that consists of silicon and

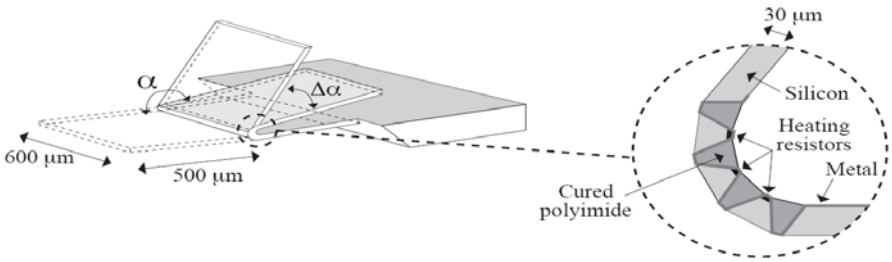

Figure 2.19: Schematic view of a 3-D structure based on a polyimide joint [27].

metal layers will results in significant micromirror curvature because of the large micromirror dimensions required for use in optical switching.

The extra steps required for this process is the need for an etch stop, and the formation of grooves by anisotropic wet chemical etching. Another problem of this process is the essential need for a mechanical limiter to control the final angle of rotation. The accuracy of assemblies is relatively low and subject to creep. Although limiters have been incorporated, these are relatively crude. Furthermore, the hinge mechanism is large (100 μm radius of curvature). It is therefore unsuitable for precision assembly of structures in this size range.

In the surface-tension self-assembly technique, a photoresist pad fills the gap between two structural parts, one is stationary and the other is movable. The movable plate is rotated into position by melting the thick photoresist at low temperature of 130 C^o. The main advantages of this method are the simplicity and the flexibility. However, it require the application of heat up to 50 min to complete the assembly. A major problem again with structures having micromirrors which ensure a curvature problem in the micromirror. Additionally, it require a mechanical limiter to achieve the required rotational angle. Although is not accurate enough for MEMS micromirrors for optical switching. Furthermore, the limiters occupy a similar area as the structure which is not suitable for the construction of a $3DRIM$.

In the thermal-plastic-deformation-assembly (TPDA) method, a bimorph of gold and polysilicon is heated in oven for 20 min at around 200 C^o or through electrical pulses of short duration at 10 15 V will cause the gold layer to yield under large compressive stresses. After relaxation, the bimorph assumes due to plastic deformation. When a current is passed through the beam, joule heating actuates the bimorph to return to its initial position. A low voltage of 10V actuated the bimorph. Additionally, assembled 3-D micromirrors through a cascade of several bimorphs

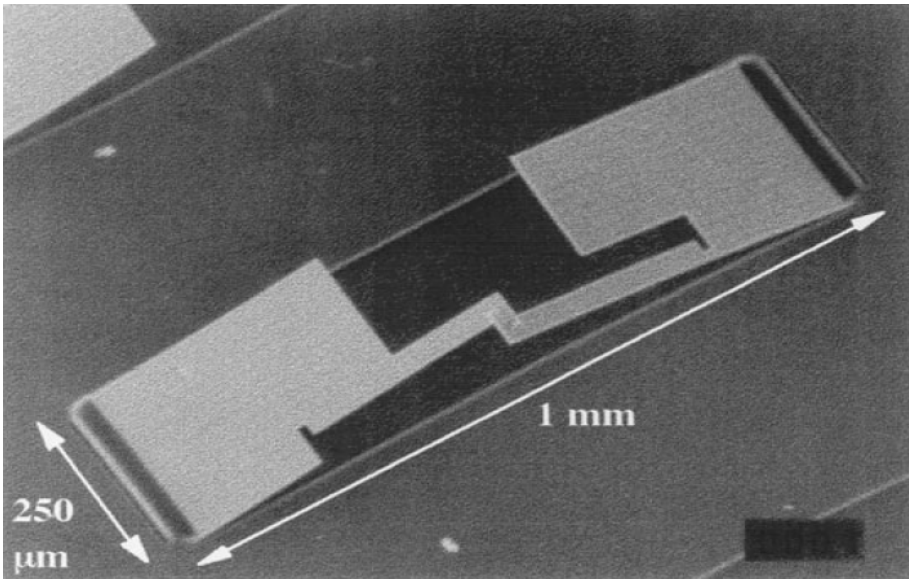

Figure 2.20: SEM of a self-assembled microstructure based surface tension technique [28]

can achieve large scanning angles and large elevation height. The well known problem of this type of assembly is the induced curvature in the micromirror. A strong magnetic field was also used to fold-out-of-plane microstructures through the use of external source [30]. The Plastic deformation magnetic assembly (PDMA) require the deposition of a magnetic material piece on the microstructure to be assembled.

2.3.2 Serial Microassembly Techniques

Serial microassembly refers to assembly tasks performed one after the other. A complete assembly task involves a series of more than one subtasks such as grasping microparts with various grasping tools, manipulation of microparts, and joining microparts. The manipulation of parts are performed through a grasping tools which has the ability to manipulate microparts in 5 or 6 degrees of freedom (DOF). Therefore, it is able to create more complex structure than other assembly methods.

A robotic base station is used to control the motion and rotation of an end-effector. This end-effector are used to grasp or handle microparts. Orthogonal tweezers microassembly [104], where a robotic system using two steel probes is used to dexterously manipulate and join microparts. Another robotic-based serial system uses microtweezers to grasp microparts and insert them into

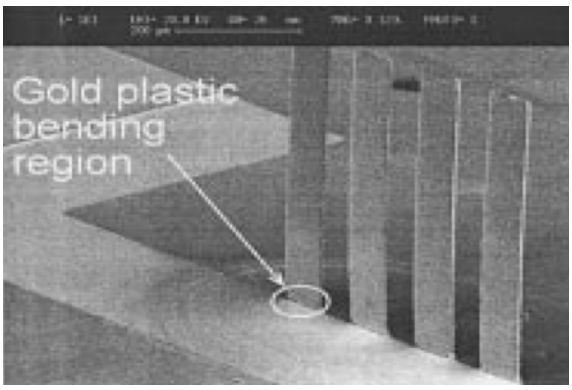

(a)

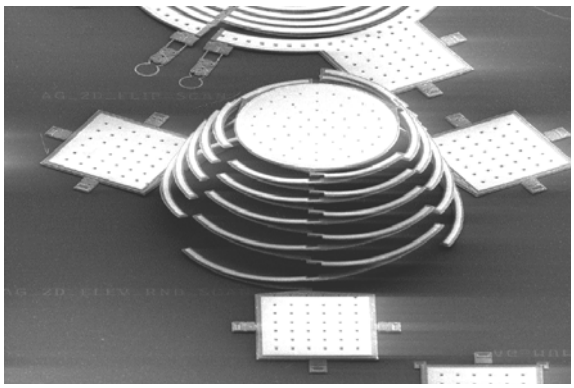

(b)

Figure 2.21: (a) SEM image of self-assembled 3-D micromirror through TPDA [29]. (b) SEM image of 3-D microstructure self-assembled by PDMA [30].

slots [105]. A commonly used tools for manipulation and grasping is microtweezers. Microtweezers are fabricated using micromachining processes such as bulk micromachining of silicon crystal [31, 106] and LIGA micromachining [107]. There are various designs of microtweezers with some designs more complex than others. Microgrippers can be generally defined as devices that "interface" with microparts using specially shaped grasping tips. The method of "interface" may consist of multiple contact points between the micropart and the microgripper. As such, microgrippers can be designed to grasp specific microparts, to hold them more securely than they could be held by microtweezers or by a pair of probes. Examples of microgrippers include surface micromachined designs that are fabricated [32, 108]

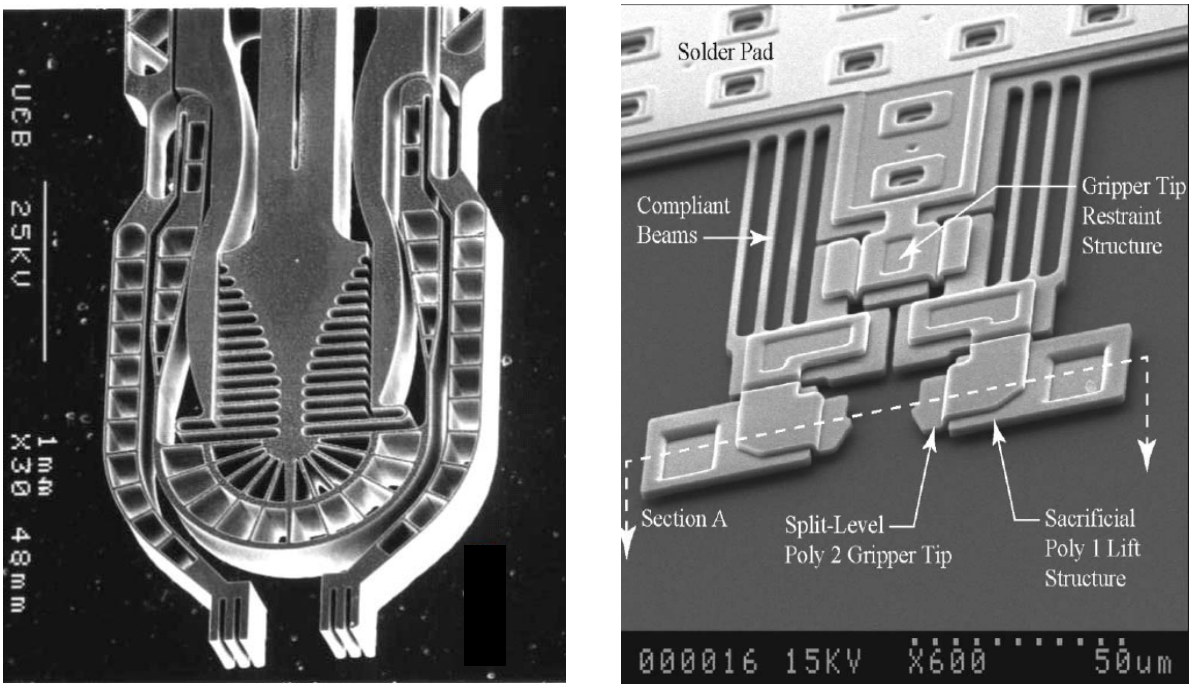

(a) (b)

Figure 2.22: (a) SEM image of microtweezers [31]. (b) SEM image of a microgripper [32].

Chapter 3

3DRIM for New Optical Switch Architectures

3.1 Introduction

To implement a high performance optical microelectromechanical systems (MEMS) switch, precise alignment of the system components, such as optical fibers, collimating lenses, and micromirrors, is critical. A small angular misalignment can cause significant power loss and high insertion loss between the input and output fibers. Angular alignment is also important for large free space optical path length (OPL). OPL is defined as the total distance the light beam travels from the input port to an output port. Scalability is another critical issue that should be considered in the design of MEMS switches for optical applications. As mentioned, 3-D MEMS switches show greater scalability than 2-D MEMS switches; however, because of their greater complexity, they are also cost more.

This chapter presents a new highly scalable architecture for a $1 \times N$ MEMS optical switch that uses only one smart micromirror capable of switching the light signal coming from an input port to a large number of output ports. The advantages of this new switch architecture are low and uniform insertion loss across all output ports, a combination of the simplicity and low cost of 2-D MEMS switches with the versatility and scalability of 3-D MEMS switches. The switch utilizes a new design concept for a 3-D rotating inclined micromirror (*3DRIM*) that is digitally operated. Fig. 3.1 shows an SEM image of the basic configuration of the first prototype of the $3DRIM$.

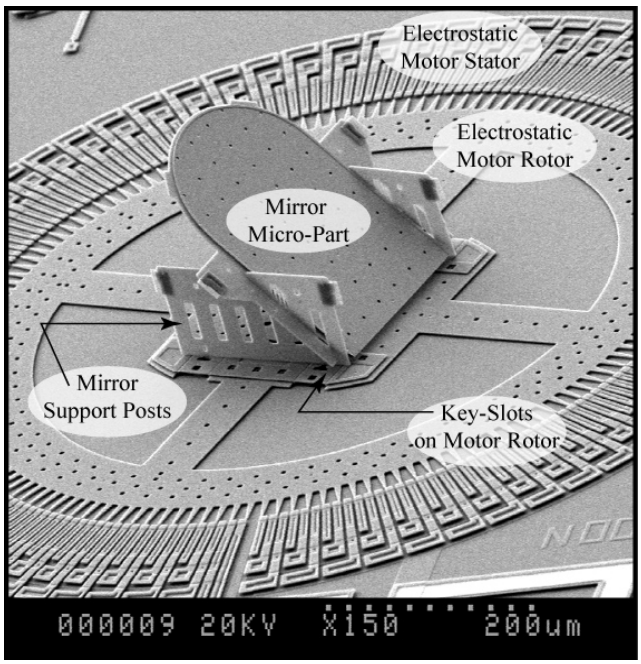

Figure 3.1: SEM image of the first prototype of the $3DRIM$. The supporting vertical posts hold the micromirror fixed at 45^o.

The $3DRIM$ has been assembled through a microassembly process [52] onto a micromotor that is capable of stepwise and continuous rotations. It achieved 480 precise steps per full revolution for switching and aligning purposes. The microassembly technique used in constructing the $3DRIM$ utilizes micro-parts fabricated with the PolyMUMPs [53] process.

A MEMS optical cross-connect (OXC) switch based on the same $3DRIM$ is also being presented. The architecture is similar to that of the $1 \times N$ switch, the difference being that each input/output port has a corresponding $3DRIM$. This switch architecture requires $2N$ of the $3DRIM$ for an $N \times N$ cross-connect switch. However it is simpler than conventional 3-D switch architecture while employing the same number of micromirrors. Moreover, the number of micromirrors required for a 2-D MEMS switch is reduced from N^2 to only $2N$. The new switch architecture is most suitable for medium-sized OXC switches.

3.2 $1 \times N$ MEMS Optical Switch Architecture

A schematic diagram of the proposed $1 \times N$ MEMS optical switch architecture is illustrated in Fig. 3.2. The switch fabric consists of two main layers. The first layer carries the input port, and the second layer carries the $3DRIM$ and all output ports. The input port is placed normal to the substrate of the second layer of the switch. The $3DRIM$ is positioned axially below the input port so that they have the same center. Output ports are positioned parallel to the substrate at equal angles around the perimeter of a circle whose center is the $3DRIM$ and equal distances along rays originating from its center. The new proposed switch architecture provides excellent symmetry for the output ports with respect to the input port in order to achieve uniform coupling loss and the maximum number of output ports. This new architecture is scalable and can readily be extended to a large $1 \times N$ optical switches.

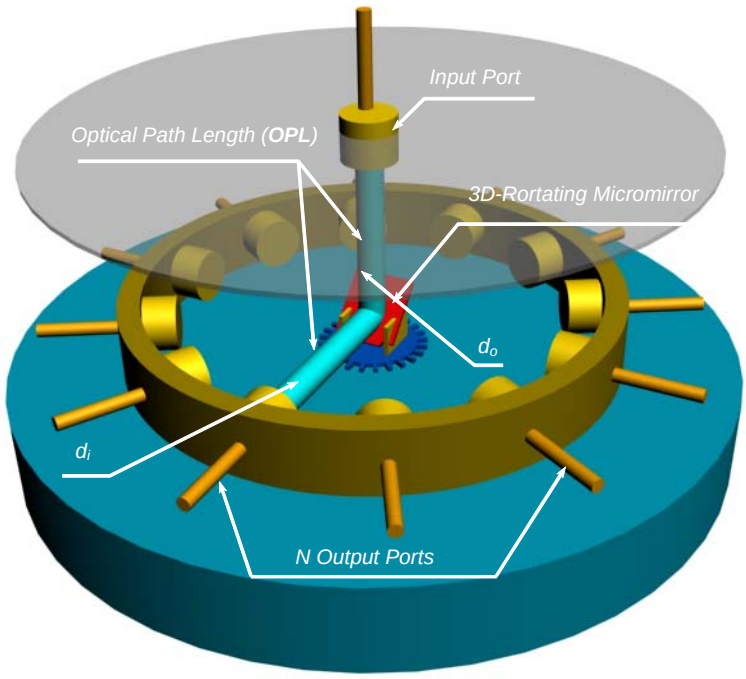

Figure 3.2: A schematic diagram of the MEMS $1 \times N$ optical switch architecture, showing the main two layers: the input and output layers. The switch utilizes only one smart micromirror to switch light from the input port to any of the output ports [33].

3.2.1 *3DRIM* Design

The main building component of the switch is the new smart $3DRIM$. The $3DRIM$ in the optical switch architecture shown in Fig. 3.2 was designed to meet the following design requirements:

1. The micromirror plane must be precisely at 45 degrees to the substrate.
2. The structure must be rigid.
3. The $3DRIM$ should be free to rotate 360 degree around its axis.
4. The $3DRIM$'s microstructures must be compatible with the design and fabrication of electrostatic micromotors.
5. The handling and joining of the constituent micro-parts must be compatible with a PMKIL [32] microassembly system.
6. The micromirror's surface must have high reflectivity and flatness in order to achieve maximum reflectivity with minimum loss.

Other fabrication processes and assembly methods were considered for the construction of a 3-D micromirror titled at 45 degrees to the substrate, but none could meet the design requirements for this system. Monolithic surface micromachining processes are not suitable since they can not create 3-D microstructures with smooth surfaces oriented at oblique angles to the substrate. Self-assembly processes were considered including polyimide joint technology [27], the surface tension self-assembly technique [28, 103], thermal plastic deformation assembly (TPDA) [29], and plastic deformation magnetic assembly (PDMA) [30]. However, self assembly methods give rise to three primary concerns. First, the process for creating the underlying electrostatic micromotor together with the fold-out micromirror and the required self-assembly layers is not commercially available, and custom fabrication would be difficult. Secondly, due to process variations, the final angle of the micromirror cannot be guaranteed with a self-assembly system.. Third, if the micromirror were simply folded out of plane without side supports it would be more prone to vibration, which may lead to intermittent coupling loss. Moreover, there was concern about heat-based self-assembly methods, in which significant micromirror curvature may occur because of the large micromirror dimensions required for optical switching.

The PMKIL microassembly system is able to avoid many of the concerns associated with other methods. It is able to assemble multiple micro-parts, even when they originate from various chips made by different micromachining processes. Further, the accuracy of the assembled microstructure, specifically the micromirror angle, and the rigidity of the assembly are designed into the micro-parts geometrically, and are a function of neither the assembly process nor the fabrication process, nor their variations. This assembly technique guarantees the desired micromirror structure. Furthermore, This process allows the use of commonly available commercial fabrication processes and does not require a custom fabrication process.

Three prototypes of the $3DRIM$ with different micromirror sizes were successfully constructed. The electrostatic micromotors used are also different sizes. The design requirement of micromotor is based on the optical switch architecture, the number of output ports, the size of the micromirror, and other parameters. The first design prototype of the $3DRIM$ consisted of three main components: the micromirror, an electrostatic stepper micromotor, and vertical *support posts*. The two *support posts*, after microassembly, support the micromirror in a fixed 45^o position. The micromirror is able to rotate around its vertical axis by a full rotation through a series of step motions. Assembly techniques for constructing larger micromirrors were also developed. The new assembly technique uses extra micro-parts to facilitate the assembly process and to achieve a more rigid structure. Stable and rigid $300 \times 380\mu$m and $400 \times 400\mu$m micromirrors were successfully constructed. Details of the fabrication and microassembly are presented in Chapter 4.

3.2.2 Switch Operation

The operation of the MEMS optical switch is as follows: The light signal coming from the input port through the first layer of the switch travels downward and hits the $3DRIM$ at a 45^o incident angle. The light beam is then reflected from the $3DRIM$ and travels horizontally, parallel to the substrate of the second layer of the switch, to the desired output port. To direct the optical beam to a specific output port, the $3DRIM$ is rotated from its rest position to the new position in a specific number of steps so that the $3DRIM$ is aligned and facing the desired output port. The purpose of the micromotor is to rotate the micromirror by the precise number of steps in order to achieve excellent alignment between the input and output ports. The electrostatic nature of

the operation of the micromotor makes it a perfect candidate for the precise stepwise motion and excellent repeatability, which are crucial factors affecting the mechanical alignment of the $3DRIM$ between the input and output ports. This alignment is critical for large free-space OPLs. When an electrostatic micromotor is designed, sufficient torque is required to compensate for the friction between the rotor bushings and the ground plane due to extra weight of the assembled microstructures.

3.2.3 Insertion Loss Characteristics

An optical beam coming from the input port collimated by an optical lens propagates to an output port. The beam is reflected by the micromirror and directed to the required output port. The propagated optical beam experience different types of losses. These losses depend on the optical path length; the incident angle, the quality of micromirror's surface which defines its reflectively; the mechanical alignment of the micromirror with the input and output ports; and the optical collimating lenses. None of the previous $1 \times N$ MEMS optical switch architectures provides a uniform insertion loss across all output ports. The insertion loss variations are due mainly to the switch architectures, presented in the previous chapter, which exhibit either different free-space OPLs and/or different incident angles. The significant variations insertion loss across output ports also requires an inline equalizer, which is considered an added cost of the switch.

The reflectivity of a single crystal silicon (SCS) micromirror coated with a gold layer is 97% [3]. A micromirror fabricated with PolyMUMPS has even lower reflectivity compared to a single crystal silicon. The degradations in the PolyMUMPS micromirror reflectivity are due mainly to the mandatory release-holes required for releasing purposes and to the small curvature in the micromirror that results from the residual stresses present in the polysilicon layers. The micromirrors used for constructing all $3DRIM$s were PolyMUMPS fabricated so that they are compatible with the PMKIL [32] assembly process. However, this method is not considered a limitation on the fabrication and assembly of the $3DRIM$ since the microassembly process can be modified to use a combined bulk and surface micromachining to construct a $3DRIM$. This topic is a good area for future research for future.

The two main factors that affect the insertion loss variations across the output ports are the free-space OPL and the incident angle of the optical beam. In the presented switch architecture,

the OPL, in the proposed structure, is equal to the sum of the input path length (d_i) and the output path length (d_o). The length of the input path length is equal to the distance from the input port to the center of the $3DRIM$. The distance d_i is identical for all output ports. The length of the output path is basically the radius of a circle whose center is the center of the $3DRIM$. The output ports are positioned on its perimeter. the distance d_o is also identical for all output ports. Hence, the total optical path length is identical for all output ports. The symmetry employed in the switch architecture also makes the angle of incidence encountered by an incoming optical beam from the input port identical for all output ports: 45 degrees. All output ports use identical GRIN lenses to achieve a long free-space OPL and minimum insertion loss. Hence, the factors that affect the insertion loss are exactly the same for all output ports, resulting in a uniform optical signal level at all output ports.

Although the optical switch architecture in [15] has the same free-space OPL for all output ports, the incident angle differs from one output port to another. The incident angle has a significant effect on the insertion loss across output ports. Therefore, the insertion loss is different for different output ports in the switch reported in [15]. Furthermore, not all points on the perimeter are used due to significant loss increase when the incident angle is increased beyond 60^o. This limitation leads to a 25% reduction in the possible number of output ports.

In contrast, the switch architecture proposed here offers both identical free-space OPL and identical incident angles for all output paths, and hence, an identical uniform signal level at all output ports. None of the reported 2-D or 3-D MEMS optical switches can offer both identical incident angles and OPLs for all output ports from the same input port, which are essential for achieving a uniform optical signal level at all output ports.

Another important point of comparison is the maximum number of output ports for each switch architecture for the same OPL. Considering the limitations of the switch architecture reported in [15] and provided that identical optical collimating leses are used, the ratio of the maximum possible number of output ports in our switch architecture to the one reported in [15], is equal to 8/3.

3.2.4 Switch Architecture Scalability

The scalability of an optical MEMS switch is considered one of the most challenging and limiting factors in any switch architecture. 2-D MEMS switches show a limited scalability due to the higher non-uniformity of the insertion loss across output ports. Insertion loss is the primary factor that defines the maximum number of output ports in a MEMS switch architecture. In the proposed switch architecture, the free-space OPL and the physical dimensions and arrangement of the optical collimating lenses used for the input and output ports define the maximum possible number of output ports by setting the maximum allowable input-to-output insertion loss and cross-talk levels between output ports acceptable in the optical switch.

GRIN lenses, pigtailed to a single- or multi-mode optical fiber, were chosen as the collimating optics since they yield excellent collimation of optical beams for long free-space OPLs [109]. Furthermore, they are not sensitive to small misalignments either at the input or output ports. A schematic drawing of a single-mode fiber attached to a GRIN lens is shown in Fig. 3.3. The GRIN lens used has a refractive index $n(r)$ that varies quadratically with the radial distance r from its center, expressed as

$$n(r) = n_o \left(1 - \frac{Ar^2}{2}\right) \tag{3.1}$$

where n_o is the refractive index on the GRIN lens optical axis and $A^{1/2}$ is the gradient constant [109]. The output at the endface of the single-mode fiber has a Gaussian profile with a $2w_o$ waist diameter, defined here as the distance between the points at which the optical power drops to

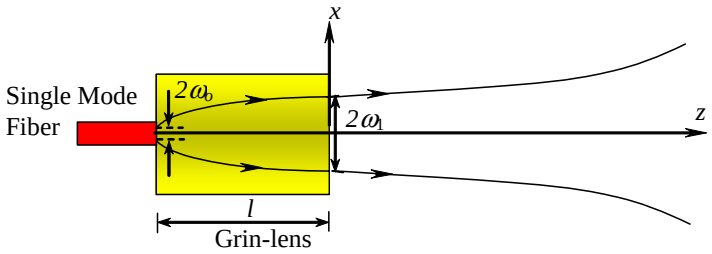

Figure 3.3: A schematic diagram of a GRIN lens pigtailed to a single-mode fiber. The single-mode fiber has an output Gaussian beam with a waist of w_o at its end face.

$1/e^2$ of its maximum. The optical beam at the endface of the GRIN lens is also a Gaussian beam with waist w_1 and radius of curvature R_1. The waist w_1 of the Gaussian beam depends on physical properties of the GRIN lens physical properties and the numerical aperture of the attached singe-mode fiber and is calculated as follows

$$\omega_1 = \frac{\lambda}{\pi \omega_o n_o \sqrt{A}} \tag{3.2}$$

where λ is the operating wave length [109]. Using a quarter-pitch GRIN lens, in which the pitch p of the Grin lens is defined as $p = L\sqrt{A}/2\pi$ the curvature radius of the Gaussian beam R_1 is equal to ∞. With a GRIN lens that produces a large waist at its output, the optical beam can propagate in the free-space with small a divergence angle for a relatively long distance with a very small change in its radius. This factor indeed decreases the coupling loss due to free-space propagation. However, a large GRIN lens diameter minimizes the maximum allowable number of possible output ports in the $1 \times N$ optical switch. The commercially available GRIN lenses have diameters of $0.5mm$, $1.0mm$, or $1.8mm$. The physical parameters of those GRIN lenses at $\lambda = 1.310$ and 1.550 μm are shown in Table 3.1 [110] along with the values calculated for the Gaussian beam waists at the GRIN lens output face.

Table 3.1: GRIN lenses physical properties at $\lambda = 1.310$ and 1.550 μm

	$D05$	$D10$	$D18$
Diameter	0.5 mm	1.0 mm	1.8 mm
n_o	1.616	1.592	1.590
$A^{1/2}$	1.349	0.597	0.327
$\omega_o@\lambda = 1.311$ μm	41.0 μm	94.0 μm	172.3 μm
$\omega_o@\lambda = 1.550$ μm	48.6 μm	111.6 μm	203.8 μm

An electromagnetic analysis of the dependency of the insertion loss dependency on the free-space propagation on the GRIN lens physical parameters, and on the micromirror sizes was performed in order to test the maximum number of output ports for a specific insertion loss and cross-talk level. The analysis was based on a fast hybrid simulation method developed at the University of Waterloo [111, 112]. This fast hybrid method is a combination of the physical optics

and electromagnetic reciprocity theorem that uses Gaussian beams to model the propagation of light from fibers through different optical components. The method has better accuracy than ray tracing methods and is able to model all type of losses, polarization effects, and micromirror size effects, which are major factors affecting optical switch performance.

Three micromirrors with dimensions of 200 × 280 μm (Fig. 3.1), 300 × 380 μm, and 400 × 420 μm (Fig. 3.4(a) and (b), respectively) were fabricated and assembled on different micromotors. The simulations used these three dimensions in conjunction with a variety of GRIN lenses. To simulate the insertion loss as a function of the dimensions of the micromirrors, when the simulation was performed, the width was kept constant while the height was changed.

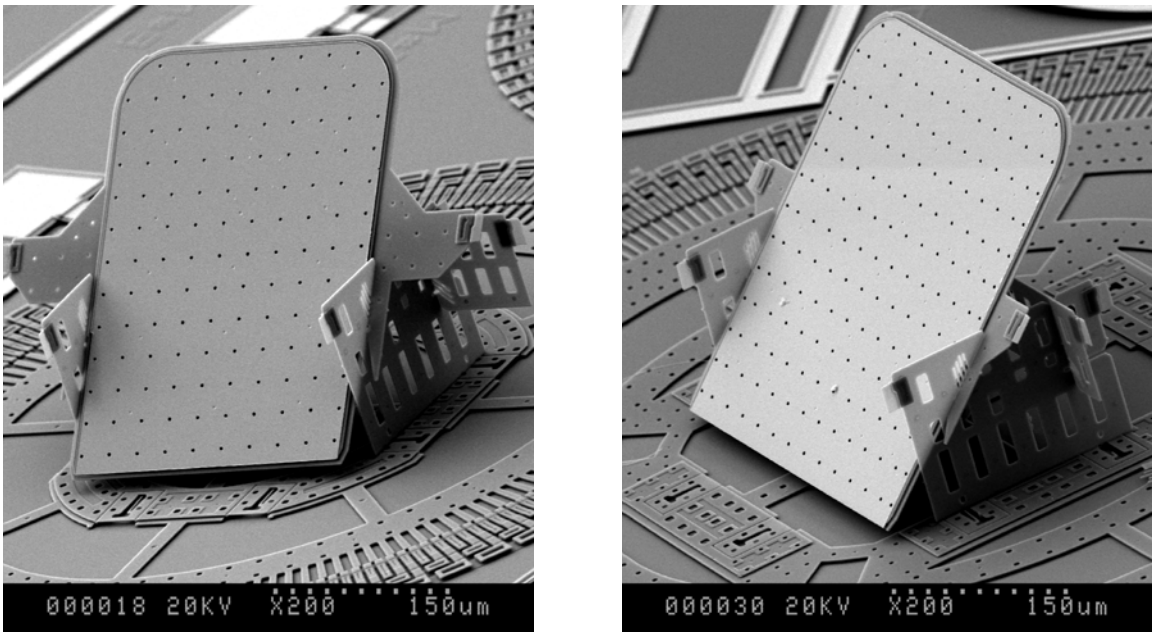

(a) (b)

Figure 3.4: SEM of assembled 3$DRIM$s. (a) A M300 micromirror. (b) A M400 micromirror.

3.2.5 The M200 Micromirror

The M200 micromirror has a width $w = 200$ μm which is kept constant in this case. The height of the micromirror height h is changed to determine its effect on the insertion loss in the switch. The polarization and reflection losses are included in all analysis. The incident angle of the

Gaussian beam is 45^o. Fig. 3.5 shows plots of the insertion loss as a function of the height of the micromirror using the same GRIN lenses at both the input and output ports for both operating wavelengths: $\lambda = 1.310$ and 1.550 μm. Using the D05 GRIN lens with a diameter of 0.5 mm, Gaussian beams with waists 41 and 48.6 μm are generated at the GRIN lens output face for $\lambda = 1.310$ and 1.550 μm, respectively. The insertion loss is unchanged at $h = 150$ μm for both wavelengths indicating that the M200 micromirror is able to capture almost all of the optical beam's power and reflect it to the output port. Moreover, the insertion loss increases significantly when d_o is increased from 1.0 mm to 20.0 mm as shown in Fig. 3.5(a) and (b). It should be noted that the value d_i is kept constant at 500 μm. The increased insertion loss is due to the divergence of the beam due to the free-space propagation.

When the D10 GRIN lens with a diameter 1.0 mm is used, Gaussian beams of waists of 94.0 and 111.6 μm are generated at the GRIN lens output face for $\lambda = 1.310$ and 1.550 μm, respectively. Since the waist of the generated Gaussian beams is larger for a D10 GRIN lens than for a D05 one, a smaller insertion loss is expected for longer a OPL. Fig. 3.5(c) and (d) show the insertion loss as a function of the height of the micromirror for both wavelengths. The insertion loss increases only a small amount beyond heights of $h = 280$ μm. Small difference in insertion loss of 0.45 and 0.44 dB are noticed between OPLs of 1.0 and 20.0 mm for $\lambda = 1.310$ and 1.550 μm, respectively.

Fig. 3.5(e) and (f) show the insertion loss for the same micromirror using the D18 GRIN lens with a diameter of 1.8 mm. The generated Gaussian beam waists are 172.3 and 203.8 μm for $\lambda = 1.310$ and 1.550 μm, respectively. The Gaussian beam waist is larger than either width or height of the micromirror. Hence, the expected insertion loss is larger and unacceptable. As is clear from the plots in Fig. 3.5(e) and (f), a micromirror with a height of $h = 280$ μm captures only part of the optical beam, which results in a large loss of 5.12 dB. No significant insertion loss variation results for OPLs of 1.0 and 20.0 mm ($\simeq 0.05$ dB), which indicates a small diversion angle of the Gaussian beam with a large waist compared to the previously generated Gaussian beams from D05 and D10 GRIN lenses.

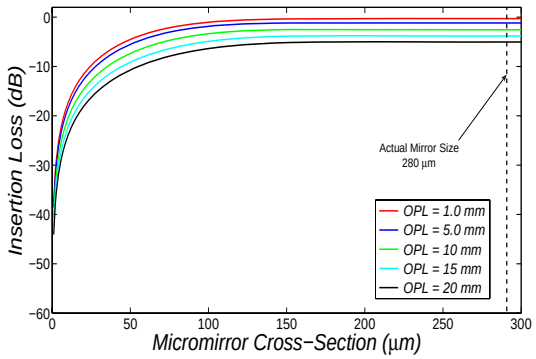

(a) GRIN lens Diameter = 0.5 mm, $\lambda = 1.310$ μm.

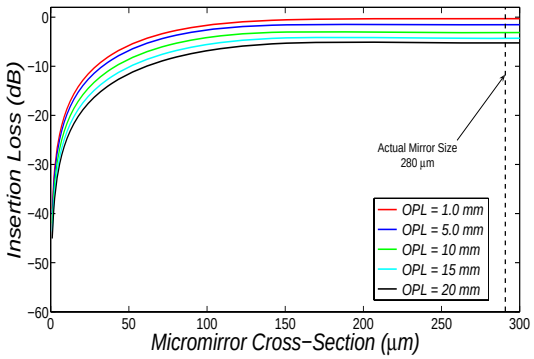

(b) GRIN lens Diameter = 0.5 mm, $\lambda = 1.550$ μm.

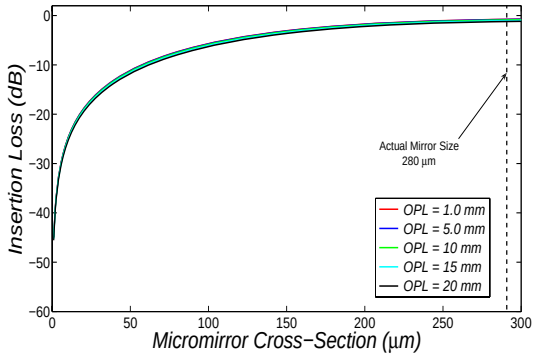

(c) GRIN lens Diameter = 1.0 mm, $\lambda = 1.310$ μm.

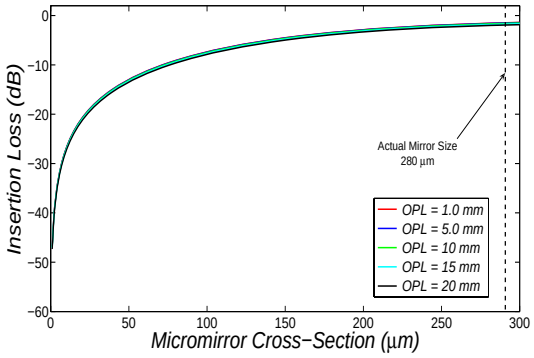

(d)GRIN lens Diameter = 1.0 mm, $\lambda = 1.550$ μm.

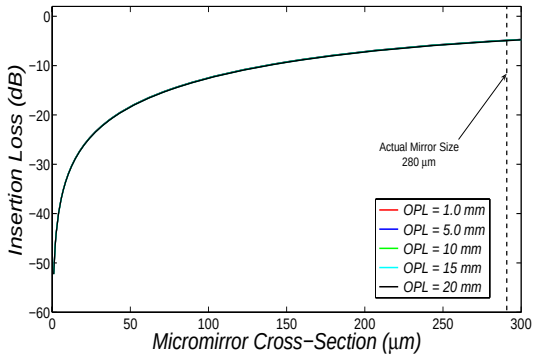

(e)GRIN lens Diameter = 1.8 mm, $\lambda = 1.310$ μm.

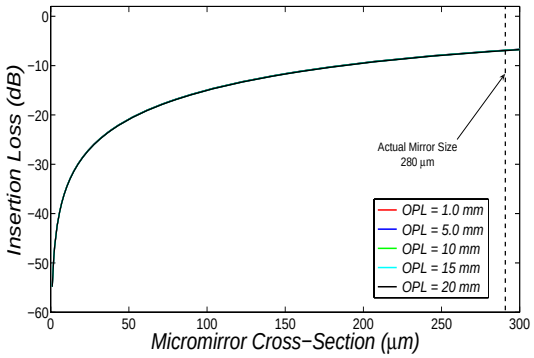

(f)GRIN lens Diameter = 1.8 mm, $\lambda = 1.550$ μm.

Figure 3.5: Insertion loss between the input and output ports using GRIN Lenses with different diameters at different operating wavelengths. The width of the M200 micromirror used in switching is 200 μm.

3.2.6 The M300 Micromirror

The M300 micromirror has a width $w = 300$ μm. The width is again kept unchanged, and the height h is varied in order to determine its effect on the insertion loss in the switch. Fig. 3.6 shows plots of the insertion loss as a function of the height of the micromirror using identical GRIN lenses at both the input and output ports. The same GRIN lenes are again used to calculate the insertion loss for the M300 micromirror. When the D05 GRIN lens is used, the micromirror captures and reflects the whole optical beam as is clear from Fig. 3.6(a) and (b). However, the insertion loss increases significantly as the OPL increases. The performance of the D05 GRIN lens is expected to be unaffected for larger micromirrors since the M200 micromirror has dimensions larger than the generated Gaussian beam waist. Better insertion loss is obtained using the D10 GRIN lens. Insertion losses of 0.78 and 1.04 dB are calculated for OPL of 20.0 mm at $\lambda = 1.310$ and 1.550 mum, respectively. The D18 GRIN lens has better insertion loss with the M300 micromirror. However, the micromirror is not able to capture and reflect all of the power of the optical beam. Moreover, no significant changes in the insertion loss are noticed for different OPLs. At an OPL of 20 mm, insertion losses of 1.3 and 2.26 dB were calculated for $\lambda = 1.310$ and 1.550 μm, respectively.

3.2.7 The M400 Micromirror

When the M400 micromirror is used, the simulated insertion losses for D05 and D10 GRIN lenses are the same as with the M300 micromirror (Fig. 3.7(a), (b), (c), and (d)) because both micromirrors capture almost all of the power of the optical beam and reflect it towards the output port. A noticeable change occurs when the D18 GRIN lens is used: this lens generates a Gaussian beam with waists of 172.3 and 203.8 μm at $\lambda = 1.310$ and 1.550 μm, respectively. Insertion losses of 1.3 and 2.26 dB are calculated for a micromirror with height of $h = 400$ μm (Fig. 3.7(e) and (f)). When micromirror height is increased to 550 μm, better insertion loss is obtained: equal 0.6 and 1.2 dB at $\lambda = 1.310$ and 1.550 μm, respectively.

A summary of the results of the simulation for the M200, M300, and M400 micromirrors using different GRIN lenses is provided in Table 3.2. The results of the simulation for the modified M400 is summarized in Table 3.3.

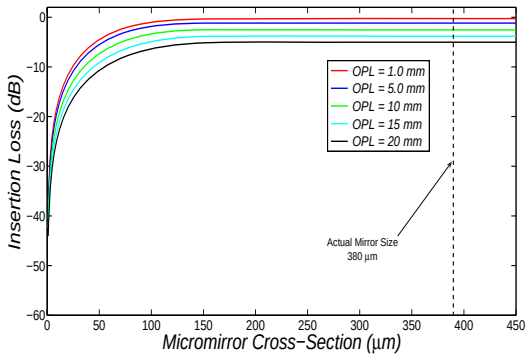

(a) GRIN lens Diameter = 0.5 mm, $\lambda = 1.310$ mum.

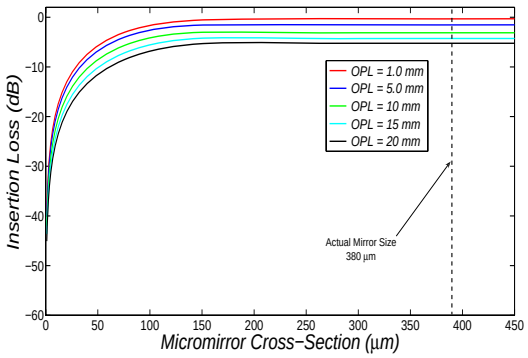

(b) GRIN lens Diameter = 0.5 mm, $\lambda = 1.550$ mum.

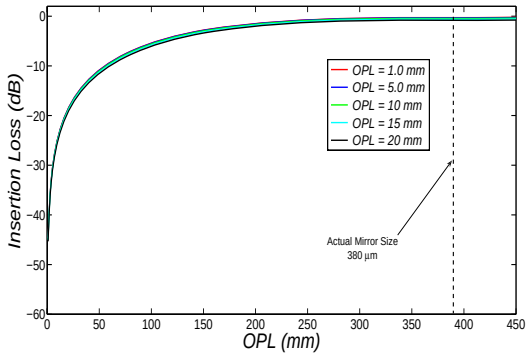

(c) GRIN lens Diameter = 1.0 mm, $\lambda = 1.310$ mum.

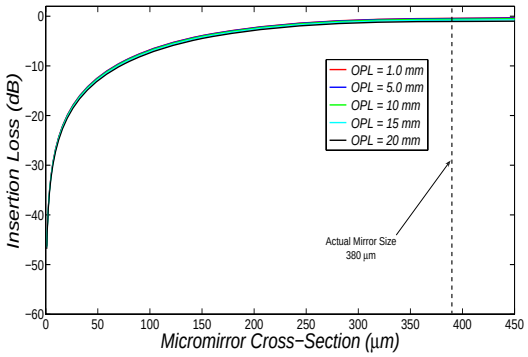

(d)GRIN lens Diameter = 1.0 mm, $\lambda = 1.550$ mum.

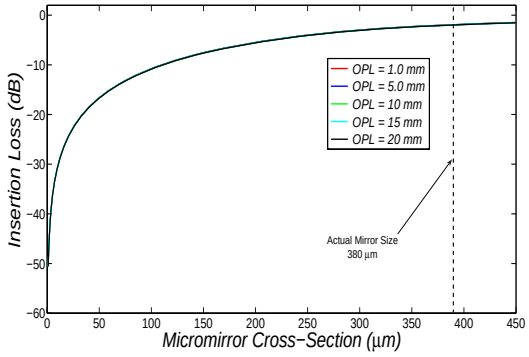

(e)GRIN lens Diameter = 1.8 mm, $\lambda = 1.310$ mum.

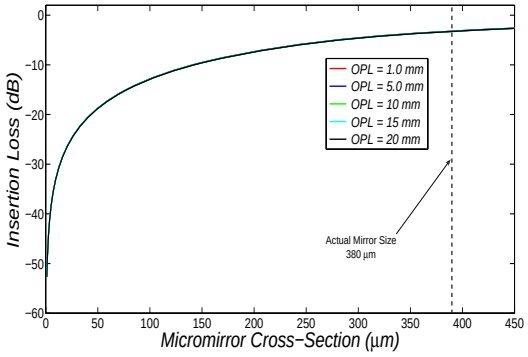

(f)GRIN lens Diameter = 1.8 mm, $\lambda = 1.550$ mum.

Figure 3.6: Insertion loss between the input and output ports using GRIN Lenses with different diameters at different operating wavelengths. The width of the M300 micromirror used in switching is 300 μm.

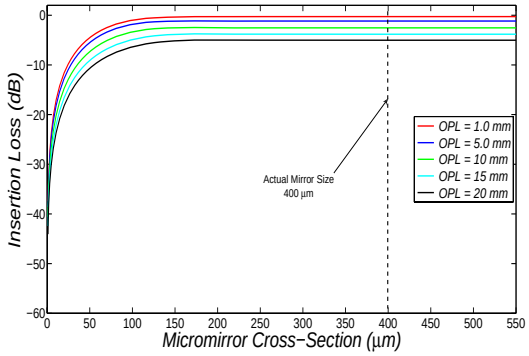

(a) GRIN lens Diameter = 0.5 mm, $\lambda = 1.310$ mum.

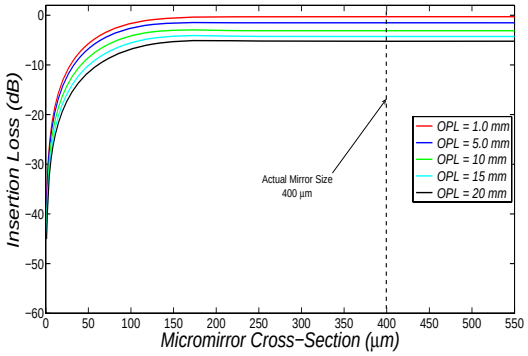

(b) GRIN lens Diameter = 0.5 mm, $\lambda = 1.550$ mum.

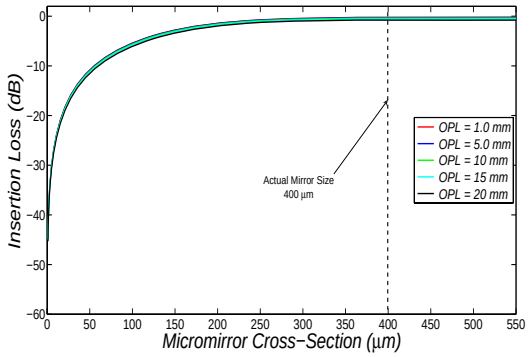

(c) GRIN lens Diameter = 1.0 mm, $\lambda = 1.310$ mum.

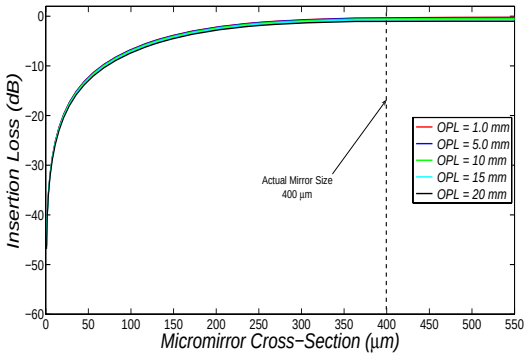

(d)GRIN lens Diameter = 1.0 mm, $\lambda = 1.550$ mum.

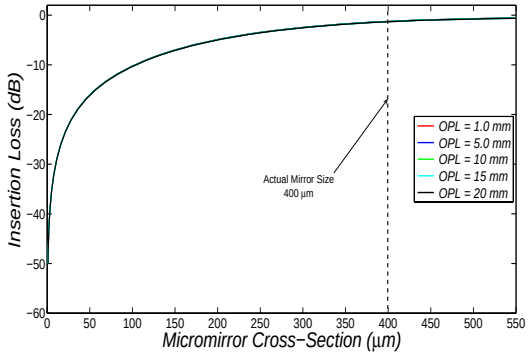

(e)GRIN lens Diameter = 1.8 mm, $\lambda = 1.310$ mum.

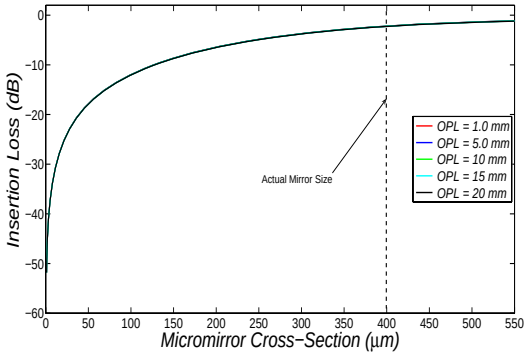

(f)GRIN lens Diameter = 1.8 mm, $\lambda = 1.550$ mum.

Figure 3.7: Insertion loss between the input and output ports using GRIN Lenses with different diameters at different operating wavelengths. The width of the M400 micromirror used in switching is 400 μm.

Table 3.2: Summary of the results of the insertion loss simulation from Fig. 3.5, 3.6, and 3.7.

M200 Micromirror						
OPL	$\lambda = 1.310$ μm			$\lambda = 1.550$ μm		
(mm)	D05	D10	D18	D05	D10	D18
1.0 mm	0.30 dB	0.81 dB	5.07 dB	0.32 dB	1.56 dB	7.13 dB
5.0 mm	1.18 dB	0.84 dB	5.07 dB	1.54 dB	1.59 dB	7.13 dB
10.0 mm	2.55 dB	0.93 dB	5.08 dB	3.13 dB	1.68 dB	7.14 dB
15.0 mm	3.85 dB	1.07 dB	5.10 dB	4.29 dB	1.82 dB	7.15 dB
20.0 mm	5.05 dB	1.26 dB	5.12 dB	5.24 dB	2.00 dB	7.17 dB
M300 Micromirror						
OPL	$\lambda = 1.310$ μm			$\lambda = 1.550$ μm		
(mm)	D05	D10	D18	D05	D10	D18
1.0 mm	0.28 dB	0.26 dB	1.99 dB	0.30 dB	0.41 dB	3.32 dB
5.0 mm	1.17 dB	0.30 dB	1.99 dB	1.53 dB	0.46 dB	3.32 dB
10.0 mm	2.54 dB	0.41 dB	2.00 dB	3.12 dB	0.60 dB	3.33 dB
15.0 mm	3.82 dB	0.58 dB	2.01 dB	4.28 dB	0.80 dB	3.34 dB
20.0 mm	5.03 dB	0.79 dB	2.04 dB	5.24 dB	1.04 dB	3.36 dB
M400 Micromirror						
OPL	$\lambda = 1.310$ μm			$\lambda = 1.550$ μm		
(mm)	D05	D10	D18	D05	D10	D18
1.0 mm	0.27 dB	0.23 dB	1.27 dB	0.30 dB	0.31 dB	2.21 dB
5.0 mm	1.17 dB	0.27 dB	1.27 dB	1.53 dB	0.36 dB	2.22 dB
10.0 mm	2.54 dB	0.39 dB	1.28 dB	3.12 dB	0.51 dB	2.22 dB
15.0 mm	2.82 dB	0.57 dB	1.29 dB	4.28 dB	0.74 dB	2.23 dB
20.0 mm	5.02 dB	0.78 dB	1.3 dB	5.24 dB	1.02 dB	2.26 dB

Table 3.3: Summary of the results of the insertion loss simulation from Fig. 3.7 for the modified M400 micromirror with a proposed height of 550 μm.

OPL	$\lambda = 1.310$ μm			$\lambda = 1.550$ μm		
(mm)	D05	D10	D18	D05	D10	D18
1.0 mm	0.27 dB	0.21 dB	0.57 dB	0.30 dB	0.22 dB	1.15 dB
5.0 mm	1.17 dB	0.25 dB	0.58 dB	1.52 dB	0.27 dB	1.15 dB
10.0 mm	2.54 dB	0.37 dB	0.58 dB	3.12 dB	0.45 dB	1.16 dB
15.0 mm	2.82 dB	0.56 dB	0.60 dB	4.28 dB	0.70 dB	1.17 dB
20.0 mm	5.02 dB	0.78 dB	0.60 dB	5.24 dB	1.00 dB	1.20 dB

Another important parameter that limits the scalability of an optical switch is the optical cross-talk between output ports. The cross-talk of the m200 micromirror was simulated using the three GRIN lenses. It was assumed that the angular pitch of the output ports is equal to the diameter if the GRIN lens. For the D05 GRIN lens, the angular pitch between two adjacent output ports is equal to its diameter d_o. Fig. 3.8 shows the insertion loss and the cross-talk plots as a function of the OPL for the D05 GRIN lens. Similar results are shown for the D10 and D18 GRIN lenses in Fig. 3.9 and 3.10, respectively. Requiring a cross-talk level limits the maximum OPL and hence the maximum number of possible output ports. Fig. 3.11 shows the maximum number of output ports for the three GRIN lenes plotted against the OPL. Based on the specified level of the insertion loss and the cross-talk, the number of output ports can be determined from the previous simulation results.

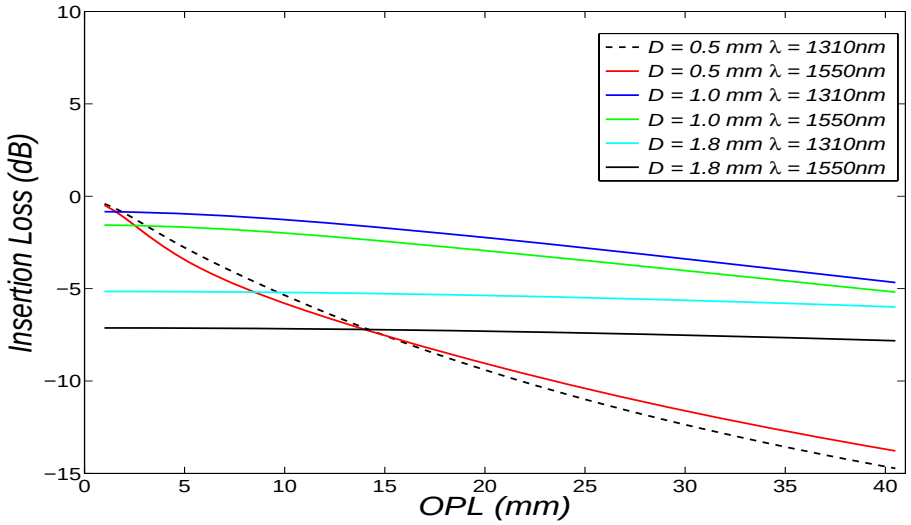

(a)

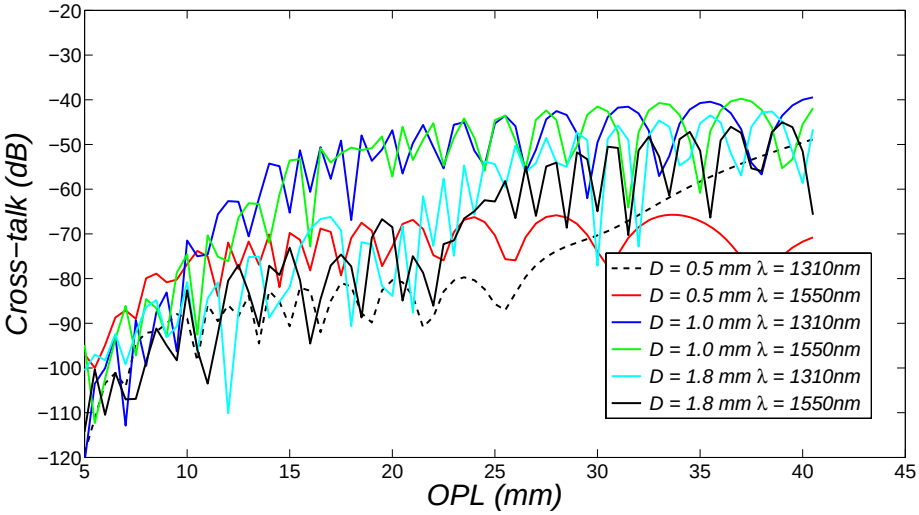

(b)

Figure 3.8: (a) Insertion loss simulation for the 200 × 280 μm micromirror as a function of the OPL. (b) Cross-talk simulation results between two output ports with an angular separation equal to the GRIN lens pitch as a function of the OPL.

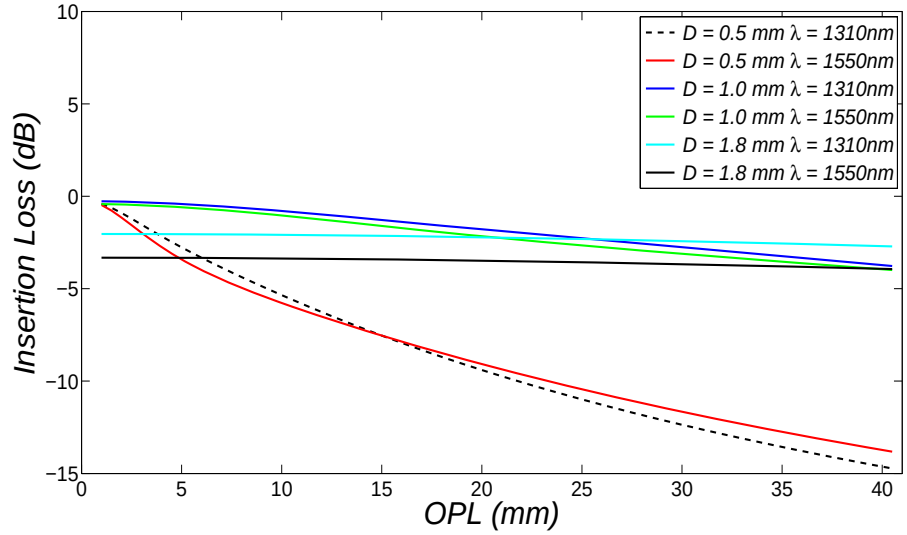

(a)

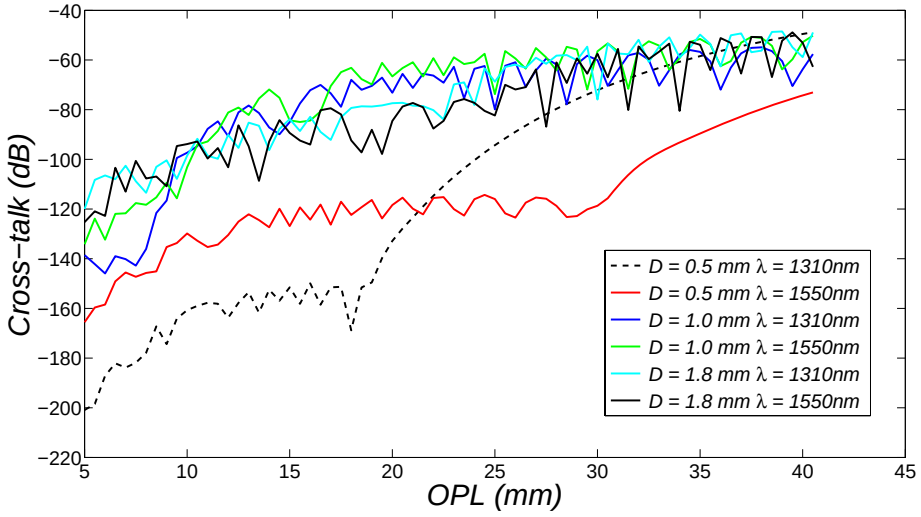

(b)

Figure 3.9: (a) Insertion loss simulation for the 300×380 μm micromirror as a function of the OPL. (b) Cross-talk simulation results between two output ports with an angular separation equal to the GRIN lens pitch as a function of the OPL.

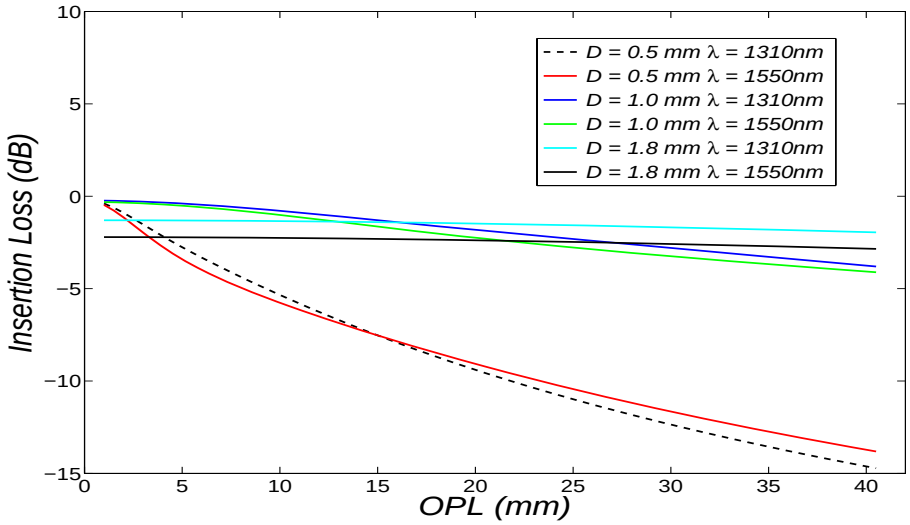

(a)

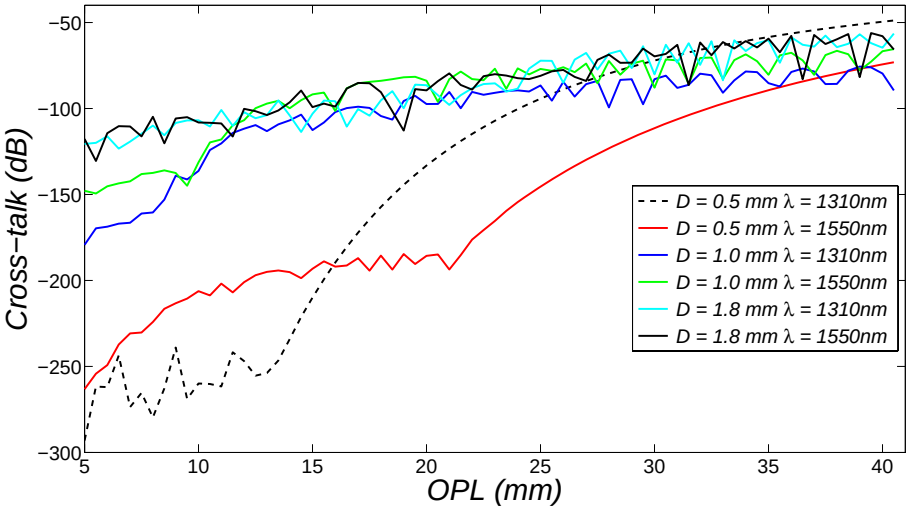

(b)

Figure 3.10: (a) Insertion loss simulation for the 400 × 400 μm micromirror as a function of the OPL. (b) Cross-talk simulation results between two output ports with an angular separation equal to the GRIN lens pitch as a function of the OPL.

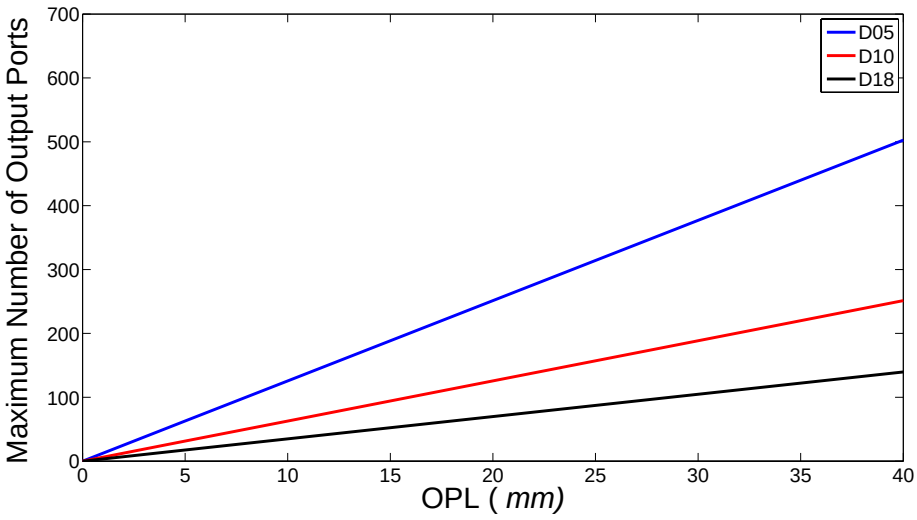

Figure 3.11: Number of possible output ports in a $1 \times N$ optical MEMS switch using D05, D10, and D18 GRIN lenses as optical coupling lenses.

3.3 $N \times N$ MEMS Optical Cross-Connect Architecture

A new optical cross-connect (OXC) switch architecture has been designed and implemented using the $3DRIM$. A schematic diagram of the proposed $N \times N$ MEMS OXC switch architecture is illustrated in Fig. 3.12. The new switch architecture provides add/drop channels for each input and output port. In this $N \times N$ switch architecture, there are N input ports, N output ports, and $2N$ $3DRIM$s. The number of micromirrors required in this OXC architecture is equal to the number of input and output ports and is the same as in the 3-D MEMS OXC switch. This number is less than that required for the 2-D switch which needs N^2 micromirrors. The switch fabric consists of two main layers. The first layer carries the input and output ports. The ports are normal to the substrate of the first layer and parallel to each other. They are also placed in a specific arrangement in order to maximize the number of ports as well as to minimize the insertion loss. The second layer carries all of the $3DRIM$s. Each input and output port has an associated $3DRIM$. A $3DRIM$ is positioned axially below each input or output port. This arrangement of the $3DRIM$s in the second layer of the cross-connect matches the arrangement of the input and output ports in the first layer. In addition, each input (output) port has an associated port for dropping (adding) an optical signal. Thus architecture offers a strictly non-blocking $N \times N$

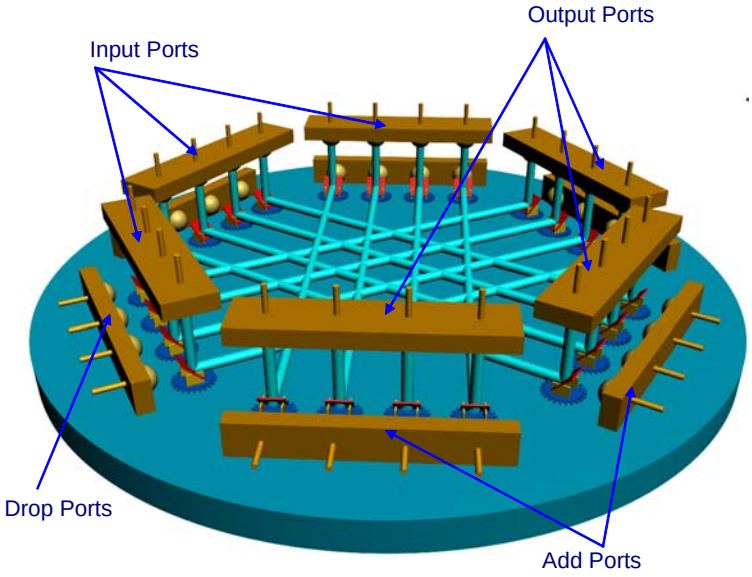

Figure 3.12: A schematic diagram of the proposed OXC architecture using the $3DRIM$.

OXC switch.

If an optical beam needs to be switched from the input port I_1 to the output port O_3, as shown in Fig. 3.13, the switching operation in the OXC switch is as follows: the light beam coming from the input port I_1 through the first layer of the OXC travels downward and hits the input $3DRIM$, IM_1, at a 45^o angle in the second layer of the OXC. The light beam is then reflected from the input $3DRIM$, IM_1, and propagates horizontally, parallel to the substrate of the second layer, to the desired output $3DRIM$, OM_3. Both input and output $3DRIM$s have to be rotated and aligned in order for the light beam to be directed to the requested output port O_3, as shown in Fig. 3.13. The optical beam hits the output $3DRIM$, OM_3, at an incident angle of 45^o. The reflected optical beam is directed to the output port O_3 in the first layer. When the optical beam is switched from any input to any output port, it undergoes double reflections from two $3DRIM$s.

Depending on the arrangement of the $3DRIM$ in the second layer and the number of steps per full rotation of the micromotor, the $3DRIM$ can be controlled to rotate and align simultaneously. In other words, a $3DRIM$ from the input set and another one from the output set are rotated so that they reflect an incoming optical beam toward the required output port. Several arrangements

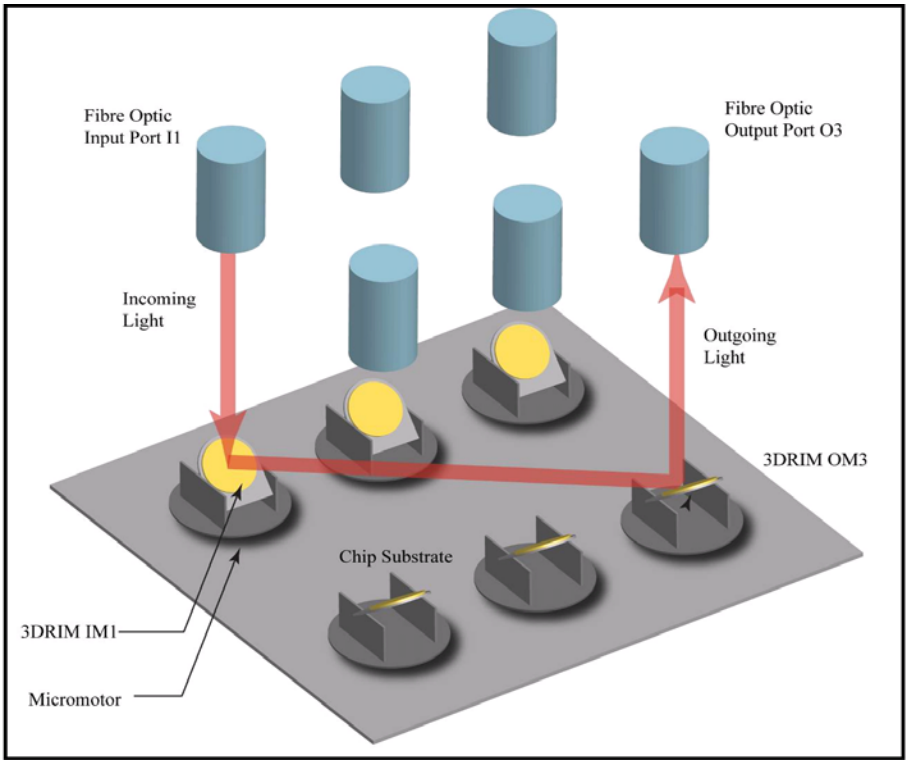

Figure 3.13: A schematic diagram of optical switching in the proposed OXC switch architecture using the $3DRIM$.

have been proposed for the $3DRIM$s in the second layer, as shown in Fig. 3.14. Assuming that the pitch of the $3DRIM$ is 1.0 mm and the maximum allowable optical path length is OPL_{max}, the maximum possible number of input and output ports can be determined for each configuration in Fig. 3.14.

3.3.1 Micromirrors in a Circle Configuration

The input $3DRIM$ sets occupies a semicircle and the other half of the circle is occupied by the output $3DRIM$ set. A circle having a diameter of OPL_{max} has a perimeter of πOPL_{max}. If an $N \times N$ OXC switch is assumed, the maximum number of output ports that occupies the semicircle, using a $3DRIM$ with a pitch of $1mm$, is

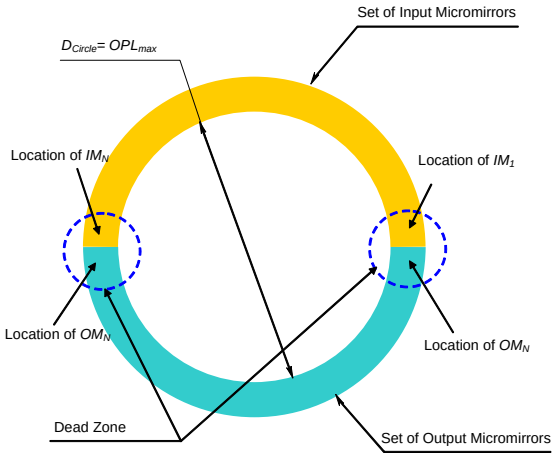

(a) Circle

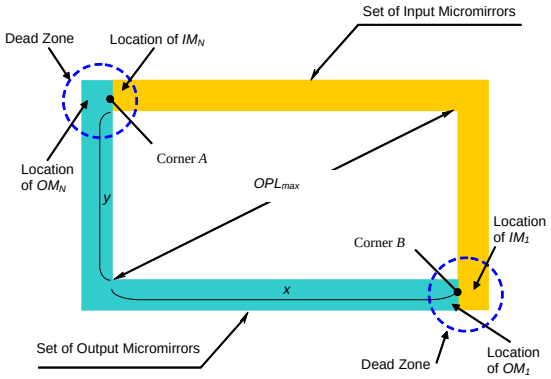

(b) Rectangle

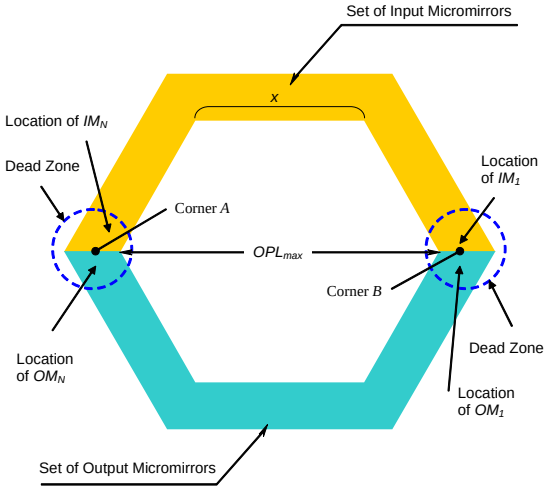

(c) Hexagonal

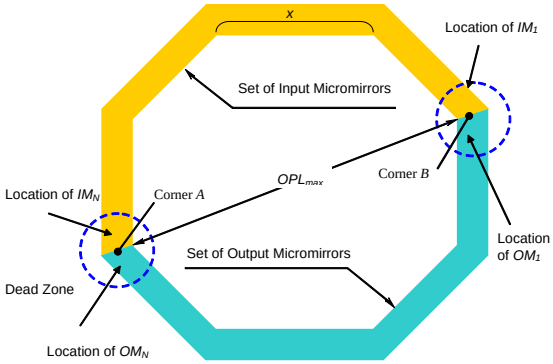

(d) Octagonal

Figure 3.14: Possible micromirror arrangements in the second layer of the OXC.

$$N^c_{max} = \frac{\pi}{2}\, OPL_{max} \tag{3.3}$$

The disadvantages of using a circle arrangement for the input and output ports are

1. The input port I_1 using the micromirror IM_1 is not able to correctly connect with the output port O_2 using the micromirrors OM_2 because of the unclear path between them.
2. This configuration uses a chip area of $\pi\, OPL^2_{max}$, a small portion of the wafer area is used and the rest of the area is wasted.
3. Using the same arrangement for the collimating optical lenses is different.

Hence, not all points on the perimeter of the circle can be occupied by a $3DRIM$. This area appears in Fig. 3.14(a), defined as the dead zone. This limitation makes the maximum possible number of output micromirrors less than N^c_{max}.

3.3.2 Micromirrors in a Rectangle Configuration

When the micromirrors are arranged in a rectangle, the maximum OPL_{max} exists between the two corners of the rectangle A and B. The set of input $3DRIM$s occupies two adjacent sides of the rectangle, and the output $3DRIM$s occupy the other two sides of the rectangle, as illustrated in Fig. 3.14(b). The relationship between the width x and height y of the rectangle is

$$OPL^2_{max} = x^2 + y^2 \tag{3.4}$$

The maximum number of output ports, N^s_{max} is

$$N^s_{max} = x + \sqrt{OPL^2_{max} - y^2} \tag{3.5}$$

For the special case of a square arrangement of the micromirrors, in which $x = y$, the maximum number of output ports $N^s_{max} = \sqrt{2}\, OPL_{max}$, which is less than in the case of a circle arrangement as calculated in Eq. 5.2 for the same OPL_{max}. The square arrangement has the same disadvantage of a dead zone (Fig. 3.14(b)), which makes $N^s_{max} < \sqrt{2}\, OPL_{max}$. However, the $3DRIM$ sets along the x or the y sides have a linear arrangement. This arrangement can be easily matched by similar arrangements of collimating lenses. In addition, no chip area will be wasted since the $3DRIM$ sets can be diced and assembled.

3.3.3 Micromirrors in Hexagonal and Octagonal Configuration

For hexagonal configurations, the maximum value for OPL_{max} exists between the two corners A and B as shown in Fig. 3.14(c).

The set of input $3DRIM$ occupies three adjacent sides of the hexagon, and the output $3DRIM$s occupy the other three sides. The maximum number of output ports is

$$N^h_{max} = 1.5\, OPL_{max} \tag{3.6}$$

The maximum number of output ports in the hexagonal configuration is less than in the circle configuration but larger than in the square one. For octagonal geometry, the longest distance between two points is between corners A and B and is equal to OPL_{max}. The maximum possible number of output ports is

$$N^o_{max} = \frac{\sqrt{2}}{cos(\pi/8)}\, OPL_{max} \tag{3.7}$$

Ideally, increasing the number of sides in a polygon eventually produce a circle. Fig. 3.15(a) shows an SEM image of a simple 4×4 configuration of $3DRIM$s for an OXC switch. The input micromotors are placed on one side, and the output micromotors are placed on the other side facing the input micromotors. Two M300 micromirrors have already been assembled for OXC switch testing and verification. Fig. 3.15(b) shows an SEM image of the assembled micromirrors.

3.4 Micromotor Design and Fabrication

The driving voltage of electrostatic micromotors is in the order of several tens of volts which is significantly high. However, the power consumption is minimal compared to most microactuators, which makes electrostatic micromotors attractive actuators for many applications. Adding the extra microstructures on the top of them increases the friction between the rotor bushing and the substrate, which in turn, results in an increase in the driving voltage required to rotate the micromotor rotor. This extra assembled microstrcurures pushes the edges of the required driving voltage to the level of the breakdown voltage in the rotor-stator air gap. Several methods of increasing the generated motive torque, which is equivalent to decreasing the required driving

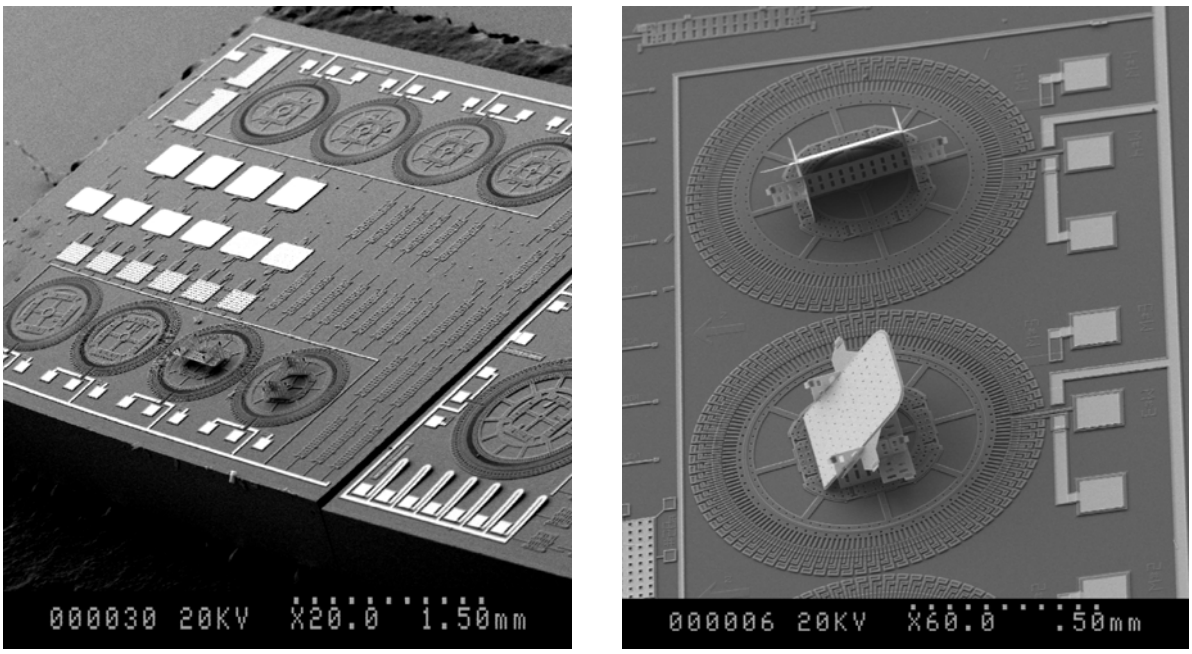

(a) (b)

Figure 3.15: (a) SEM image of 4×4 cross-connect configurations of micromotors ready for micromirror assembly. (b) SEM of two assembled M300 micromirrors.

voltage, have been explored in order to make the $3DRIM$ possible along with all the advantages it offers for optical switching.

3.4.1 Current Electrostatic Micromotor Design Techniques

Fig. 3.16 depicts the electrostatic micromotor's physical dimensions. Definitions of these physical dimensions are listed in Table 3.4. These physical dimensions are considered the design parameters of the micromotor. An optimum design of a micromotor involves the optimization of these parameters to obtain the highest generated driving torque. For this research, the design and fabrication were focused on electrostatic micromotors with a rotor-to-stator-pole ratio of $2 : 3$, although the modeling of the micromotors was not limited by this assumption. This ratio provides a maximum average of the generated motive torque and the minimum torque ripples [36].

Using a specific fabrication process imposes some limitation on the choice of the design parameters. The PolyMUMPs fabrication process is used in all micromotor designs and fabrication.

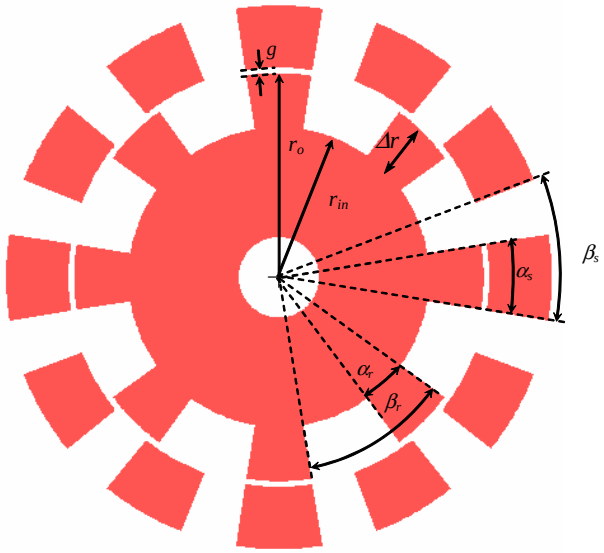

Figure 3.16: A schematic drawing of the micromotor design parameters.

In this process, the structural layer used to fabricate a rotor is POLY1: a polysilicon layer with a thickness of 2 μm. The minimum rotor-stator gap allowed in this fabrication process is 2 μm. Practically, it should be 2.25 μm in polygon layers to avoid any fabrication problems that result from the shortening of the space between the rotor and stator poles.

The purpose of a micromotor design is to generate enough torque to override the losses encountered by the micromotor rotation that result mainly from the friction between the rotor bushings and the substrate. The generated torque of an electrostatic micromotor is a result of the application of a potential difference between the rotor and stator poles, which generates electrostatic forces that act on the rotor poles. The generated electrostatic forces are categorized into three main components: the axial, radial, and tangential force components, as illustrated in Fig. 3.17. The axial force component is generated on the top surface area A_a of the rotor poles. This force component indirectly affects the micromotor operation by reducing the frictional force encountered by the rotor bushing by levitating the rotor body. The radial force component is generated on the rotor pole area A_r that faces the stator pole. This force component attracts the rotor toward the stator pole, which results in an unbalanced effect on the micromotor's operation. To cancel this effect, the micromotor has to be symmetrically excited on both sides of the rotor.

Table 3.4: Physical dimensions of an electrostatic micromotor.

Parameter	*Definition*
β_r	rotor pole pitch
α_r	rotor pole width
β_s	stator pole pitch
α_s	stator pole width
r_o	rotor radius
$\triangle r$	rotor tooth height
g	gap between rotor and stator poles
N_r	number of rotor poles
N_s	number of stator poles

Hence, an axial force having the same magnitude and opposite direction is generated on the other side of the rotor poles. This type of excitation balances the generated radial forces and minimizes their effects on the operation of the micromotor. The third force component is the tangential component, which is responsible for the generated torque required to rotate the rotor. This force component is generated on the side face area A_t of the rotor pole and is significantly larger at the edges near the stator poles. These assumptions about the generated force components are valid for a rotor made of good conducting materials. The generated electrostatic force can be controlled by a good design of the physical dimensions of the electrostatic micromotor. Hence the main task in designing an electrostatic micromotor is to maximize the generated tangential electrostatic forces while minimizing the radial force component.

The physical dimensions of an electrostatic micromotor shown in Table 3.4 control the micromotor's response and the generated torque at an applied voltage V_o. The generated torque is usually calculated using the so-called stored electrical co-energy concept, which is defined as $\frac{1}{2}CV_o^2$, where C and V_o represent the capacitance and the voltage difference between the driving electrodes of the rotor and stator poles, respectively. Two common methods are used to design electrostatic micromotors: analytical and numerical.

In the analytical method [36], the capacitance between the rotor and stator poles is calculated

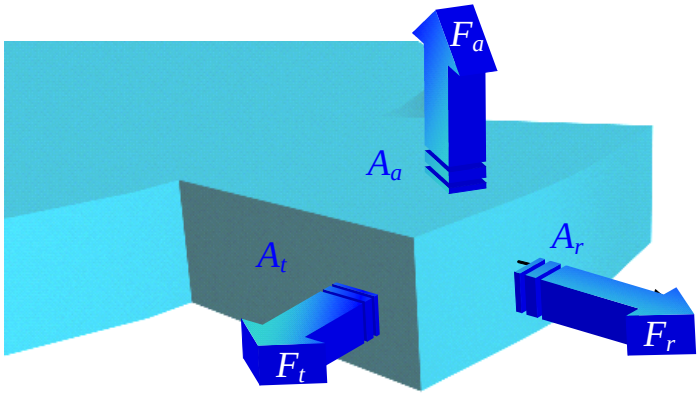

Figure 3.17: The generated electrostatic force components acting on a rotor pole as a result of an applied potential difference between the rotor and stator poles.

using the known ideal capacitor formula $C = \epsilon A/d$, where ϵ is the dielectric constant of the gap material, A is the common area of the capacitor plates, and d is the separation distance between the two plates. The generated torque is defined as the rate of change in the stored electrical co-energy with respect to a change in the rotor angle θ (i. e., the direction of rotation) and is expressed as

$$T = \frac{V_o^2}{2}\frac{dC}{d\theta} \tag{3.8}$$

The capacitance vas a function of the rotation angle θ of the rotor must be calculated in order to find the driving torque-phase curve for any micromotor. This curve is important for the dynamic characterization of the micromotor [113]. Eq. 3.8 provides acceptable values for capacitors with a large area A compared to the separation distance d. In the case of micromotors fabricated using the bulk micromachining process, the surface areas of the rotor and stator poles are large compared to the gap distance d. In the surface micromachining fabrication process, rotor is made of a layer having a thickness of around 2 μm and a gap distance g of 2 μm. Comparable dimensions for the rotor thickness and the gap cause Eq. 3.8 fail to calculate the capacitance accurately. In addition, if the RPS design technique is used, the dimensions of the rotor area A_r facing the stator pole are also comparable to the gap size. These dimensions cause the analytical

formulation using the ideal capacitor formulation to be inappropriate for the optimization of electrostatic micromotors designed with the RPS design technique.

A numerical formulation, on the other hand, needs large memory resources and a significantly longer computational time for modeling and simulating electrostatic micromotors. However, a numerical method such as the finite element method (FEM) is more accurate for modeling fringe fields and for providing accurate calculations of the rotor-stator capacitance. 2-D and 3-D FEM models are used to simulate electrostatic micromotors and they require significantly different computational times. The 2-D FEM model is faster and more appropriate for design and optimization. The 3-D FEM model is more appropriate for verification purposes. Another technique for calculating the driving torque is the Maxwell stress tensor method [114]. This method calculates the electrostatic forces generated on the surfaces of the rotor poles from the FEM simulations. Then, the cross product of the radial distance and the electrostatic force over the surface of the rotor pole is integrated in order to find the generated motive torque.

To apply numerical optimization algorithms, automated finite element modeling needed to be implemented into the design process. The physical dimensions of a micromotor are the only data necessary for the automated mesh generation and the force and torque calculations. Not all the physical dimensions are required to be optimized for the micromotor design, since some are usually set by the required application and/or the fabrication process. In addition, they are not all independent parameters. The reduction in the number of parameters efficiently narrows the focus of the design and optimization of an electrostatic micromotor to a few physical dimensions, which makes the design more efficient and faster. The rotor radius r_o is usually set by the design requirement or by the application of the micromotor. The generated torque is inversely proportional to the gap distance g. Hence it is usually recommended that the gap be keep at the minimum value the fabrication process allows, to minimize the driving voltage. The rotor-pole pitch β_r and the stator-pole pitch β_s are equal to $2\pi/N_r$ and $2\pi/N_s$, respectively. In a salient pole micromotor with rotor-to-stator-pole ratio of 2:3, $\beta_r/\beta_s = 2/3$. Hence, once the the number of rotor poles N_r is chosen, the parameters N_s, β_r, and β_s are automatically set and are included indirectly in the micromotor design process. The independent micromotor parameters required for the design and optimization process are N_r, α_r, α_s, and $\triangle r$.

Also included as an independent input design parameter is another micromotor parameter

that will account for the new geometry of the rotor poles that employ the *RPS* design technique. This parameter is introduced in Section 3.4.3.

3.4.2 Conventional Methods For Increasing the Generated Motive Torque

The driving torque of electrostatic micromotors can be increased by several methods. The first method is to increases the driving voltage supplied to the stator poles. The generated motive torque is proportional to the square of the voltage signal applied to the stator poles. The increase in the applied voltage is limited by the breakdown of the air in the gap between the rotor and stator poles that operates according to Paschen's law of air breakdown voltage [115]. The second method is to increase the thickness of the rotor and stator. In the PolyMUMPs fabrication process, the rotor layer is made of the polysilicon structural layer POLY1, which has a thickness of 2 μm. Increasing the thickness of the rotor layer significantly increases the generated driving torque given the same micromotor dimensions. A micromotor with a double-thickness layer that combines the POLY1 and POLY2 structural layers has been fabricated in order to achieve a total thickness of 3.5 μm, as shown in Fig. 3.18. The fabrication of a double-thickness rotor is not consistent for all PolyMUMPS runs and possible variations and failures exist in different fabrication runs. Fig. 3.19 shows a microscopic image of another micromotor with double-thickness rotor from a previous run. Both rotor and stator poles were totally etched, and only a disk remains from the rotor. The double-thickness method can be used to design and fabricate only rotor poles with widths of more than 5 microns due to the mandatory fabrication rules for achieving a double-thickness layer. Smaller structure size is not possible, which is considered a limitation when the number of rotor poles is increased. A better method is to customize a fabrication process to fabricate the POLY1 layer with a larger thickness or to use SOI wafers that provide a rotor with a high-aspect ratio [15, 24] in order to fabricate the micromotor.

The third method of increasing the generated motive torque of electrostatic micromotors is to increase the number of rotor poles. This technique has been successfully used to design micromotors with large dimensions. The fabricated large micromotors generate sufficient driving torque to rotate the rotor [26]. The large number of rotor poles significantly increases the generated motive torque. A finite element simulation [26] of the generated motive torque showed that the torque was significantly larger than in a micromotor with physical dimensions derived from an

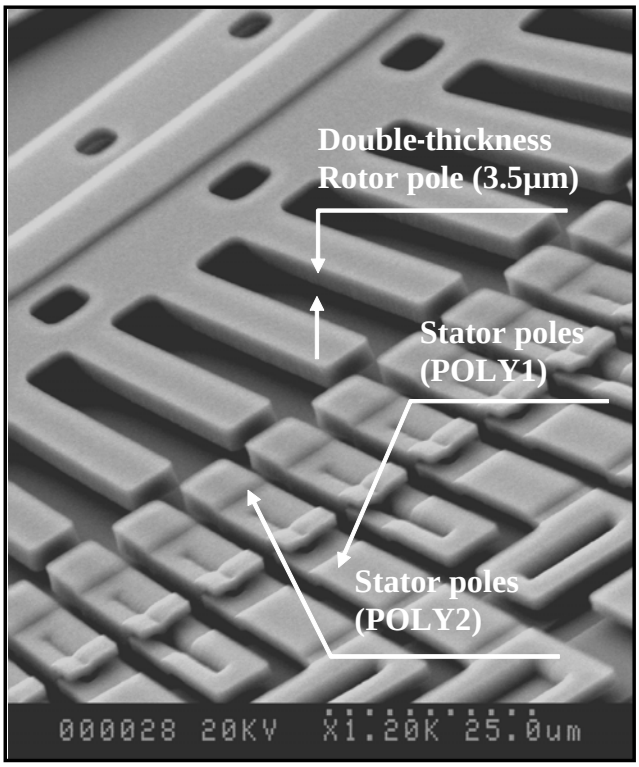

Figure 3.18: SEM image of double-thickness rotor and stator poles fabricated with the Poly-MUMPs process.

analytical formulation [36] based on a smaller number of rotor poles.

Increasing the number of rotor poles has several advantages. First, the generated electrostatic force for the whole micromotor increases, thereby increasing the overall generated motive torque of the micromotor sufficiently to override the friction between the rotor bushing and the substrate and the friction resulting from the extra weight of the micromirror and its supports. Second, a precise rotation step is achieved for excellent alignment between the input and output ports. Third, the large number of micromotor steps allows a larger number of output ports, which increases the scalability of the switch compared to other switch architectures [15]. Depending on the design and physical dimensions of the micromotor, a larger number of steps per full rotation can be achieved. Only fabrication process limitations can limit the number of steps for any micromotor.

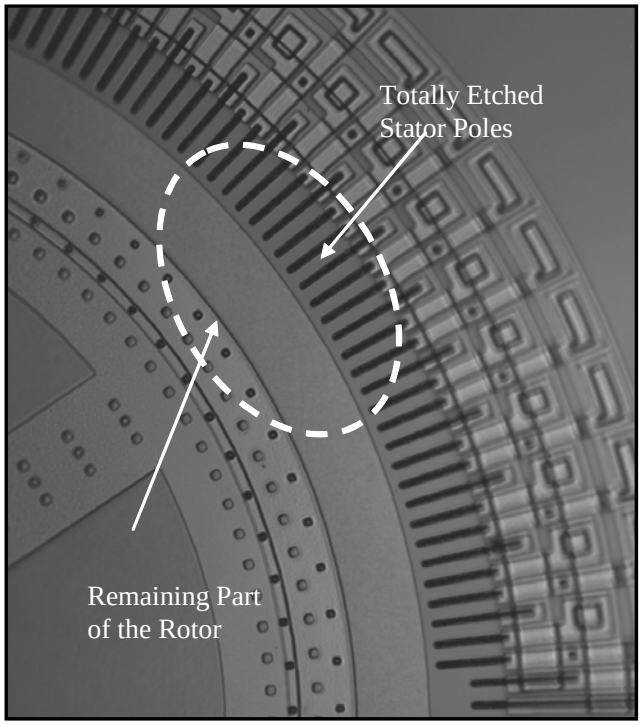

Figure 3.19: Microscopic image of the failure of a PolyMUMPs fabrication to produce a double-thickness rotor and stator poles.

3.4.3 The Rotor-Pole-Shaping Technique

In all previously fabricated electrostatic micromotors, the rotor poles are regular pie-shaped elements. The goal of the design of micromotors is to optimize the dimensions of the rotor poles by setting their width α and the their depth $\triangle r$. After a FEM analysis of a micromotor was performed, it become apparent that the shape of the rotor poles plays an important role in controlling the the potential distribution in the rotor-stator gap area and hence in the distribution of the generated electric field. This factor will, in turn, significantly affect the generated motive torque. Section 3.4.4 describes an examination of the behavior of the electric field in the rotor-stator gap in an electrostatic micromotor and the generated electrostatic forces acting on the rotor poles using a developed 2-D FEM model.

The electric field between two conductors is directed from the conductor with the higher potential (stator poles) to the conductor with the lower potential (rotor poles). The generated electric field, normal to the surface of both conductors, is related to the distribution of the potential in

the gap region by the simple gradient formula $E = -\nabla V$. The electrostatic force components, as calculated according to the Maxwell stress tensor, are therefore normal to the the associated rotor pole surface they are generated on. Since the tangential force component is generated on the rotor pole's side surface A_t, the geometrical location and orientation of this surface (i.e., A_t) play an important role in specifying the distribution and direction of the generated electric field and hence the electrostatic forces. In the previously fabricated micromotors, this surface is in the radial direction and is specified by the equation $\theta = c$, where c is a constant angle.

The research introduces a new design technique called the rotor-pole-shaping (RPS). With this technique, the rotor pole assumes a new trapezoidal shape, as shown in Fig. 3.20. This simple proposed shape of the rotor pole shows the effectiveness of the new design technique. A new design parameter (θ_{sh}) is introduced that specifies the new shape of the rotor pole, modifying it from the regular pie shape, where $\theta_{sh} = 0$, to the new proposed simple trapezoidal shape. A 2-D FEM is used to calculate the tangential driving force and the motive torque as a function of (θ_{sh}). Other rotor shapes are possible and will be investigated in future work.s

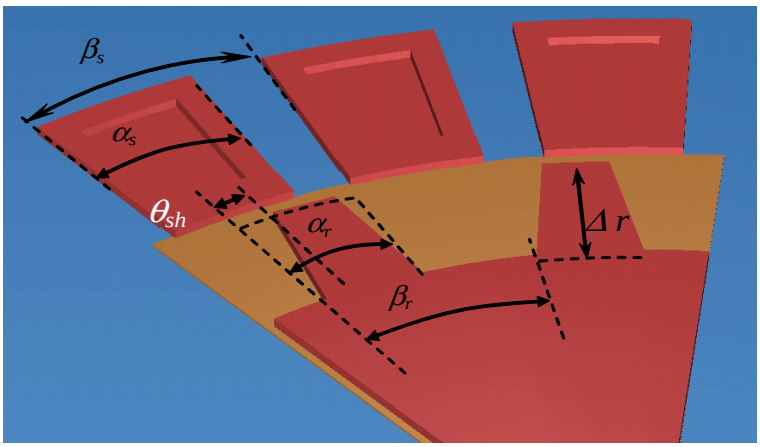

Figure 3.20: A schematic drawing of the micromotor design parameters with the new shape of the rotor pole.

3.4.4 Finite Element Model

To accurately model, design, and optimize a micromotor's performance, a finite element analysis (FEA) was performed in order to calculate the distribution of the electric potential and electric

field in the gap between the rotor and stator poles. Once the field is known, the driving electrostatic force and torque on the rotor poles can be determined and used to compare different micromotor designs. To simplify and automate the optimization of a micromotor design. optimization, this research has developed a 2-D FEM macro using the ANSYS APDL script language The ANSYS macro is used to optimize the micromotor‘s performance by increasing the driving torque for a given applied voltage.

Because of the micromotor's angular symmetry, it can be constructed from the repeating N_{sec} times only one identical pattern, called the micromotor sector, centered around its axis in a cylindrical coordinate space. The current analysis exploited this periodicity by considering only the analysis of one sector, thereby significantly minimizing the required simulation time, especially for large micromotors comprised of many such sectors. With the rotor-to-stator-pole ratio set at $2:3$ and the number of rotor poles N_r, the micromotor sector angle is defined as $\theta_{sec} = 2\beta_r = 4\pi/N_r$, with a total number of sectors $N_{sec} = N_r/2$. If a micromotor with $N_r = 200$ is considered, the single sector represents $1/100$ of the original model.

To be able to model only one sector that represents the actual micromotor, appropriate boundary conditions have to be applied to account for the periodicity and the continuity of the electrostatic fields in the air surrounding the gaps between the rotor and stator poles. An illustration for a micromotor sector is shown in Fig. 3.21. One edge of the sector is defined as the higher sector (HS) edge and the other edge as the lower sector (LS) edge. All HS edges should have the same potential distribution because of the symmetry of the micromotor. The same assumption is valid for the LS edges. On the other hand, the LS edge is physically connected to the HS edge of the adjacent sector and vice versa. This configuration means that all LS and HS edges have the same distribution of the potential along their interface areas. This distribution defines the potential periodic boundary condition (PPBC) between both edges of the micromotor sector. The PPBCs are applied between all nodes on the HS edge and the corresponding nodes on the LS edge according to the following constraint equation:

$$V(r,\theta)|_{right\ edge} = V(r,\theta+\theta_{sec})|_{left\ edge} \tag{3.9}$$

Using PPBC when the micromotor sector is modeled accounts for the effect of the potential on

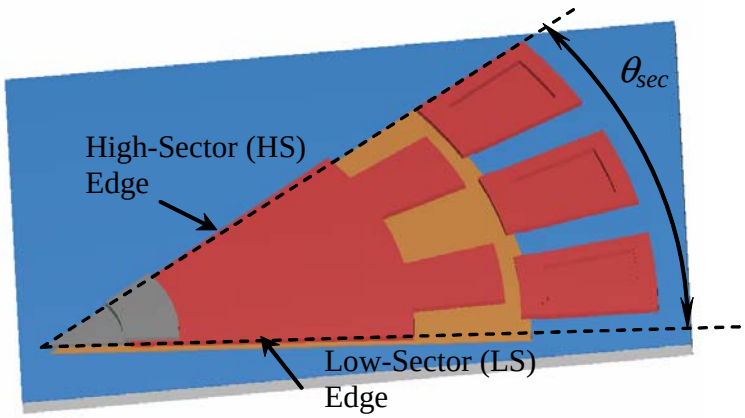

Figure 3.21: 3-D schematic drawing of the micromotor sector to be used for FEA in ANSYS with the sector angle N_{sec} and total number of sectors $N_{sec} = N_r/2$.

other attached sectors at the lower and higher edges. The rotor and stator poles are modeled as perfect conductors (a very good approximation of polysilicon based on its conductivity). Hence, only air will be meshed. To account for the extended air surrounding the rotor and stator poles, infinite elements from ANSYS are used to terminate the air region. Those infinite elements are considered an absorbing boundary condition that does not reflect back any electrostatic field. In some other works, a zero potential boundary condition is applied at a specific distance from the excited stator pole [116] to terminate the air region and truncate the electrostatic field. This technique can be implemented using several precalculations of positions at which the potential decays away from the excited stator pole. This process is time consuming. Furthermore, this technique is not appropriate for automated modeling since it does not ensure accurate boundary conditions if the dimensions of the micromotor change. In addition, for large micromotors, because f the large number of sectors and the correspondingly small sector angle, the zero potential distance could make the model larger than it would if the PPBC were applied to the actual sector model. The infinite element technique is more suitable for parametric models and provides a more accurate representation of the field continuity.

Fig. 3.22(a) shows a 2-D simulation of the potential distribution in one micromotor sector. One stator pole has a potential of $100V$ and the other two stator poles and the rotor poles are grounded. A solution for the whole micromotor can be constructed by replicating the solution

for the simulated sector. It is clear from the results in Fig. 3.22(a) that the potential distribution at the LS edge matches that at the HS edge. The generated electrostatic fields and forces are shown in Fig. 3.22 (b) and (c).

3.4.5 Numerical Simulation Results

The numerical simulations of an electrostatic micromotor with a rotor diameter of 800 $<;\mu$m were performed using the 2-D FEM ANSYS macro. The gap g was kept at the minimum value allowed by the fabrication process for all micromotors: 2 μm. Although all simulations were performed for $g = 2$ μm, g was increased to 2.25 μm in the fabricated micromotors to avoid any fabrication problems encountered in previous fabrications runs. Throughout this section, the applied voltage V_o is 100V unless otherwise specified. The stator pole width α_s is set equal to $\beta_r/2$. The simulation process involved variations of the four micromotor parameters, i.e., N_r, α_r, and $\triangle r$, θ_{sh}, to search for the micromotor dimensions that provide the maximum generated motive torque.

The optimization of the motive torque is based on changing the rotor-pole-shaping parameter θ_{sh} from 0 to $\alpha_r/3$. The value $\theta_{sh} = 0$ corresponds to the regular pie shape of the rotor poles. The corresponding motive torque for each value of θ_{sh} is calculated and compared to the case of the regular pie-shaped rotor pole (i.e. $\theta_{sh} = 0$). Because they are considered a good starting point, the analytical formulations from [36] were used to calculate the initial micromotor dimensions supplied to the 2-D FEM macro. Table 3.5 lists those dimensions. The calculated motive torque is 466 $pN.m$.

Fig. 3.23(a) shows a plot of the motive torque as a function of the number of rotor poles N_r, which varies from 60 to 300 in steps of 10. The maximum number of N_r is based on the fabrication limitation. Increasing N_r beyond 300 causes the width of the rotor poles to be smaller than the minimum width that can be fabricated with the PolyMUMPS fabrication process. All other micromotor parameters are kept unchanged in order to determine the effect of N_r on the motive torque. The motive torque increases as N_r is increased and reaches a maximum value, beyond which it starts to decrease slightly.

The effect of the inner rotor radius (equal to $r_o - \triangle r$) on the motive torque was also plotted. Again, all micromotor parameters were kept unchanged, and the inner rotor radius was varied

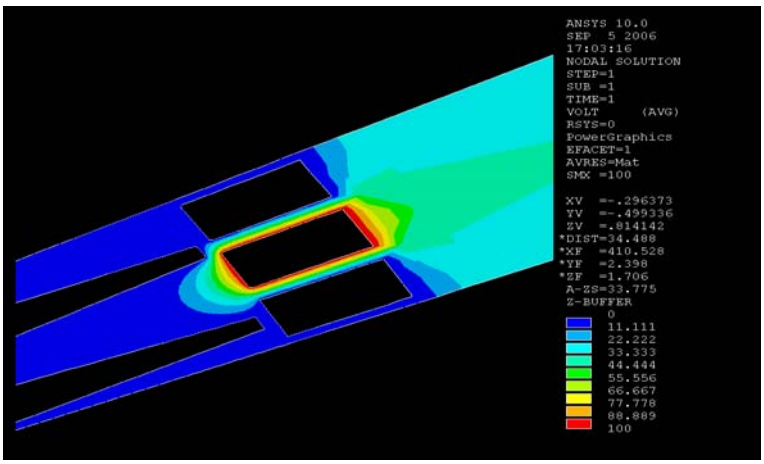

(a)The distribution of the potential in the air region of the micromotor sector.

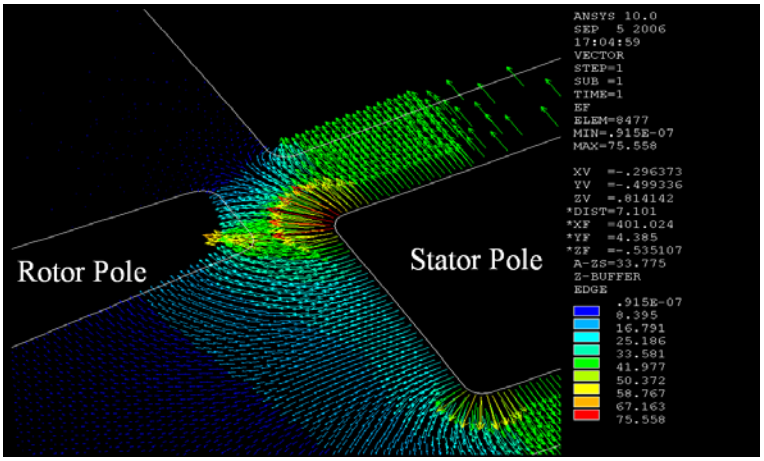

(b) The electric field in the gap region.

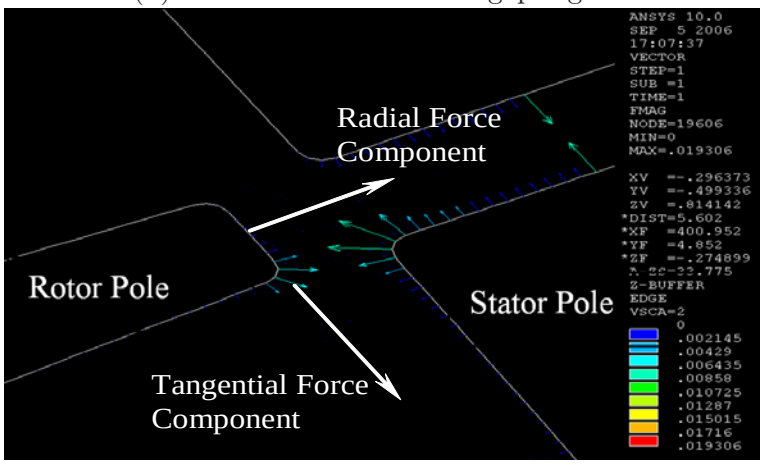

(c) The electrostatic forces generated on the rotor pole in one micromotor sector.

Figure 3.22: Simulation results of a 2-D FEM model using the PPBC. The potential in (a) has the same values at both edges of the sector.

Table 3.5: Physical dimensions of the micromotor using the analytical optimization formulation from [36].

Parameters	*Optimization*	Values
β_r	$2\pi/N_r$	6^o
α_r	π/N_r	3^o
β_s	$2\pi/N_s$	4^o
α_s	π/N_r	3^o
r_o	specified by the design requirements	$400\mu m$
$\triangle r$	$r_o \times \alpha_r$	$> 21\mu m$
g	lower limit of the fabrication	$2\ \mu m$
N_r	$2N_s/3$	60
N_s	$3\pi r_o/20g$	90

from its value as shown in Table 3.5 down to 300 μm. The motive torque was increased slightly when the inner rotor pole was decreased or the rotor pole length $\triangle r$ was increased, as shown in Fig. 3.23(a).

Fig. 3.24 shows the motive torque of the micromotor as a function of the rotor-pole-shaping parameter θ_{sh}. The curves in the figure correspond to a different number of rotor poles; however, in each curve, the number of rotor poles is unchanged. The driving torque increases as θ_{sh} is increased until it reaches a maximum value and starts to decrease again. This behavior of the driving torque clearly shows its dependency on the rotor-pole-shaping parameter θ_{sh}. Table 3.6 lists the physical dimensions of six micromotors having a maximum motive torque each at a specific N_r. The table also lists the maximum calculated motive torque at the optimum θ_{sh} and the percentage increase in the motive torque compared to the case when $\theta sh = 0$. A 25-35% increase in the motive torque is obtained when the rotor poles are reshaped using a simple trapezoidal shape. A further increase in the micromotor motive torque is possible if different shapes are assumed for the micromotor rotor poles. The results of the testing with the proposed simple shape of the rotor prove the ability of the RPS technique to increase the motive torque of electrostatic micromotors that have the same physical dimensions and applied driving voltage.

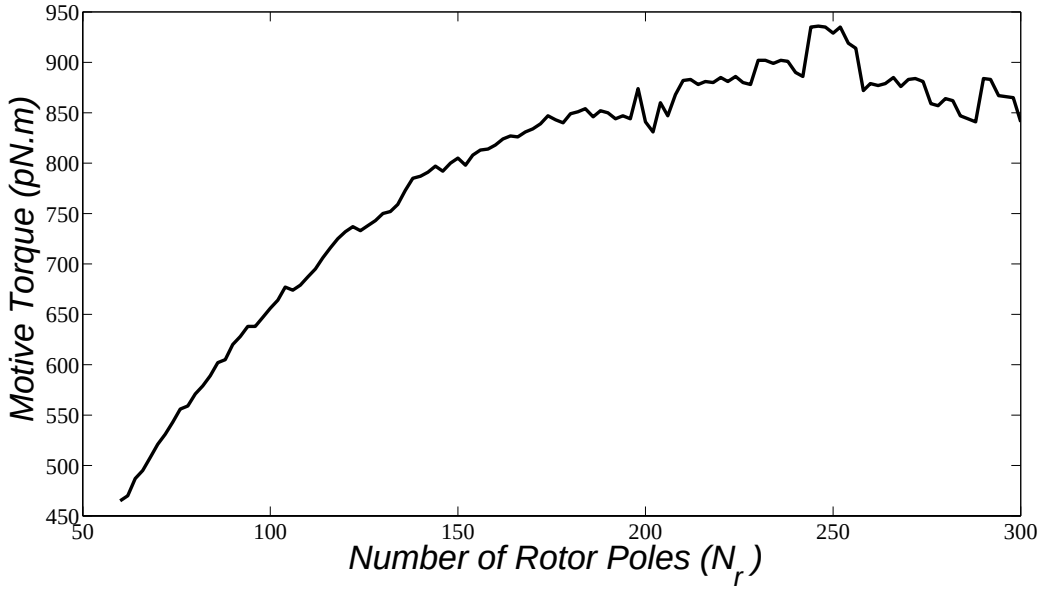

(a)

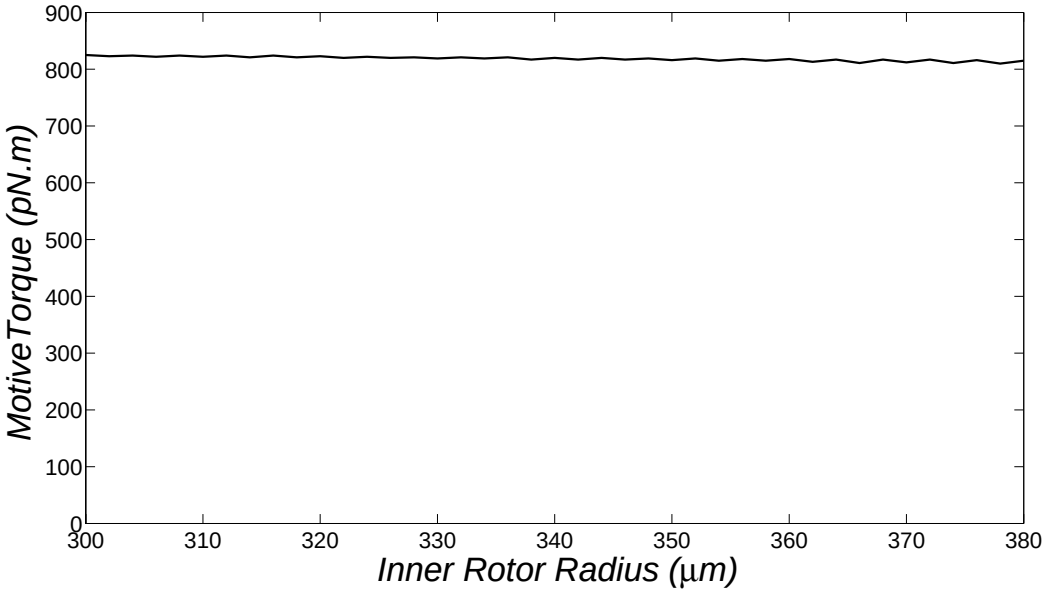

(b)

Figure 3.23: (a) Motive torque as a function of the number of rotor poles N_r. (b) Motive torque as a function of the inner rotor radius.

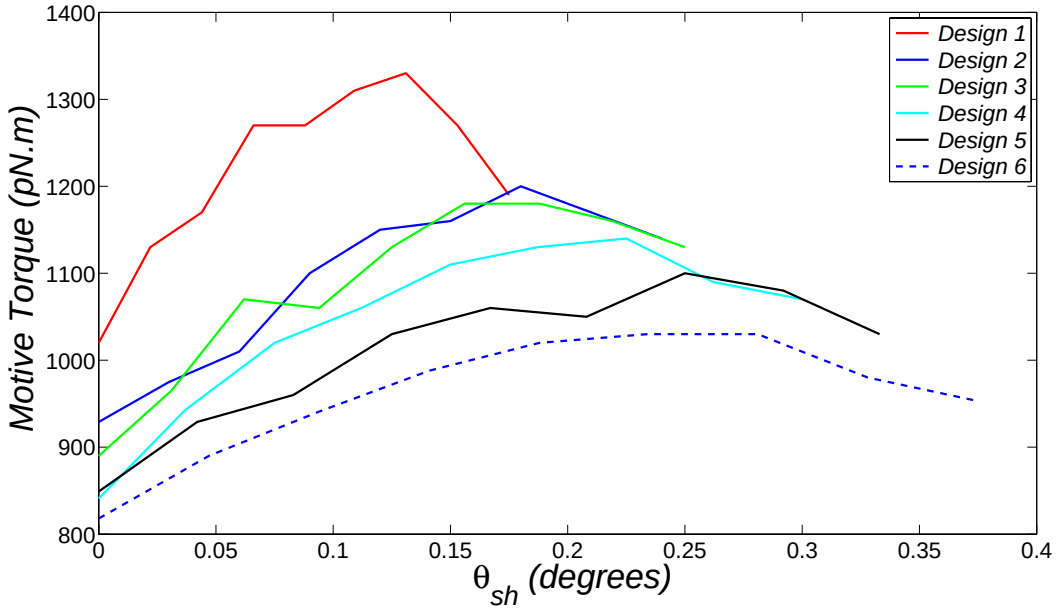

Figure 3.24: Driving torque as a function of the rotor-pole shaping parameter θ_{sh} for different numbers of rotor poles with a gap and rotor diameter of 2 μm and 800 μm, respectively.

A comparison of the optimum values for motive torque obtained for the six micromotor designs with those calculated in Table 3.5 reveals up to 180% an increase in the motive torque is shown in Table 3.6.

Plots of the tangential and normal force components generated on the rotor poles are shown in Fig. 3.25. When the parameter θ_{sh} is changed, the distribution of the electrostatic forces changes. This effect leads to an increase in the tangential force component. Beyond specific values of θ_{sh}, the tangential force component starts to decrease again.

An important parameter for a micromotor is its driving torque versus its rotor position curve. Fig. 3.26 shows the phase-torque curves for the six design cases plotted in Fig. 3.24 as calculated by the 2-D ANSYS macro. Curve-fitting of the phase-torque curves in Fig. 3.26 was performed using a sinusoidal function of the form $T(\theta) = asin\ (b\ \theta + c)$. Table 3.7 lists the coefficient values using the curve-fitting tools in Matlab software. These curves are essential when dynamic analysis of such micromotors is performed.

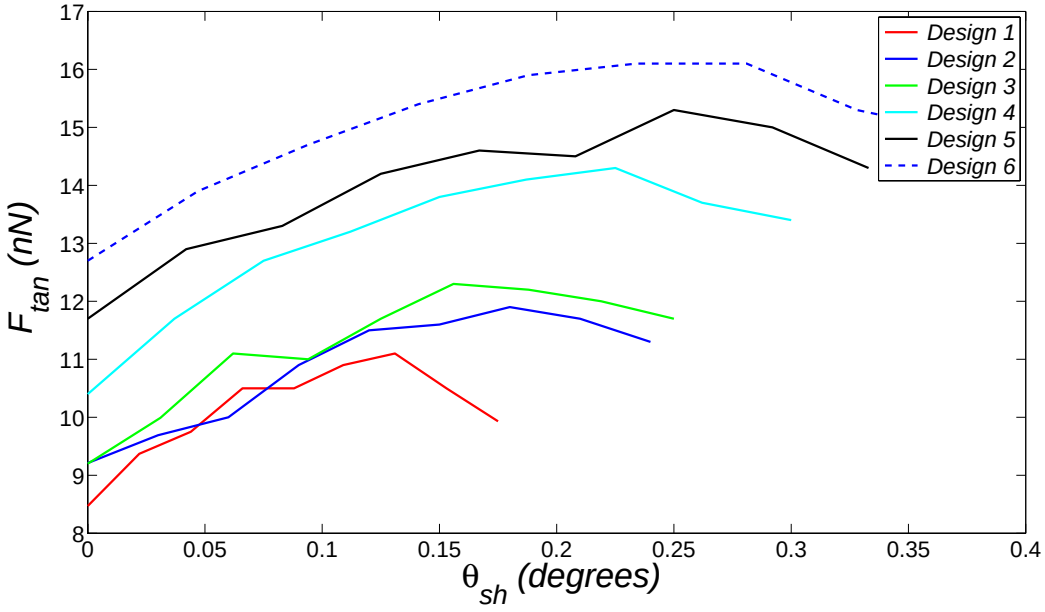

(a)

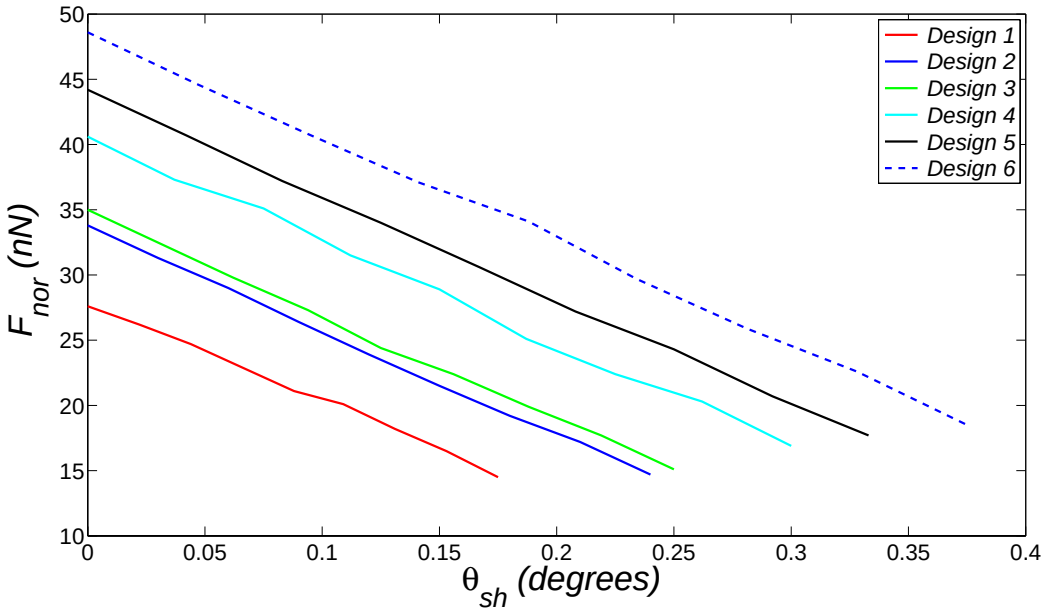

(b)

Figure 3.25: Plots of the generated (a) tangential and (b) normal force components acting on the rotor poles as a function of θ_{sh}.

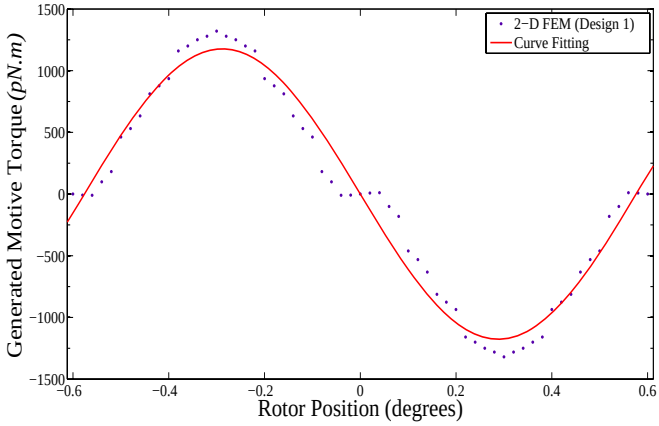

(a) Micromotor *Design* 1

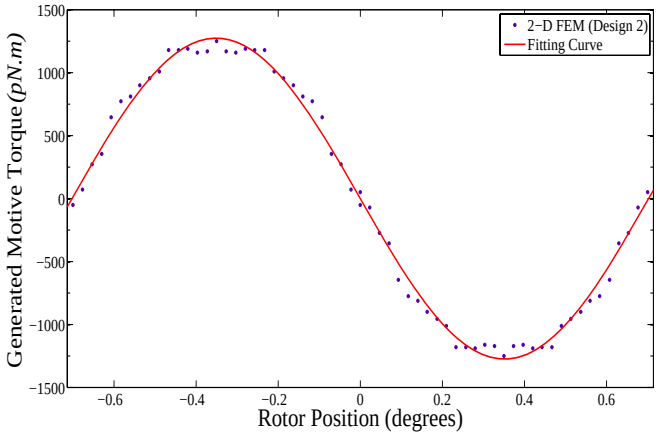

(b)Micromotor *Design* 2

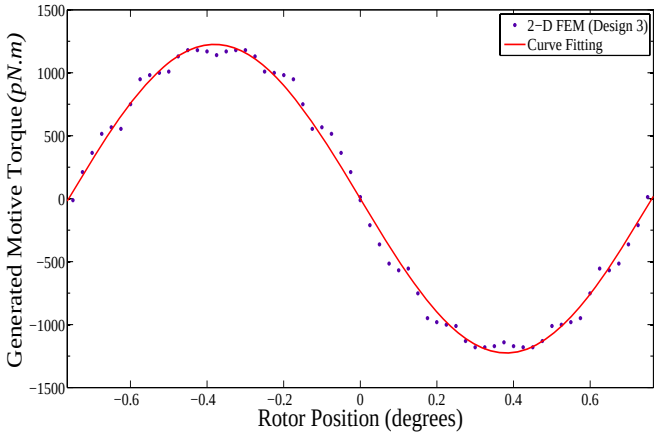

(c)Micromotor *Design* 3

Figure 3.26: Driving torque as a function of rotor-pole position for different micromotor designs.

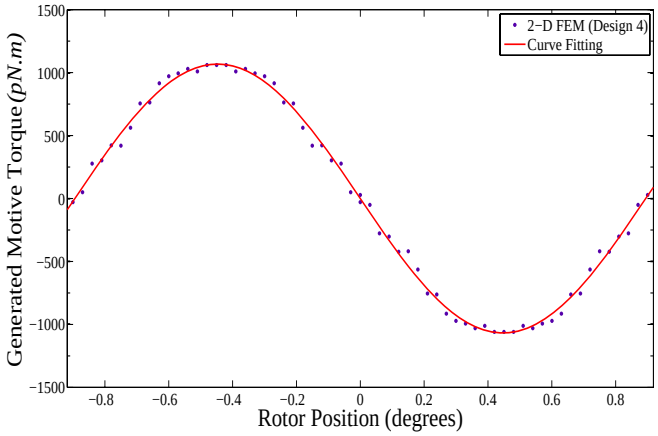

(d)Micromotor *Design* 4

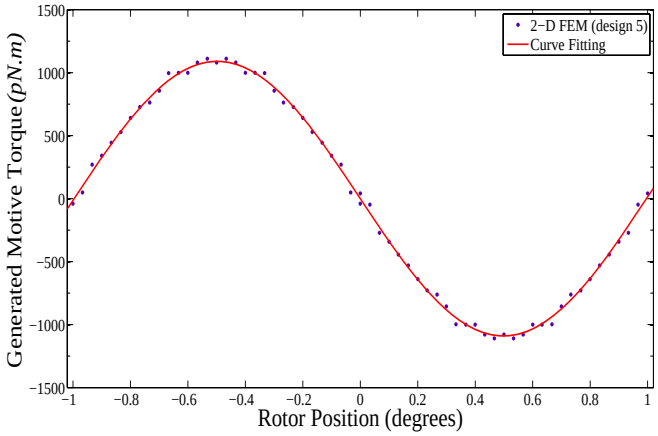

(e) Micromotor *Design* 5

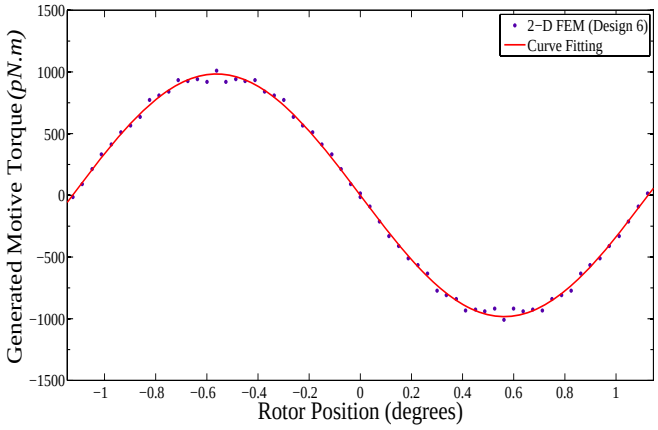

(e) Micromotor *Design* 6

Figure 3.26: Driving torque as a function of rotor-pole position for different micromotor designs (continued).

Table 3.6: The optimized micromotor dimensions for the maximum generated motive torque for different numbers of rotor poles (N_r).

Parameters	*Design*1	*Design*2	*Design*3	*Design*4	*Design*5	*Design*6
N_r	300	250	240	200	180	160
β_r	1.20^o	1.44^o	1.5^o	1.8^o	2.0^o	2.25^o
α_r	0.525^o	0.72^o	0.75^o	0.9^o	1.0^o	1.125^o
β_s	0.80^o	0.95^o	1.0^o	1.2^o	1.33^o	1.5^o
α_s	0.60^o	0.72^o	0.75^o	0.9^o	1.0^o	1.125^o
Optimum θ_{sh}	0.109^o	0.18^o	0.188^o	0.255^o	0.255^o	0.234^o
$F_{tan}(\ nN)$	161	119	122	143	153	161
$F_{nor}(\ nN)$	297	192	199	224	243	297
$T_{max}\ (nN.m)$	1.31	1.20	1.18	1.14	1.10	1.03
% Increase of T ($w.r.t\ T(\theta_{sh}=0)$	28.43 %	29.17%	32.84%	35.55%	29.56%	25.01 %
% Increase of T ($w.r.t\ T$ from [36])	181.1 %	157.5 %	153.2%	144.6%	136.1%	121.0%

3.5 Experimental Test Results

The operation of the micromotor has been tested before and after the microassembly of different types of micromirrors using the custom-designed test-module shown in Fig. 3.27. The test-module consists of a zero-insertion-force (ZIF) socket on a printed circuit board. The printed circuit is a two-sided board and routs the input signals to four 21-pin terminal block connectors at each side of the board. The board and the 16 banana sockets, four at each side of the board, are assembled on a plexiglass sheet. The banana sockets provide 16 simultaneous input signals to the board through the terminal block connectors. The test-board circuit can be used for other projects.

The experimental test setup is shown in Fig. 3.28(a). A four-channel pulse generator is used to provide the input voltage signal to the micromotor (Fig. 3.29). The four channels are synchronized through one input timing signal with a period of T_o. The output voltage ranges

Table 3.7: Curve fitting of the driving torque ($T(\theta)$) for micromotors with a diameter of 800 μm. The curve-fitting takes the form of $T(\theta) = asin(b\,\theta + c)$.

Parameters	a	b	c
Micromotor *Design* 1	1176	5.451	3.142
Micromotor *Design* 2	1274	4.472	3.142
Micromotor *Design* 3	1225	4.126	3.142
Micromotor *Design* 4	1067	3.513	3.142
Micromotor *Design* 5	1090	3.154	3.142
Micromotor *Design* 6	982.9	2.792	3.142

can be varied from 2V to 20V in steps of 0.05V. Each channel has an individual pulse width, duty cycle, and delay settings. The micromotors require an actuation voltage of more than the 20V provided by the pulse generator. A homemade four-channel high-voltage amplifier with a fixed gain of 10 was used to provide the high voltage signal required to drive the micromotors. The minimum resolution of the combined pulse generator and the high voltage amplifier is 1V. To obtain less than 1V resolution from the amplifier, four 20-turns variable potentiometers are placed at the input ports of the high-voltage amplifier channels. The input signal is supplied to the high-voltage amplifier through the variable potentiometer, which sets the required output resolution from the amplifier.

To test the operation of the micromotor, three synchronized input voltage signals are applied to the three input pads of the micromotor. The input signals from the pulse generator and the high-voltage amplifier supplied to the micromotor are shown in Fig. 3.30. The physical dimensions of the fabricated micromotor are listed in Table 3.8. A 16V signal was able to successfully drive the micromotor at 1.25 rpm. The micromotor was able to rotate at a lower voltage of 14V with the same rpm. However, the micromotor stopped after a few rotations. Increasing the rotation speed requires a higher voltage for a faster rotor response, although it is not the highest measured rpm at this applied voltage. The micromotor is able to rotate at 42 rpm with a 20V signal. On the other hand, the $3DRIM$, constructed from a micromotor with assembled micro-parts starts, rotates at an applied voltage of 40V. At 70V applied voltage, the $3DRIM$ rotates at 1250 rpm.

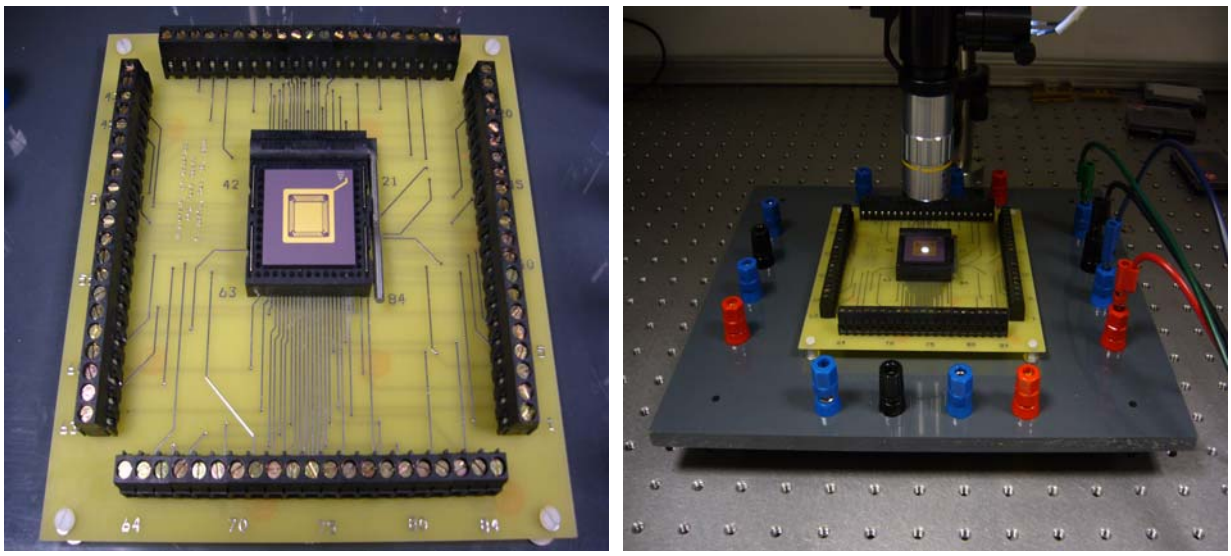

(a) (b)

Figure 3.27: Custom test board assembly for testing fabricated micromotors before and after microassembly of micromirrors. (a) The assembled ZIF-socket in the printed-circuit board. (b) The printed-circuit board with the 16 banana sockets assembled on a plexiglass sheet.

Testing of the micromotor was conducted in an air environment. Better performance is expected in a vacuum because the negative effect of air damping is eliminated.

Fig. 3.31 shows the optical test setup for the proposed $1 \times N$ MEMS optical switch. A HeNe laser is used for easy alignment between the input and output ports. The laser beam output is in the form of a Gaussian beam distribution with a beam diameter ($2w_o$) equal to $810\mu m$. A combination of a plano-convex and a plano-concave lens is used in a telescopic assembly to achieve a collimated Gaussian beam with a new smaller waist. The telescopic assembly has a demagnification factor of 5. The output Gaussian beam from the telescopic assembly has a beam diameter of 1/5 the entering Gaussian beam's diameter. In this case, the Gaussian beam output from the telescopic lens assembly has a beam diameter of 162 μm, which is suitable for the assembled micromirror size. The purpose here is to measure the micromirror loss. The reflected beam power is measured using an optical power detector, as shown in Fig. 3.31. The measured loss is equal to 1.1 dB. Many factors contribute to micromirror losses. For example, the PolyMUMPs fabrication process requires the use of etch release holes on the micromirror's

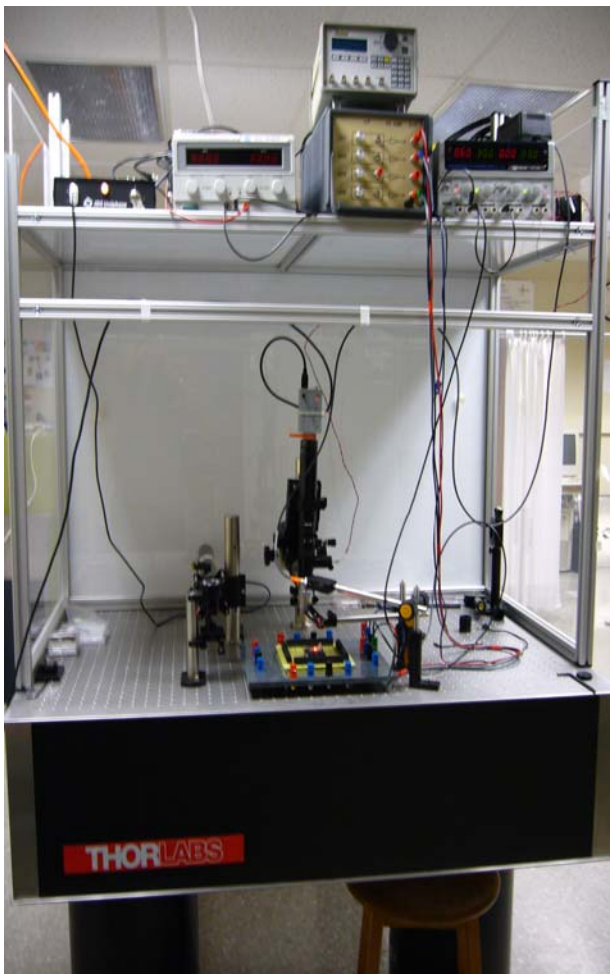

(a)

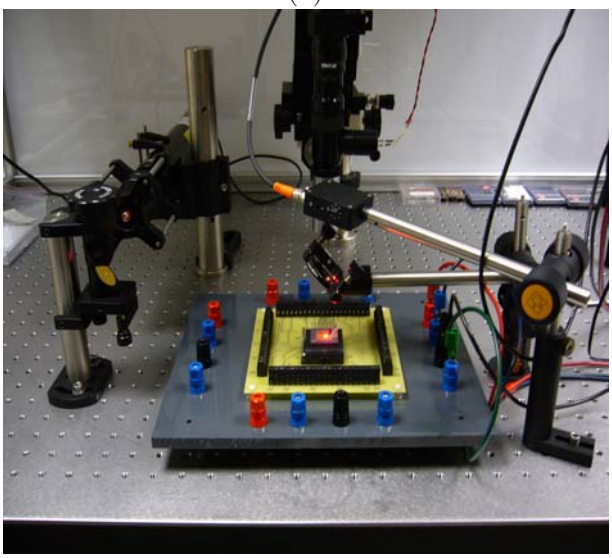

(b)

Figure 3.28: (a) Photograph of the micromotor experimental test setup. (b) Photograph of the optical experimental test setup.

(a) (b)

Figure 3.29: (a) Four-channel pulse generator. (b) Four-channel high-voltage amplifier.

surface, which reduce the reflection area and may diffract the light. As well, the micromirror does not have perfect surface flatness due to the residual stresses present in the gold layer. Although these are small, they contribute to the micromirror losses, and a loss of $0.1 \sim 0.3$ dB in reflectively is expected because of the micromirror's gold coating.

The proposed experimental setup shows more flexibility when testing the optical and mechanical switch performances than a packaged switch. The testing of a packaged switch will be limited to one 3DRIM that consists of a specific design of the electrostatic micromotor and the size of the assembled micromirror. In addition, the OPL will be fixed between the input and the output ports and can not varied. However, the packaged switch is expected to have better and more stable performance that leads to the minimum insertion loss. On the other hand, the proposed experimental setup is able to test all aspect of the mechanical and optical performances of the optical switch. First, the OPL can be varied since the distance between the 3DRIM and an output port is not fixed. This setup will provide us with more flexibility in measuring the insertion loss as a function of the OPL. Second, since three diffract micromirror sizes were assembled in different micromotor design, the effect off the micromirror size on the insertion loss can be tested.

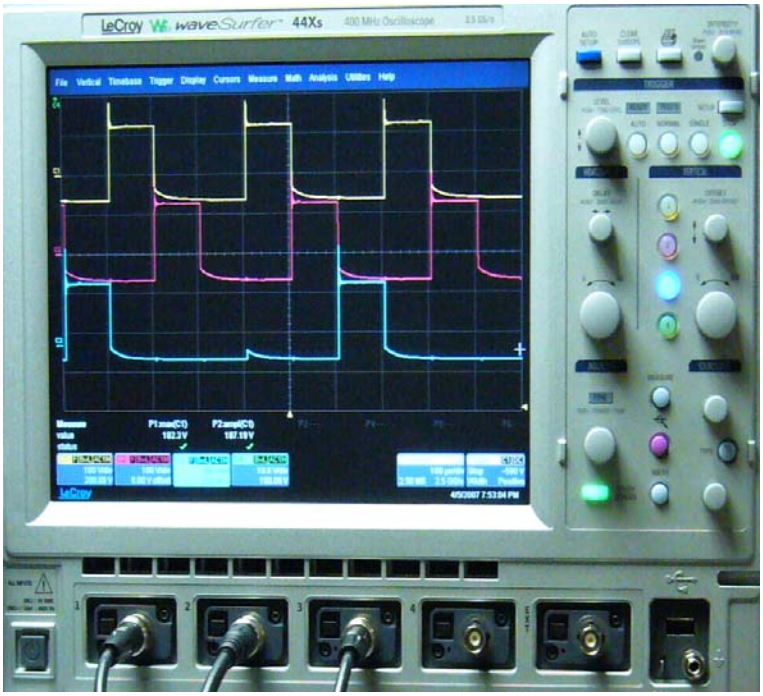

Figure 3.30: Voltage signal pattern from the high-voltage amplifier applied to the micromotor.

Table 3.8: The physical dimensions of the fabricated electrostatic micromotor.

Micromotor Parameters	r_o	g	rpp	rpw	spp	spw	Δr	θ_{sh}	Bearing Diameter
Value	$400\mu m$	$2.25\mu m$	2.25^o	1.2^o	1.5^o	1.2^o	$30\mu m$	0.4^o	$70\mu m$

In addition, different sizes of the GRIN lens can be tested with different micromirrors to test the maximum scalability of the proposed $1 \times N$ optical MEMS switch. Third, the driving voltage and the transient response of different 3DRIMs can be tested as well to optimize the switching time and be able to use input-signal-shaping to enhance the response and stability of micromotor response. Since several designs of the micromotor were fabricated, the mechanical performance of these micromotors will be tested as well. The proposed experimental test setup shows more flexibility compared to a packaged optical switch.

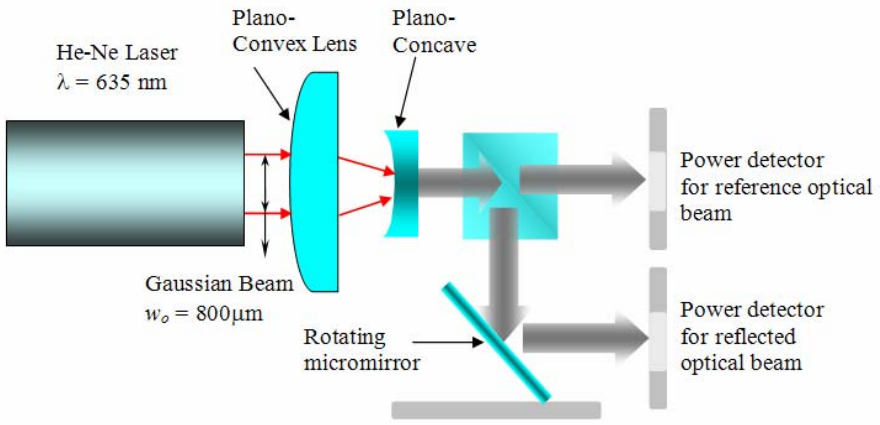

Figure 3.31: A schematic diagram of the optical test setup for the $1 \times N$ optical MEMS switch.

Chapter 4

3DRIM Design, Fabrication, and Microassembly

4.1 Introduction

This chapter presents the design, fabrication, and microassembly of the $3DRIM$ (Fig. 4.1). A robotics-based microassembly process has been successfully applied to the construction of a novel micromirror design for use in optical switching. The microassembly process is based on a passive microgripper, key, and inter-lock (PMKIL) assembly system [32]. Details of the assembly process include the methodology for constructing the $3DRIM$, the design of the micromirror micro-parts, and the design of the tools (microgrippers) that are mounted to the robot to handle the microparts will be presented. The results of the assembly process are presented along with a description of several $3DRIM$ prototypes.

4.2 *3DRIM* Design Methodology

The functioning of the proposed optical switch architectures presented in Chapter 3 relies on the operation of the $3DRIM$ which had to meet the requirements of the proposed switch architecture. To achieve this goal, several design choices were made. The micromirror to be used in optical switching requires high flatness and would ideally be a bulk-micromachined silicon crystal with a highly reflective metal layer deposited on it. The use of silicon crystal provides a thicker

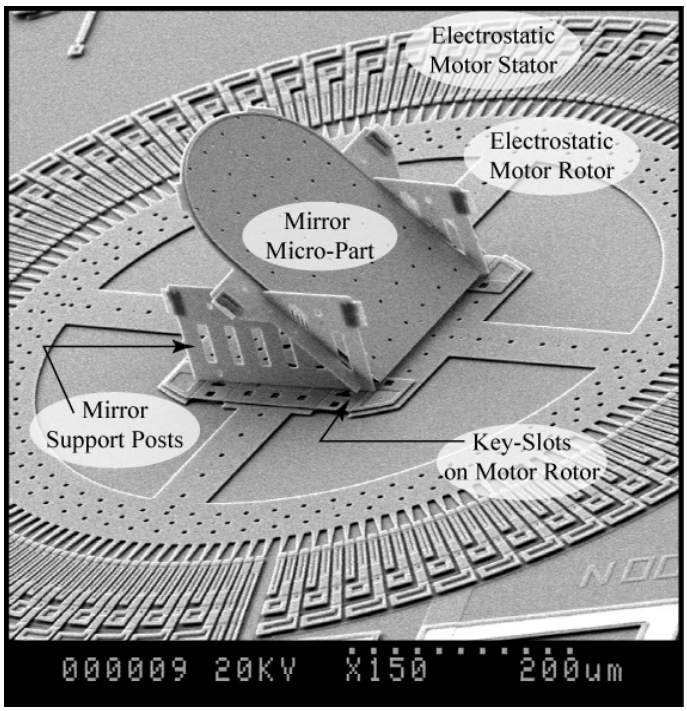

Figure 4.1: SEM image of an assembled $3DRIM$.

structural layer for the micromirror. The extra thickness significantly increases the micromirror flatness. Since all the constituent microparts were fabricated using the PolyMUMPs process, the micromirrors currently used in this process are not ideal. However, even these micromirrors are not ideal for the developed $3DRIM$ because it requires a high level of flatness, the PolyMUMPs process is more convenient to use for providing the initial concept at this stage. Currently, all micromirrors fabricated with PoyMUMPs are a "double thickness" structure, composed of 3.5 μm of polysilicon plus 0.5 μm of gold as a reflective surface, for a total of 4 μm.

Since the process is a surface-micromachining one, etch holes had to be arrayed every 30 μm along the surface of the micromirror to facilitate the etch-release from the substrate. As a result, about $1-5\%$ of the micromirror surface has holes, and about 5% is not reflective. Additionally, due to internal stresses existing in large polysilicon sheets, the PolyMUMPs micromirrors have a slight curvature. These internal stresses are due to the deposition of thin film layers at different temperatures plus the difference in the coefficient of thermal expansion between the gold and polysilicon layers. The calculation of the resulting micromirror curvature can be found in [117].

To maximize the versatility of the *3DRIM* system,and allow its use in configurations for $1 \times N$ [118], and $N \times M$ optical cross-connects [119], the micromotor must be able to rotate continuously in either direction, without mechanical restriction. Therefore, the entire *3DRIM* structure is designed to be assembled on top of the micromotor and has no attachment or connections with other parts of the substrate. The accuracy needed to achieve a precise 45-degree angle between the micromirror and the substrate is built into the microparts that comprise the *3DRIM* in the same way that pieces of a jigsaw puzzle, or Lego blocks can fit together only in a specific way. In other words, although the assembly process itself may have variations, the assembled micromirror microparts will fit together only in a particular way, and will only fit together with a pre-designed accuracy. The micromirror microparts are also designed to interlock with each other in such a way that creates a highly rigid structure. High rigidity is important, since it is undesirable for the micromirror to bend or flex during the acceleration and deceleration of the micromotor and for the micromirror microparts to vibrate due to external disturbances.

The design of the *3DRIM* must complement the design of the electrostatic micromotor, as the two elements must work together. Therefore, any conflicts between the design requirements for each element must be resolved. An example is the mass of the *3DRIM* structure. the required high level of flatness in the micromirror could be provided by a single-crystal silicon (SCS) micromirror with a thickness ≥ 10 μm. The structure supporting the micromirror should also be as rigid as possible and should therefore have thick sidewalls. However, the mass of a thicker micromirror or the mass of a highly rigid structure will be great. Since a given micromotor design has only a finite amount of torque, a structure with a higher mass will have a negative impact because the system's switching time and the driving torque required to rotate the *3DRIM* will increase. Therefore, an optimized micromotor design that uses the RPS design technique had to be employed to maximize the driving torque [54]. The *3DRIM* structure should also be as symmetrical as possible and centered on the micromotor rotor in order to provide a more balanced inertial load for the micromotor.

The microparts used to construct the *3DRIM* must be designed to incorporate the "*modular features*" of the PMKIL microassembly system. This will ensure that the microparts scan be easily handled and joined when using the PMKIL microassembly system. To be compatible with the assembly system, each micropart must incorporate three modular design features: an interface

feature, a tether feature, and a joint feature [120]. Fig 4.2 shows SEM pictures of microparts used in the assembly the *3DRIM* with their three modular features. The interface feature allows the robot (via a microgripper tool) to securely grasp the micropart. The tether feature is used to secure the micropart to the chip during the grasping task or chip transport. After a micropart is grasped, the tethers that hold it are designed to break away, allowing it to be removed from the chip. The joint feature is a micromechanical joint that allows microparts to be joined. To create a joint, a joint feature is lined up with a mating joint feature at the target joint site. Different types of joint features are used for different designs, as described in the following sections. It should be noted, that these three modular features are standardized and have been simply added to the design of the 3$DRIM$ parts. The features other than their locations in the micropart, are not customized for the micromirror and the microparts. A more detailed description of the assembly process is provided in the next section.

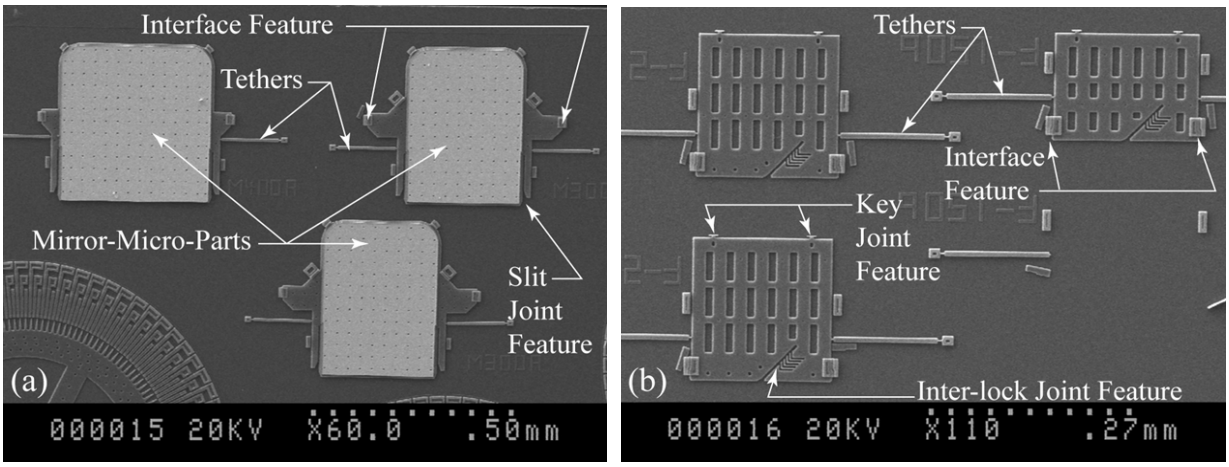

(a) (b)

Figure 4.2: SEM images of the microparts secured to the substrate via the tether features. (a) Micromirrors. (b) Micromirror *support posts*. Note the interface features to which the microgripper tips mate with.

4.3 The Microassembly Process

This section discusses in details the microassembly process for constructing the $3DRIM$ as shown in Fig. 4.1. First, the setup of the microassembly robot is described, followed by a description of the microparts used in the assembly, the process for grasping the microparts from the chip, and the process for assembling the microparts.

4.3.1 Bonding a Microgripper to the Robotic Workstation

Before microassembly operations can be performed, an appropriate "grasping tool" designed to grasp microparts, must first be bonded to the end-effector (probe pin) of the robotic workstation [121]. This grasping tool is referred to as a microgripper. Fig 4.3 shows SEM images of actual microgrippers used to grasp the micromirror and the *support posts* during the assembly of the *3DRIM*. The tip-to-tip separation distance of the microgripper is 204 μm, which allows this microgripper to grasp microparts with interface features 204 μm away from each other.

The microgrippers used with this system are fabricated by the PolyMUMPs process. For convenience, they are located on the same chip as the other microparts, as shown in Fig. 4.3(a). The bonding system uses an adhesive that is cured by ultraviolet (UV) light. Once bonded, a microgripper can be used for many grasping and joining cycles. Should a microgripper no longer be needed for a particular size of micropart, the a solvent is used to dissolve the UV-adhesive, the unnecessary microgripper is brushed off, fresh (un-cured) UV adhesive is applied, and a new microgripper is bonded to the end-effecter. Details of the microgripper bonding procedure and equipment are provided in [121]. The microgrippers used here have a passive design, in that they are not actuated by any external control. They employ a compliant mechanism that "self-opens" during micropart grasping and "self-releases" microparts after they are joined to other microstructures. Due to the different sizes of the microparts, three different sizes of microgripper with different tip-to-tip separation distances are used to complete one micropart assembly process. The microgrippers used for each specific micropart are referred to microgrippers A, B, and C, which have tip-to-tip separation distances of 204, 290, 496 μm, respectively. For convenient, any $3DRIM$ incorporates micropart handeled by only two types of microgrippers. This redesign of the features of the micropart's interface results in fewer microgripper changes but larger microparts

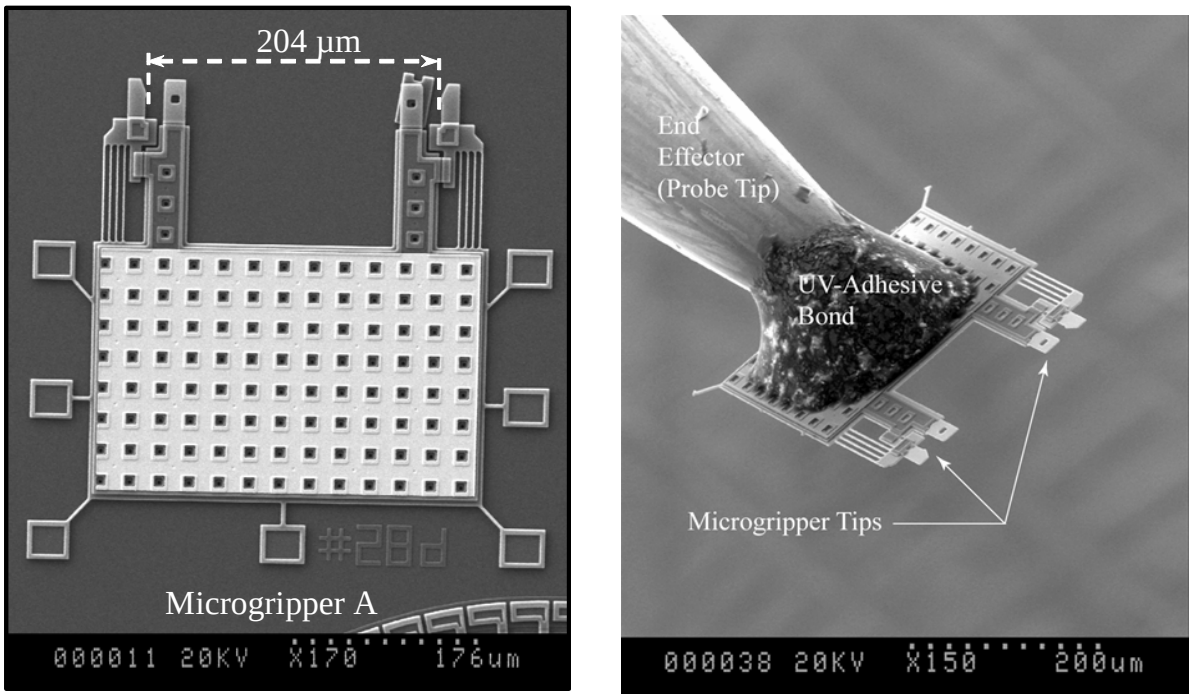

(a) (b)

Figure 4.3: SEM images of a microgripper used for the assembly. (a) A microgripper on the chip substrate held by tethers. (b) A microgripper bonded with UV-adhesive to the end effecter (probe pin) of the robotic workstation.

weight. Note that larger microparts mean more assembled weight on the micromotor which results in more friction and requires larger driving voltages.

In future, each micropart can be designed to minimize its dimensions and weight. The result would be that several microgrippers would be used to complete one assembly task. This will not cause a significant problem in the mass production but would provide optimum performance of the assembled micromirror and microparts in terms of switching times and driving voltage.

4.3.2 Overview of the Assembly Process

The process of assembling the *3DRIM* involves the sequential addition of microparts. Firstly, to assemble the microparts onto the electrostatic micromotor rotor and subsequently to assemble the microparts into those previously assembled, each micropart must proceed through five tasks:

1. The micropart is grasped by the microgripper.
2. The micropart is removed from its original location on the substrate.
3. The micropart is translated and rotated and through space.
4. The re-oriented micropart is joined to other microparts.
5. The micropart is released by the microgripper.

Currently, these five operations are performed by tele-robotic control, using a human operator. Future work is required in order for these operations to be automated, which would be a significant achievement because it would minimize the assembly time. Fig. 4.2 shows SEM images of the microparts used to construct the first $3DRIM$ design while they were lying in their fabricated positions on the substrate of the chip. Fig. 4.2(a) shows the micromirrors, and Fig. 4.2(b) shows the *support posts*. It should be noted that these microparts are attached to the substrate via tethers, which are designed to hold the microparts securely onto the chip during transportation, but are also designed to break away during the grasping operation. As shown, Each micropart has a built-in interface feature, that is designed specifically to mate with the microgripper tips shown in Fig. 4.3.

Microparts used in the assembly of a *3DRIM* can be categorized into three main types: the *support posts*, the *cross-support posts*, and the micromirrors. A detailed description of each micropart is provided in the corresponding sections. The *support post* microparts are designed in different sizes to achieve different design requirements, so that the required *3DRIM* with different dimensions can be constructed. All *support posts* have four main features, the location of which depends on the assembly technique used. These features: the interface feature, the tether feature, the key-joint feature, and the interlock-joint feature. The *support posts* are directly assembly and joined to the micromotor rotor through two key-joint features. In one micromirror design, they serve as the micromirror carriers. In other designs, they carry two *cross-support posts* to form a rigid structure for subsequent micromirror assembly. *Support posts* may have one or more interlock-joint features with different orientations (vertical, horizontal, or at 45^o to the substrate). The inter-lock joint is used to join two microparts securely. In the design described below, double inter-lock joints between a micromirror and two *support posts* are formed in order to secure

the micromirror at 45°. In other modified micromirror assembly design techniques, the *cross-support post* is used to facilitate the micromirror insertion into the *support post*'s inter-lock slits. The assembled $3DRIM$ using this modified technique shows enhanced rigidity of the $3DRIM$ structure.

Task 1: Grasping the Micropart

Fig. 4.4 shows a sequence of video images of the grasping operation. The field of view is 427 H × 320 V μm, and the depth of focus is 1.5 μm. Therefore, all objects closer to or further from the focal plane appear out of focus. The true optical resolution is 0.8 μm, and the digital resolution is $\simeq$ 0.33 μm/pixel as visible on a monitor.

Fig. 4.4 (a) shows the microgripper about 30 μm above the target micropart. In these images, the micropart is a micromirror *support post*. The microgripper tips and the interface features of all microparts have a special complementary geometry [122]. When the microgripper tips are inserted into the interface feature, the tips pass under the edges of the interface feature and at the same time pass over the body of the micropart. This configuration keeps the micropart securely within the microgripper during subsequent operations. Fig. 4.4(b) shows the initial stage of the microgripper insertion into the interface feature and Fig. 4.4(c) shows the completed grasp. It should be noted that the microgripper self-opens when it is pushed into the interface feature of the micropart. There is no active control of the tips. The force generated during the insertion and grasping is not sufficient to break the tethers, therefore, which can be noted in Fig. 4.4(c), which shows that the micropart is still tethered to the substrate, although it has been fully grasped. If the micropart was not tethered to the substrate, the microgripper would not be able to grasp it because there would be no reaction force generated to self-open the tips.

Task 2: Removing the Micropart from the Chip Surface

To remove the micropart from the chip, force is applied in the x-direction to break the tethers. The deflection of the tethers can be observed in Fig. 4.4(d). The tethers that hold the microparts are made of POLY1: they are 150 μm long, 8 μm wide, and have a narrow notch at each end to create a stress concentration point. The tethers are designed to break at these notches when 100 μN or more are applied at the interface feature in the x-direction. Fig. 4.4 (e) shows the

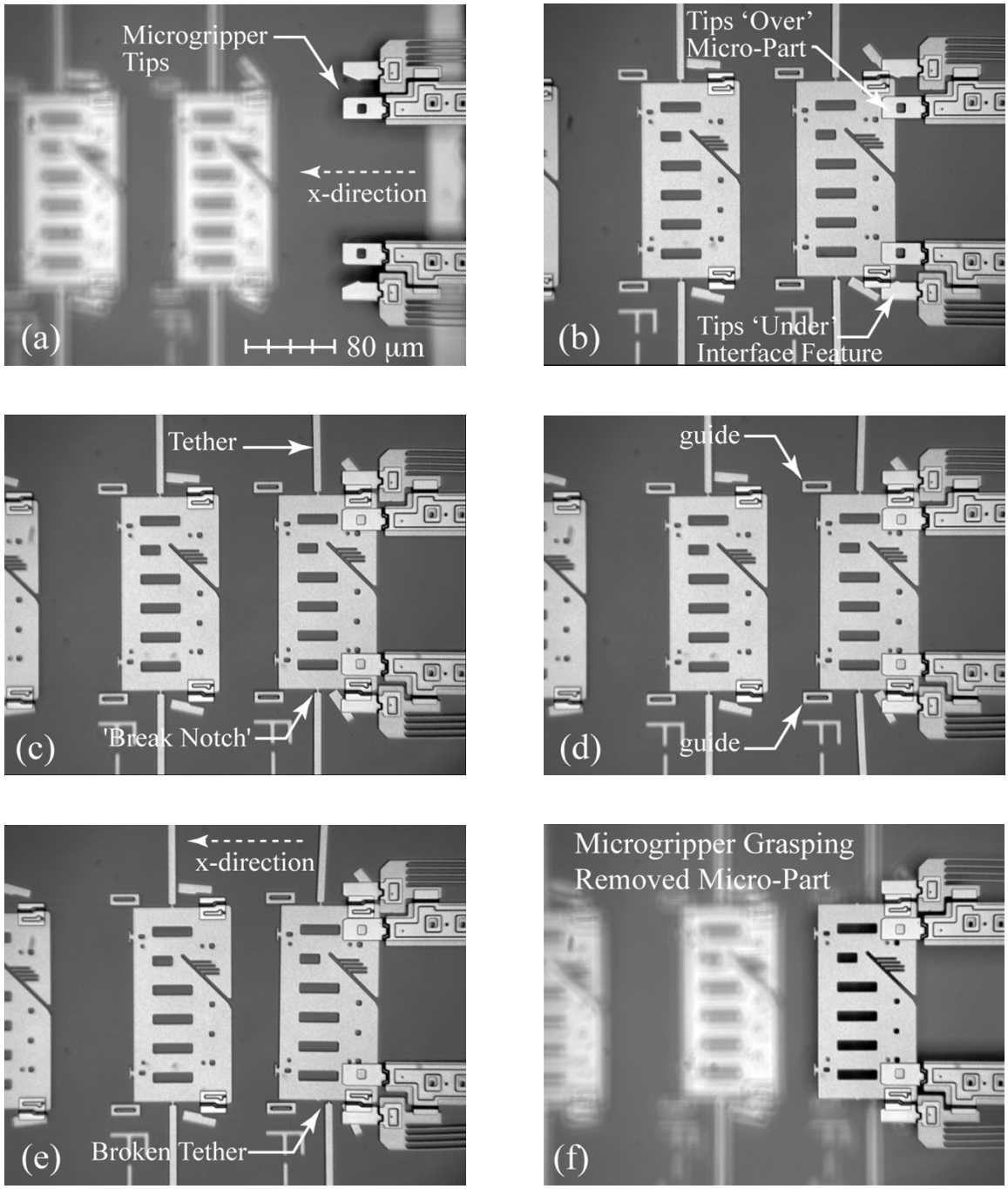

Figure 4.4: Sequence of Microscope images showing the grasping of a micropart (micromirror *support post*).

micropart after the first tether is broken. To break the second tether, the microgripper pushes the micropart further in the x-direction. The guides shown in Fig. 4.4(d) help to maintain the stress concentration on the remaining tether, until after sufficient displacement in the x-direction, when the second tether breaks. At this point, the micropart is free from the substrate but still in the grasp of the microgripper. Fig. 4.4(f) shows the microgripper grasping the micropart 40 μm above the substrate. The micromirror's *support post* micropart is now ready to be assembled into the micromotor rotor.

Task 3: Translating and Rotating the Micropart in Space

The microgripper exerts a holding force on the micropart it grasps to keep it from shifting during manipulation. When the microgripper is in the rest position, as shown in Fig. 4.3(b), it has a space of 200 μm between the compliant (flexible) tips. The space between the grasp edges of the interface feature on a micropart is 208 μm wide; therefore, the microgripper tips are elastically deflected by 4 μm each during the initial insertion of the tips (Fig. 4.4b). When the grasping of the micropart is complete, the microgripper tips are each deflected by 2 μm. When the microgripper and the microparts are designed, different interference values can be selected, allowing holding forces suitable for a particular application.

It can be seen from Fig. 4.4 that the microparts are grasped in such a way that they are planar with the microgripper and with the chip substrate. To build the $3DRIM$, the microparts must be reoriented and translated in such a way that they are perpendicular to, and lined up with, the joint feature they must joined with. In the case of the *support posts*, they must be perpendicular to the micromotor rotor on the substrate (i.e., 90° to the substrate). The micromirror must be perpendicular with respect to the interlock-joint axis on the *support post*, which is at 45° to the substrate. The robotic workstation [121] used to assemble the microparts has six axes: x, y, and z translations and yaw, pitch, and roll rotations. In our micromirror assembly, only the first five axes are sufficient to perform the assembly. The sixth axis would be used only if a more complicated design is performed with true 3-D rotation angles.

Task 4: Joining the Micropart to Other Microparts

Two different joining systems are used for creating the joints required to construct the $3DRIM$: the key-lock joint system and the inter-lock joint system [120]. The key-lock joint system works as follows: one micropart has a double key feature on its lower edge, and the other has a mating double key-slot, as illustrated in Fig. 4.5(a). In the case of the $3DRIM$, the *support posts* have the double key, as shown in Fig. 4.2(b), and the micromotor rotor is equipped with the double key-slot. The joint is formed when the keys are inserted into the wide region of the key-slots, and then the micropart is translated laterally until the keys pass under the narrow region of the key-slot. The keys become wedged into the narrow region, and when the microgripper is retracted from the *support post*, the *support post* remains locked into the micromotor rotor.

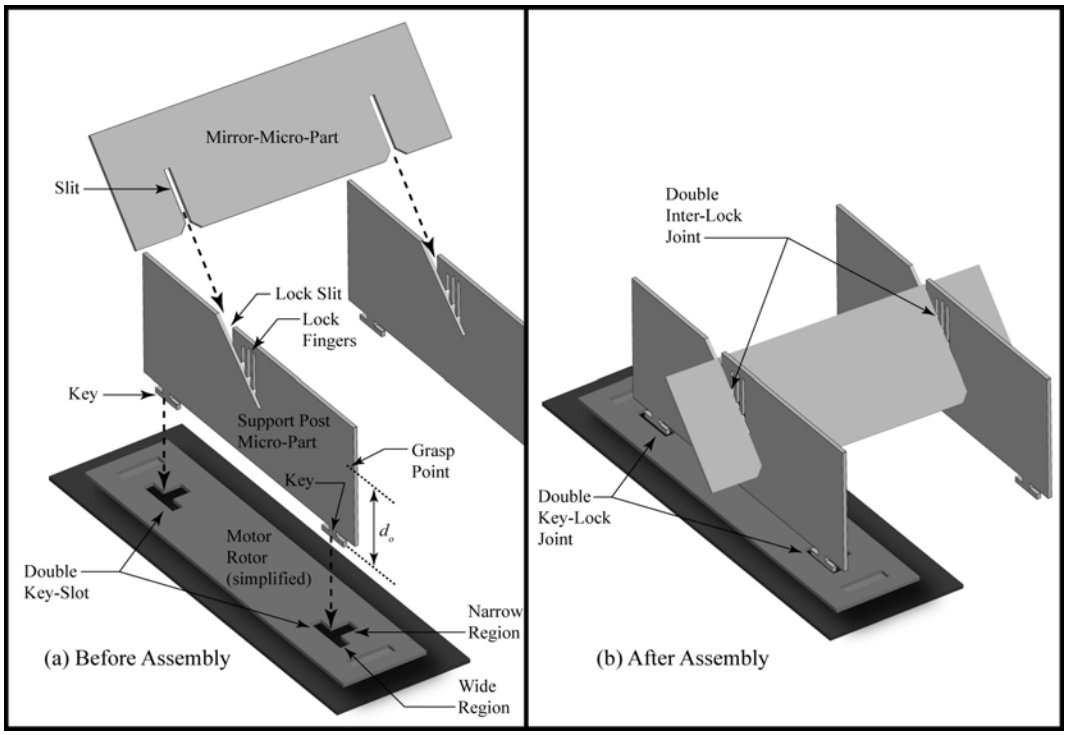

Figure 4.5: Illustration of the principle of operation of the key-lock joints.

The inter-lock joint system works as follows: One micropart has a slit feature, and the other has a lock slit feature, as illustrated in Fig. 4.5(a). In the case of the $3DRIM$, the micromirror has two slit features, and each *support post* has a single lock-slit, as shown in Fig. 4.5(a) and (b), respectively. To create a joint, the two slit features on the micromirror are aligned with each

lock-slit on the *support posts*. The micromirror is then inserted into the *support post*, thereby creating a double inter-lock joint, as illustrated in Fig. 4.5(b). The lock-slits employ lock fingers which press firmly against the inserted micromirror, and thereby wedge it in place, to create a secure joint.

The $3DRIM$ shown in Fig. 4.1 is assembled from three microparts. Fig. 4.6 shows a sequence of video images that illustrate the process of creating an inter-lock joint. Before the inter-lock joint can be made, two *support posts* must be joined by key-lock into the micromotor rotor. This operation is not shown; however, the results of the operation can be seen in Fig. 4.6(a) and Fig. 4.6(c). In these images, the microscope is focused on the top and bottom, respectively, of the assembled *support posts*. Once the *support posts* are assembled, the micromirror can be assembled into them. Fig. 4.6(a) shows the microgripper grasping the micromirror and holding it in an orientation parallel to the chip substrate, and about 100 μm above the substrate. This orientation is not suitable for performing the joint operation, and the micromirror must be rotated so that its plane is at 45° to the substrate.

Fig. 4.6(b) shows the micromirror at 45∘ to the substrate. Due to the limited depth of focus of the microscopy system, the micromirror is out of focus, and appears as a dark blur, since the co-axial light from the microscope is not reflected back into the microscope. As a result, it is difficult for the human operator of the robotic workstation to see the micromirror clearly. The micromirror to be inserted properly into the *support posts*, its position with respect to those *support posts* must be accurately localized. This step is performed with a touch-based and target-based calibration procedure [32]. To accurately determine the distance from the bottom edge of the micromirror to the entry point of the lock slits on the *support posts*, the microgripper is moved down toward the substrate (via the robot), one micron at a time. When the operator observes contact between the micromirror and the micromotor rotor, as shown in Fig. 4.6(c), the motion is stopped, and the z-position of the robot is recorded. The bottom edge of the micromirror is also localized visually in the x and y directions with respect to the micromotor rotor, and those positions are recorded. Since the geometry and orientation of the *support posts*, the micromotor rotor, and the micromirror are all known, the location of the lock-slits with respect to the two slits is determined by calculation. Next, the micromirror and the *support posts* are brought into alignment, as shown in Fig. 4.6(e), based entirely on the numerical calculation

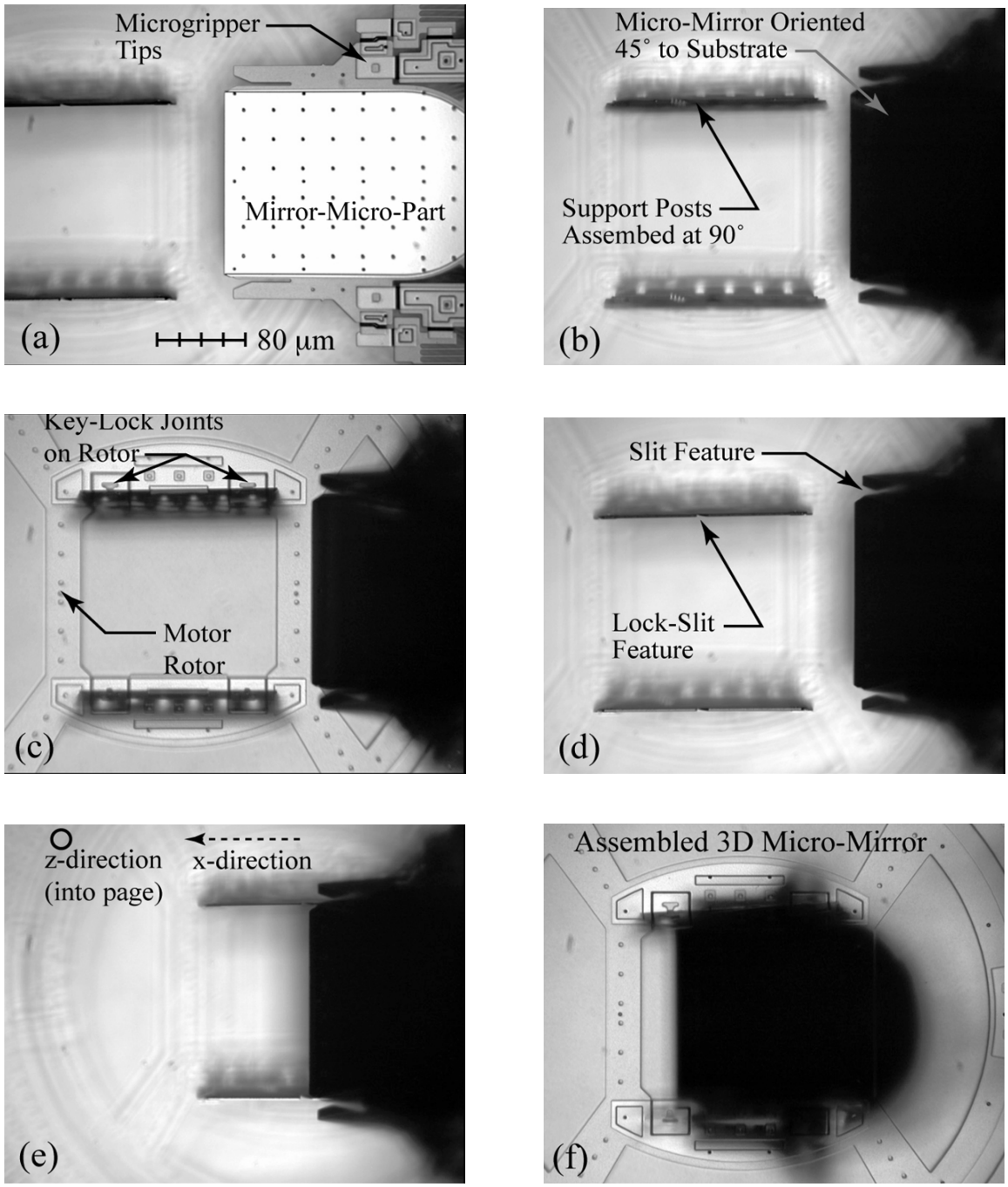

Figure 4.6: Sequence of microscope images showing the joining of the micromirror into dual *support post* microparts.

previously performed. The insertion trajectory vector is programmed into the robot (in this case a simple vector at 45° to the substrate), and the microgripper is commanded to move along that vector. This joining procedure relies heavily on the robot and on the initial calibration for the insertion vector to be maintained. However, it relies very little on the skill of the operator. The operator is in the control loop, but only to the extent that permits the robot to either advance along the insertion trajectory or to retract along it. The operator visually watches for any unusual occurrences during the joint attempt that may indicate a problem. In that case, the joint attempt is aborted, the calibration procedure is performed again, and the microparts are realigned for another joint attempt. Fig. 4.6(f) shows the micromirror successfully inserted into the *support posts* to form a double inter-lock joint.

Task 5: Releasing the Assembled Micropart

Once the micropart has been joined, releasing it from the grasp of the microgripper is straightforward shown in Fig. 4.5(b), the microgripper is retracted along a vector opposite to the initial insertion vector. This retraction exerts a force on the lock fingers (Fig. 4.5(a)) of the *support posts*. Because the lock fingers are at a 45° angle to the retraction vector, the lock-fingers wedge against the micromirror, thereby preventing it from being pulled out of the inter-lock joint. The micromirror is thus locked into the *support posts*. As a result, when the microgripper is retracted further from the micromirror, the microgripper tips self-open and release the interface feature of the micromirror. The completed assembly of the $3DRIM$ is shown in Fig. 4.6(f).

4.3.3 Micromotor-Rotor Key-Slot Fabrication

Fig. 4.7 shows the dimensions for the key-lock joint design. The key is 2 μm tall, as shown in Fig. 4.7(b). Hence, the key-slot requires a height clearance of more than 2 μm for the *support post* keys to be inserted into it. The PolyMUMPs process offers only two releasable polysilicon structural layers. The deposition of the structural layers and the sacrificial layers is conformal. Those two structural layers are used to fabricate the micromotor rotor and the key-slot features. The micromotor rotor is made of a 2 μm POLY1 polysilicon layer. Dozens of dimple features 0.75 μm high are used to raise the rotor above the substrate in order to minimize the friction. The key-slot feature can not be made of the POLY1 layer, since the vertical clearance between

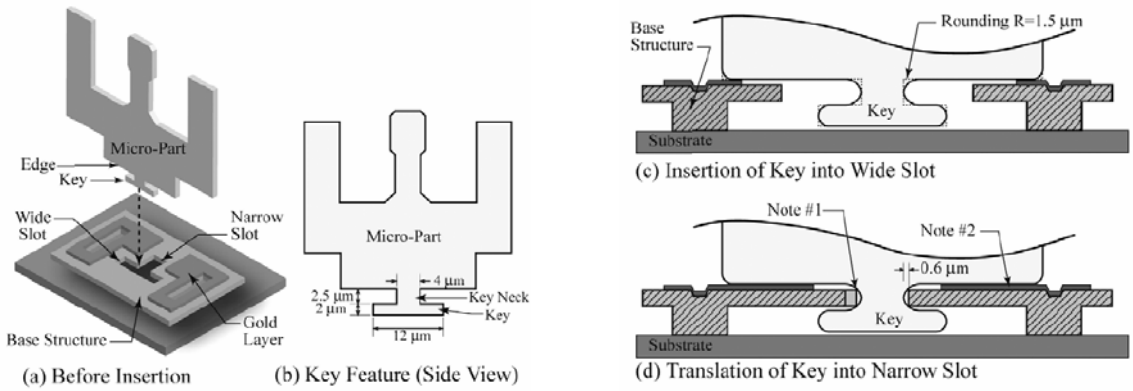

Figure 4.7: Key-lock joint design [32].

the rotor and the substrate is 0.75 μm, which is not enough for the key to be inserted into the key-slot. Hence, the key-slot must be fabricated with the POLY2 layer. On top of the POLY1 layer, a 0.75 μm oxide layer is deposited before the deposition of the 1.5 μm POLY2 polysilicon layer.

In the initial design of the key-slot using the POLY2 layer, a cavity was etched into the rotor layer (made of POLY1) followed by the deposition of the POLY2 layer. The key-slot is patterned onto the deposited POLY2 layer as shown in Fig. 4.8(a) and (b). After the fabricated micromotor rotor undergoes the release process, only 1.5 μm of height clearance is available between the POLY2 layer and the substrate. This clearance is not enough for the insertion of the *support post* keys. For the required clearance of more than 2.0 μm to be achieved, a "sacrificial layer" of POLY1 is patterned on the rotor layer in the cavity directly below the location of the key slot (Fig. 4.8(c)). This sacrificial layer is referred to as a sacrificial part made of POLY1, is not physically attached to the rest of the rotor layer, and will be washed out in the release process. POLY2 has a conformal deposition on the top of the POLY1 layer as shown in Fig. 4.8(d). After the removal of the sacrificial part, the clearance between the POLY2 layer and the substrate in the cavity region is 3.5 μm. This clearance is enough for the insertion of the key into the key-slot. In addition, there is no physical contact between the key and the substrate, which will prevent friction between them. Fig. 4.9(a) shows an SEM picture of the unreleased sacrificial part.

To ensure the easy and complete removal of the sacrificial parts, the design dimensions of

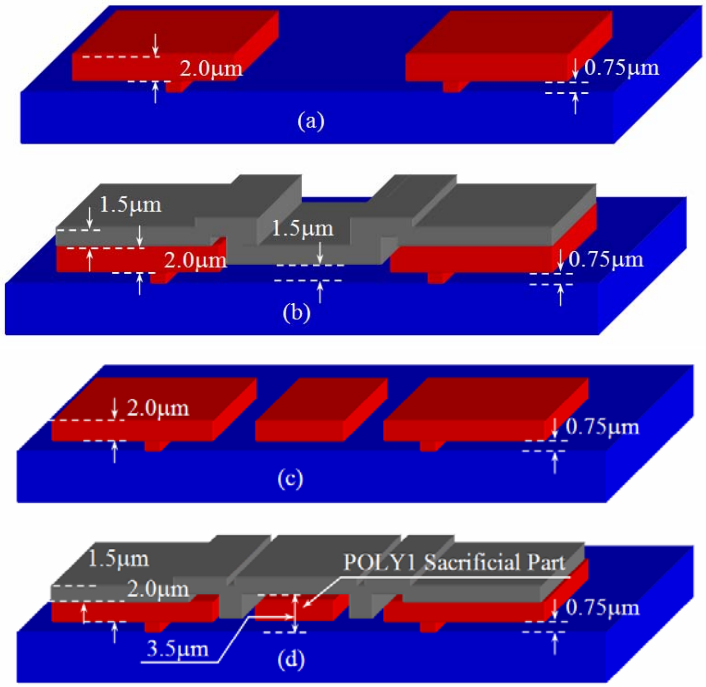

Figure 4.8: Schematic diagram of the key-slot design (a) Deposition of the POLY1 and patterning of the rotor and cavity required for the key-slot feature. (b) Conformal deposition of the POLY2 layer on top of POLY1. The clearance between the POLY2 layer and the substrate is 1.5 μm. (c) Deposition and patterning of the rotor and cavity with a sacrificial part left in the cavity. (d) Conformal deposition of the POLY2 layer on top of the POLY1. A clearance of 3.5 μm is achieved when the sacrificial part made of the POLY1 layer is removed.

the sacrificial part must be carefully considered. This sufficient clearance must exist around the sacrificial POLY1 layer; otherwise, it will be locked beneath the key-slot feature. Fig. 4.9(b) shows an SEM image of eight key-slot features, in which the sacrificial parts under six of them were washed out through the release process and two remained in their positions. In some cases, the remaining sacrificial parts have to be removed manually by the human operator using the microgripper tips. This manual removal is time-consuming and, if necessary, must be performed before the assembly of the *support posts* starts. Future work will attempt to characterize the wash out process during the release phase, to determine whether 100% of the sacrificial parts can be washed away.

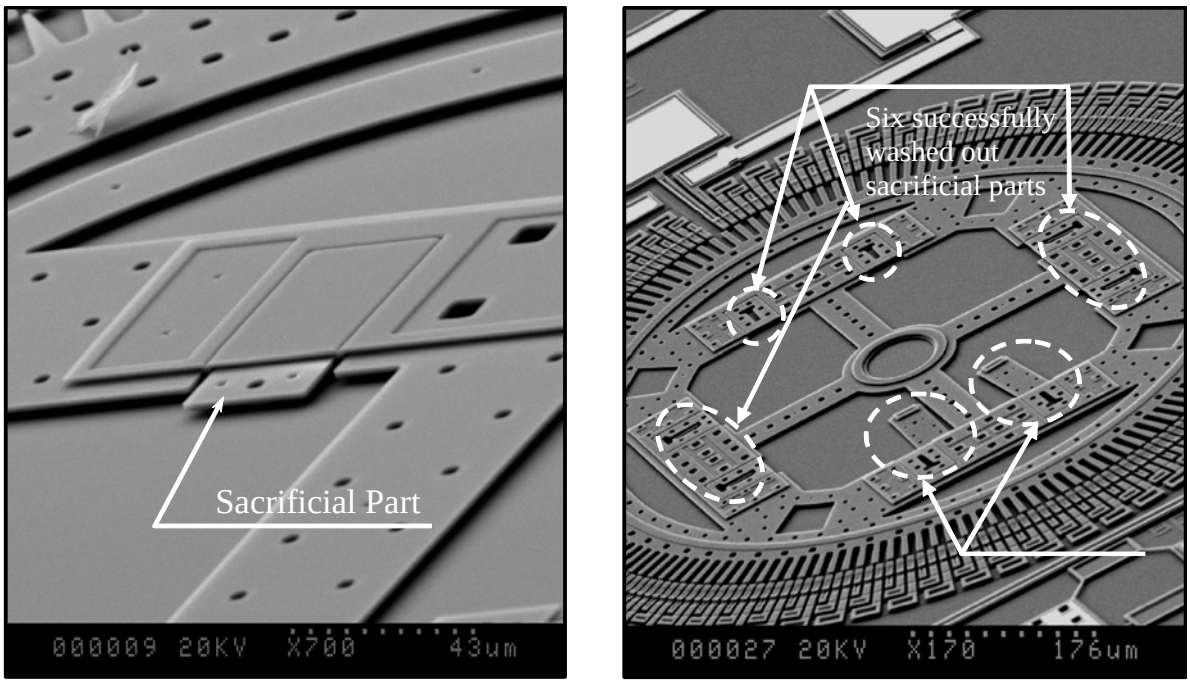

(a) (b)

Figure 4.9: (a) SEM image of an unreleased sacrificial part. (b) SEM image of the micromotor with eight key-slots from which six sacrificial parts were successfully washed out through the release process and only two remained.

4.4 Microassembly of the *3DRIM* Incorporating Large Micromirrors

The previous construction of the $3DRIM$ required the assembly of three microparts: two *support posts* and a micromirror. The assembly process was successful in assembling a 200×280 μm micromirror. The previously described assembly technique steps were followed in an attempt to assemble a larger micromirror. The initial attempt to assemble a 400×480 μm micromirror was unsuccessful. It is useful to describe this unsuccessful assembly attempt and explain the cause of its failure because the analysis helps to explain the assembly techniques that was successfully developed for larger micromirrors. The initial attempt to assemble the large micromirror used two *support posts* and one micromirror. The two *support posts* are identical: 200×200 μm. The modular features included in the *support post* design are the interface feature, the key-lock feature,

and the inter-lock-joint feature. When assembled to the micromotor rotor, the lock-slit feature is oriented at 45° to the substrate. The dimensions of the micromirror used in this assembly are 400×480 μm. The same steps were followed in assembling the *support posts* as in the small micromirror assembly.

4.4.1 Problems with the Support Post Assembly

The two *support posts* were grasped, translated, rotated, and assembled through double-key-lock joints. Fig. 4.10(a) shows a SEM image of both *support posts* assembled in position. Both grasping and assembly were straightforward. However, after the assembly, it was noticed that the *support posts* were not in a good vertical position. The separation distance between the bases of the two *support posts* is designed to be 400 μm to fit with the width of the micromirror. Therefore, the distance between the top edges of the *support posts* should also be 400 μm. However, this was not the case, since both *support posts* were tilted from their ideal vertical positions. Such a deviation results in either a larger or smaller separation distance between the top edges of the *support posts*; the amount of the separation depends on the direction in which both *support posts* are tilting. Assuming the *support posts* have a tilt angle θ_{tilt}, the deviation of the top edge from its vertical position is $H sin\ \theta_{tilt}$, where H is the support post height. Further, the top edge is at an actual height of $H cos\ \theta_{tilt}$, which is less than the proposed height H. An inaccurate value for the tilt angle in turn makes the numerical calculation of the slit position also inaccurate.

In the present case, both *support posts* were tilted away from each other, and the distance between the top edges of the *support posts* was larger than 440 μm, which indicates a deviation angle of more than 5° for each support post. With this type of deviation, the assembly of the micromirror is almost impossible. The large height of the *support posts*, even with a small tilt angle, makes the separation distance significantly larger than the ideal joining distance of the inter-lock feature design. The deviation in the tilt angle of both *support posts* needed to be corrected so that they would return to an ideal vertical position. This correction was attempted using the microgripper to tilt the *support posts* back into their vertical positions. However, when the *support posts* were pushed in this way, the key tip moved out of the narrow key-slot on the micromotor rotor, which made the *support post* no longer secure and therefore unstable. This problem occurred because the length of the original key-slot design is too short. Fig.4.10(c) shows

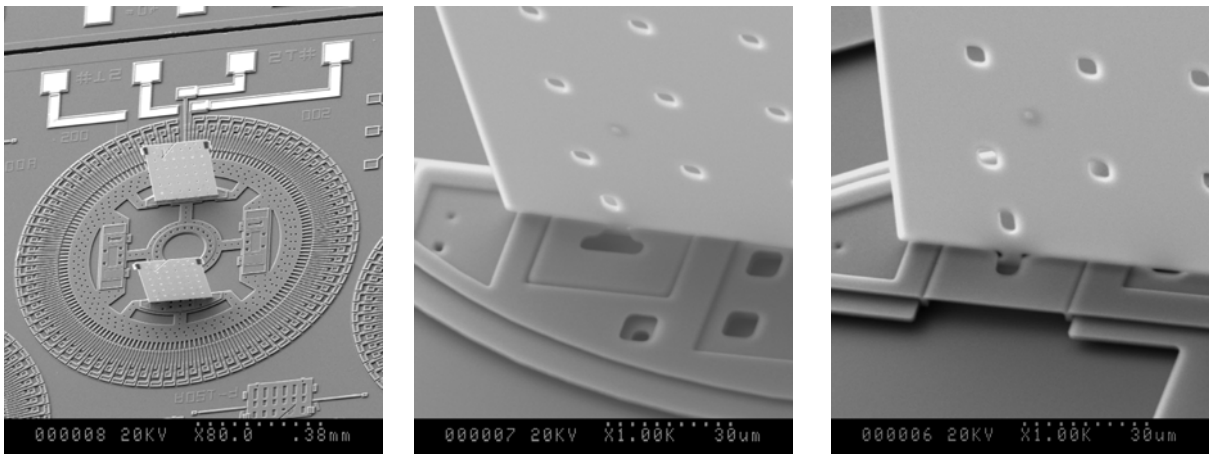

(a) (b) (c)

Figure 4.10: (a) SEM images of the assembly of the two supports through a double key-lock joint with a micromotor rotor. SEM images of a close-up view of the key-lock joint. (b) Front view. (c) Back view.

a SEM image of the key-lock joint of the *support post* before the micromirror assembly. It can be seen clearly in the image that the key-lock joint is not secure enough to keep the *support post* in its position during the next assembly step.

4.4.2 Unsuccessful Micromirror Assembly

The micromirror was grasped successfully, translated, and aligned with both *support posts*. The micromirror is next rotated by 45° with respect to the substrate so that it can be assembled into the *support posts* slits. Due to the limited depth of focus of the microscope system, the micromirror is out of focus and appears as a dark blur throughout the assembly process. As a result, it is difficult for the operator of the robotic workstation to see the micromirror clearly. This joining procedure therefore relies heavily on the robot and on the initial calibration to maintain the insertion vector.

During the insertion of the micromirror, a sudden rotation of the entire structure was noticed, and the attempt to insert the micromirror insertion attempt was terminated. Fig. 4.11 (a) shows SEM images of the unsuccessful $3DRIM$ assembly. The failure of the micromirror assembly can be explained as follows:

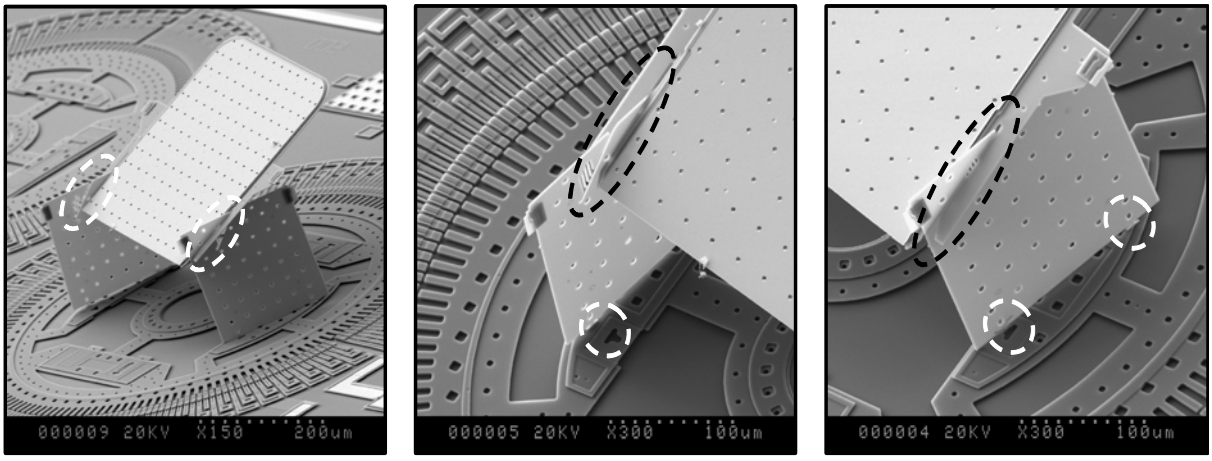

(a) (b) (c)

Figure 4.11: (a) Failure of the assembly of a large micromirror, showing that the key has slipped out of the assembled *support posts* after the micromirror assembly, (a) SEM image of the left support post. (b) SEM image of the right support post.

1. The two *support posts* were not secure enough in the double key-slots. They were also not vertical enough to maintain the designed separation distance between the slits located on the micromirror.

2. The numerical value for the insertion location was not correctly calculated due to inaccurate knowledge of the tilting of the *support posts*.

3. Throughout the insertion of the micromirror, uneven friction forces exist between the lock fingers in the *support posts* and the micromirror slits on both sides. These forces develop a torque on both *support posts*.

4. This developed torque rotates one or both *support posts* and causes the key to slide out of the key-slot in the rotor (Fig. 4.11(b) and (c)). The rotation of the *support posts* occurs before the micromirror is fully inserted thus the inter-lock joint is not completed.

4.5 Method I: Microassembly Design Technique Using Three Supporting Microparts

Construction of the previous $3DRIM$ involved the assembly of two *support posts* and the micromirror. The main task of the *support posts* is to hold the micromirror in a specific pre-designed orientation with respect to the substrate. The assembly was successful for micromirrors with dimensions up to 200×280 μm. To assemble larger micromirrors, *support posts* with larger lights are required. When the construction of the larger $3DRIM$ was attempted, the larger *support posts* and the separation distance between them made the assembly challenging and led to many failures. The main problem was the tilting of the *support posts* and the unstable key-lock joints.

To avoid these difficulties the microassembly process was successfully improved through the design of a new *cross-support post*. A snap-key-lock joint [32] and a new modified design for the key-lock joint also improved the rigidity of the joint. The new design uses either a vertical or horizontal *cross-support post* to hold the main *support posts* in a perfectly vertical position. Details of the assembly and the design of the microparts design are presented in the next section. Fig. 4.12 shows the required microparts with their assembly orientations. This new assembly strategy has proven successful in overcomes the difficulties associated with the assembly of large micromirrors.

4.5.1 *Support Post* Microassembly with the New Key-Lock Joint

To have a secure joint, a more secure design was used for the key-lock joint, called a snap-key-lock joint [32]. The modified key-slot design holds the double keys of the *support posts* more securely. Fig. 4.13 shows two designs of the key-slot that was used in further assembly attempts. The first key-slot has a snap-lock to secure the key of the *support post*. This design perform better from two points of view:

1. The *support posts* remain in their vertical positions after the assembly or show a very small tilting angle.

2. The joint is more secure and rigid. Since the snap-lock feature of the key secures it in the *support post*, the snap-key-lock joint is difficult to release or separate.

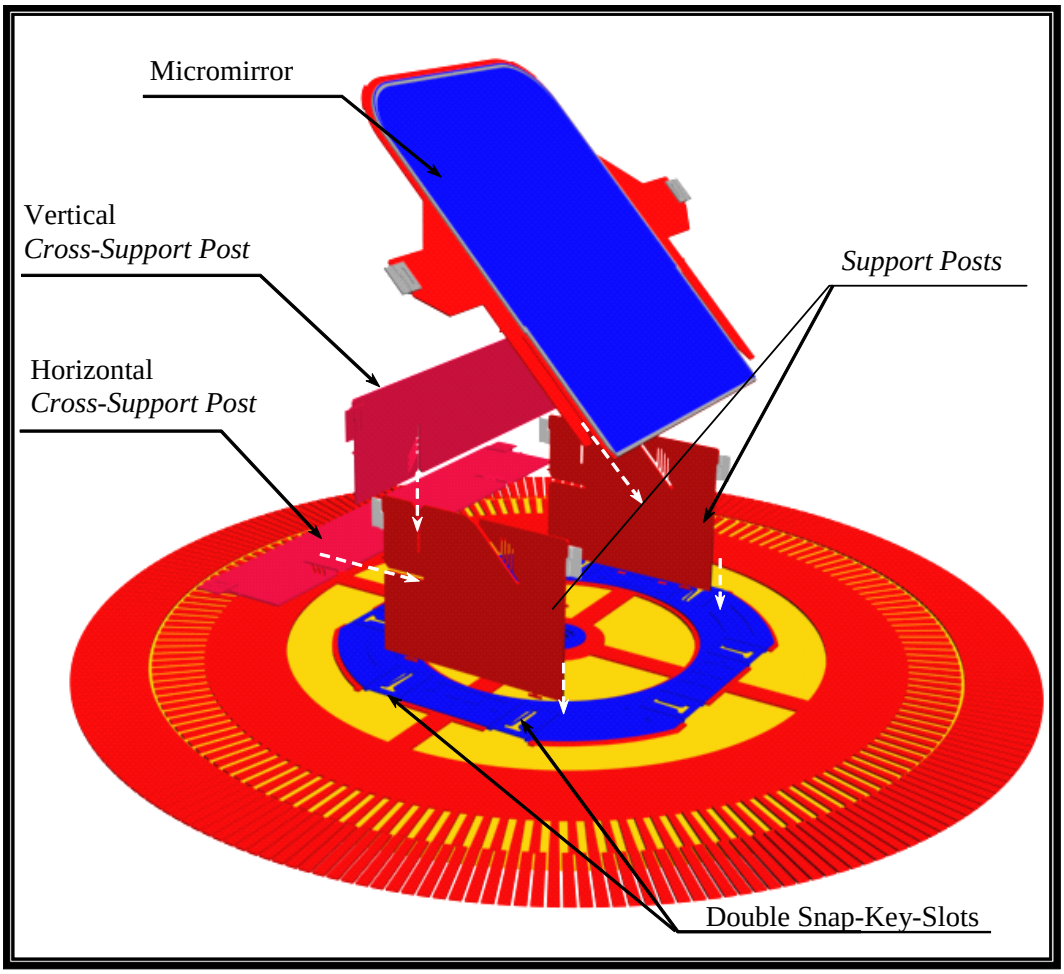

Figure 4.12: Schematic drawing of microparts used in the first modified design assembly technique. A new cross support post is introduced and is assembled either in a vertical or horizontal orientations through the *support posts*.

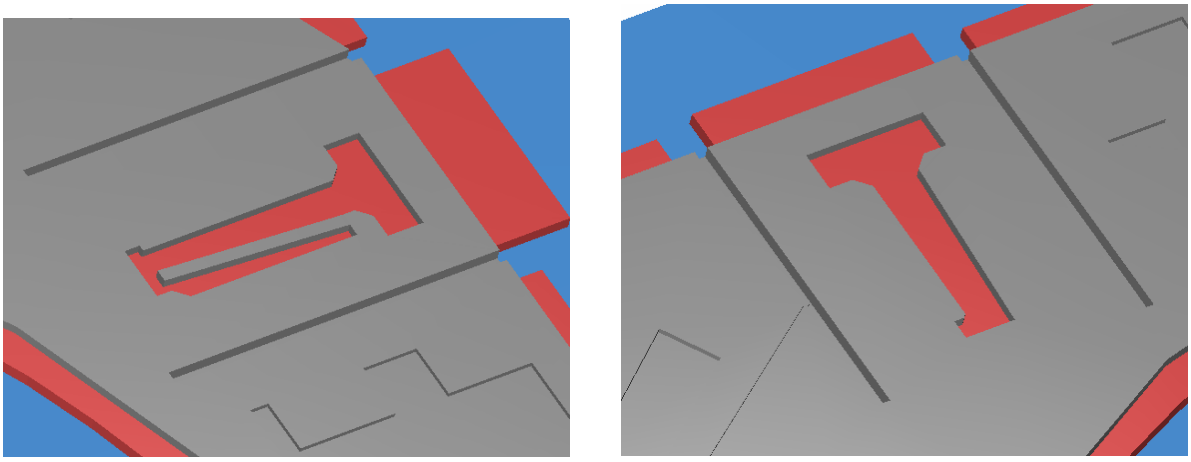

(a) (b)

Figure 4.13: Schematic drawing of (a) Snap-key-lock and (b) modified key-lock joint used in further attempts to assemble the $3DRIM$.

The new modified key-lock slot shown in Fig. 4.13 (b) has a longer narrow wedge, which will significantly decrease the possibility of the *support post* key slipping out of the key slot.

The steps in assembling the *support post* using the snap-key-lock joint are similar to those in the previous assembly with the original key-lock joint. However, when a snap-key-lock joint is assembled, a force is applied by the microgripper on the *support post* to translate the keys into the narrow region of the slot and to pass the snap-lock into a secure position. The microgripper holding the *support post* has some flexibility and is not rigid enough to push the key totally inside the snap-key slot. A moment is developed on the microgripper due to stiction, friction, and the elastic forces between the keys and the slots. This moment causes the microgripper tips to bend. It is difficult for the keys to slide smoothly into the narrow region and pass into the snap-lock. A small vibration force can cause the key to proceed further into the key-slot base and become totally engaged. Presently, a manual vibration is applied to the base of the robot to stimulate the movement of the key inside the snap-key-slot. The amplitude and frequency of the vibration can control the speed and smoothness of the movement of the key and guide it into the slot.

Following the same steps for the translation and rotation of the *support posts*, four *support posts* were assembled into two different micromotor rotors. The first two *support posts* were assembled successfully in a rotor that has a double snap-key-lock joint, as shown in Fig. 4.14

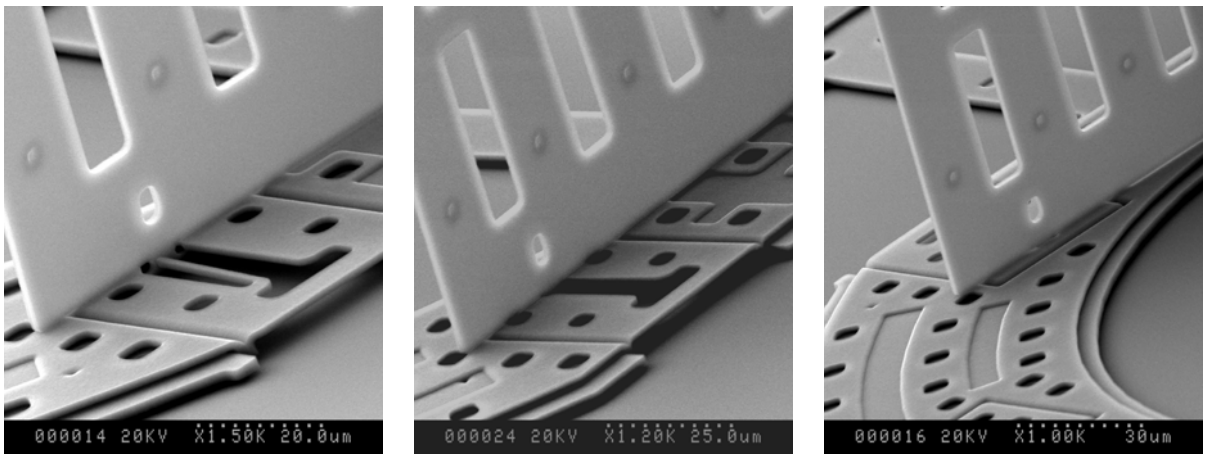

(a) (b) (c)

Figure 4.14: SEM images of (a) Front view of a snap key-lock joint.(b) front view of a modified-key-lock joint. (c) Back view of a modified key-lock joint. The joined *support post* has a height of 150 μm.

(a). The second set of the *support posts* were assembled in another rotor that has the modified key-lock joints, as shown in Fig. 4.14(b). The back view appears in Fig. 4.14(c), which shows a secure and rigid attachment of the two *support posts* to the micromotor rotor. The new designs of the key joints result in support posts that are more secure than with the former design.

4.5.2 *Cross-Support Post* Design and Assembly

The micromirror to be assembled is 300×380 μm. The previously assembled *support posts* have a height of 150 μm and a width of 200 μm. The separation distance between the slits of the *support posts* is the same as width of the the micromirror. The only connection between the *support posts* is the micromotor rotor. Although the *support posts* are more stable with the double snap-key-lock joints, an attempt is made to insert the micromirror through the 45-degree inter-lock joint, the *support posts* are free to tilt in either direction. The tilt may be the result of the free rotation of the micromotor rotor or of any small misalignment in insertion of the micromirror, which most often happens. If the micromirror assembly is successful, the *support posts* are joined by means of the micromirror and become more rigid. Assembling smaller microparts in either a vertical or horizontal direction is much easier than assembling assembly large micromirrors at 45°.

A new micropart called a *cross-support post*, was designed to be assembled before the micromirror. The *cross-support post* is joined either vertically or horizontally to the two *support posts* through double inter-lock-joints. The new *cross-support post* has an interface feature and an inter-lock joint feature. It does not have a key-lock feature since it will be joined directly to the *support posts* through the inter-lock joint feature. The *cross-support post* was designed according to the following parameters:

1. Its weight must be smaller to insure that the added weight will cause only a minimum increase in the friction between the rotor and the substrate.

2. It must have a low profile. The *support post* is wider large than 300 or 400 μm, depending on the required dimensions of the micromirror that is being assembled. The lower profile ensures easy and secure grasping and handling of the micropart.

3. It must be able to be grasped by the same microgripper used to grasp micromirrors larger than 200 μm.

Based on the features required in the *cross-support posts*, the following dimensions were chosen: 92×490 μm. The depth of the inter-lock slit is 46 μm, so a 92 μm height is enough to ensure that the *cross-support post* is rigid. The width of 490 μm was chosen to match the interface feature of the microgripper used to grasp large micromirrors. The tip separation with microgripper C is 490 μm. The two slits of the inter-lock joint are either 300 or 400 μm away from each other, depending on the dimensions of the micromirror that is being assembled.

The *support posts* need additional horizontal or vertical slits in order to form the inter-lock joint with the *cross-support post*. For the convenience of allowing either horizontal or vertical orientation assembly of the *cross-support post*, both slits were added to the same *support post*. Fig. 4.15(a) and (b) show video images of the assembly of a *cross-support post* in a horizontal and vertical orientation, respectively. The two *support posts* are now more rigid and maintain an almost perfect verticality. Fig. 4.15(b) clearly shows the top edges of the *support post* and the *cross-support post* in excellent vertical positions. The assembly of the micromirror should thus be easier than the first attempt to assemble a large micromirror.

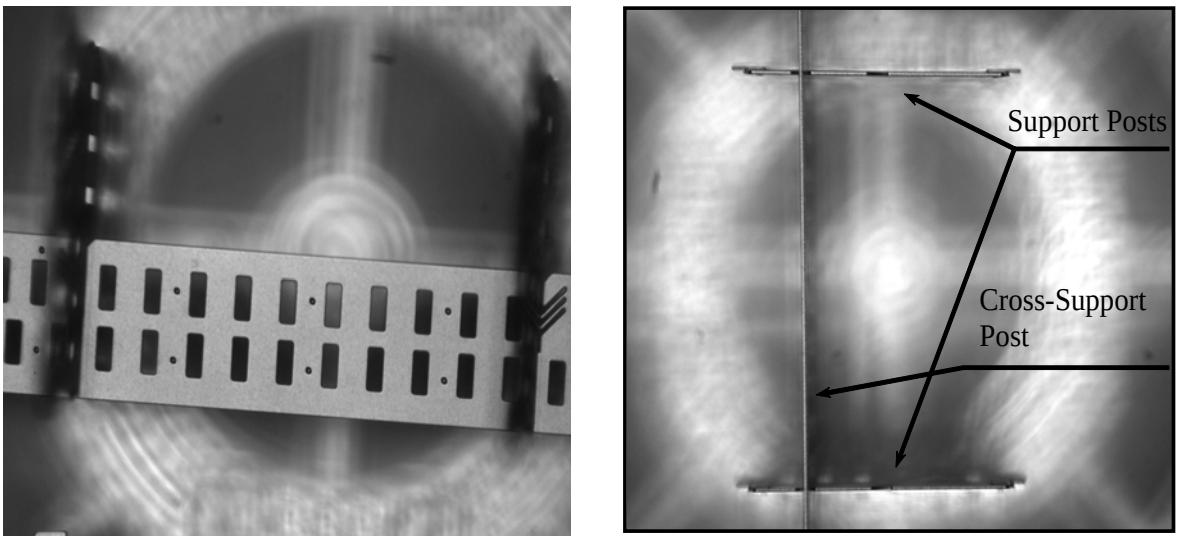

(a) (b)

Figure 4.15: Video images of already-assembled (a) horizontal and (b) vertical *cross-support posts* in two pre-assembled *support posts* to form double inter-lock joints.

4.5.3 Micromirror Assembly

The steps of grasping, removing, and assembling the micromirror in the two *support posts* are identical to those for the assembly of the small micromirror. The large micromirror is significantly bigger and heavier than all other microparts that must be grasped and assembled. For these reasons, two type-C microgripper with four and five flexible beams were used. Different design considerations have to be taken into account when the number of flexible beams is chosen. The grasping, handling, and releasing of the micromirror are different assembly steps that require different designs.

After successfully being grasped, the micromirror is translated, rotated, and oriented at 45° with respect to the substrate. The micromirror is first joined to two *support posts* that are connected by a horizontal *cross-support post*. The touch-based and target-based calibration procedure is performed to numerically locate the 45-degree oriented slit in the two *support posts*. Fig. 4.16(a) shows a horizontal *cross-support post* joining two *support posts*. The 3-D micromirror is shown in Fig. 4.16(b). The inter-lock joint between the micromirror and the *support posts* holds the micromirror firmly at a precise 45-degree angle. A second micromirror was assembled in a

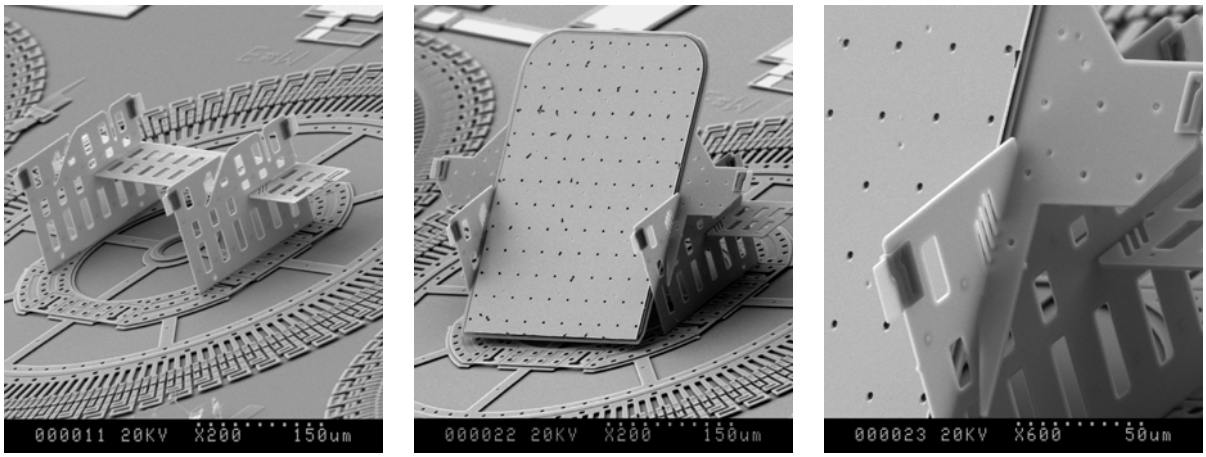

(a) (b) (c)

Figure 4.16: SEM images of an assembled $3DRIM$ incorporates a 300×380 μm micromirror and a horizontal *cross-support post*.

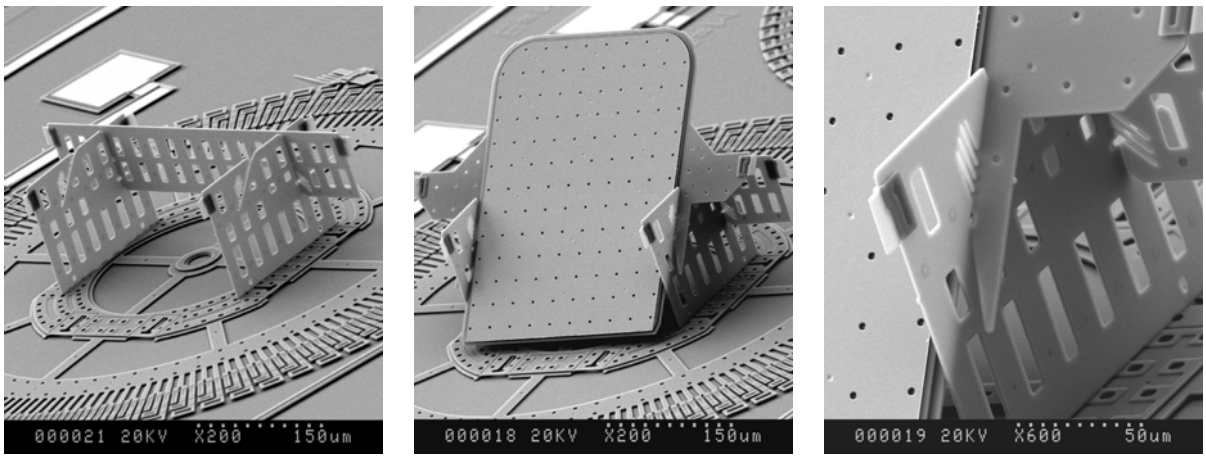

(a) (b) (c)

Figure 4.17: SEM images of an assembled $3DRIM$ incorporates a 300×380 μm micromirror and a vertical *cross-support post*.

second micromotor that has a vertical *cross-support post* joining the pre-assembled *support posts* (Fig. 4.17).

Experience gained through the several assemblies led to the conclusion that the insertion of the *cross-support post* in a vertical orientation is relatively faster and more secure than in a horizontal orientation. With a vertical insertion, the wide opening of the vertical slits can be seen clearly, which is not the case with a horizontal insertion. A horizontal insertion relies on the numerical calculations to determine the position of the slits. The same assembly technique was performed using a vertical *cross-support post* to construct a 400×400 μm micromirror (Fig. 4.18). It can be seen that interface features of the M400 micromirror are closer to body of the micromirror than in the case of the M300 micromirror.

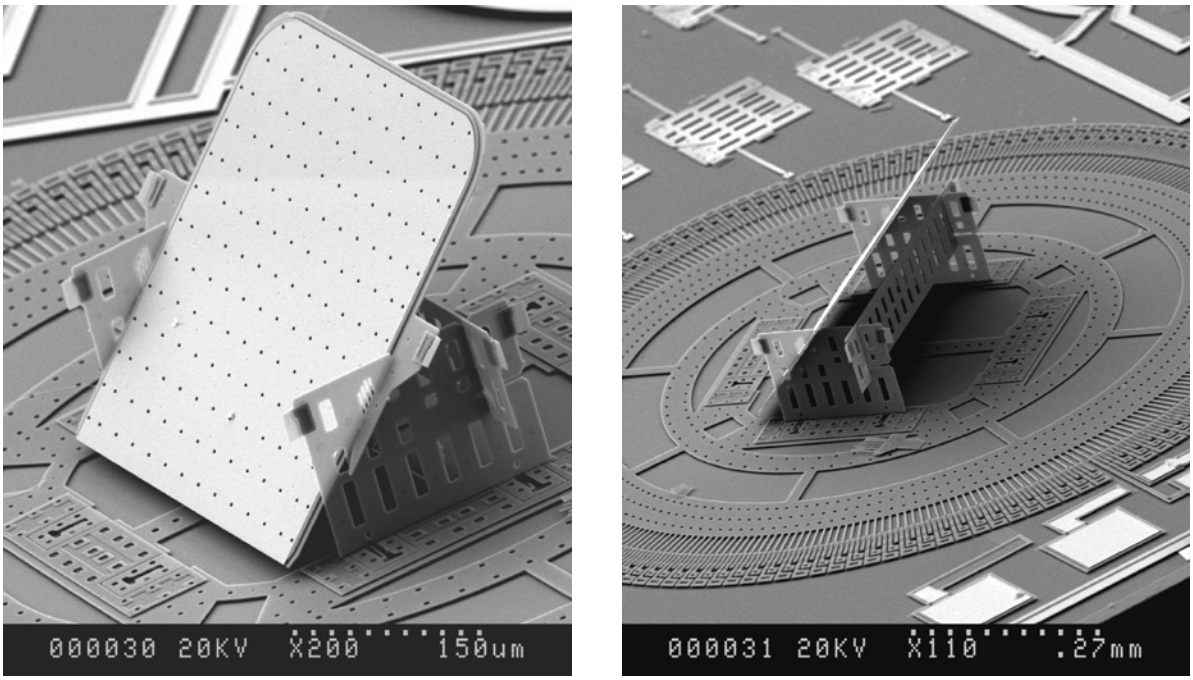

(a) (b)

Figure 4.18: SEM images of an assembled $3DRIM$ incorporates a 400×400 μm micromirror and a vertical *cross-support post*.

4.6 Method II: Microassembly Design Technique Using Four Microparts

The second design assembly technique for constructing a prototype of the $3DRIM$ involves the assembly of four microparts plus the micromirrors. Two microgrippers, A- and C-type, with tip-to-tip distances of 204 and 494 μm, respectively, are used to grasp the microparts. In this assembly technique, two wide low-profile cross *support posts*, two *cross-support posts*, and a micromirror were used. In this design technique, two *cross-support posts* are assembled on top of two wide low-profile *support posts*. The micromirror is then joined to the *cross-support posts* through double inter-lock joints, as shown in Fig. 4.19.

The low profile of the *support posts* (92 μm) makes them easy to grasp and assemble micromotor rotor's double key-slots. The *support post* width of 490 μm was designed to mate with microgripper C for grasping purposes in order to minimize the number microgrippers used. The *support posts* have double vertical lock-slits with lock-fingers. The separation distance between the double lock-slits can be chosen to be either 302 or 402 μm to accommodate a micromirror assembly with a width of 300 or 400 μm, respectively. After the two *support posts* are assembled, two *cross-support posts* are joined vertically through double inter-lock joints. The two *cross-support posts* are identical and are 200×200 μm. The features included are the grasping feature, the vertical inter-lock joint feature, and a 45-degree inter-lock feature.

As mentioned, the vertical insertion makes it easier in that to locate the vertical slits in the *support posts*. Further, the low profile and short separation distance between the *support posts* make the assembly of the *cross-support post* straightforward. Fig. 4.20(a) and (b) show video images of top views of the micromotor, focusing on the top edges of the *support posts* and the *cross-support posts*, respectively. It is clear from Fig. 4.20 that all the assembled microparts maintain excellent verticality with respect to the substrate.

Fig. 4.21(a) shows a 3-D schematic of the assembly of the four microparts before the final insertion of the micromirror. The final step in constructing the $3DRIM$ is the grasping and insertion of the micromirror. The steps of grasping and insertion are similar to those for small micromirrors. Fig. 4.21(b) shows a schematic drawing of the proposed prototype of the $3DRIM$.

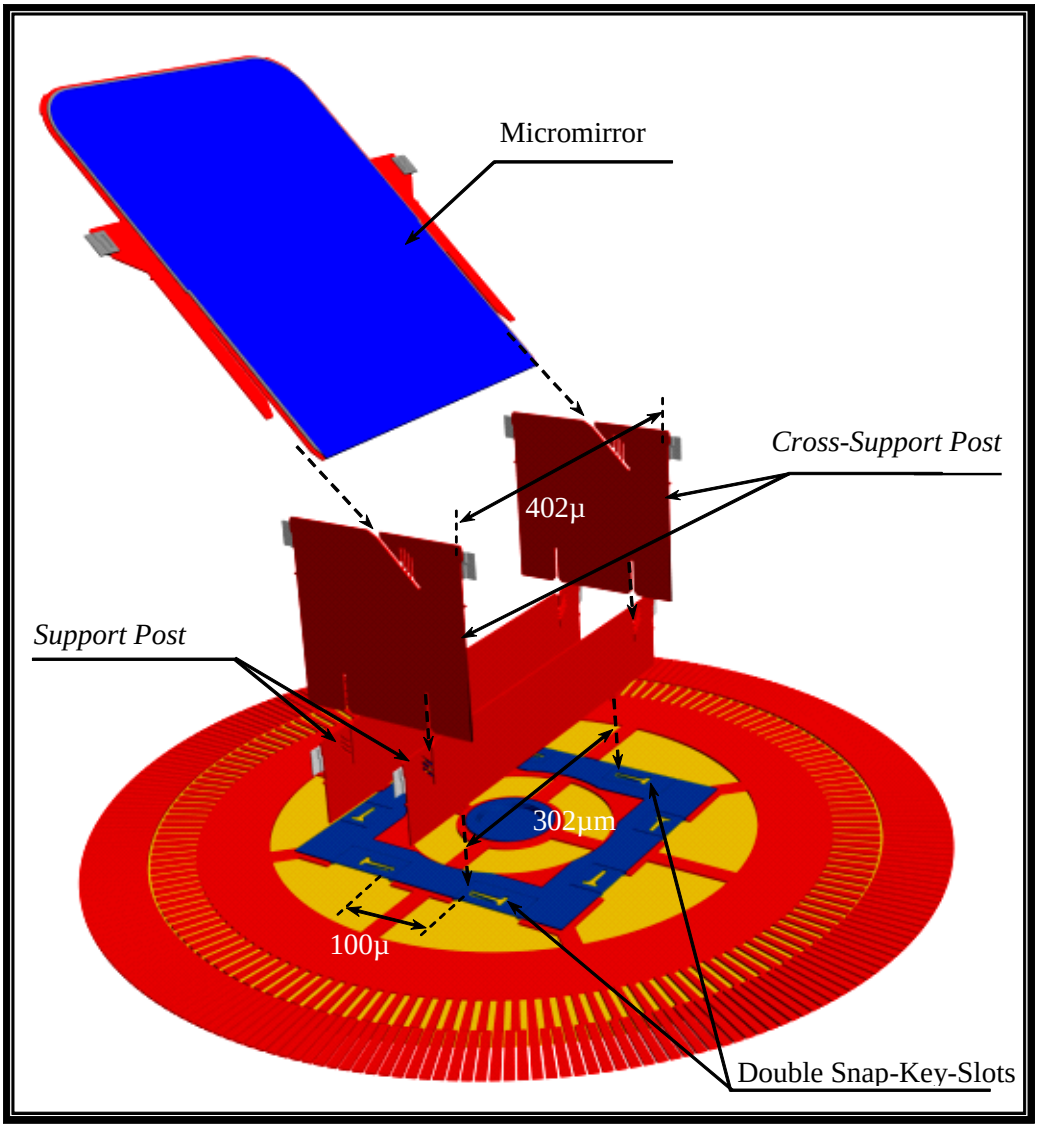

Figure 4.19: Schematic drawing of the microparts used in the second assembly technique.

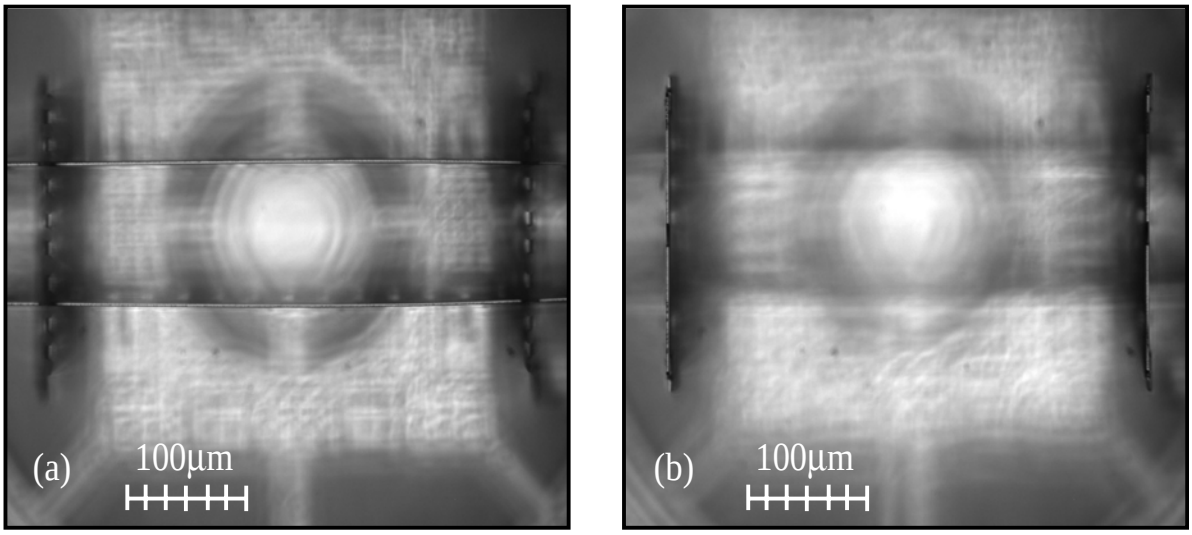

(a) (b)

Figure 4.20: Video images of the assembled microparts, focusing on the top edges of (a) *support posts* and (b) *cross-support posts*.

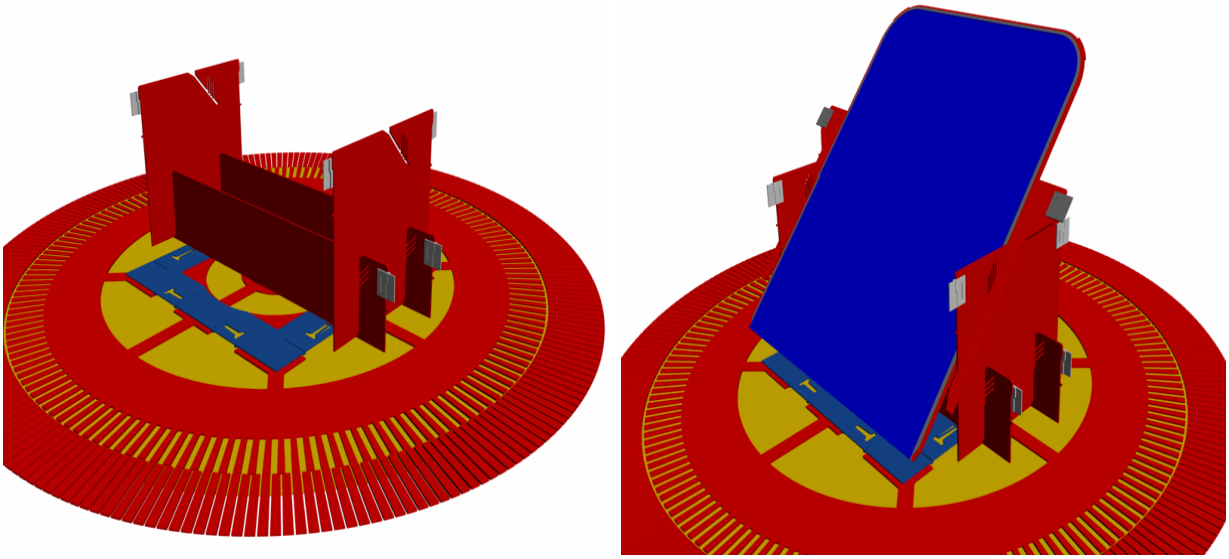

(a) (b)

Figure 4.21: Schematic drawing of the 3$DRIM$ (a) before and (b) after the final assembly of the micromirror.

4.7 Experimental Results and Discussion

The assembly of the micromirrors and microparts onto the top of the electrostatic micromotors was successfully performed. Preliminary performance tests of the electrostatic micromotor in combination with the $3DRIM$, have produced good results.

The main goal of the experimental assembly work was to construct a working prototype consisting of the micromirror and the supporting microparts mounted on the electrostatic micromotor. In this regard, the experiment was a success in that five $3DRIM$s devices of different designs were assembled. The secondary goal of the experimental assembly work was the development of new assembly techniques that could effectively and efficiently achieve the first goal. Some of these new techniques were successful, while others were not, which provided useful information for expanding the possible capabilities of the PMKIL microassembly system. It is important to note, that for any MEMS device that requires assembly, the assembly rate (number of assemblies/time) and the yield (number of successful assemblies/number of assemblies attempted) must be as high as possible. This stipulation applies equally to the success of the $3DRIM$ device. However, since this $3DRIM$ work is in its initial stages, with only conceptual designs being assembled, there was no emphasis on achieving a high assembly rate or yield. When a $3DRIM$ prototype device with the desired performance characteristics is developed, and when the suitable assembly techniques are defined, then the goal of future work will be to maximize the assembly rate and yield of the system.

Prior to this work, the PMKIL microassembly system typically handled microparts from 60×60 μm to 200×200 μm in size. Since some of the microparts used for the $3DRIM$ construction were larger than this, the assembly process required the development of new assembly techniques that can handle the bigger microparts and can deal with the unique aspects of the $3DRIM$ construction. However, the majority of the assembly steps, such as bonding the microgrippers, grasping the microparts or breaking the tethers, remained the same as those used to assemble other devices.

The assembly process proceeded smoothly for most steps. However, a discussion is required regarding some of the unique challenges encountered in the assembly of a $3DRIM$, including the following in order of importance, listed:

1. limited depth of focus when microparts are joined at oblique angles
2. difficulty in creating key-lock joints for large microparts
3. limited visual field of view when large microparts are handled and joined
4. difficulty of joining microparts onto a rotatable base (micromotor rotor) that can rotate slightly during assembly

These four challenges are mentioned specifically since they require future work in order to be resolved/minimized. As can be observed in Fig. 4.6, any microparts that are at angles of more than two degrees to the substrate appear out of focus in the video images. As the angle approaches 90° to the substrate, the ability to discern features on the microparts becomes increasingly difficult with a video microscopy system. For this reason, when the creation of an inter-lock joint was attempted, identification of the joint's features, such as the slit and lock-slit, was difficult. This challenge, in turn, made it difficult to correctly align two microparts prior to an attempt to create an inter-lock joint. To resolve this problem, a more effective image feedback system is required. A proposed system for future work involves the use of multiple microscopy cameras, in order to obtain images at different angles. Such a system also requires an interconnected software reference system so that common reference point, with x, y and z position information, will appear on each video image. This improvement will significantly help achieve the correct alignment between the microparts prior to a joining operation.

An important requirement of the double key-lock joint system is the need to keep the microgripper tips which hold on to the micropart, as close as possible to the bottom edge of the micropart where the double key features are located. This position is necessary for the creation of a secure key-lock joint by means of a single inserting and sliding motion. The reason for this requirement is related to the "grasp point" indicated in Fig. 4.5(a). The grasp point is the position of the interface feature that the microgripper mates with in order to hold on to the micropart. The distance d_o indicates the distance from the grasp point, to a line that passes through both key features. For a key-lock joint to be created, after the keys are inserted into the wide region of the slot, the micropart must be translated parallel to the substrate, so that the keys can slide into the narrow region of the slot. However, to ensure a strong joint, an interference fit has been designed between the keys and the slot. As a result of this interference, stiction, friction, and

elastic forces make it difficult for the keys to slide smoothly into the narrow region. To force the keys into the narrow region, force is applied by the microgripper. When the distance d_o is small (< 20 μm), this force is easily transferred, and the keys overcome the stiction and friction, and slide into position. However, when the distance d_o is large (> 30 μm), a moment is developed on the microgripper. Since the microgripper tips have some flexibility, they start to bend rather than force the keys to slide into the narrow region. For the *support posts* used in the $3DRIM$, the distance d_o is often 80 to 150 μm or more, which makes it impossible to fully slide the keys into the slot. As a result, an inefficient and time-consuming two-step process had to be used during the assembly experiments, to assemble the *support posts* into the micromotor rotor. In order to prevent this problem in the future, the microgripper tips must be designed to be more rigid along the direction in which they apply the sliding force for the key-lock joints, and must be designed to grasp microparts in such a way that the distance d_o is kept at a minimum.

The field of view of the video microscope system is $427H \times 320V$ μm, with an optical resolution of 0.8 μm. However, the largest microparts handled and joined are over 400 μm wide. Since they are held in the vertical direction, both edges of the microparts cannot be viewed simultaneously. This limitation complicates the grasping and joining procedures, since the camera must be moved back and forth on its manual translation stage to allow the operator to monitor the grasping and joining of large microparts. The solution is not as simple as using a microscope system with a larger field of view because the larger field can be achieved only at the cost lower resolution. The resolution required for the joint features of this work must be at least sub-micron. Therefore, future work must develop a suitable system for viewing large microparts.

One of the interesting challenges of assembling the $3DRIM$ is that the base micropart (the micromotor rotor) is free to rotate, which means that during the assembly operation, if any forces are applied in such a way that there is a net imbalance about the micromotor axis of rotation, the micromotor rotor will rotate. Since the key-slot joints and inter-lock joints require translation of a component along the plane of the micromotor rotor, they were designed to ensure that the net force created during assembly would pass through the center of rotation, and thereby not rotate the micromotor. This case is ideal and usually works. However, there were a few cases in which an initially small imbalance caused by an insertion that was not sufficiently aligned or that moved out of alignment would create a small rotation, leading to a greater imbalance of force, which

would lead to more rotation, and soon. This situation could be corrected by aborting the joint attempt, re-aligning the micropart by rotating the robot axes, and trying again. However, for future work, it is worth investigating ways of restraining the rotating micromotor rotors during the assembly operation. Methods to be considered could be the use of tethers that can be broken away after assembly, or a temporary layer of material that could be deposited to secure the rotors and then rinsed away after assembly.

4.7.1 Experimental Microassembly Problems

The size and weight of the micromirror are large compared to those of all other fabricated and assembled microparts. The weight is at least one order of magnitude more than that of any other micropart. Hence the grasping and handling of the micromirror are more challenging. Microgrippers with four and five flexible beams were used to grasp and insert the micromirror. The four-beam microgripper was successful in grasping the micromirror, as shown in Fig. 4.22(a). The five-beam microgripper broke the tether of the micromirror before achieving the full grasping. However, it has a larger handling force than the four-beam one.

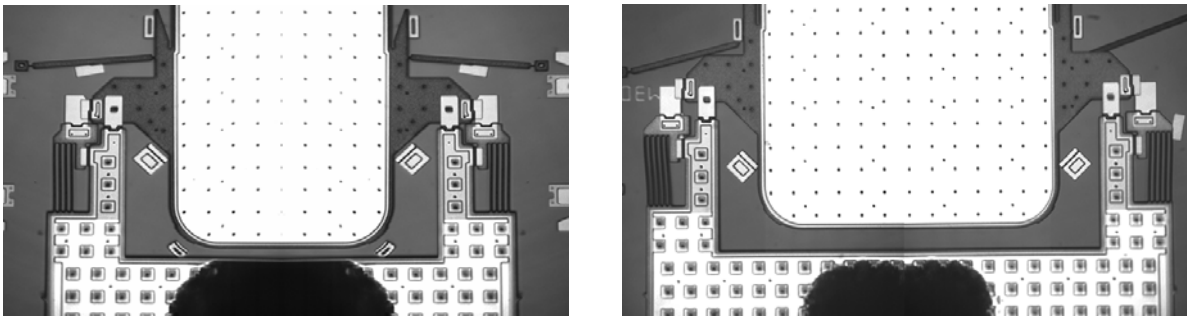

(a) (b)

Figure 4.22: Video images of the graspingof the 300 × 300 μm micromirror. The microgripper has (a) five and (b) four flexible beams.

The flexible beams in the microgripper have a square cross-section which means that they have the same stiffness along both cross-sectional axes. When the 300 μm micromirror is inserted through the *support post* slits, the microgripper bends out of plane. The friction forces in the direction of insertion are larger than the force required to bend the microgripper, which resulted

in a change in the direction the micromirror is inserted, which should be 45° to the substrate. The inter-lock joints were not successfully completed, and the microgripper released the micromirror in this position. To prevent future bending and failure of the micromirror assembly, the stiffness of the microgripper has to be increased in the direction normal to its surface.

When a wide low profile *support post* is inserted into the key-slot, the *support post* bends due to the friction force it faces when the key is translated from the wide wedge to the narrow wedge. The interface feature of the wide *support post* is located at its outer edges which are 490 μm away from each other. The microgripper exerts a holding force on the *support post* to hold it. The direction of insertion and the large distance between the interface features causes the *support post* to bend and makes the process of joining through the key-slot difficult. One solution is to make the interface features inside the *support post* and aligned with the key features. The grasping and handing of the *support post* will then not be affected due to the location of the interface features in the *support posts*.

The hole pattern in the micromirror causes a scattering loss, which is significant and should be minimized for better optical performance. A good micromirror surface quality was obtained by avoiding most of the mandatory fabrication rules of the PolyMUMPs process, as shown in Fig. 4.23(a). However, the etch holes should be included in the micromirror design to avoid any release and stiction problems. Attempts at minimizing the etch holes in the micromirror resulted in surface problems. The gold layer broke around the etch holes in one of the fabrication runs as shown in Fig. 4.23(b).

4.8 Summary

In summary, a successful design, fabrication, and microassembly of a $3DRIM$ were achieved. The $3DRIM$ incorporates different sizes of micromirrors. The first construction of a $3DRIM$ involves the assembly of three microparts: two *support posts* and a micromirror. The two *support posts*, key-joined to the micromotor rotor, hold the micromirror through a double inter-lock joints at a 45-degree angle with respect to the rotor surface. This simple assembly procedure, suite micromirrors with dimensions less than 200 μm in width and fails for assembling larger micromirror.

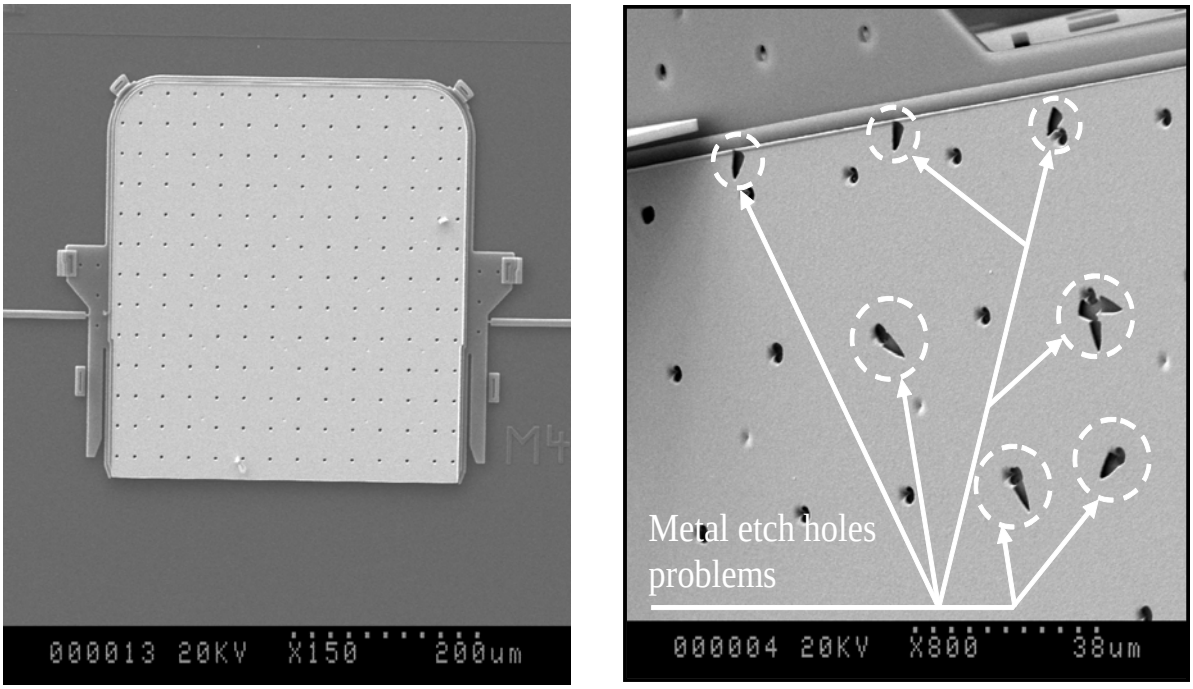

(a) (b)

Figure 4.23: (a) Avoiding the PolyMUMPs mandatory fabrication rules results in a better-quality of the surface of the micromirror. (b) A problem with the etch holes arises when attempts are made to further decrease their size.

Two assembly techniques were developed and were able to construct $3DRIM$s that incorporates a large micromirrors with different sizes. The first technique used a newly designed micropart called *cross-support post* for enhancing the verticality and the rigidity of the two *support posts* before the assembling the micromirror. The low profile of the *cross-support post* and the vertical/horizontal insertion makes its assembly an easy step in the whole assembly process. Although in this assembly technique, which include one extra assembly of micropart, the successful constructions of $3DRIM$s that uses a 300×380 μm and 400×400 μm micromirrors were successful.

The second technique assembles four microparts as a holding structure of a 400×400 μm micromirror in the $3DRIM$. In this assembly technique, two wide low profile *support posts* were assembled first, followed by vertical insertions of two *cross-support posts*. The micromirror is inter-lock joined to the *support posts* at a 45-degree orientation.

Both assembly techniques provide a rigid structure for the $3DRIM$. However, the assembly time, the number of microparts used, and the number of microgripper used to complete one assembly process are important parameters to decide on the assembly technique to choose. Since both assembly techniques provide similar micromirror performance in terms of its rigidity, the ease of assembly is the factor to precede with in future manufacturing of the $3DRIM$. The assembly technique which involves the insertion of one *cross-support post* in a vertical orientation is the easiest method to proceed with.

A natural extension of the $3DRIM$ will be to extend its application into more complex optical signal processing, i.e., wavelength-selective switch. In the next chapter, grating structures have been selected to explore the selectivity of the switch. For this reason, we proposed that the micromirror surface be replaced by a suitable gratings instead of the flat reflective surface. An analytically-based rigorous electromagnetic method capable of modeling a finite grating structure having an arbitrary cross-sectional profile were developed in order to optimize the grating structures in the new proposed wavelength-selective switch.

Chapter 5

Electromagnetic-Theoretical Analysis of Finite Gratings

5.1 Introduction

In previous chapters of this research, the design, fabrication, and microassembly of 3$DRIM$s incorporating different sizes of micromirrors were concluded. The scalability of the new switch architectures utilizing one or several 3$DRIM$s was tested to provide a large numbers of output ports that was not possible by the the 2-D MEMS-based switch and costly yo achieve with the 3-D one. The next stage is to integrate into the MEMS switch the capability for selecting different wavelengths from the switched optical beam. A brief presentation of two proposed wavelength-selective MEMS switches is introduced.

The first MEMS wavelength-selective switch consists of a 3$DRIM$ and four grating-assisted waveguides. The input port is positioned normal to the 3$DRIM$ as shown in Fig. 5.1(a). The inclined angle of the micromirror in this 3$DRIM$ is considered as a design parameter. The micromirror of the 3$DRIM$ in this structure does not have any gratings, only reflective surface. The four waveguides are identical and are place as shown in Fig. 5.1(a). Each waveguide has a finite surface grating at its side facing the 3$DRIM$. The reflected light beam by the 3$DRIM$ will be directed to one of the waveguides. The design of the surface-coupler grating is the most important factor such that at a specific incident angle, only a specific wavelength will be coupled to the waveguide. Changing the incident angle of the incoming optical beam will couple another

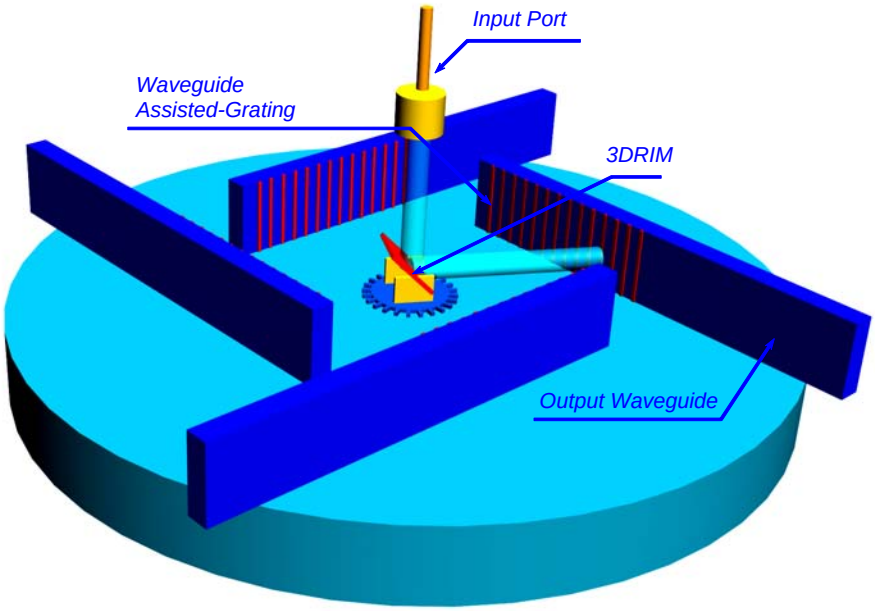

(a)

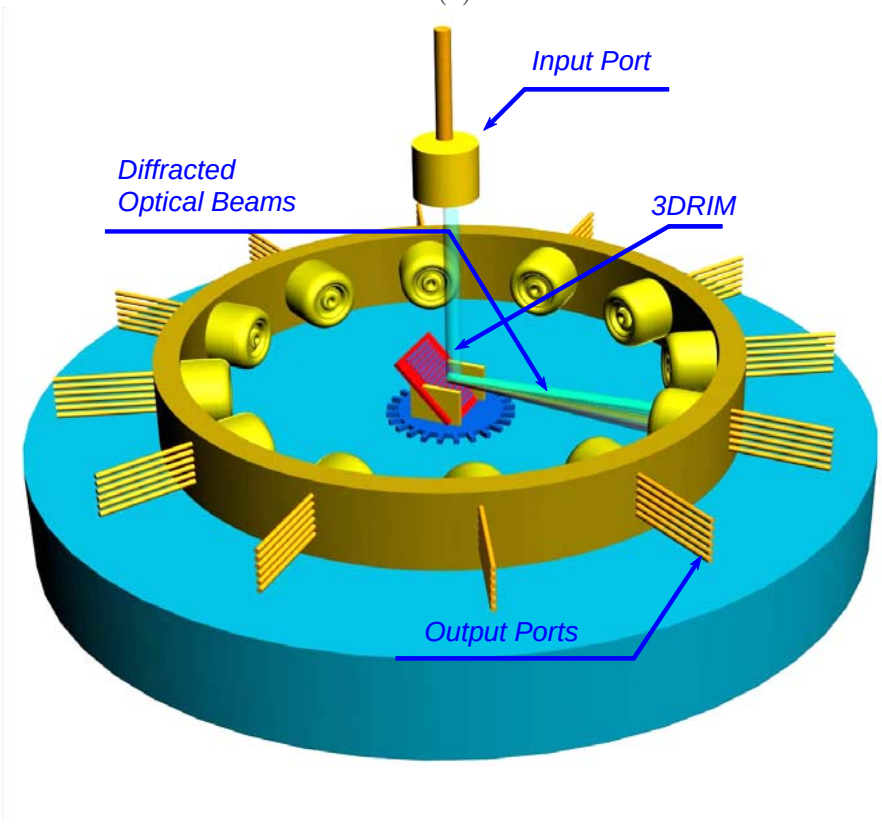

(b)

Figure 5.1: Schematic diagrams of a proposed switch structure for wavelength selection.

wavelength to the waveguide. This structure allows a specific wavelength selection to a the required output waveguide. Rotating the $3DRIM$ to direct the light beam to another waveguide allows for switching a specific wavelength to this waveguide.

The second wavelength-selective switch structure is shown in Fig. 5.1(b) In order to have a wavelength-selectivity in this switch architecture, the micromirror and the receiving ports need to be redesigned. The micromirror in the $3DRIM$ should have a surface gratings. This gratings structure disperses the incident light beam into several directions. The diffracted angles of the light beams depend on several parameters such as the grating period, incident angle, and wavelength λ of the incident light beam. If a light composed of different λ such as optical signal from a WDM networks, each light component will be scattered along different angle. This is achieved by utilizing the grating's ability of spreading light of different wavelengths into different angles The relationship between the incidence and diffraction angles, and the wavelength is given by the well known grating equation.

$$kd\ (sin\ \alpha + sin\ \beta) = 2\pi m \tag{5.1}$$

where d is the grating period, α is the incident angle of the optical beam, β is the diffracted angle, and m is the diffraction order. The profile of the grating control the power coupled into each diffracted beam. The angular variations in the diffracted optical beams can be converted to space variations. The space variations in the diffracted optical beams will enable the reception of these beams separately. The design of such switch include the design of the surface gratings on the $3DRIM$'s micromirror. A good design of the surface grating minimizes the power coupled in the diffracted zero-order and maximize the power coupled into a specific diffracted order. The second design issue is the design of the output port receiver. The output port should be able to covert the angular differences in the diffracted optical beams into a space variations to allow a selection of the required or all diffracted beams. The design and fabrication of the grating structure are the key of this MEMS optical wavelength-selective switch.

This chapter presents a rigorous analytically-based series formulation of the scattered fields from a finite grating made of a large number of 2-D grooves with arbitrary cross-section engraved on a perfect conducting plane for an arbitrary angle incident electromagnetic plane wave as shown in Fig. 5.2. We will first model the scattering from a single groove problem. This formulation

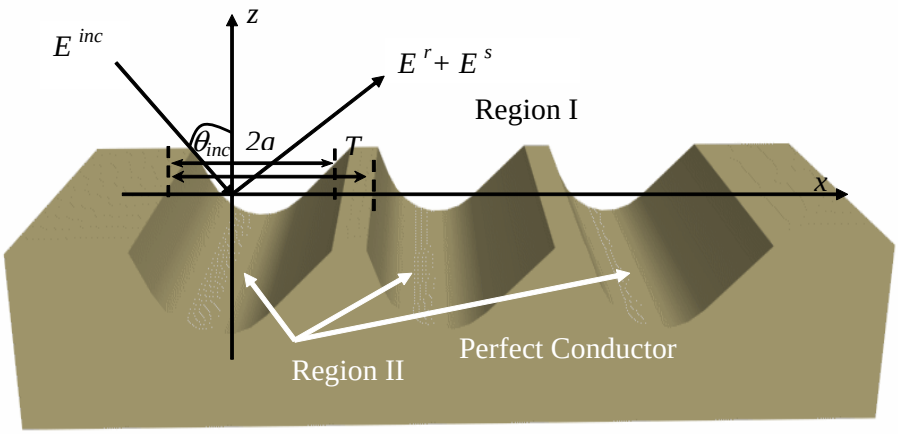

Figure 5.2: A Schematic diagram of the finite general-shaped grooves with a total number of grooves P. The grooves are identical with a period T and a groove aperture width of $2a$. The incident electric field is polarized along y-axes with incident angle θ_{inc}.

will serve as the basis for the multiple groove and will also explain the technique approach in a simple way.

The incident electromagnetic plane wave has either electric or magnetic field polarized along the groove axis (y-axis). In the problem formulation, space is divided into two regions, namely, an upper-half space (region I) and a general-shaped grooves region (region II). Region (I) is an open region while region (II) is a semi closed region. All grooves can have arbitrary dimensions and spacing. In our formulation of the grooves fields, we considered identical grooves, although not a limitation to our proposed method. In Section 5.9, further discussion is provided for the case of non-identical grooves. We relaxed all the constrains of identical grooves and spacing and provided a complete formulation of a non-identical grooves with arbitrary groove-spacing.

Field formulations are identical for identical arbitrary grooves. Each general-shaped groove, as shown in Fig. 5.3, has a total thickness of D and is divided into an L number of layers with uniform layer thickness d ($D = Ld$). For each layer of the general-shaped groove, there are two unknown harmonic field coefficients. In the bottom layer, layer L, there is only one unknown harmonic series coefficients because of the perfect conducting condition at the bottom of the groove ($z = -D$). Matching the fields between two successive layers will provide a set of linear equations relating

the unknown harmonic field coefficients. This process will yield a linear system of equations of all unknown harmonic fields for all layers. Finally, fields in the upper half-space above the grooves are expressed in terms of a Fourier integral type form. Applying the boundary conditions between fields in the upper-half space and the fields from all grooves will provide us with a series form representation of the scattered field in the spectral domain. Further manipulation of the boundary conditions would lead to a system of linear equations for the unknown harmonic coefficients of the first layer in each groove. Combining this system of equations with the previously established linear system of equations, obtained from the application of boundary conditions between the general-shaped grooves interlayers, will provide a coefficient matrix that can be efficiently solved with numerical algorithms. The Scattered fields in the upper half-space are then expressed as Fourier's series summations where the unknowns are the harmonics coefficients of the first layer in each groove. Having determined the first layer unknown harmonics coefficients of each groove, a rigorous analytical-based series solution of the scattered filed is available and near and far field solutions can be calculated. No analytical methods, to the best of our knowledge, are available to solve such multiple general-shaped grooves in a perfectly conducting plane. Only fully numerical methods can deal with such arbitrary finite grooves shape [123, 124]. Comparing numerical methods with our developed rigorous fast method will show the advantages of our scheme in terms of computational time and resources needed to solve a problems with respect to various parameters of the general-shaped grooves.

5.2 A Historical Review of Scattering Formulations

The first theoretical study of a scattering by diffraction gratings belongs to Lord Rayleigh [125]. The purpose of Lord Rayleigh's work was to find the amplitudes and angles of the diffracted fields in the half space above the grating profile. Lord Rayleigh assumed a normally incident plane wave on a grating surface with sinusoidal profile. He also assumed that the diffracted fields are a superposition of the specularly reflected plane wave, a finite number of secondary plane waves propagating in the directions of the higher order grating spectra of optics, and an infinite sequence of evanescent waves whose amplitudes decrease exponentially with distance from the grating. Soon later he generalized the problem by assuming a plane wave obliquely incident on

the grating surface. Lord Rayleigh assumed that the discrete spectrum of the diffracted field is valid in the grating grooves and above the grating profile. This assumption is questionable. Hence, difficulties occur when applying the boundary conditions on the grating surface since this representation of the diffracted field does not in general apply at the grating surface.

Many researchers test the validity and limitations of Lord Rayleigh's assumption (RH) [126, 127]. They found that it can be applied to any surface grating profile. However, If the grating tends to be deeper than a specific value, RH fails dramatically to solve the problem. So RH is valid for a shallow grating. For example, for a sinusoidal grating ($f(x) = A cos\ Kx$), the method will converge if ($AK < 0.448$) and fails beyond that [126]. The work continues after that by many researchers to find reliable methods for solving the problem of diffraction by grating.

Desanto [128, 129] derived a linear equations for the amplitude coefficients using Green's theorem for sinusoidal grating. The equations appear simple but difficult to solve. In later work, Desanto generalized his method for any arbitrary grating profile for perfectly reflecting periodic surfaces. His method depends on expanding the surface fields in a Fourier-series modified by the physical optics approximation. Then using Green's theorem to relate the diffracted wave amplitudes to the integrals over the grating surface times the expansion coefficients [129].

Integral methods [130]; and differential methods [131, 132, 133] have been extensively applied to the problem of diffraction. The main differential methods are the coupled mode analysis and coupled wave analysis. In the modal representation, fields inside the grating are expanded in terms of weighted summation over all possible modes [134, 135]. The summation includes both forward and backward propagating modes. The backward propagating modes are due to diffraction in the grating volume (when the grating fringes are slanted) and due to the reflection at the $z = d$ boundary. Each individual νth mode satisfies the wave equation and thus Maxwell's equations and may be either evanescent or propagation.

In the coupled wave representation [136], the fields inside the modulated medium are expanded in terms of the space harmonic components (i) in the periodic structure. The space harmonics inside the grating are phase matched to the diffracted orders (either propagating or evanescent) outside the grating. However, space harmonics does not satisfy the wave equation individually. The sum of all harmonics does satisfy wave equation and so Maxwell's equations. The partial space harmonic field may be visualized as inhomogeneous plane waves (a plane wave with varying

amplitude along the planar phase front). These inhomogeneous plane waves are not independent and they couple energy back and forth between each other in the modulated medium.

Modeling of scattering from finite periodic grating has become important in the field of micro-optics for optical switching and multiplexing/demultiplexing applications. The accurate simulation of scattered near-field from finite grating clearly show the phase interactions of the near field. This in turn opens a rich opportunity for optical near-field manipulation of nano and micro-optical device. Light scattering is utilized as an important nondestructive tool for surface defects measurements [137]. Compact and low cost optical MEMS devices for wavelength routing, switching and filtering, beam shaping, steering, and focusing, near field imaging and manipulation, and optical disk design are some important applications involving scattering from grating structures. Hence rigorous, robust, versatile, and fast analysis methods would form an essential part of the design optimization of devices in such applications.

Far-field scattering from a limited number of groove shapes was rigorously analyzed using fast analytical methods based on a series summation solution of scattered fields. Rectangular, [138, 139, 140, 141] circular, [142, 143, 144, 145] and elliptical grooves [122] were individually analyzed mainly for far field calculations with a specific formulation for each structure. In the case of elliptical or circular shapes, groove can not be filled with arbitrary dielectric material, but can be filled with circular or elliptical cross-section rods. Analysis of circular and elliptical grooves was extended to double grooves with considerable computational complexity [146]. On the other hand, a rectangular groove was considered as the simplest groove shape to be analyzed and was easily extended to multi-grooves [147]. A very limited number of works on the analysis of near-field scattering from general-shaped groove has been reported in the literature.

Most of the methods used to solve the problem of optical diffraction by gratings assume infinite grating structures. No analytical based methods treat the finite arbitrary-shaped gratings up-to-date. The Physical optics can analyze grating with moderately large apertures, when the groove size is comparable to the wavelength, physical optics fails. However the method is fast with acceptable accuracy results for large groove apertures. Very limited number of works on the analysis of near-field scattering from general-shaped grooves have been reported in the literature based on analytical formulation. Only fully numerical methods, *e.g.*, integral equation formulation with the use of boundary element method (BEM)to solve the equations has been

reported [123, 124].

5.3 Single Groove Problem Formulation

Fig. 5.3 depicts the geometry of the 2-D scattering problem. A general-shaped groove in a conducting plane is a canonical structure for the proposed electromagnetic scattering study. Consider the problem of TE scattering from the general-shaped groove where the incident electric field is polarized along the groove axis (y-axis). The problem space is divided into two regions: the upper half-space which contains the incident, reflected, and scattered fields, and the general-shaped groove region. In region I ($z > 0$), a uniform plane electromagnetic wave of $E_y^{inc}(x, z)$ with an incident angle θ_{inc}, is incident on the general-shaped groove. Region II ($-D < z < 0$ and $-a < x < a$), is an infinitely long (in the y direction) general-shaped groove. The problem is considered a 2-D problem with no dependence on the y-coordinate. The wavenumbers in regions I and II are $k_0 = \omega\sqrt{\mu_0\varepsilon_0}$ and $k = \omega\sqrt{\mu\varepsilon}$, respectively. Throughout the chapter, the assumed $\exp(j\omega t)$ time-harmonic factor is suppressed.

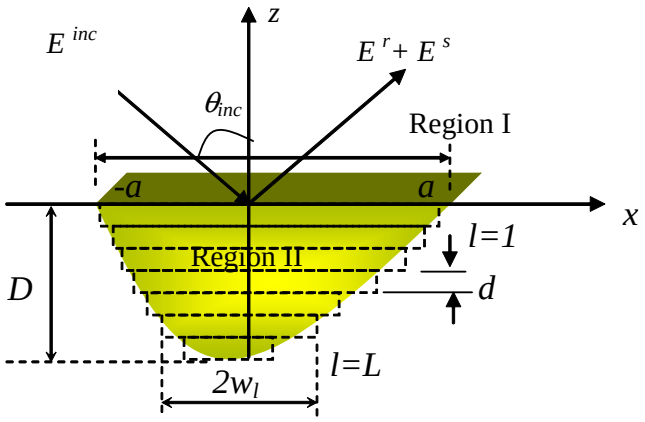

Figure 5.3: Schematic drawing of the general-shaped groove of the scattering problem.

5.3.1 Fields in the Upper Half-Space (Region I)

The total electric field in the upper-half space (region I) is considered a summation of incident, specularly reflected, and scattered fields. The incident and reflected fields are plane waves in the

form

- incident E-field:

$$E_y^{inc}(x,z) = \exp(-jk_x x + jk_z z), \tag{5.2}$$

- reflected E-field:

$$E_y^{r}(x,z) = -\exp(-jk_x x - jk_z z), \tag{5.3}$$

where $k_x = k_0 \sin \theta_{inc}$ and $k_z = k_0 \cos \theta_{inc}$. The scattered field is represented as a Fourier-type integral form and is written as

$$E_y^s(x,z) = \frac{1}{2\pi}\int_{-\infty}^{\infty} \tilde{E}_y^s(z,\zeta)\exp(j\zeta x)d\zeta. \tag{5.4}$$

The scattered field must satisfy the Helmholtz equation and the radiation boundary conditions. In addition, the scattered field should be decaying to zero at infinity (radiation boundary condition). This will lead us to write the scattered field as

$$E_y^s(x,z) = \frac{1}{2\pi}\int_{-\infty}^{\infty} \tilde{E}_y^s(\zeta)\exp(j\zeta x - j\kappa_0 z)d\zeta, \tag{5.5}$$

where

$$\kappa_0 = \begin{cases} \sqrt{k_0^2 - \zeta^2} & k_0 > \zeta \\ -j\sqrt{\zeta^2 - k_0^2} & k_0 < \zeta \end{cases}. \tag{5.6}$$

The propagation factor κ_0 along the z-axis is defined in a way to provide a propagating field for $k_0 > \zeta$ and decaying field at infinity when $k_0 < \zeta$ $[E_y^s(z = \infty, \zeta) = 0]$. The tangential magnetic field component in region I along the x-axis can be derived from Maxwell's equation. The incident, reflected, and scattered tangential magnetic fields components, respectively, are

- incident H-field:

$$H_x^{inc}(x,z) = \frac{k_z}{\omega\mu_0}\exp(-jk_x x + jk_z z), \tag{5.7}$$

- reflected H-field:

$$H_x^r(x,z) = \frac{k_z}{\omega\mu_0}\exp(-jk_x x - jk_z z), \tag{5.8}$$

- scattered H-field:

$$H_x^s(x,z) = \frac{-1}{2\pi\omega\mu_0}\int_{-\infty}^{\infty}\tilde{E}_y^s(\zeta)\exp(j\zeta x - j\kappa_0 z)\kappa_0 d\zeta. \tag{5.9}$$

5.3.2 Fields in the General-Shaped Groove (Region II)

Analytical expressions for the fields inside the general-shaped groove cavity are not possible. However, we can divide the general-shaped groove into L layers with each layer has a thickness of d with total groove depth $D = Ld$. The width of an arbitrary interlayer l is $2w_l = a_l + b_l$, as can be seen in Fig. 5.4. The first layer ($l = 1$) has a common interface with the upper half-space. Fields in the interlayers of the general-shaped groove, through a staircase approximation (see Fig. 5.4), must satisfy Maxwell's equations subject to the boundary conditions at the perfectly conducting walls of the groove (stair-case approximation), i.e., $E_y^{inc}(x = -a_l, z) = E_y^{inc}(x = a_l, z) = 0$. Thus, an analytical form of the fields in an individual layer is possible. The error introduced by the staircase approximation is minimized when L exceeds a reasonable number. This will be demonstrated in Section 5.8 with numerical simulations. The electric and magnetic fields' tangential components in each interlayer can be written as

$$E_y^l(x,z) = \sum_{n=1}^{\infty}\sin\ \beta_n^l(x + a_l)(A_n^l e^{j\zeta_n^l(z+D_{l-1})} + B_n^l e^{-j\zeta_n^l(z+D_l)}), \tag{5.10}$$

$$H_x^l(x,z) = \frac{1}{\omega\mu_r\mu_0}\sum_{n=1}^{\infty}\zeta_n^l\sin\ \beta_n^l(x + a_l)(A_n^l e^{j\zeta_n^l(z+D_{l-1})} - B_n^l e^{-j\zeta_n^l(z+D_l)}). \tag{5.11}$$

Here, $\beta_n^l = n\pi/2w_l$, $w_l = (a_l + b_l)/2$, $D_l = ld$, and $\zeta_n^l = (k^2 - {\beta_n^l}^2)^{1/2}$ for the lth layer; β_n^l determines the harmonic field variation along the x-axis and D_l gives the total thickness measured from the groove interface. A_n^l and B_n^l are the unknown harmonic coefficients for each interlayer, where the superscript l is the layer index and subscript n is the harmonic index. ζ_n^l will be either a real value representing a propagating field or imaginary value representing a decaying or amplifying fields depending on the assumed z-dependent propagation direction of the fields. The last expression of the electric field in the layers assumes a nonhomogenous plane wave

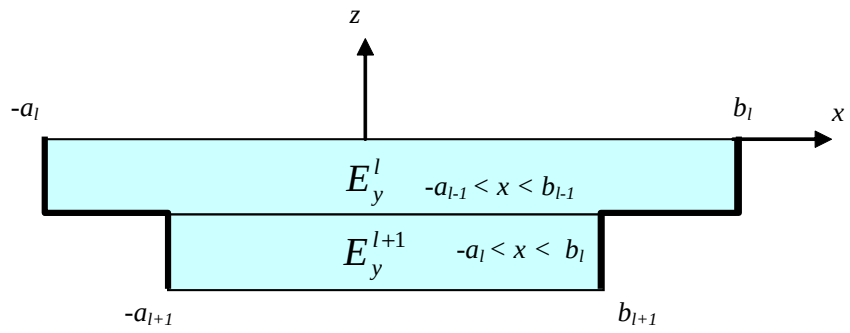

Figure 5.4: Schematic drawing of two inter-layers of the general-shaped groove.

traveling in the positive and negative z-directions with sinusoidal amplitudes variation along the x-direction. This form of electric field variation along the z-axis provides a stable representation of the electric field when applying the boundary conditions between the two layers[148] (l and $l-1$) at $z = -D_{l-1}$. In the last layer (layer L), the electric field satisfies the boundary condition imposed at the bottom wall of the perfectly conducting plane $E_y^{inc}(x, z = D) = 0$, giving

$$E_y^L(x,z) = \sum_{n=1}^{\infty} A_n^L \sin\ \beta_n^L(x + a_L) \sin\ \zeta_n^L(z + D), \tag{5.12}$$

$$H_x^L(x,z) = \frac{1}{\omega\mu_r\mu_0} \sum_{n=1}^{\infty} \zeta_n^L A_n^L \sin\ \beta_n^L(x + a_L) \cos\ \zeta_n^L(z + D). \tag{5.13}$$

Here, β_n^L, w_L, and ζ_n^L are defined as before, for $l = L$.

5.3.3 Boundary Conditions at the Layer Interfaces

Fields are expressed for each inter-layer of the groove with unknown harmonic-field coefficients. A relationship between the unknown field coefficients of the inter-layers is needed to complete the formulation of the fields in the groove. We apply the tangential boundary conditions at the interfaces between the layers in the general-shaped groove (region II) for both tangential electric and magnetic fields. This will give us a set of linear equations for the unknown harmonic field coefficients, A_n^l and B_n^l, for each layer. The boundary conditions will be applied first at the interface of the bottom two layers ($l = L-1, L$) and then at the successive layers interfaces

I. BC between layers $L, L-1$ at $z = -D_{L-1}$

- $E_y^L(x, z = -D_{L-1}) = E_y^{L-1}(x, z = -D_{L-1})$;

$$\begin{aligned}\sum_{n=1}^{\infty} A_n^L \sin\ \beta_n^L(x + a_L) \sin\ (\zeta_n^L d) \\ = \sum_{n=1}^{\infty} \sin\ \beta_n^{L-1}(x + a_{L-1})(A_n^{L-1} e^{-j\zeta_n^{L-1} d} + B_n^{L-1}).\end{aligned} \tag{5.14}$$

- $H_x^L(x, z = -D_{L-1}) = H_x^{L-1}(x, z = -D_{L-1})$;

$$\begin{aligned}\sum_{n=1}^{\infty} \zeta_n^L A_n^L \sin\ \beta_n^L(x + a_L) \cos\ (\zeta_n^L d) \\ = \sum_{n=1}^{\infty} \zeta_n^{L-1} \sin\ \beta_n^{L-1}(x + a_{L-1})(A_n^{L-1} e^{-j\zeta_n^{L-1} d} - B_n^{L-1}).\end{aligned} \tag{5.15}$$

II. BC between layers $l, l+1$ at $z = -D_l$

- $E_y^{l+1}(x, z = -D_l) = E_y^l(x, z = -D_l)$;

$$\begin{aligned}\sum_{n=1}^{\infty} \sin\ \beta_n^{l+1}(x + a_{l+1})(A_n^{l+1} + B_n^{l+1} e^{-j\zeta_n^{l+1} d}) \\ = \sum_{n=1}^{\infty} \sin\ \beta_n^l(x + a_l)(A_n^l e^{-j\zeta_n^l d} + B_n^l).\end{aligned} \tag{5.16}$$

- $H_x^{l+1}(x, z = -D_l) = H_x^l(x, z = -D_l)$;

$$\begin{aligned}\sum_{n=1}^{\infty} \zeta_n^{l+1} \sin\ \beta_n^{l+1}(x + a_{l+1})(A_n^{l+1} - B_n^{l+1} e^{-j\zeta_n^{l+1} d}) \\ = \sum_{n=1}^{\infty} \zeta_n^l \sin\ \beta_n^l(x + a_l)(A_n^l e^{-j\zeta_n^l d} - B_n^l).\end{aligned} \tag{5.17}$$

Multiplying Eq. (5.14) by $\sin\ \beta_s^{L-1}(x + a_{L-1})$ and integrating both sides with respect to x from $-a_{L-1}$ to b_{L-1}, we obtain

$$A_s^{L-1} e^{-j\zeta_s^{L-1} d} + B_s^{L-1} = \frac{1}{w_{L-1}} \sum_{n=1}^{\infty} A_n^L \sin\ (\zeta_n^L d) I E_{s,n}^{L-1,L}, \tag{5.18}$$

where,

$$IE_{s,n}^{L-1,L} = \int_{-a_L}^{b_L} \sin\ \beta_s^{L-1}(x+a_{L-1}) \sin\ \beta_n^{L}(x+a_L)dx. \tag{5.19}$$

Similarly, multiplying Eq. (5.51) by $\sin\ \beta_s^L(x+a_L)$ and integrating both sides with respect to x from $-a_L$ to b_L, we obtain

$$A_s^L = \sum_{n=1}^{\infty} \frac{\zeta_n^{L-1}}{\zeta_s^L} \frac{IH_{s,n}^{L,L-1}}{w_L} \frac{e^{-j\zeta_n^{L-1}d}}{\cos\ (\zeta_s^L d)} A_n^{L-1} - \sum_{n=1}^{\infty} \frac{\zeta_n^{L-1}}{\zeta_s^L} \frac{IH_{s,n}^{L,L-1}}{w_L \cos\ (\zeta_s^L d)} B_n^{L-1}, \tag{5.20}$$

where

$$IH_{s,n}^{L,L-1} = \int_{-a_L}^{b_L} \sin\ \beta_n^{L-1}(x+a_{L-1}) \sin\ \beta_s^{L}(x+a_L)dx. \tag{5.21}$$

Combining Eqs. (5.18) and (5.20) in a matrix form, we obtain

$$\begin{bmatrix} \mathbf{exp}_{L-1} & \mathbf{I} \\ \mathbf{BA}_{L-1} & -\mathbf{BB}_{L-1} \end{bmatrix} \begin{bmatrix} \mathbf{A_{L-1}} \\ \mathbf{B_{L-1}} \end{bmatrix} - \begin{bmatrix} \mathbf{AA_L} \\ \mathbf{I} \end{bmatrix} [\mathbf{A}_L] = 0. \tag{5.22}$$

Here,

$$aa_L(s,n) = \frac{IE_{s,n}^{L-1,L}}{w_{L-1}} \sin\ (\zeta_n^L d), \tag{5.23}$$

$$ba_{L-1}(s,n) = \frac{\zeta_n^{L-1}}{\zeta_s^L} \frac{IH_{s,n}^{L,L-1}}{w_L} \frac{e^{-j\zeta_n^{L-1}d}}{\cos\ (\zeta_s^L d)}, \tag{5.24}$$

$$bb_{L-1}(s,n) = \frac{\zeta_n^{L-1}}{\zeta_s^L} \frac{IH_{s,n}^{L,L-1}}{w_L \cos\ (\zeta_s^L d)}. \tag{5.25}$$

where $aa_L(s,n)$, $ba_{L-1}(s,n)$, and $bb_{L-1}(s,n)$ are elements of the matrices $\mathbf{AA}_L$, $\mathbf{BA}_{L-1}$, and $\mathbf{BB}_{L-1}$, respectively, $\mathbf{exp}_{L-1}$ is a diagonal matrix with the elements $\exp(-j\zeta_s^{L-1}d)$, and $\mathbf{I}$ is the identity matrix. Equation (5.53) relates the harmonic coefficients in the last two layers of the groove ($l = L, L-1$). For the boundary conditions between layers in Eqs.(5.16) and (5.17), we follow the same procedure as for Eqs. (5.14) and (5.51). We multiply Eq. (5.16) by $\sin\ \beta_s^l(x+a_l)$ and integrate from $-a_l$ to b_l, to yield

$$A_s^l e^{-j\zeta_s^l d} + B_s^l = \frac{1}{w_l} \sum_{n=1}^{\infty} IE_{s,n}^{l,l+1} (A_n^{l+1} + B_n^{l+1} e^{-j\zeta_n^{l+1} d}), \tag{5.26}$$

where

$$IE_{s,n}^{l,l+1} = \int_{-a_{l+1}}^{b_{l+!}} \sin\ \beta_n^{l+1}(x + a_{l+1}) \sin\ \beta_s^l (x + a_l) dx. \tag{5.27}$$

For the magnetic field boundary conditions in Eq. (5.17), we multiply Eq. (5.17) by $\sin\ \beta_s^{l+1}(x + a_{l+1})$ and integrate from $-a_{l+1}$ to b_{l+1} , to obtain

$$A_s^{l+1} - B_s^{l+1} e^{-j\zeta_s^{l+1} d} = \sum_{n=1}^{\infty} \frac{\zeta_n^l IH_{s,n}^{l+1,l}}{\zeta_s^{l+1} w_{l+1}} (A_n^l e^{-j\zeta_n^l d} - B_n^l), \tag{5.28}$$

where

$$IH_{s,n}^{l+1,l} = \int_{-a_{l+1}}^{b_{l+1}} \sin\ \beta_n^l (x + a_l) \sin\ \beta_s^{l+1}(x + a_{l+1}) dx. \tag{5.29}$$

Combining Eqs. (5.56) and (5.58) in one matrix, we obtain

$$\begin{bmatrix} \mathbf{exp}_l & \mathbf{I} \\ -\mathbf{BA}_l & \mathbf{BB}_l \end{bmatrix} \begin{bmatrix} \mathbf{A}_l \\ \mathbf{B}_l \end{bmatrix} + \begin{bmatrix} -\mathbf{AA}_{l+1} & -\mathbf{AB}_{l+1} \\ \mathbf{I} & -\mathbf{exp}_{l+1} \end{bmatrix} \begin{bmatrix} \mathbf{A}_{l+1} \\ \mathbf{B}_{l+1} \end{bmatrix} = \mathbf{0}. \tag{5.30}$$

Here,

$$aa_{l+1}(s,n) = \frac{IE_{s,n}^{l,l+1}}{w_l}, \tag{5.31}$$

$$ab_{l+1}(s,n) = \frac{IE_{s,n}^{l,l+1}}{w_l} e^{-j\zeta_n^{l+1} d}, \tag{5.32}$$

$$ba_l(s,n) = \frac{\zeta_n^l IH_{s,n}^{l+1,l}}{\zeta_s^{l+1} w_{l+1}} e^{-j\zeta_n^l d}, \tag{5.33}$$

$$bb_l(s,n) = \frac{\zeta_n^l IH_{s,n}^{l+1,l}}{\zeta_s^{l+1} w_{l+1}}. \tag{5.34}$$

where, $aa_{l+1}(s,n)$, $ab_{l+1}(s,n)$, $ba_l(s,n)$, and $bb_l(s,n)$ are elements of the matrices $\mathbf{AA}_{l+1}$, $\mathbf{AB}_{l+1}$, $\mathbf{BA}_l$, and $\mathbf{BB}_l$, respectively. Equations (5.53) and (5.59) will provide us with a set of linear

relationships between the unknown harmonic coefficients in all interlayers that when matched with the fields in the upper half-space with the appropriate boundary conditions will lead to a linear set of equations. Solving the resulting system for the unknown harmonic coefficients for each layer in the general-shaped groove will lead to a solution for the scattered fields.

5.3.4 Field Matching at the Region I and II Interface ($z = 0$)

It is necessary to match the tangential field components of the electric and magnetic fields from the upper half-space (region I) with the fields in the first layer in the general-shaped groove (region II). First, the tangential electric-field continuity along x-axis ($z = 0$) yields

$$E_y^s(x,0) = \begin{cases} E_y^1(x,0), & |x| < a \\ 0. & |x| > a \end{cases} \tag{5.35}$$

Taking the Fourier-transform of both sides yields

$$\tilde{E}_y^s(\zeta) = \sum_{n=1}^{\infty} (A_n^1 + B_n^1 e^{-j\zeta_n d}) \beta_n^1 a^2 G_n(a\zeta), \tag{5.36}$$

where

$$G_n(\zeta) = \frac{e^{-j\zeta}\,(-1)^n - e^{j\zeta}}{\zeta^2 - (\beta_n^1 a)^2}. \tag{5.37}$$

$\tilde{E}_y^s(\zeta)$ and $E_y^s(x)$ form the Fourier-transform pair of the electric fields at the interface ($z = 0$). In Eq. (34), $\tilde{E}_y^s(\zeta)$ is expressed with a fast convergent series in terms of the unknown harmonic field coefficients of the first layer ($l = 1$) in region II. Next, the tangential magnetic field continuity at the interface $z = 0$ along $-a < x < a$ gives

$$\begin{aligned} &\frac{2k_z}{\omega\mu_0} \exp(-jk_x x) - \frac{1}{2\pi\omega\mu_0} \int_{-\infty}^{\infty} \tilde{E}_y^s(\zeta) e^{j\zeta x} \kappa_0 d\zeta \\ &= \frac{1}{\omega\mu_r\mu_0} \sum_{n=1}^{\infty} \zeta_n^1 \sin\ \beta_n^1 (x + a_l)(A_n^1 - B_n^1 e^{-j\zeta_n^1 d}). \end{aligned} \tag{5.38}$$

Substituting Eq. (5.66) in Eq. (5.68) yields

$$
\begin{aligned}
2k_z \exp(-jk_x x) - \frac{1}{2\pi}\int_{-\infty}^{\infty}\left[\sum_{n=1}^{\infty}(A_n^1 + B_n^1 e^{-j\zeta_n^1 d})\beta_n^1 a^2 G_n(a\zeta)e^{j\zeta x}\kappa_0\right]d\zeta \\
= \frac{1}{\mu_r}\sum_{n=1}^{\infty}\zeta_n^1 \sin\ \beta_n^1(x+a_l)(A_n^1 - B_n^1 e^{-j\zeta_n^1 d}).
\end{aligned}
\tag{5.39}
$$

Multiplying Eq. (5.69) by sin $\beta_m^1(x+a)$ and integrating from $(-a$ to $a)$ gives

$$
\begin{aligned}
2k_z\beta_m^1 a^2 G_m(k_x a) - \frac{1}{2\pi}\sum_{n=1}^{\infty} a^2\beta_n^1\beta_m^1(A_n^1 + B_n^1 e^{-j\zeta_n^1 d})R_{m,n}(k_0) \\
= \frac{1}{\mu_r}a\zeta_m^1(A_m^1 - B_m^1 e^{-j\zeta_m^1 d}),
\end{aligned}
\tag{5.40}
$$

where

$$
R_{m,n}(k_0) = \int_{-\infty}^{\infty} a^2 G_n(a\zeta)G_m(-a\zeta)\kappa_0 d\zeta. \tag{5.41}
$$

This integration can be determined by residue calculus. Details of the calculation of the integration can be found in [149, 150]. Rearranging Eq. (5.41) in a simple form, gives

$$
\begin{aligned}
2k_z a^2 G_m(k_x a) = \frac{1}{2\pi}\sum_{n=1}^{\infty}\left(a^2\beta_n^1 R_{m,n}(k_0)\right)A_n + \frac{a}{\mu_r}\frac{\zeta_m^1}{\beta_m^1}A_m^1 \\
+ \frac{1}{2\pi}\sum_{n=1}^{\infty}\left(a^2\beta_n^1 R_{m,n}(k_0)e^{-j\zeta_n^1 d}\right)B_n^1 - \frac{a}{\mu_r}\frac{\zeta_m^1}{\beta_m^1}e^{-j\zeta_m^1 d}B_m^1
\end{aligned}
\tag{5.42}
$$

Or, in a matrix form,

$$
[\mathbf{C}] = \begin{bmatrix} \mathbf{CA} & \mathbf{CB} \end{bmatrix}\begin{bmatrix} \mathbf{A}_1 \\ \mathbf{B}_1 \end{bmatrix}, \tag{5.43}
$$

where

$$
C(m) = 2k_z a^2 G_m(k_x a), \tag{5.44}
$$

$$
CA(m,n) = \frac{1}{2\pi}a^2\beta_n^1 R_{m,n}(k_0) + \frac{a}{\mu_r}\frac{\zeta_m^1}{\beta_m^1}\delta_{mn}, \tag{5.45}
$$

$$
CB(m,n) = \frac{1}{2\pi}a^2\beta_n^1 R_{m,n}(k_0)e^{-j\zeta_n^1 d} - \frac{a}{\mu_r}\frac{\zeta_m^1}{\beta_m^1}e^{-j\zeta_m^1 d}\delta_{mn}. \tag{5.46}
$$

5.4 Numerical Implementation, and Validations

The representation in Eq. (5.43) is a linear system of equations with N equations and $2N$ unknowns. To determine the unknown harmonic field components of the generalized groove interlayer and hence the scattered field in a series form, we find a relationship between the unknown harmonic coefficients A_n^l and B_n^l of the first layer to be used in (5.43) for a direct matrix inversion solution scheme. In this method of the solution, successive direct matrix inversions are needed using Eqs. (5.53) and (5.59) to find a direct relation between A_n^l and B_n^l with A_n^L of the last layer. To be able to find the matrix inversions, all matrices should be of square dimensions, which forces us to choose the same number of harmonics N in each interlayer of the groove. We experienced instability in our attempts to solve by such a direct matrix inversion strategy. When the interlayer widths ($2w_l$) become much smaller than the operating wavelength λ, β_n^l will have large values leading to large imaginary values of the corresponding ζ_n^l. In the formulating equations, the exponential term $\exp(-j\zeta_n^l d)$ will become extremely large, causing instability in the matrix inversions and in the solution of the system of equations. This type of solution will work well for grooves with all interlayer widths, $2w_l > \lambda/2$.

A stable solution scheme for the whole system, combining Eqs. (5.53), (5.59), and (5.43) can be used to find the unknown harmonic coefficients in all interlayers simultaneously with the freedom to choose a variable number of modes in each interlayer. The choice of the numbers of harmonics in a specific interlayer is based on its physical dimensions, which determines the corresponding values of β_n^l and ζ_n^l in that particular interlayer. Thus, the number of harmonics is then equal to all propagating modes plus two or three evanescent modes in each interlayer. In this way, we can avoid any instability in the system of equations without loss of accuracy. The coefficient matrix $\mathbf{M}$ formed from Eqs. (5.53), (5.59), and (5.43) will take the form of banded matrix (Eq. (5.47)). These types of matrices can be efficiently solved for the unknown harmonic-field coefficients by using the standard Gaussian elimination method:

$$\mathbf{M} = \begin{bmatrix}
\mathbf{CA} & \mathbf{CB} & 0 & 0 & 0 & 0 & 0 & \cdots & \cdots & 0 \\
\mathbf{exp}_1 & \mathbf{I} & -\mathbf{AA}_2 & -\mathbf{AB}_2 & 0 & 0 & 0 & \cdots & \cdots & 0 \\
-\mathbf{BA}_1 & \mathbf{BB}_1 & \mathbf{I} & \mathbf{exp}_2 & 0 & 0 & 0 & \cdots & \cdots & 0 \\
0 & 0 & \mathbf{exp}_2 & \mathbf{I} & -\mathbf{AA}_3 & -\mathbf{AB}_3 & 0 & \cdots & \cdots & 0 \\
0 & 0 & -\mathbf{BA}_2 & \mathbf{BB}_2 & \mathbf{I} & \mathbf{exp}_3 & 0 & \cdots & \cdots & 0 \\
0 & 0 & 0 & 0 & 0 & \vdots & \vdots & \ddots & \ddots & 0 \\
0 & 0 & 0 & 0 & 0 & \vdots & \vdots & \ddots & \ddots & 0 \\
0 & 0 & 0 & 0 & 0 & \vdots & \vdots & \ddots & \ddots & 0 \\
0 & 0 & 0 & 0 & 0 & 0 & 0 & \mathbf{exp}_{L-1} & \mathbf{I} & -\mathbf{AA}_L \\
0 & 0 & 0 & 0 & 0 & 0 & 0 & \mathbf{BA}_{L-1} & \mathbf{BB}_{L-1} & \mathbf{I}
\end{bmatrix}. \tag{5.47}$$

The coefficient matrix $\mathbf{M}$ is a square with the dimensions $N_M \times N_M$, where

$$N_M = 2\sum_{l=1}^{L-1} N_l + N_L. \tag{5.48}$$

where N_l is the number of harmonics in each interlayers of the groove. The elements of the coefficient matrix are matrices formed previously from the application of boundary conditions between groove interlayers and the upper half-space and first layer of the groove.

5.5 Numerical Simulation Results

In this section, we will provide numerical examples for a single groove based on the formulation in the previous section for different groove shapes and compare the results with published results in the literature. We will study convergence, stability, and effect of the choice of the number of interlayers and number of harmonics in each interlayer of the groove.

The first example to consider is the scattering of normal incident plane wave fields from a rectangular groove similar to the one in Ref. [34]. The width and depth of the rectangular groove are λ and $\lambda/4$, respectively, λ being the operating wavelength. The incident electric field is polarized along the groove axis (y-axis). The rectangular groove will be divided into L number of layers. The parameter L will vary from 10 to 100 to determine the scattered field's dependence

Table 5.1: Modal Field Coefficients of the Scattered Fields From Rectangular Groove With Normal Incident Plane Wave for Different Number of Layers.

Number of	Coefficient A				Coefficient B			
groove interlayers	A_1	A_2	A_3	A_4	B_1	B_2	B_3	B_4
$L = 10$	1.4662	0.0101	0.0083	0.0003	1.4662	0.0102	0.2290	0.0000
$L = 20$	1.4662	0.0112	0.0083	0.0002	1.4662	0.0112	0.2500	0.0000
$L = 30$	1.4662	0.0115	0.0083	0.0001	1.4662	0.0116	0.2574	0.0000
$L = 40$	1.4662	0.0117	0.0083	0.0001	1.4662	0.0118	0.2612	0.0000
$L = 50$	1.4662	0.0118	0.0083	0.0001	1.4662	0.0119	0.2635	0.0000
$L = 60$	1.4662	0.0119	0.0083	0.0001	1.4662	0.0120	0.2651	0.0000
$L = 70$	1.4662	0.0119	0.0083	0.0001	1.4662	0.0120	0.2662	0.0000
$L = 80$	1.4662	0.0120	0.0084	0.0001	1.4662	0.0120	0.2670	0.0000
$L = 90$	1.4662	0.0120	0.0084	0.0001	1.4662	0.0121	0.2677	0.0000
$L = 100$	1.4662	0.0120	0.0084	0.0001	1.4662	0.0121	0.2682	0.0000

on the number of layers in the groove. The number of harmonics in this case will be the same in each layer since all layers are of the same width. In this special case, direct matrix inversion of Eqs. (5.53) and (5.59) is possible and will not encounter any stability problem. The scattered fields at the interface of the rectangular groove compared to the results from [34] and the solution by HFSS (finite element method solver) are shown in Fig. 5.5. As can be seen from the results, fields calculated for $L = 40$ and higher are identical, indicating a robust convergence of the solution. Boundary conditions are clearly satisfied at the rectangular groove edges as well as on the perfect conducting plane. Table 1 shows the calculated coefficients in the first layer ($l = 1$) in the rectangular groove for different number of layers. Increasing the numbers of layers beyond ($L = 40$) does not affect the harmonic coefficients and hence the scattered fields as seen in Fig. 5.5(a). A comparison between our results with $L = 40$, Ref. [34], and simulation from Microwave studio (MWS) is presented in Fig. 5.5(b).

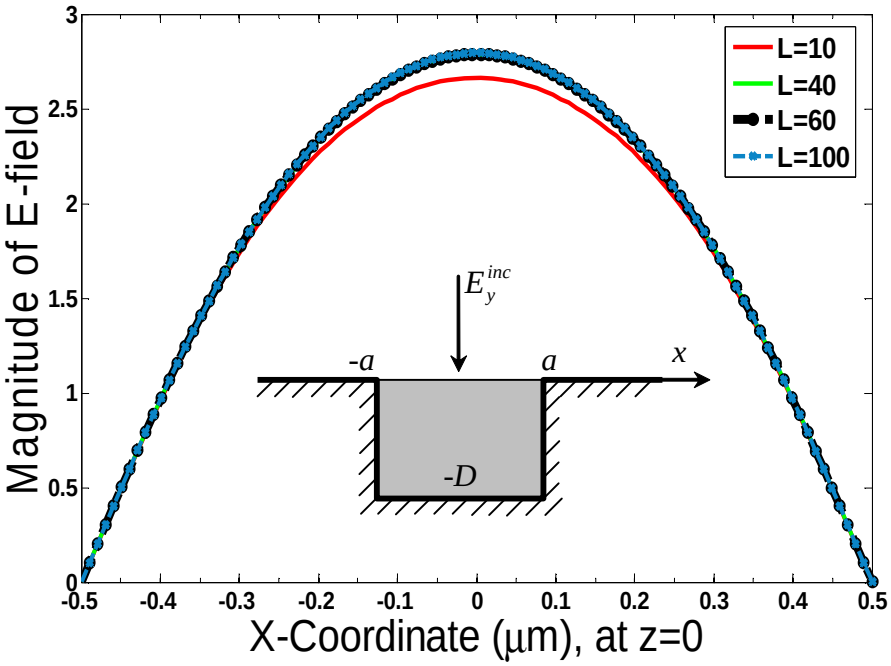

(a)

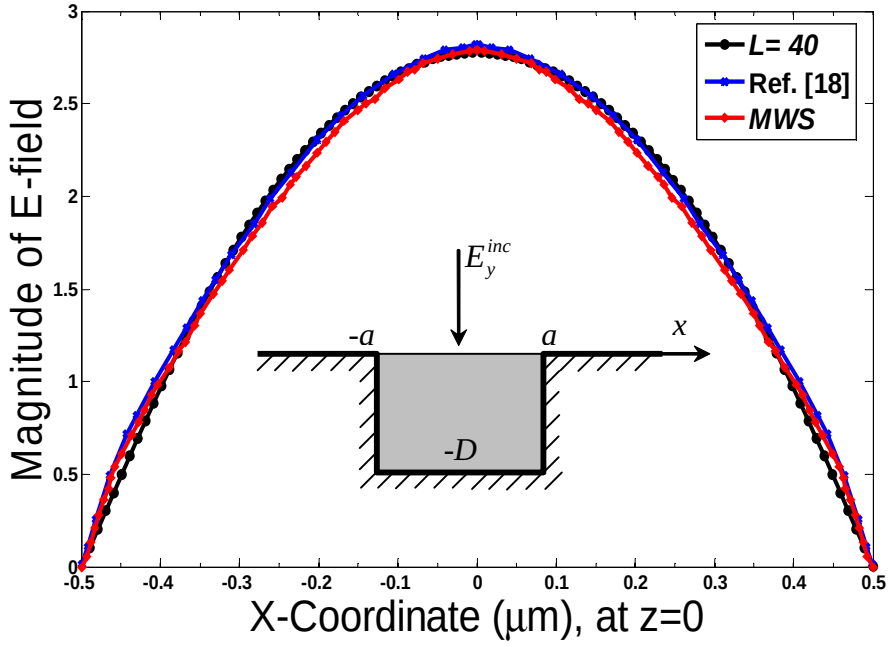

(b)

Figure 5.5: Scattered field at the interface of rectangular groove with width ($2a$) and depth (D) equal to λ and $\lambda/4$, respectively, and normal incident field. (a) Results for $L = 40, 60, 100$ have complete overelap, and (b)comparison between results from Ref. [34], MWS, and $L = 40$.

Next, the dependence of the scattered fields at the rectangular groove on the number of harmonics in the interlayers is presented in Fig. 5.6. No detectable changes in the fields occur when the number of chosen harmonics is four or more, showing robust convergence of the method for a small number of harmonics (N). Table 2 lists the coefficients for various numbers (N) of harmonics. Calculation of the field coefficients and the scattered field did not encounter any instability problem when the number of layers or harmonics increases beyond the convergence requirements. As a measure of the versatility of the method, we tested the scattered field's sensitivity to the groove sidewall angles deviating from ideal vertical walls. Usually in rectangular groove fabrication, sidewalls are not exactly vertical and deviate from the ideal case with some inclination angle. We calculated the scattered fields as the groove left side wall slope starts to deviate from 90°. The aperture width and depth of the rectangular groove are again, λ and $3\lambda/2$, respectively. As seen in Fig. 5.7, the scattered field at the groove interface is no longer symmetric and the point of maximum value shifts away from the center to the left as the slope increases.

The second example to consider is a triangular-shaped groove. The reason to test on such a groove is to show the stability of the method, since the fields in the bottom layers of the groove decay fast as we approach the bottom. Use of the direct matrix inversion for this example encounters stability problems and does not converge to the correct answers. With the method proposed here, the simulation was stable and no convergence problems were encountered in the calculation. In Fig. 5.8, the scattered field at the groove interface for the isosceles right triangle (IRT) groove with aperture width, $2a = 1.2\lambda$, is plotted for different numbers of layers L ($L = 10, 30, 60, 80,$ and 100). For $L = 60$, fields converge well and are identical. Scattered fields at the triangle groove are tested for different incident angles of the plane wave as shown in Fig. 5.9 for the same groove dimensions. The method was also tested for different depths and widths of the triangular groove. Increasing the depth (D) of the triangular groove from a to $5a$, while maintaining the width at $2a$, will vigorously test the stability and convergence properties of our method. In Fig. 5.10, we show the scattered fields for different groove depths. The solution was stable and no convergence problems were encountered for all values of the groove depth (D). In Fig. 5.11, the width of the triangular groove was increased from $2a$ to $3a$, with the depth (D) kept fixed at $2a$.

Table 5.2: Field Coefficient of the Scattered Field From Rectangular Groove With Normal Incident Plane Wave and Number of Layers $L = 80$.

Number of	Coefficient A							
Harmonics	A_1	A_2	A_3	A_4	A_5	A_6	A_7	A_8
$N_1 = 4$	1.4662	0.0120	0.0082	0.0000	-	-	-	-
$N_1 = 5$	1.4662	0.0125	0.0082	0.0000	0.0791	-	-	-
$N_1 = 6$	1.4660	0.0139	0.0083	0.0000	0.0001	0.0000	-	-
$N_1 = 7$	1.4661	0.0141	0.0083	0.0000	0.0001	0.0000	0.0414	-
$N_1 = 8$	1.4661	0.143	0.0084	0.0001	0.0000	0.0000	0.0000	0.0000
Number of	Coefficient B							
Harmonics	B_1	B_2	B_3	B_4	B_5	B_6	B_7	B_8
$N_1 = 4$	1.4662	0.0121	0.2670	0.0000	-	-	-	-
$N_1 = 5$	1.4662	0.0126	0.2674	0.0000	0.0828	-	-	-
$N_1 = 6$	1.4660	0.0140	0.2723	0.0000	0.0851	0.0000	-	-
$N_1 = 7$	1.4660	0.0142	0.2725	0.0000	0.0852	0.0000	0.0442	-
$N_1 = 8$	1.4661	0.0144	0.2747	0.0000	0.0860	0.0000	0.0449	0.0000

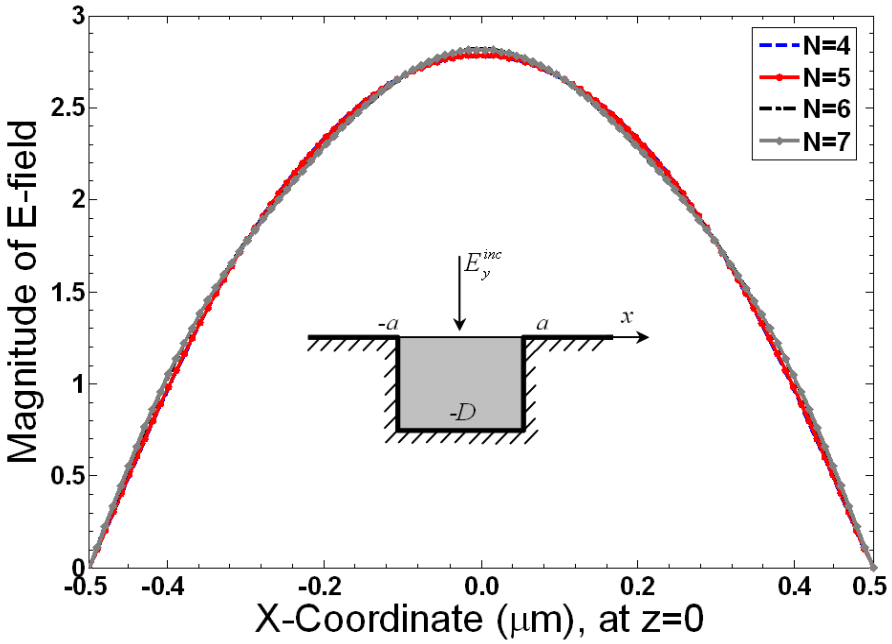

Figure 5.6: Scattered field at the interface of rectangular groove where $2a = \lambda$, and $D = \lambda/4$, and $\theta_{inc} = 0$ for different number of harmonics in the rectangular groove interlayers and $l = 80$.

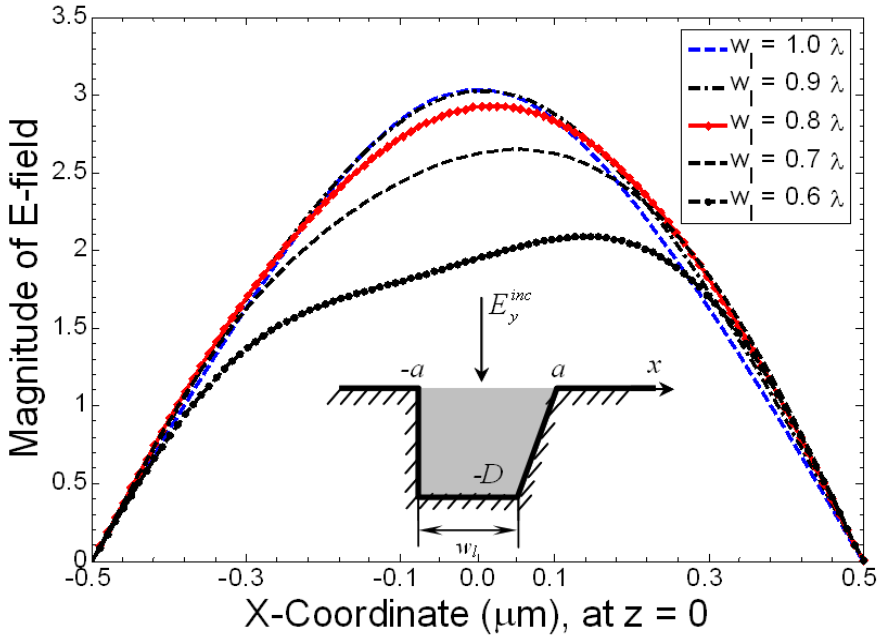

Figure 5.7: Scattered field at the interface of a rectangular groove with aperture width $2a = \lambda$ and groove depth $D = 1.5\lambda$, and several values of w_l for a normal incident field.

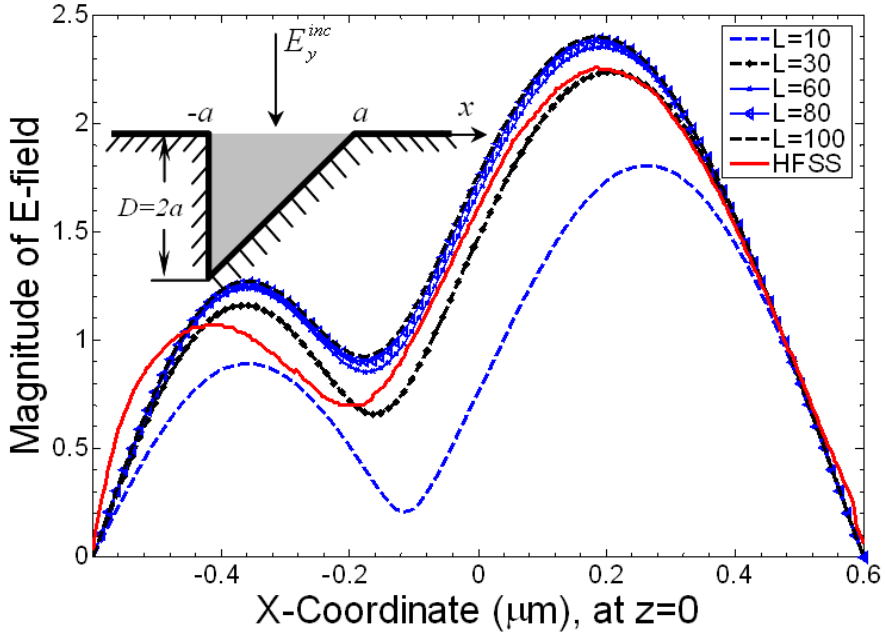

Figure 5.8: Plot of the scattered field at the groove interface for IRT groove with its aperture width ($2a$) equal to 1.2λ and normal incidence field for different number of grooev layers.

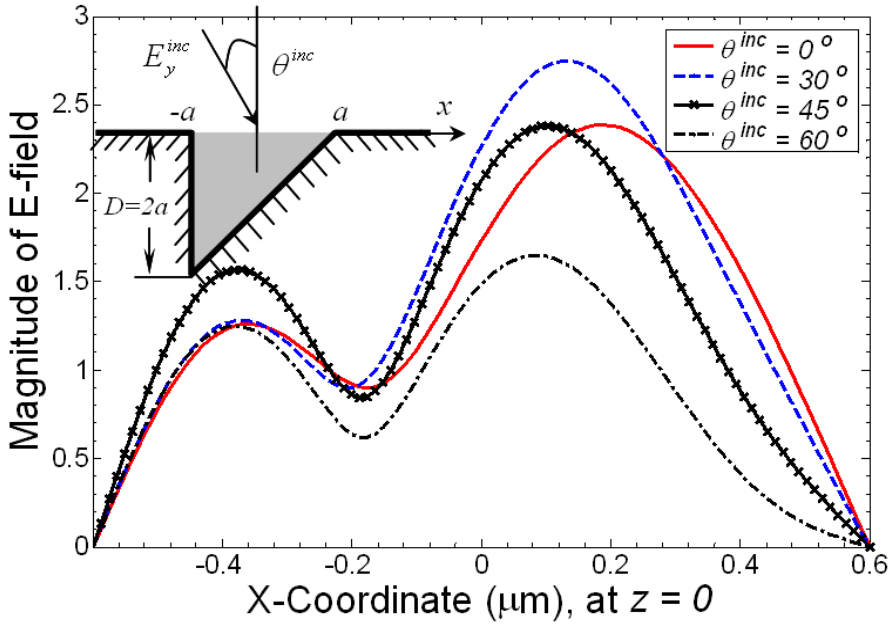

Figure 5.9: Plot of the scattered field at the groove interface form triangular (IRT) groove with its aperture width ($2a$) equal to 1.2λ and various θ_{inc}.

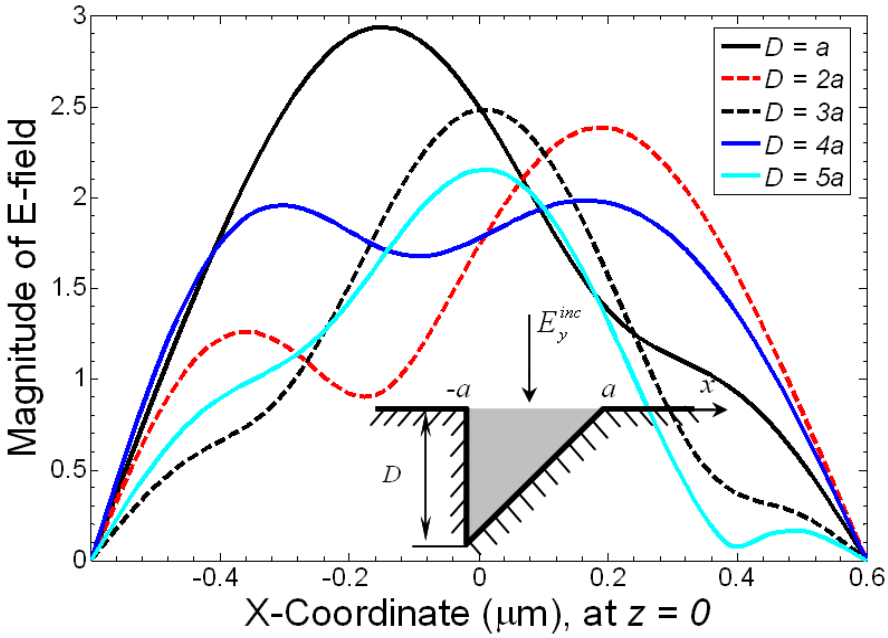

Figure 5.10: Plot of the scattered field at the groove interface form triangular groove with its aperture width ($2a$) equal to 1.2λ and various depths and $\theta_{inc} = 0$.

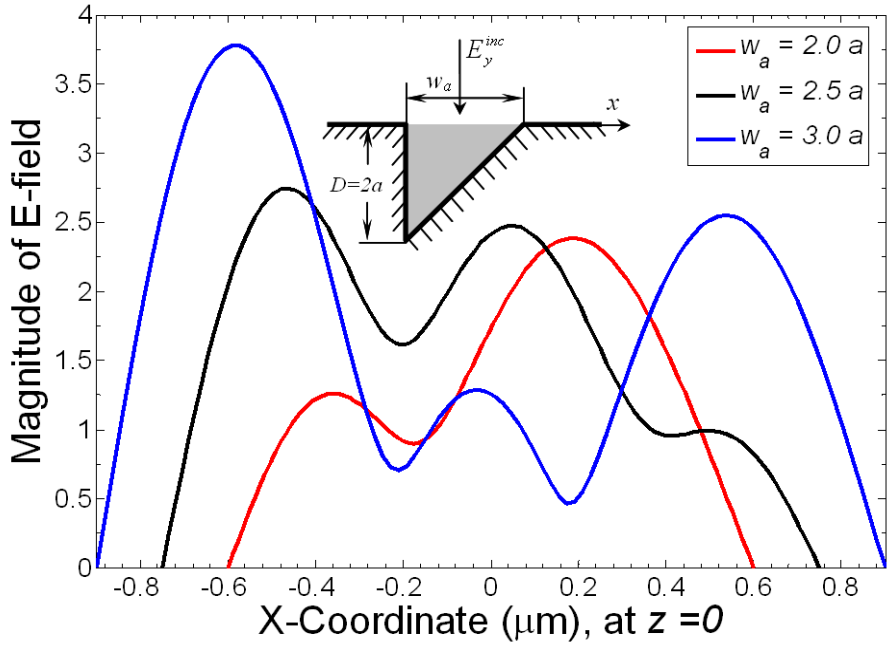

Figure 5.11: Plot of the scattered field at the groove interface form triangular groove its with depth, $D = 2a$ ($a = 0.6\lambda$), and various aperture widths for $\theta_{inc} = 0$.

5.6 Multiple General-Shaped Grooves Formulation

Fig. 5.12 depicts the geometry of the two dimensional scattering problem. The general-shaped grooves are identical and have the same period T with total number of grooves equal to P with the width a groove width $2a$. The grooves profile can be described by the function $z = f(x)$ with no variation along y-axis. Consider a TE scattering problem from the multiple grooves where the incident electric field is polarized along the groove axes (y-axis). The formulation is equally applicable for the case where the incident magnetic field is polarized along y-axes. The problem space is divided into two regions: upper half space (region I) which contains the incident, specularly reflected, and scattered fields and the multiple general-shaped grooves region (region II). In region (I) ($z > 0$) a uniform plane electromagnetic wave of $E_y^{inc}(x, z)$ with an incident angle, θ_{inc} is assumed to be incident on the grooves. Region (II) ($-D < z < 0$, and $-a < |x - pT| < a$) is an infinitely-long (in y-direction) general-shaped groove pattern where p is the groove number. Again, the wave numbers in region (I) and (II) are $k_0 = \omega\sqrt{\mu_0\varepsilon_0}$ and $k = \omega\sqrt{\mu\varepsilon}$, respectively.

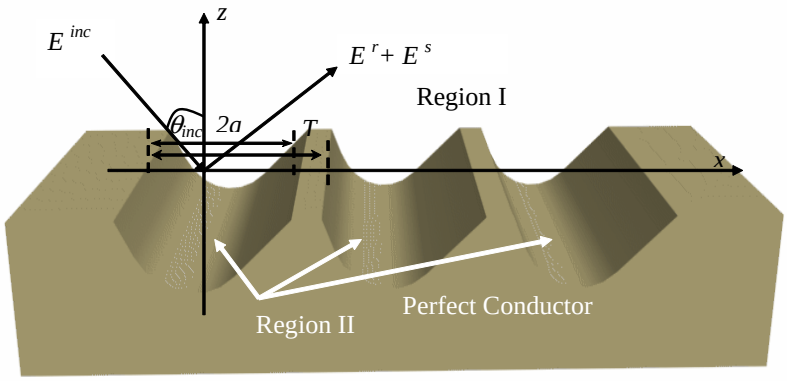

Figure 5.12: (a) A Schematic diagram of the finite general-shaped grooves with total number of grooves P. The grooves are identical with a period T and a groove aperture width of $2a$. The incident electric field is polarized along y-axes with incident angle θ_{inc}.

5.6.1 Fields in The General-Shaped Grooves (Region II)

In region II, there are a total number of $(P+1)$ general-shaped grooves. All grooves are assumed to be identical and filled with the same dielectric material constant ϵ_r (although it is not a

limitation of the proposed method, see section 5.9). Hence, the field representations inside each individual groove will be the same for all grooves with different unknown harmonics coefficients that will be calculated later for specific scattering problem parameters. In section 5.3.2, each general-shaped groove is divided into L number of layers, with individual layer thickness of d and total groove depth $D = Ld$. The width of an arbitrary interlayer l is $2w_l = a_l + b_l$, as can be seen in Fig. 5.12. The first layer in each groove ($l = 1$) has a common interface with upper-half space. The electric and magnetic fields tangential component in the first layer($l = 1$) for the pth groove, can be written as:

$$E_y^{p,1}(x,z) = \sum_{n=1}^{\infty} \sin\ \beta_n^1(x + a - pT) \times (A_n^{p,1} e^{j\zeta_n^1 z} + B_n^{p,1} e^{-j\zeta_n^1(z+d)}), \qquad |x - pT| \le a \tag{5.49}$$

$$H_x^{p,1}(x,z) = \frac{1}{\omega\mu_r\mu_0} \sum_{n=1}^{\infty} \zeta_n^1 \sin\ \beta_n^1(x + a - pT) \times (A_n^{p,1} e^{j\zeta_n^1 z} - B_n^{p,1} e^{-j\zeta_n^1(z+d)}). \qquad |x - pT| \le a \tag{5.50}$$

Here, $A_n^{p,l}$ and $B_n^{p,l}$ are the nth unknown harmonic coefficients of the first layer ($l = 1$) for the pth groove. Throughout the chapter, subscript "n" is the harmonic index and superscripts "p" and "l" are the groove and layer numbers, respectively. β_n^1 and ζ_n^1 are similarly defined before. For the identical groove case considered here, β_n^1 and ζ_n^1 are identical (hence superscript p is redundant). Application of the boundary conditions between tangential electric and magnetic fields in general-shaped groove interlayers result in a linear set of equations by combining all unknown space harmonics coefficients of the general-shaped groove. The derived boundary conditions in matrix form of the pth groove between layers l and $l + 1$ are

$$\begin{bmatrix} \mathbf{exp}^l & \mathbf{I} \\ -\mathbf{BA}^l & \mathbf{BB}^l \end{bmatrix} \begin{bmatrix} \mathbf{A}^{p,l} \\ \mathbf{B}^{p,l} \end{bmatrix} + \begin{bmatrix} -\mathbf{AA}^{l+1} & -\mathbf{AB}^{l+1} \\ \mathbf{I} & -\mathbf{exp}^{l+1} \end{bmatrix} \begin{bmatrix} \mathbf{A}^{p,l+1} \\ \mathbf{B}^{p,l+1} \end{bmatrix} = \mathbf{0}, \tag{5.51}$$

In the case of identical grooves, physical properties (*i.e.* w_l, D_l, a_l, b_l β_n^l, and ζ_n^l) are identical for all grooves and hence the groove number "p" is redundant. As can be seen from Eqs. (5.16)-(5.19), the matrices elements depend only on the physical parameters of the grooves. Hence,

matrices $\mathbf{AA}^{l+1}$, $\mathbf{AB}^{l+1}$, $\mathbf{BA}^{l}$, and $\mathbf{BB}^{l+1}$ are identical for all grooves and the groove number is suppressed to make the formulation simple. $A_n^{p,1}$ and $B_n^{p,1}$ are the unknown harmonic coefficients of the vector matrices $\mathbf{A}^{p,1}$ and $\mathbf{B}^{p,1}$, respectively. Next, the derived boundary conditions in matrix form between the bottom two layers in any groove($l = L-1, L$), are

$$\begin{bmatrix} \mathbf{exp}^{L-1} & \mathbf{I} \\ \mathbf{BA}^{L-1} & -\mathbf{BB}^{L-1} \end{bmatrix} \begin{bmatrix} \mathbf{A}^{p,L-1} \\ \mathbf{B}^{p,L-1} \end{bmatrix} - \begin{bmatrix} \mathbf{AA}^{L} \\ \mathbf{I} \end{bmatrix} \left[\mathbf{A}^{p,L}\right] = 0, \tag{5.52}$$

5.6.2 Field Matching at the Region I and II Interface ($z = 0$)

It is necessary to match the tangential field components of the electric and magnetic fields from the upper half space (region I) with the fields in the first layer in the general-shaped grooves (region II). First, the tangential electric-field continuity along x-axis ($z = 0$), using Eqs. (5.2-5.4) and (5.49), yields

$$E_y^s(x,0) = \begin{cases} E_y^{p,1}(x,0), & |x - pT| < a \\ 0. & Otherwise \end{cases} \tag{5.53}$$

Taking Fourier transform of both sides yields

$$\tilde{E}_y^s(\zeta) = \sum_{p=0}^{p=P} \sum_{n=1}^{\infty} \beta_n^1 a^2 e^{-jpT\zeta} G_n(\zeta a)(A_n^{p,1} + B_n^{p,1} e^{-j\zeta_n^1 d}), \tag{5.54}$$

where,

$$G_n(\zeta) = \frac{e^{-j\zeta}\,(-1)^n - e^{j\zeta}}{\zeta^2 - (\beta_n^1 a)^2}.$$

$\tilde{E}_y^s(\zeta)$ and $E_y^s(x)$ form the Fourier transform pair of the electric fields at the interface ($z = 0$). In Eqs. (5.54), $\tilde{E}_y^s(\zeta)$ is expressed with a fast convergent series in terms of the unknown harmonic fields coefficients of the first layer ($l = 1$) of all grooves in region II. Next, the tangential magnetic-field continuity at the interface $z = 0$ along $-a < x - pT < a$ gives

$$\begin{aligned} &\frac{2k_z}{\omega\mu_0} \exp(-jk_x x) - \frac{1}{2\pi\omega\mu_0} \int_{-\infty}^{\infty} \tilde{E}_y^s(\zeta) e^{j\zeta x} \kappa_0 d\zeta \\ &= \frac{1}{\omega\mu_r\mu_0} \sum_{n=1}^{\infty} \zeta_n^1 \sin\ \beta_n^1 (x + a - pT)(A_n^{p,1} - B_n^{p,1} e^{-j\zeta_n^1 d}). \end{aligned} \tag{5.55}$$

Substituting Eq. (5.54) in Eq. (5.55) yields

$$
\begin{aligned}
2k_z \exp(-jk_x x) - \frac{1}{2\pi} \sum_{p=0}^{p=P} \sum_{n=1}^{\infty} \beta_n^1 a^2 (A_n^{p,1} + B_n^{p,1} e^{-j\zeta_n^1 d}) \\
\times \int_{-\infty}^{\infty} G_n(\zeta a) e^{-jpT\zeta} e^{j\zeta x} \kappa_0 d\zeta \\
= \frac{1}{\mu_r} \sum_{n=1}^{\infty} \zeta_n^1 \sin\ \beta_n^1 (x + a - pT) \times (A_n^{p,1} - B_n^{p,1} e^{-j\zeta_n^1 d}).
\end{aligned} \tag{5.56}
$$

Multiplying Eq. (5.56) by $\sin\ \beta_m^1(x + a - qT)$ and integrate from $(qT - a)$ to $(qT + a)$ gives

$$
\begin{aligned}
2a^2 k_z e^{-jqTk_x} G_m(k_x a) = \frac{1}{2\pi} \sum_{p=0}^{p=P} \sum_{n=1}^{\infty} a^2 \beta_n^1 R_{m,n}^{q,p}(k_0) A_n^{p,1} \\
+ \frac{a\zeta_m^1}{\beta_m^1 \mu_r} \delta_{m,n} \delta_{p,q} A_m^{q,1} \\
+ \frac{1}{2\pi} \sum_{p=0}^{p=P} \sum_{n=1}^{\infty} a^2 \beta_n^1 e^{-j\zeta_n^1 d} R_{m,n}^{q,p}(k_0) B_n^{p,1} \\
- \frac{a\zeta_m^1}{\beta_m^1 \mu_r} e^{-j\zeta_m^1 d} \delta_{m,n} \delta_{p,q} B_m^{q,1},
\end{aligned} \tag{5.57}
$$

where

$$
R_{m,n}^{q,p}(k_0) = \int_{-\infty}^{\infty} a^2 G_n(\zeta a) G_m(-\zeta a) e^{-j(p-q)T\zeta} \kappa_0 d\zeta. \tag{5.58}
$$

This integration can be determined by residue calculus. [149] Rewriting Eq. (5.57) in a matrix form

$$
\begin{aligned}
\begin{bmatrix} \mathbf{C}^0 \\ \mathbf{C}^1 \\ \vdots \\ \vdots \\ \mathbf{C}^P \end{bmatrix} &= \begin{bmatrix} \mathbf{CA}^{0,0} & \mathbf{CA}^{0,1} & \cdots & \cdots & \mathbf{CA}^{0,P} \\ \mathbf{CA}^{1,0} & \mathbf{CA}^{1,1} & \cdots & \cdots & \mathbf{CA}^{1,P} \\ \vdots & \vdots & & & \vdots \\ \vdots & \vdots & & & \vdots \\ \mathbf{CA}^{P,0} & \mathbf{CA}^{P,1} & \cdots & \cdots & \mathbf{CA}^{P,P} \end{bmatrix} \begin{bmatrix} \mathbf{A}^{0,1} \\ \mathbf{A}^{1,1} \\ \\ \\ \mathbf{A}^{P,1} \end{bmatrix} \\
&+ \begin{bmatrix} \mathbf{CB}^{0,0} & \mathbf{CB}^{0,1} & \cdots & \cdots & \mathbf{CB}^{0,P} \\ \mathbf{CB}^{1,0} & \mathbf{CB}^{1,1} & \cdots & \cdots & \mathbf{CB}^{1,P} \\ \vdots & \vdots & & & \vdots \\ \vdots & \vdots & & & \vdots \\ \mathbf{CB}^{P,0} & \mathbf{CB}^{P,1} & \cdots & \cdots & \mathbf{CB}^{P,P} \end{bmatrix} \begin{bmatrix} \mathbf{B}^{1,1} \\ \mathbf{B}^{2,1} \\ \vdots \\ \vdots \\ \mathbf{B}^{P,1} \end{bmatrix}.
\end{aligned} \tag{5.59}
$$

where,

$$C^q(m) = 2a^2 k_z e^{-jqTk_x} G_m(k_x a), \tag{5.60}$$

$$CA^{q,p}(m,n) = \frac{1}{2\pi} a^2 \beta_n R^{q,p}_{m,n}(k_0) + \frac{a\zeta_m}{\beta_m \mu_r} \delta_{m,n}\delta_{p,q}, \text{ and} \tag{5.61}$$

$$CB^{q,p}(m,n) = \frac{1}{2\pi} a^2 \beta_n e^{-j\zeta_n d} R^{q,p}_{m,n}(k_0) - \frac{a\zeta_m}{\beta_m \mu_r} e^{-j\zeta_m d} \delta_{m,n}\delta_{p,q}. \tag{5.62}$$

Here, $C^q(q,p)$, $CA^{q,p}(q,p)$, and $CB^{q,p}(q,p)$ are elements of the matrices $\mathbf{C}^q$, $\mathbf{CA}^{q,p}$, and $\mathbf{CB}^{q,p}$, respectively. $\mathbf{CA}^{q,p}$ and $\mathbf{CB}^{q,p}$ are square matrices of dimensions equal to number of modes (N_1) in the first layer ($l = 1$) of all grooves. The following matrix compact form of Eq. 5.63 is useful later on when forming the coefficient matrix $\mathbf{M}$ of the scattering problem.

$$\mathbf{C}^q = \sum_{p=0}^{p=P} \mathbf{CA}^{q,p}\mathbf{A}^{q,1} + \sum_{p=0}^{p=P} \mathbf{CB}^{q,p}\mathbf{B}^{q,1}. \tag{5.63}$$

5.7 Numerical Implementation, and Validations

In order to calculate the unknown harmonic coefficients of all groove layers, Eq. (5.59) need to be solved for the unknown harmonics of the first layer ($l = 1$) for each groove. Then all other unknown harmonics coefficients can be determined from Eqs. (5.52) and (5.51). Equation (5.59) is a linear system of equations of the unknowns $A^{p,1}_n$ and $B^{p,1}_n$ of the first layers of all grooves with total number of unknown $N_u = 2N_1(P+1)$ and the number of equations $N_e = N_1(P+1)$, where N_1 and $(P+1)$ are the number of unknown harmonics coefficients in the first layer ($l = 1$) and the total number of grooves, respectively. Two methods of solutions can be used to solve the linear system of in Eq. (5.59). The first method "Direct Method" uses Eqs. (5.51) and (5.52) to find a direct relations between the two unknown series $A^{p,1}_n$ and $B^{p,1}_n$ using direct matrix inversions. From equation (5.51), unknown harmonic coefficients of the first layer ($l = 1$) are related to those in layer ($l = L-1$) by

$$\begin{bmatrix} \mathbf{A}^{p,1} \\ \mathbf{B}^{p,1} \end{bmatrix} = \sum_{l=1}^{L-2} \begin{bmatrix} \mathbf{exp}^l & \mathbf{I} \\ -\mathbf{BA}^l & \mathbf{BB}^l \end{bmatrix}^{-1} \begin{bmatrix} \mathbf{AA}^{l+1} & \mathbf{AB}^{l+1} \\ -\mathbf{I} & \mathbf{exp}^{l+1} \end{bmatrix} \begin{bmatrix} \mathbf{A}^{p,L-1} \\ \mathbf{B}^{p,L-1} \end{bmatrix}. \tag{5.64}$$

Substituting Eqs. (5.52) in (5.64), yields

$$\begin{bmatrix} \mathbf{A}^{p,1} \\ \mathbf{B}^{p,1} \end{bmatrix}_1 = \sum_{l=1}^{L-2} \begin{bmatrix} \mathbf{exp}^l & \mathbf{I} \\ -\mathbf{BA}^l & \mathbf{BB}^l \end{bmatrix}^{-1} \begin{bmatrix} \mathbf{AA}^{l+1} & \mathbf{AB}^{l+1} \\ -\mathbf{I} & \mathbf{exp}^{l+1} \end{bmatrix} \times \begin{bmatrix} \mathbf{exp}^{L-1} & \mathbf{I} \\ \mathbf{BA}^{L-1} & -\mathbf{BB}^{L-1} \end{bmatrix}^{-1} \begin{bmatrix} \mathbf{AA}^L \\ \mathbf{I} \end{bmatrix} \left[\mathbf{A}^{p,L}\right]. \tag{5.65}$$

The last equation is valid for all grooves since they are assumed to be identical. It relates the unknown harmonics coefficients series $A_n^{p,1}$ and $B_n^{p,1}$ in layer ($l = 1$) with $A_n^{p,L}$ of the last layer of the same groove ($l = L$). When combined with Eq. (5.59), a new linear system of equations is formed and solved for the unknown harmonic coefficients $A_n^{p,L}$. Using this procedure of solution, all matrices defined in previous equations for all groove layers $\mathbf{AA}^l$, $\mathbf{AB}^l$, $\mathbf{BA}^l$, and $\mathbf{BB}^l$ where $l = 1.....L$, are forced to be square for direct matrix inversions. Hence choosing the same number of unknown harmonic coefficients in all groove layers. Depending on the shape of the grooves, last method suggested encounters numerical instability and convergent problems. More details can be found in reference [151].

In the second method, the Adaptive Method, the number of unknown harmonic coefficients in each layer is chosen based on the physical geometry of the problem to avoid convergence instability in the solution [151]. Then combining the linear system of equations in Eq. (5.59) with Eqs. (5.51) and (5.52) we obtain one linear system to be solved simultaneously for all unknown harmonic coefficients. In building the coefficient matrix based on combining Eqs. (5.51), (5.52), and (5.59), we have experienced several ways of arranging the unknown harmonic field coefficients and have developed a time-efficient and optimum scheme of building and solving the coefficients matrix. Unknown coefficients $A_n^{p,1}$ and $B_n^{p,1}$ for each general-shaped groove will be arranged in an ascending order, *i.e.*, first layer $A_n^{p,1}$ and $B_n^{p,1}$ followed by second layer $A_n^{p,2}$ and $B_n^{p,2}$ of the same general-shaped groove and so on for each successive groove. Following previous procedure for building the coefficient matrix, the following square matrix is obtained:

$$\mathbf{M} = \begin{bmatrix} \mathbf{GC}^{0,0} & \mathbf{GC}^{0,1} & \cdots & \cdots & \mathbf{GC}^{0,P} \\ \mathbf{GC}^{1,0} & \mathbf{GC}^{1,1} & \cdots & \cdots & \mathbf{GC}^{1,P} \\ \vdots & \vdots & \ddots & & \vdots \\ \vdots & \vdots & & \ddots & \vdots \\ \mathbf{GC}^{P,0} & \mathbf{GC}^{P,1} & \cdots & \cdots & \mathbf{GC}^{P,P} \end{bmatrix}. \tag{5.66}$$

The coefficient matrix $\mathbf{M}$ has a three matrixes hierarchy levels. It is composed of $(P+1)\times(P+1)$ square matrices $\mathbf{GC}^{q,p}$. The diagonal matrices $\mathbf{GC}^{q,p}$ (where $q = p$) are the individual scattering coefficient matrix of single general-shaped grooves. $\mathbf{GC}^{q,p}$ are square matrices with dimensions N_{GC}, where ,

$$N_{CG} = 2\sum_{l=1}^{L-1} N_l + N_L. \tag{5.67}$$

The diagonal matrices, $\mathbf{GC}^{p,p}$, are identical for identical grooves and take the form of:

$$\mathbf{GC}^{p,p} = \begin{bmatrix} \mathbf{CA}^{p,p} & \mathbf{CB}^{p,p} & 0 & 0 & 0 & 0 & 0 & \cdots & \cdots & 0 \\ \mathbf{exp}^1 & \mathbf{I} & -\mathbf{AA}^2 & -\mathbf{AB}^2 & 0 & 0 & 0 & \cdots & \cdots & 0 \\ -\mathbf{BA}^1 & \mathbf{BB}^1 & \mathbf{I} & \mathbf{exp}^2 & 0 & 0 & 0 & \cdots & \cdots & 0 \\ 0 & 0 & \mathbf{exp}^2 & \mathbf{I} & -\mathbf{AA}^3 & -\mathbf{AB}^3 & 0 & \cdots & \cdots & 0 \\ 0 & 0 & -\mathbf{BA}^2 & \mathbf{BB}^2 & \mathbf{I} & \mathbf{exp}^3 & 0 & \cdots & \cdots & 0 \\ 0 & 0 & 0 & 0 & 0 & \vdots & \vdots & \ddots & \ddots & 0 \\ 0 & 0 & 0 & 0 & 0 & \vdots & \vdots & \ddots & \ddots & 0 \\ 0 & 0 & 0 & 0 & 0 & \vdots & \vdots & \ddots & \ddots & 0 \\ 0 & 0 & 0 & 0 & 0 & 0 & 0 & \mathbf{exp}^{L-1} & \mathbf{I} & -\mathbf{AA}^L \\ 0 & 0 & 0 & 0 & 0 & 0 & 0 & \mathbf{BA}^{L-1} & \mathbf{BB}^{L-1} & \mathbf{I} \end{bmatrix}. \tag{5.68}$$

The elements of the matrix $\mathbf{GC}^{p,p}$ are matrices with their dimensions dependent on the number of modes in each layer of the groove. The groove superscript "p" is again dropped for the elements of the diagonal matrices since those elements does are identical for all grooves. Detail of a single general-shaped groove matrix formulation can be found in previous work [151]. The off diagonal

matrices $\mathbf{GC}^{q,p}$ $(q \neq p)$ in the coefficient matrix $\mathbf{M}$ represent the coupling between corresponding grooves q and p with the same dimensions of the diagonal matrices $\mathbf{GC}^{p,p}$, where

$$\mathbf{GC}^{q,p} = \begin{bmatrix} \mathbf{CA}^{q,p} & \mathbf{CB}^{q,p} & \cdots & \cdots & 0 \\ 0 & 0 & \cdots & \cdots & 0 \\ \vdots & \vdots & \ddots & & \vdots \\ \vdots & \vdots & & \ddots & \vdots \\ 0 & 0 & \cdots & \cdots & 0 \end{bmatrix}. \tag{5.69}$$

Here, $q, p = 0, 1, ...P$, and $q \neq p$. The elements of the $\mathbf{GC}^{q,p}$ are all zeros except the first two elements in the first row, $\mathbf{CA}^{q,p}$ and $\mathbf{CB}^{q,p}$, which are square matrices with dimensions $N_1 \times N_1$ (where N_1 is the number of modes in the first layer). Detail of the formulations are in Eqs. (5.61) and (5.62). Strong coupling exists between successive two general-shaped grooves. Going further away from the diagonal of the coefficient matrix $\mathbf{M}$, weak coupling can be seen.

5.8 Numerical Simulation Results

In this section we present the simulation results of two finite gratings, rectangular and isosceles right triangle (IRT) finite grooves. The results presented for the finite rectangular grooves are for verifications. The new results for the IRT finite grooves show the the stability, robustness, and versatility of the developed method. Near and far fields are calculated and compared to HFSS (A commercial finite element simulator) [152] and results from the published literature. Based on the simulation results, we will study the convergence, stability, effect of the choice of the number of interlayers, and number of harmonics in each interlayer of the grooves.

The first example is the scattering of a plane wave from a finite number of rectangular grooves with dimensions from refrence [35]. The rectangular grooves are assumed to be identical with a width, depth, and period of $2a = 0.8\lambda$, $D = 0.4\lambda$, and $T = 1.6\lambda$, respectively, λ being the operating wavelength. The incident electric field is polarized along the grooves axis (y-axis) with an incident angle $\theta_{inc} = 30^o$. Analytical solution of rectangular grooves are available in [153, 35] where analytical field formulation is possible in the rectangular grooves. In order to model the rectangular grooves using multi-layers (for the sake of validation only), the grooves will be divided into L number of layers. The number of harmonics in this case will be the same in each layer

of the grooves since all layers are almost of the same width. In this special case, direct matrix inversion using Eq. (5.65) is possible and will not encounter any stability problem.

The rectangular grooves are divided into L number of layers. The parameter L varies from 10 to 100 to determine the scattered field's dependence on the number of layers in the grooves. In Fig. 5.13(a), the scattered field is plotted for different number of groove interlayers L. Boundary conditions are clearly satisfied at the rectangular grooves edges as well as on the perfect conducting plane. Noting that fields calculated for $L = 30$ and higher are identical, indicating a robust convergence of the solution. The number of included harmonics in the grooves interlayers are investigated. Fig. 5.13(b) shows the scattered fields at the grooves interface for differen number of harmonics. Increasing the number of retained harmonics fields shows the detailed behavior of the scattered field at the groove edges (higher order harmonics). Furthermore, the simulation is stable when retaining a number of harmonics, $N = 10$, beyond the sufficient number for accurate field calculations, which shows a high robustness and stability of the proposed method. The scattered fields at the interface of the rectangular grooves compared to the results from the solution by HFSS (finite element method solver) are shown in Fig. 5.13(c). In Fig. 5.14, we calculated the scattered near and far-fields for different number of rectangular grooves $P = 2, 6,$ and 12. The far fields in Fig. 5.14 are compared with that in ref. [35]. It is worth noting that far-field calculation is not sensitive to the number of groove layers and retained harmonics. A far-field calculated with a number of layers $L = 10$ and harmonics $N = 4$ shows a good agreement with those calculated using a higher number of layers and harmonics.

The next example is the finite number of Isosceles right triangle (IRT) grooves. The reason to test on such a finite grooves is to show the stability of the method since the fields in the bottom layers of the grooves decay faster as we approach the bottom because of the term $\exp(-j\zeta d)$ [151]. The direct matrix inversion method for this example encounters stability problems and does not converge to the correct answers. With the method proposed here, the simulation was stable and no convergence problems were encountered in the calculation.

The IRT grooves are identical with equal width and depth of 1.2λ. The period of the IRT is $T = 1.3\lambda$. The simulation will be carried out for a number of grooves $P = 3$. Conventional vector-based methods, e.g., coupled-mode [154] and coupled-wave [155] theories, are not able to solve finite grating. Only fully numerical methods [124] are able to solve finite grating with

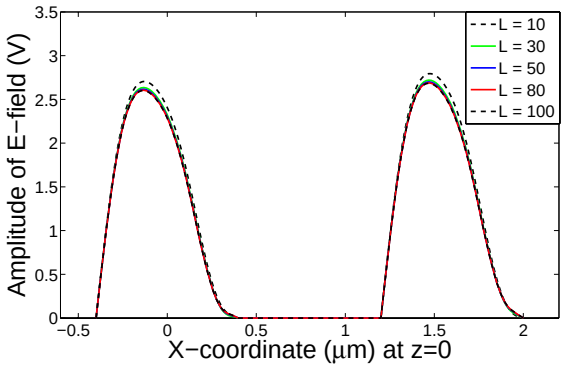

(a) $L = 10, 30, 50, 80,$ and 100, a complete overlaps for $L > 30$.

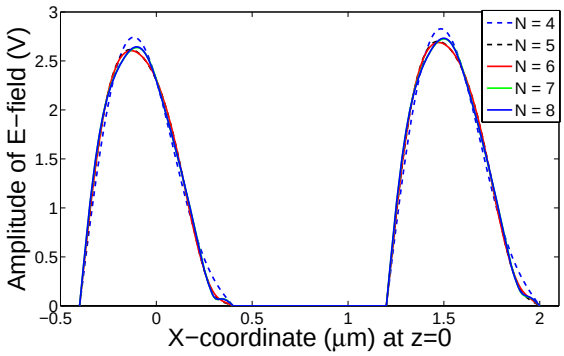

(b) $N = 4, 5, 6, 7,$ and 8.

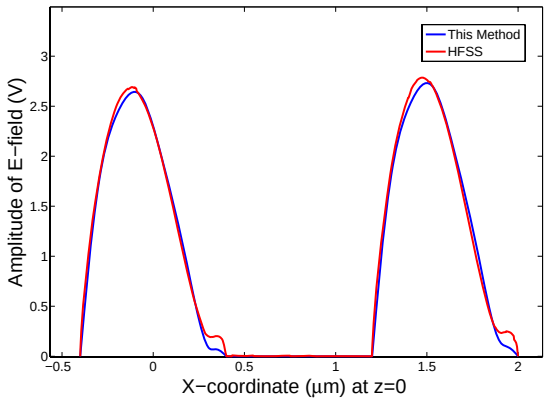

(c) Comparison between simulation from HFSS and results for $L = 30$ and $N = 7$.

Figure 5.13: Scattered field at the interface of rectangular grooves with the following parameters $2a = 0.8\lambda$, $D = 0.4\lambda$, $T = 1.6\lambda$, and $\theta_{inc} = 30^o$.

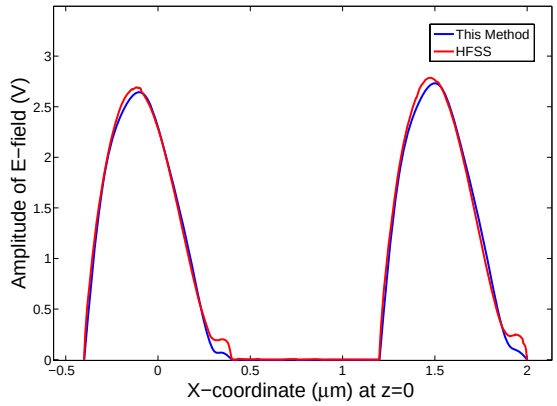

(a) Near-field, $P = 2$ grooves.

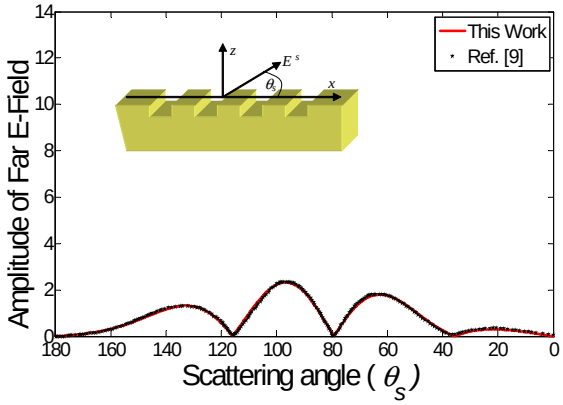

(b) Far-field, $P = 2$ grooves.

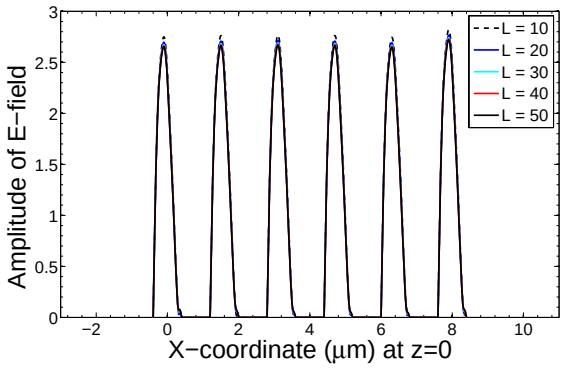

(c) Near-field, $P = 6$ grooves.

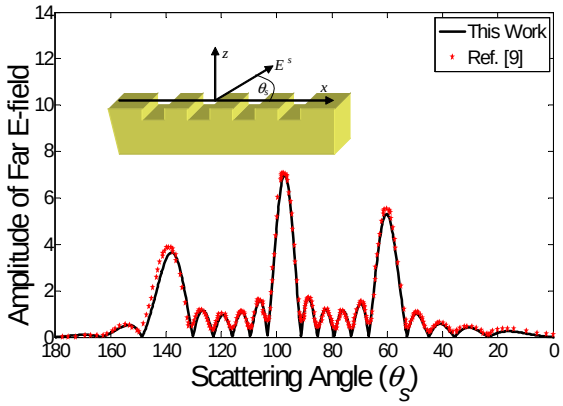

(d) Far-field, $P = 6$ grooves.

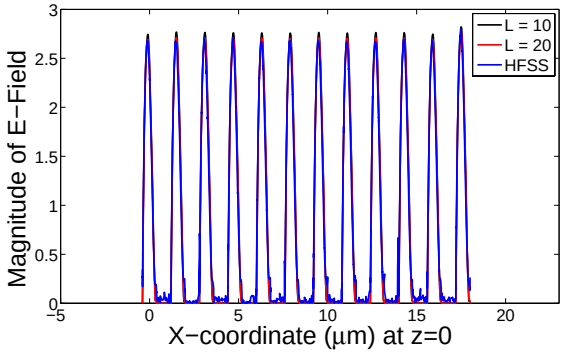

(e) Near-field, $P = 12$ grooves.

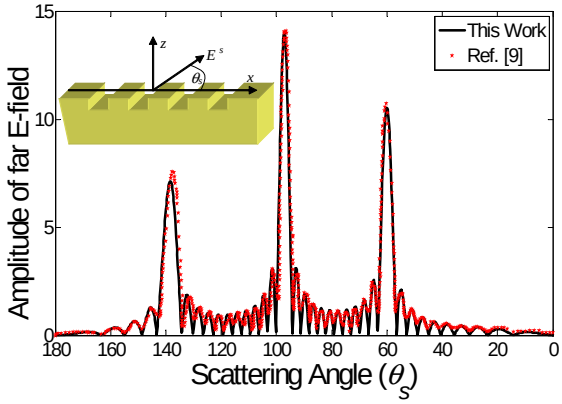

(f) Far-field, $P = 12$ grooves.

Figure 5.14: Scattered near and far-fields of rectangular grooves having the same parameters as Fig. 5.13 for different number of grooves P. Far-field plots in b, d, and f are compared results from Ref. [35].

significant expensive simulation time and resources for large structures, which is not the case for our proposed method. The electric field in the incident plane wave is polarized along y-axis with an incident angle $\theta_{inc} = 0^o$.

Fig. 5.15 shows the scattered fields at the grooves interface with the upper half space for different number of interlayers and different number of retained harmonics. Calculation of the field harmonic coefficients and the scattered field did not encounter any instability problem when the number of layers or harmonics increases beyond the convergence requirements. For a number of layers, $L = 70$, no noticeable changes can be detected in the near field. The number of layers for accurate field calculation is a function of the groove physical dimensions. The number of retained harmonics for the simulation to converges to the correct solution, $N = 8$, is larger than the case of rectangular grooves. This is expected because of larger dimensions in the case of IRT grooves.

Fig. 5.16-5.18 show the scattered far and near fields plots from IRT grooves with $P = 3, 5,$ and 9 grooves, respectively. The simulations were performed for $\theta_{inc} = 0^o$ and 45^o. The effect of changing the incident field angle is clear in the far and near fields plots where the main beam of the scattered field is shifted from $\theta_s = 90^o$ to $\theta_s = 45^o$ when changing the incident angle from $\theta_{inc} = 0^o$ to $\theta_{inc} = 45^o$. The number of grooves affects the main beam width of the scattered field. The propagation of the near fields from the groove interface in the z-direction shows clearly the near field interactions and coupling as shown in Fig. 5.16-Fig.5.18 parts (b) and (c).

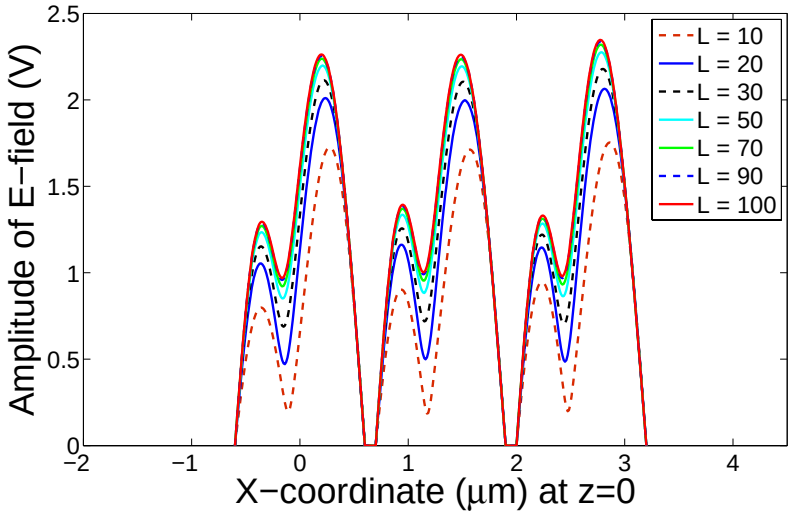

(a) $L = 10, 30, 50, 70, 90,$ and 100, a complete overlaps for $L > 70$.

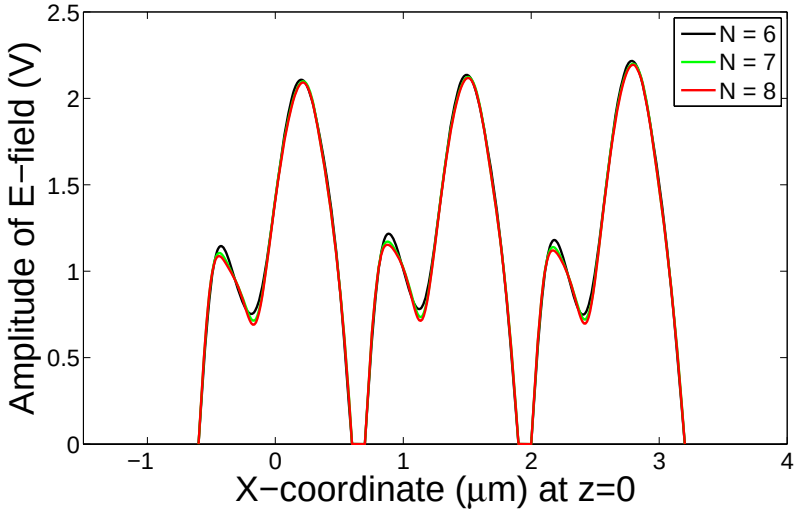

(b)$N = 6, 7,$ and 8.

Figure 5.15: Scattered field at the interface of IRT grooves with the following parameters $2a = 1.2\lambda$, $T = 1.3\lambda$, and $\theta_{inc} = 0^o$.

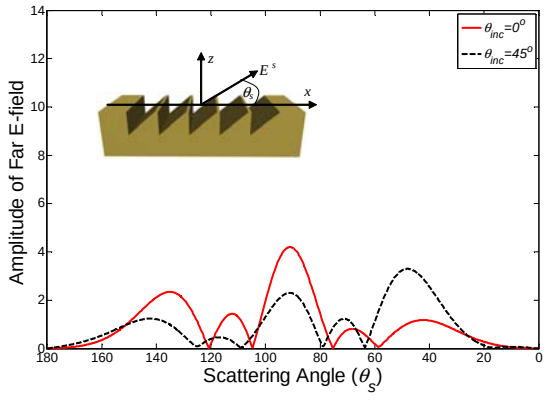

(a) Far-field for $\theta_{inc} = 0^o$ and 45^o.

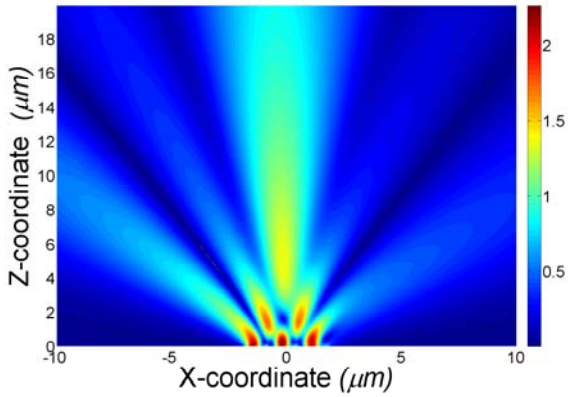

(b) Near-field for $\theta_{inc} = 0^o$.

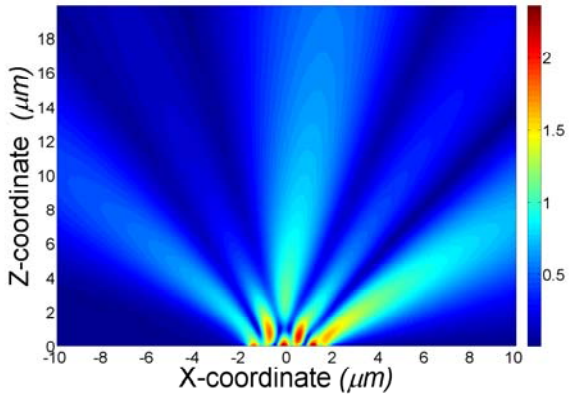

(c) Near-field for $\theta_{inc} = 45^o$

Figure 5.16: Scattered near and far-fields of IRT having the same parameters as Fig. 5.15. The incident angle $\theta_{inc} = 0^o$ and 45^o and number of grooves $P = 3$.

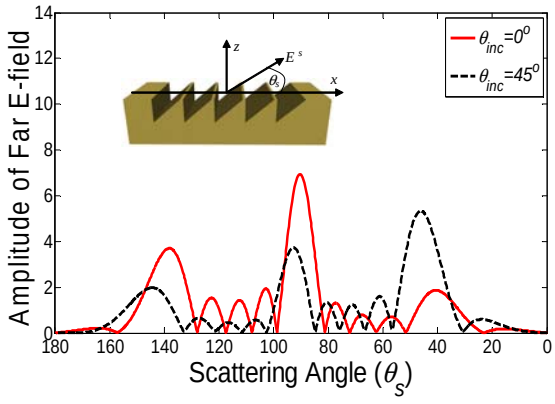

(a) Far-field for $\theta_{inc} = 0^o$ and 45^o.

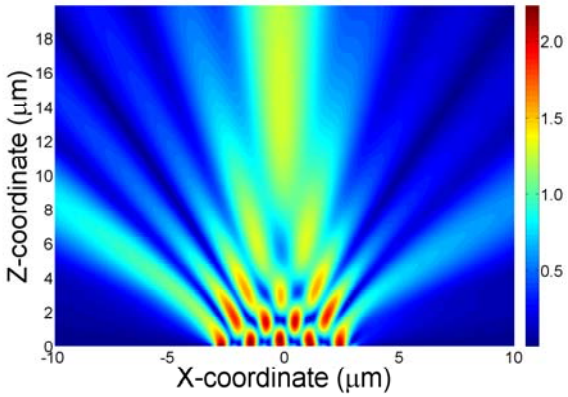

(b) Near-field for $\theta_{inc} = 0^o$.

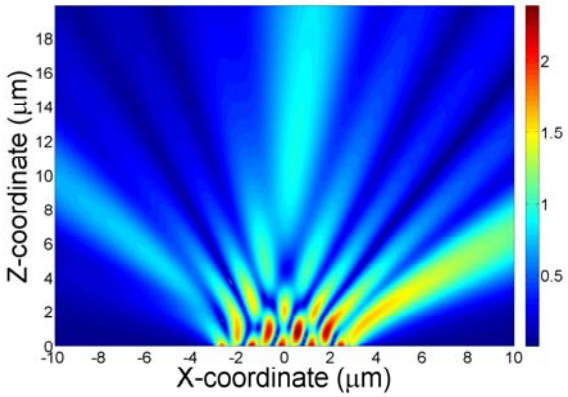

(c) Near-field for $\theta_{inc} = 45^o$

Figure 5.17: Scattered near and far-fields of IRT having the same parameters as Fig. 5.15. The incident angle $\theta_{inc} = 0^o$ and 45^o and number of grooves $P = 5$.

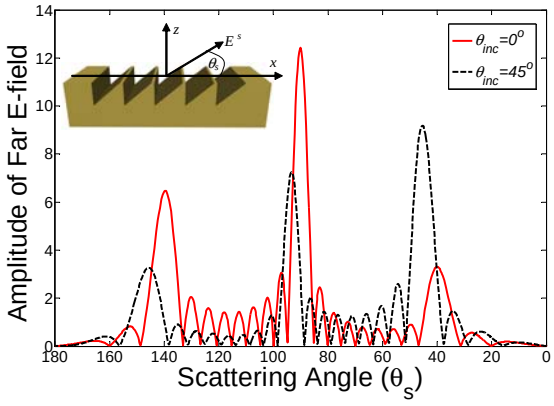

(a) Far-field for $\theta_{inc} = 0^o$ and 45^o.

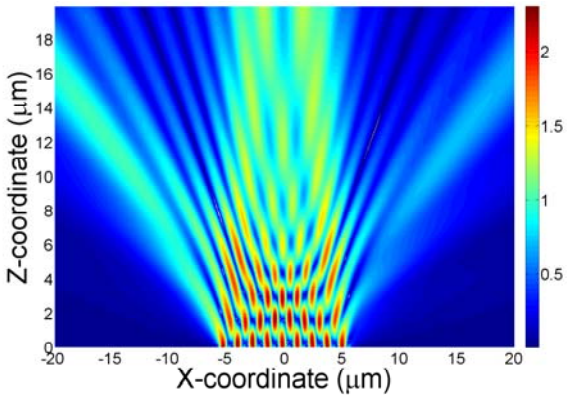

(b) Near-field for $\theta_{inc} = 0^o$.

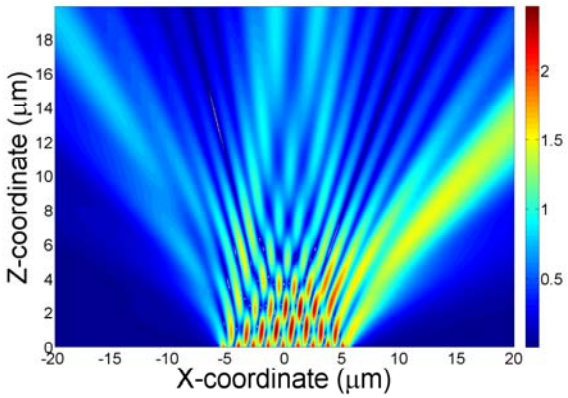

(c) Near-field for $\theta_{inc} = 45^o$

Figure 5.18: Scattered near and far-fields of IRT having the same parameters as Fig. 5.15. The incident angle $\theta_{inc} = 0^o$ and 45^o and number of grooves $P = 9$.

5.9 Discussions on Further Generalization of the Formulation

The formulation in section 5.6 is applicable to identical general shaped grooves with the same period between them. These assumptions are not considered limitations in the problem formulation and can be further relaxed. In this section, we will further discuss the extension of our previous formulation for non-identical general-shaped grooves with different groove-periods. Fig. 5.19 shows a schematic drawing of the a non-identical general-shaped grooves with different groove-periods between successive grooves.

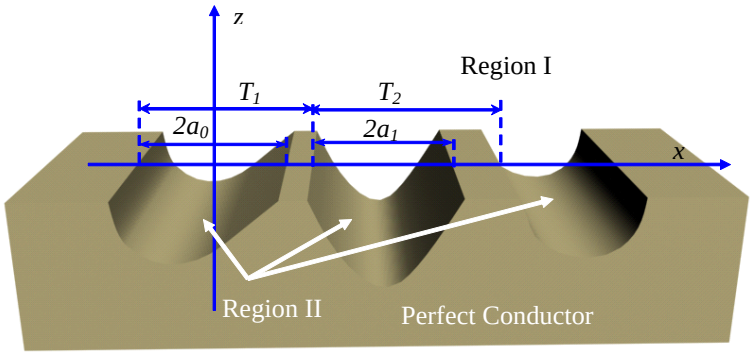

Figure 5.19: A Schematic diagram of a nonidentical multiple general-shaped grooves with different groove periods.

The groove physical parameters are defined for each individual groove as $\beta_n^{p,l}$, $\zeta_n^{p,l}$, ϵ_r^p, D_l^p, a_l^p, b_l^p, and T_p, where now the superscript p is added to account for the groove number. These physical parameters are different and will affect the formulation of the and the results of the scattering problem significantly. The freedom in choosing each groove physical parameters allow more flexibility in design and optimization of a finite number of grooves for a specific application. The electric and magnetic fields tangential components of groove p in layer l are rewritten as

$$E_y^{p,l}(x,z) = \sum_{n=1}^{\infty} \sin\ \beta_n^{p,l}(x + a_l^p - T_p) \times (A_n^{p,l} e^{j\zeta_n^{p,l}(z+D_{l-1}^p)} + B_n^{p,l} e^{-j\zeta_n^{p,l}(z+D_l^p)}), \qquad |x - T_p| \le a \tag{5.70}$$

$$H_x^{p,l}(x,z) = \frac{1}{\omega\mu_r^p\mu_0}\sum_{n=1}^{\infty}\zeta_n^{p,l}\sin\ \beta_n^{p,l}(x+a_l^p) \times (A_n^{p,l}e^{j\zeta_n^{p,l}(z+D_{l-1}^p)} - B_n^{p,l}e^{-j\zeta_n^{p,l}(z+D_l^p)}). \qquad |x-T_p| \le a \tag{5.71}$$

Here, $\beta_n^{p,l} = n\pi/2a_l^p$ and $\zeta_n^{p,l} = (k_p^2 - \beta_n^{p,l^2})^{1/2}$,are defined as before. The superscript represents the layer number and the subscripts are the harmonic and layer indexes. The electric and magnetic fields in Eqs. (5.49) and (5.50) are for general shaped grooves with arbitrary physical dimensions filled with a dielectric material ϵ_r^p. Following this formulations of the fields inside the grooves, and noting that the formulation of the fields in the upper half region are not changed, Eqs. (5.57) and (5.58) can be written as :

$$\begin{aligned} 2a_p^2k_ze^{-jT_qk_x}G_m(k_xa_1^p) &= \frac{1}{2\pi}\sum_{p=0}^{p=P}\sum_{n=1}^{\infty}(a_1^p)^2\beta_n^{p,1}R_{m,n}^{q,p}(k_0)A_n^{p,1} \\ &+ \frac{a_1^p\zeta_m^{p,1}}{\beta_m^{p,1}\mu_r}\delta_{m,n}\delta_{p,q}A_m^{q,1} \\ &+ \frac{1}{2\pi}\sum_{p=0}^{p=P}\sum_{n=1}^{\infty}(a_1^p)^2\beta_n^{p,1}e^{-j\zeta_n^{p,1}d}R_{m,n}^{q,p}(k_0)B_n^{p,1} \\ &- \frac{a_1^p\zeta_m^{p,1}}{\beta_m^{p,1}\mu_r^p}e^{-j\zeta_m^{p,1}d}\delta_{m,n}\delta_{p,q}B_m^{q,1}, \end{aligned} \tag{5.72}$$

where

$$R_{m,n}^{q,p}(k_0) = \int_{-\infty}^{\infty}a_1^qa_1^pG_n(\zeta a_1^q)G_m(-\zeta a_1^p)e^{-j(T_p-T_q)\zeta}\kappa_0 d\zeta. \tag{5.73}$$

Following the steps as before, we can formulate the coefficient matrix $\mathbf{M}$. Note that the diagonal matrices in the coefficient matrix $\mathbf{M}$ are now nonidentical. Each matrix formulate an individual groove. The simulation time will increase due to the formation of the diagonal matrices since they are no longer identical. This formulation will allow for the simulation of a nonidentical generalized shape groove and allow for changing individual groove parameters and measure its effect on the final simulation results.

Chapter 6

Summary of Contributions and Future Work

6.1 Summary of Contributions

This thesis has demonstrated the design and the fabrication of a $1 \times N$ and an $N \times N$ digital optical MEMS switch and OXC, respectively. Both architectures are based on a smart 3-D rotating inclined micromirror ($3DRIM$). The $3DRIM$ was constructed through a microassembly process using a passive microgripper, key and inter-lock (PMKIL) assembly system. The electrostatic micromotor used provides an excellent method for rotating the micromirror to achieve a repeatable alignment that leads to minimum optical insertion loss between the input and output ports of the switch.

The $1 \times N$ MEMS optical switch architecture was able to handle a large number of output ports and resulted in uniform insertion losses over all output channels through the symmetry employed in the switch design. This switch also does not require signal equalization. The scalability of the this architecture was test by a fast hybrid method that is able to model the micromirrors and the collimating lenses, and the their misalignments, losses ro predict the insertion loss and the cross-talk level. Insertion loss and cross-talk are important factors affecting the switch scalability. Several $3DRIM$ incorporating different sizes of micromirrors and different GRIN lenses were simulated.

The second switch architecture that employs the $3DRIM$ is an $N \times N$ optical cross-connect

(OXC) switch. The design of an $N \times N$ OXC uses only $2N$ of the $3DRIM$. This OXC architecture is useful for medium sized OXCs that the 2-D MEMS switch architectures can not handle due to the excessive loss when the size of the switch is increased beyond 16×16, is simpler than the 3-D one.

An electrostatic micromotor was chosen as the actuator of the $3DRIM$ since it offers continuous rotation as well as a small precise stepwise motions with excellent repeatability. Because of the extra assembled microstructures on the top of the micromotor, The value of the excitation voltage of the $3DRIM$ was significantly large. This research has also developed a RPS design technique to optimally reshape the rotor pole's physical dimensions in order to maximize the generated motive torque and consequently to decrease the driving voltage of the micromotor. To achieve this goal, a 2-D FEM ANSYS macro to simulate the micromotor and to calculate the generated motive torque was developed. For micromotors with large dimensions compared to the gap size, the memory requirement and the computational time are significantly large. Thus, the periodic potential boundary conditions were employed to simulate only one sector of the micromotor, which significantly decreases the required simulation time. The targeted performance of the $3DRIM$ was achieved through several PolyMUMPs fabrication runs.

A successful design, fabrication, and microassembly of the $3DRIM$ were achieved. The first construction of a $3DRIM$ involves the assembly of three microparts: two *support posts* and a micromirror. The two *support posts*, key-joined to the micromotor rotor, hold the micromirror through a double inter-lock joints at a 45-degree angle with respect to the rotor surface. This simple assembly procedure, suite micromirrors with dimensions smaller than 200×280 μm and fails for assembling larger micromirrors.

Two assembly techniques were developed and were able to construct $3DRIM$s that incorporates large micromirrors with different sizes. The first technique used a newly designed micropart called *cross-support post* for enhancing the verticality and the rigidity of the two *support posts* before the assembling the micromirror. The low profile of the *cross-support post* and the vertical/horizontal insertion makes its assembly an easy step in the whole assembly process. Although in this assembly technique, which include one extra assembly of micropart, the successful constructions of $3DRIM$s that uses a 300×380 μm and 400×400 μm micromirrors were successful.

The second technique assembles four microparts as a holding structure of a 400×400 μm

micromirror in the $3DRIM$. In this assembly technique, two wide low profile *support posts* were assembled first, followed by vertical insertions of two *cross-support posts*. The micromirror is inter-lock joined to the *support posts* at a 45-degree orientation.

Both assembly techniques provide a rigid structure for the $3DRIM$. However, the assembly time, the number of microparts used, and the number of microgripper used to complete one assembly process are important parameters to decide on the assembly technique to choose. Since both assembly techniques provide similar micromirror performance in terms of its rigidity, the ease of assembly is the factor to precede with in future manufacturing of the $3DRIM$. The assembly technique which involves the insertion of one *cross-support post* in a vertical orientation is the easiest method to proceed with.

The PolyMUMPS fabrication process was used to prove our concept of $3DRIM$ assembly. However, other fabrication processes such as custom fabrication using combined surface and bulk micromachining should, be considered for future fabrication in order to improve the design and quality of the mechanical and optical performance of the $3DRIM$.

The last significant contribution of this research is the development of a rigorous formulation of the electromagnetic plane wave scattering from a general-shaped groove in a perfect conducting plane. The formulation was developed in order to simulate a finite grating structure to be added to the surface of micromirror of the $3DRIM$. This grating will enable the selection of a specific wavelength for a switched optical signal. The formulation of the method utilizes the Fourier-transform representation of the scattered field for rapid convergence in the upper half-space and the staircase approximation for representing the field in the general-shaped groove. The method provides a solution for the scattered near-field from the groove and hence is considered an essential design tool for near-field manipulation in optical devices.

The formulation of a scattering from a general-shaped groove was extended to apply to multiple general-shaped grooves. The limitations caused by infinite periodic identical grooves have been resolved. The formulation is also applicable for multiple grooves with different profiles and different spacings. Each groove can be filled with an arbitrary material and can take any cross-sectional profile, yet the solution is rigorous and based on the Fourier-Integral representation of the scattered field and the staircase approximation of the groove field. The efficient formulation of the coefficient matrix results in a banded-matrix form and thus produces an efficient and

time-saving solution.

6.2 Future Work

Several further avenues of exploration are possible and include the following:

1. Investigate a custom fabrication process that is a combination of bulk and surface micromachining. The proposed fabrication process should improve the rigidity of the microparts and the microgripper. This improvement will allow for fabricating and assembling a $3DRIM$ with better mechanical and optical performances.

2. Conduct a dynamic analysis of micromotors designed with the RPS technique. Experimental data should be collected and analytical simulation should be employed in order to accurately characterize the dynamic behavior of such micromotors.

3. Use a waveform shaping of the input voltage to the micromotor for optimum transient responses.

4. Explore a self-assembly technique for the $3DRIM$ using the stress induced in bilayer structures.

5. Explore true optical delay lines: a set of $3DRIMs$ can be integrated with PBG materials for true continuous optical delay lines for antennas and satellite applications. A set of optical delay lines will serve as feeding or receiving circuits in the transceiver system.

6. Design and optimize the surface gratings that will be integrated on the micromirror of the $3DRIM$ (Fig. 5.1(b)) to allow coupling of optical power to the diffracted orders and minimize the power of the zero order diffracted beam. The output port should be able to efficiently covert the angular differences in the diffracted optical beams into a space variations to allow a selection of the required diffracted beams.

7. Design a waveguide to allow a specific guiding modes to propagate depending on the required range of wavelengths to be coupled into it (Fig. 5.1(a)). The design of the surface grating assisted-waveguide to couple a specific wavelength when it is incident at an exact angle.

8. Investigate the dependency of the coupling efficiency to the waveguide-assisted grating on the the wavelength of the incident optical beam and the waveguide physical parameters. The coupling efficiency is strongly dependent on the angle of incidence.

9. Investigate the the fabrication of gratings for implementing the waveguide-assisted grating and the micromirror's surface gratings.

Appendix A

2-D FEM ANSYS Micromotor Macro

The Macro command is:

*use, my2Dmot, r_{in}, r_o, g, r_{so}, r_{air}, r_{inf}, $thickness$, p_{rp}, p_{sp}, w_{rp}, w_{sp}, x_{div1}, x_{div3} , x_{div4}, r_{flt}, θ_{sh}, θ_d , V_0

Table A.1 lists and defines all the input parameters of the macro. The ANSYS macro automatically calculates the sector angle sec and applies the potential periodic boundary conditions. Fig. A.1 shows a meshed micromotor sector with the defined four regions. Default values of $g/4$, g, $2g$ for the parameters $xdiv1$, $xdiv3$, and $xdiv4$ are usually good approximations. These parameters can be adjusted to control the mesh density in any of the defined regions. When supplying the appropriate input micromotor parameters, the expected output results are as follows:

$F_{nor-tot}$ - The total normal force on one rotor pole.

$F_{tan-tot}$ - The total tangential driving force on one rotor pole.

T - The resulting driving torque from applying a voltage V_0.

Table A.1: Definition of supplied design parameters to the ANSYS macro my2Dmot.

Parameter	*Definition*
r_o	rotor radius
$\triangle r$	rotor pole depth
g	rotor-stator gap
r_{so}	stator outer radius
r_{air}	air region radius
r_{inf}	infinite element radius
$thickness$	rotor thickness
p_{rp}	rotor pole pitch
p_{sp}	stator pole pitch
w_{rp}	rotor pole width
w_{sp}	stator pole width
x_{div1}	element size in the first region
x_{div3}	element size in second and third regions
x_{div4}	element size in the forth region
r_{flt}	fillet curve radius of rotor poles
θ_{sh}	An angle that specifies the rotor pole shape
θ_d	A step angle to rotate the rotor
V_0	Applied voltage on stator poles

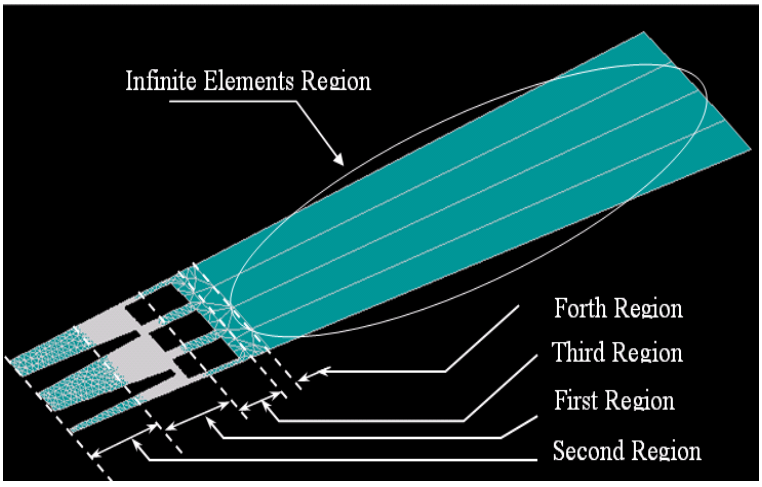

Figure A.1: Meshing of micromotor sector in the ANSYS macro.

```
! Electrostatic Analysis for Micromotor for voltage gradient
! This file is the master file that will be read by ANSYS > 8.0
! to automatically generate finite element models.
! USING TRANS!)( element for air
!*********************************************************************
!* SET PARAMETERS AND TITLE
!*********************************************************************
/TITLE, 2D Electrostatic Analysis of Micromotor By Mohamed Basha

!*********************************************************************
!* SET GRAPHICAL WINDOW
!*********************************************************************
/PLOPTS,INFO,1
/PLOPTS,LEG1,1
/PLOPTS,LEG2,1
/PLOPTS,LEG3,1
/PLOPTS,FRAME,0
/PLOPTS,TITLE,1
/PLOPTS,MINM,0
/PLOPTS,VERS,0
/PLOPTS,WINS,1
/PLOPTS,WP,0
/TRIAD,OFF

!*********************************************************************
!* SET STRUCTURAL AS PREFERENCE
!*********************************************************************
KEYW,PR_SET,1
KEYW,PR_STRUC,1
KEYW,PR_THERM,0
KEYW,PR_ELMAG,0
KEYW,PR_FLUID,0
KEYW,PR_MULTI,0
KEYW,PR_CFD,0
/PMETH,OFF

!*********************************************************************
!* START MODELING
!*********************************************************************
/PREP7

rin = arg1        ! Radius of inner rotor poles
ro  = arg2        ! Radius of outer rotor poles
tg = arg3         ! GAp between rotor and stator
rs  = ro+tg       ! Stator radius
```

```
rso = arg4        ! out sator radius
rair = arg5       ! Air radius
rinf =arg6        ! Radius of Infinite element to account for Radiation BC
thickness  = arg7 ! Thickness of the rotor

rpp = arg8        ! rotor pole pitch
spp = arg9        ! stator pole pitch
rpw = ar10        ! rotor pole width
spw = ar11        ! stator pole width
rsh = (spp-spw)/2              ! shift angle added to have symetry

rdiv1 = ro-(ro-rin)/4          ! division radius 1 for rotor
rdiv2 = rs+(rso-rs)/4          ! division radius 2 for stator
rdiv3=rso+(rair-rso)/3         ! division radius 3 for air

! Number of division for each layer
xdiv1=ar12
xdiv2=ar12
xdiv3=ar13
xdiv4=ar14
xdiv5=4
rflt=ar15           ! Fillet raduis
th = ar16           ! addimg an angle to change the shape of the rotor pole
thd =ar17           ! this angle to move the rotor to different positions
V0 = ar18           ! Applied Voltage to the Stator Pole

/PREP7
CSYS,1              ! Set the coordinate system to cylindrical

!*********************************************************************
!* GENERATE General KEYPOINTS
!*********************************************************************
! First stator KP
K, 1,rs,     -1.5*spp+rsh
K, 2,rso,-1.5*spp+rsh
K, 3,rso,-1.5*spp+spw+rsh
K, 4,rs,     -1.5*spp+spw+rsh

! Second stator KP
K, 5,rs,     -0.5*spp+rsh
K, 6,rso,-0.5*spp+rsh
K, 7,rso,-0.5*spp+spw+rsh
K, 8,rs,     -0.5*spp+spw+rsh

!  Third stator KP
```

```
K, 9,rs,     0.5*spp+rsh
K, 10,rso,0.5*spp+rsh
K, 11,rso,0.5*spp+spw+rsh
K, 12,rs,     0.5*spp+spw+rsh

!Edg points
K, 13,rs,     1.5*spp
K, 14,rso,1.5*spp


! Center Point
K, 15,0,0

! Rotor KP
K, 16,  rin,    -rpp

K, 17,  rin,    -rpp+rsh+thd
K, 18,  ro,     -rpp+rsh+th+thd
K, 19,  ro,     -rpp+rpw+rsh-th+thd
K, 20, rin,     -rpp+rpw+rsh+thd
K, 21, rin,     0+rsh+thd
K, 22, ro,      0+rsh+th+thd
K, 23, ro,      rpw+rsh-th+thd
K, 24, rin,     rpw+rsh+thd

K, 25, rin,     rpp

! Division lines for areas between Poles
K, 26, rdiv1,    -rpp
K, 27, rdiv1,    rpp

K, 28, rdiv2,    -rpp
K, 29, rdiv2,    rpp

!*********************************************************************
!* CREATE LINES FROM KEYPOINTS
!*********************************************************************
/pnum,line,1

! First Pole Lines
LSTR,       1,       2
LARC,    2,     3,        15,rso
LSTR,       4,       3
LARC,    4,     1,        15,rs
```

```
! Second Pole Lines
LSTR,       5,      6
LARC,    6,     7,        15,rso
LSTR,       8,       7
LARC,    8,     5,        15,rs
LFILLT,7,8,rflt, ,       ! generate fillete line for second pole
LFILLT,5,8,rflt, ,       ! generate fillete line for second pole

numcom, line
! Third Pole Lines
LSTR,       9,      10
LARC,    10,     11,        15,rso
LSTR,       12,      11
LARC,    12,     9,        15,rs
LFILLT,11,14,rflt, ,      ! generate fillete line for second pole
LFILLT,13,14,rflt, ,      ! generate fillete line for second pole
! Total line = 16

! Rotor lines
LSTR,       15,      16
LARC,    16,     17,        15,rin
LSTR,       17,      18
LARC,    18,     19,        15,ro
LSTR,       20,      19
LARC,    20,     21,        15,rin
LSTR,       21,      22
LARC,    22,     23,        15,ro
LSTR,       24,      23
LARC,    24,     25,        15,rin
LSTR,       15,      25
LFILLT,23,24,rflt, ,
LFILLT,24,25,rflt, ,

! Total line = 29

LARC,    26,     27,        15,rdiv1   !line 30
LARC,    28,     29,        15,rdiv2   !line 31
!LARC,    30,     31,        15,rdiv3   !line 32
!LARC,    32,     33,        15,rdiv4   !line 33

/pnum,line,0
!*********************************************************************
!* CREATE AREAS FROM LINES
!*********************************************************************
```

```
/pnum,area,1

LSEL, S, , , 17, 29, 1, 0
AL ,ALL !building the first rectangular from lines
Alls

AL ,1 ,2 ,3 ,4           ! First stator pole
AL ,5 ,6 ,7 ,8,9,10      ! Second stator pole
AL ,11 ,12,13,14,15,16  ! Third stator pole
alls

PCIRC, 0, ro, -rpp, rpp
aovlap, all
numcmp,area

ASEL,s,,,5,7,1
ASBL,all,30,,delete,delete
numcmp,area
alls

PCIRC, 0, rs, -rpp, rpp
aovlap, all
numcmp,area
alls

PCIRC, 0, rso, -rpp, rpp
aovlap, all
numcmp,area
alls

ASEL,s,,,12,15,1
ASBL,all,31,,delete,delete
numcmp,area
alls

ASEL,s,,,8,12,1
ASEL,a,,,17,19,1
AADD,all
numcmp,area
alls

PCIRC, 0, rdiv3, -rpp, rpp
aovlap, all
numcmp,area
alls
```

```
PCIRC, 0, rair, -rpp, rpp
aovlap, all
numcmp,area
alls

PCIRC, 0, rinf, -rpp, rpp
aovlap, all
numcmp,area
alls

!*********************************************************************
!* DEFINE NUMBER OF DIVISIONS IN EDGE LINES
!*********************************************************************

!first line on both sides
lsel,s,loc,y,-rpp,,,0
lsel,a,loc,y,rpp
lsel,r,loc,x,(rin+rdiv1)/2,,,0
lesize,all,xdiv3,,,,1,,,1

!Second line on both sides
lsel,s,loc,y,-rpp
lsel,a,loc,y,rpp
lsel,r,loc,x,(rdiv1+ro)/2
lesize,all,xdiv1,,,,1,,,1

!Third line on both sides
lsel,s,loc,y,-rpp
lsel,a,loc,y,rpp
lsel,r,loc,x,(ro+rs)/2
lesize,all,xdiv1,,,,1,,,1

!Forth line on both sides
lsel,s,loc,y,-rpp
lsel,a,loc,y,rpp
lsel,r,loc,x,(rs+rdiv2)/2
lesize,all,xdiv1,,,,1,,,1

!Fifth line on both sides
lsel,s,loc,y,-rpp
lsel,a,loc,y,rpp
lsel,r,loc,x,(rdiv2+rso)/2
lesize,all,xdiv3,,,,1,,,1
```

```
!Seventh line on both sides
lsel,s,loc,y,-rpp
lsel,a,loc,y,rpp
lsel,r,loc,x,(rso+rdiv3)/2
lesize,all,xdiv4,,,,1,,,1

!Eigth line on both sides
lsel,s,loc,y,-rpp
lsel,a,loc,y,rpp
lsel,r,loc,x,(rdiv3+rair)/2
lesize,all,,,3,,1,,,1

!Ninth line on both sides
lsel,s,loc,y,-rpp
lsel,a,loc,y,rpp
lsel,r,loc,x,(rair+rinf)/2
lesize,all,,,1,,1,,,1

lsel,s,radius,,rair
lsel,a,radius,,rinf
LESIZE,all, , ,4, , , , ,1    ! dividing the line into 10 divisions
alls

!*********************************************************************
!* DEFINE ELEMENT TYPE & Material Property
!*********************************************************************
ET,1,121                     ! PLANE121 element for air region
emunit,epzro,8.854e-6        ! Set free-space permittivity for
mp,perx,1,1
ET,2,110,1,1                 ! 8-node 2-D Infinite element

!*********************************************************************
!* Assigning Element type to areas
!* MESH ALL AREAS
!*********************************************************************
! shape of element

sha=1
ASEL,s ,AREA , ,12,,,0
AATT, , ,1,       0,
esize,xdiv1
mshap, sha
amesh,all

ASEL,s ,AREA , ,5,7,1,0
```

```
ASEL,a ,AREA , ,8,11,1,0
AATT, , ,1,       0,
esize,xdiv3
mshap, sha
amesh,all

ASEL,s ,AREA , ,13,,,0
AATT, , ,1,       0,
esize,xdiv4
mshap, sha
amesh,all

ASEL,s ,AREA , ,14,,,0
AATT, , ,1,       0,
mshap, sha
amesh,all

ASEL,s ,AREA , ,15,,,0
AATT, , ,2,       0,
mshkey,1
mshap, 0
amesh,all
alls

!*********************************************************************
!* MERGE ITEMS
!*********************************************************************
NSEL, S, LOC, Y, 0, W,,  ! select nodes ahead of & including crack tip
NUMMRG, NODE, 1.0E-7, 1.0E-7  ! merge nodes ahead of & including crack tip

!*********************************************************************
!* Set infinite flag in Infinite elements for simulation purposes
!*********************************************************************
nsel,s,loc,x,rinf        ! Select the outer nodes of the infinite elements
CM,INF1,node
sf,all,inf               ! Set infinite flag in Infinite elements

!*********************************************************************
!* Assigning Conductor Name for nodes on rotar & Stator
!*********************************************************************
ASEL,s ,AREA , ,1,,,0
lsla,r
NSLL,s,1
CM,COND1,node            ! Assign node component to 1st conductor ROTOR
alls
```

```
ASEL,s ,AREA , ,2,,,0
lsla,r
NSLL,s,1
CM,COND2,node            ! Assign node component to 1st conductor Stator P1
alls

ASEL,s ,AREA , ,3,,,0
lsla,r
NSLL,s,1
CM,COND3,node            ! Assign node component to 2nd conductor Stator P2
alls

ASEL,s ,AREA , ,4,,,0
lsla,r
NSLL,s,1
CM,COND4,node            ! Assign node component to 3rd conductor Stator P3
alls

!*********************************************************************
!* Set MAXWELL flag to Rotor ELEMENT
!*********************************************************************
SF, COND1, MXWF,
alls
!*********************************************************************
!* APPLY VOLTAGE BOUNDARY CONDITION
!* Coupling Boundary Condition
!*********************************************************************

! Select the first set of Node at higher edge and name it nodeh
lsel,s,loc,y,rpp
nsll,r,1
cm,nodeh,node
alls

! Select the first set of Node at lower edge and name it nodel
lsel,s,loc,y,-rpp
nsll,r,1
cm,nodel,node

! Get the number of nodes from nodel
*GET, ncount, NODE, 0, count, , ,  ! to get the number of node in the set

! to get the max node number and location to start with from nodel comp
*GET, nmaxl, NODE, 0, NUM,MAX , ,  ! Get max node number
```

```
nlocx=NX(nmaxl)
nlocy=Ny(nmaxl)
alls

! to get the max node number to start with from nodeh
nmaxh=NODE(nlocx,-nlocy,0)

!First constraint equation
!CE, 1, 0, nmaxl, VOLT, 1, nmaxh, VOLT, -1
CP, 1, VOLT, nmaxl, nmaxh
! Start Do loop to construct the remaning constraint equations
! This will apply the voltage periodic BCs

*DO, J, 2, ncount, 1
    cmsel,s,nodel,node
    *GET, nl, NODE, nmaxl, NXTL, , ,  ! to get next node number
    alls
    nlocx=NX(nl)
    nlocy=Ny(nl)
    nh=NODE(nlocx,-nlocy,0)
    nmaxl=nl
    nmaxh=nh
    alls
    CP, NEXT, VOLT, nmaxl, nmaxh
!    CE, NEXT, 0, nmaxl, VOLT, 1, nmaxh, VOLT, -1
*ENDDO
NUMCMP, CP

alls

!*********************************************************************
! APPLY VOLT BOUNDARY CONDITION at Nodes
!*********************************************************************
CMSEL,s,cond3
D,ALL,VOLT,0

CMSEL,s,cond1
D,ALL,VOLT,0

CMSEL,s,cond2
D,ALL,VOLT,V0

CMSEL,s,cond4
D,ALL,VOLT,0
alls
```

```
fini

!*********************************************************************
! Define Solution Parameters and Solve
!*********************************************************************
/SOLU
ANTYPE,STATIC,NEW
eqslv,jcg
solve

!*************************************************************************
!**** Force and Torque Calculation of the Micromotor at Rotor Nodes *******
!*************************************************************************

/post1
set
csys,1          ! To change to cylindrical System of coordinate
cmsel,s,cond1,node
*GET, ncountf, NODE, 0, count, , ,  ! to get the number of node in the set

! to get the max node number and location to start with from nodel comp
*GET, nmaxf, NODE, 0, NUM,MAX , ,   ! Get max node number
nlocxf=NX(nmaxf)
nlocyf=Ny(nmaxf)

!to get the force componenet
*GET, FY, NODE, nmaxf, FMAG ,Y , ,  ! To get the y force component
*GET, FX, NODE, nmaxf, FMAG ,X , ,  ! To get the x force component
! Theta Tangential Component
pi=22/7
Ftan = Fy*cos(nlocyf*pi/180)-Fx*sin(nlocyf*pi/180)
Fnor= - Fy*sin(nlocyf*pi/180)+Fx*cos(nlocyf*pi/180)

T=nlocxf*(180/rpp)*thickness*Ftan
Ftan_tot=Ftan
Fnor_tot=Fnor
cmsel,s,cond1,node

*DO, J, 2, ncountf, 1
    *GET, nf, NODE, nmaxf, NXTL, , ,    ! to get next node number
    ! Force Calculation
    *GET, FY, NODE, nmaxf, FMAG ,Y , ,  ! To get the y force component
    *GET, FX, NODE, nmaxf, FMAG ,X , ,  ! To get the x force component
    ! Theta Tangential Component
    Ftan = Fy*cos(nlocyf*pi/180)-Fx*sin(nlocyf*pi/180)
```

```
    Fnor= - Fy*sin(nlocyf*pi/180)+Fx*cos(nlocyf*pi/180)

    Ftan_tot=Ftan_tot+Ftan
    Fnor_tot=Fnor_tot+Fnor

    ! Torque Caculation
    nlocxf=NX(nf)
    nlocyf=NY(nf)
    T=T+nlocxf*(180/rpp)*thickness*Ftan
    nmaxf=nf
    cmsel,s,cond1,node

*ENDDO
!*********************************************************************

*cfopen,result,dat,,append
*vwrite , rin, tg, rpp, rpw, spp,spw,th, thd, rflt,V0,Fnor_tot,Ftan_tot, T
(   F8.3,'  ', F8.3,'  ',F8.3,'  ',F8.3,'  ',F8.3,'  ',F8.3,'  ',F8.3,'  ',
F8.3,'  ',F8.3,'  ',F8.3,'  ',E10.3,'  ', E10.3,'  ', E10.3)
```

Appendix B

Loss Analysis in MEMS Switches

The most important issues in the design and development of the optical MEMS switch are the coupling losses and the cross-talk between the lightguides. Fast and accurate computational methods are essential for design optimization of such complex components. These methods should be able to include all of the relevant geometrical and physical parameters of the structure. In this appendix, a fast method to model and simulate the behavior and predict the performance of complex optical MEMS switch configurations under various operational conditions is presented. The method is a combination of Beam Propagation Method (BPM) [156], a new 3-D vectorial Gaussian Beam Tracing (GBT) algorithm developed in our research group [157], physical optics method (PO) [158], and electromagnetic reciprocity theorem [159]. The input/output fibers could be of regular type with any cross-sectional geometry, tapered, GRIN, with or without attached micro-lens. In addition to MEMS micromirrors, the switch fabric may contain various types of optical components such as micro-lens, prism, dielectric slabs, etc. The lightwave propagation inside the fiber with uniform or tapered geometry is handled by BPM. Other optical coupling components such as micro-lens, prisms or other intermediate structures are analyzed by the well developed GBT method [157] in our research group at the university of waterloo. The 3D-GBT algorithm is able to model objects with small apertures by expanding the guided field, obtained by BPM simulation, in terms of several Gaussian beams, which are then propagated through various components. These beams are summed up to give the field over the output plane [157]. To accelerate the analysis/simulation process a reciprocity method is employed to further reduce the number computational steps. Our proposed method can be used to optimize the geometry of structure constrained by the minimum cross-talk level. All other parameters such as finite

dimensions of the mirror, mirror losses, path length effects, polarization dependence, and all possible mechanical misalignments (axial and angular) of the fibers, mirrors, lens, can be accurately modeled.

Figure B.1 depicts the geometry of a simple optical MEMS switch. The switch consists of two single mode fibers and a micromirror with width W and hight H. Fields at the micromirror, input, and output fibers are expressed in terms of thier local coordinate systems. The input and output coordinate systems, (x_i, y_i, z_i) and (x_o, y_o, z_o), are centered at the endfaces of the input and output fibers, respectively, as shown in the Fig. B.1. The z_i and z_o axes coincide with the axes of the input and output fibers, respectively. The main coordinate system is centered at the surface of the micromirror such that the Z-axis is normal to the surface of the micromirror. A simple coordinate transformations between the micromirror and both input and output coordinate systems are derived to facilitate the development of the algorithm.

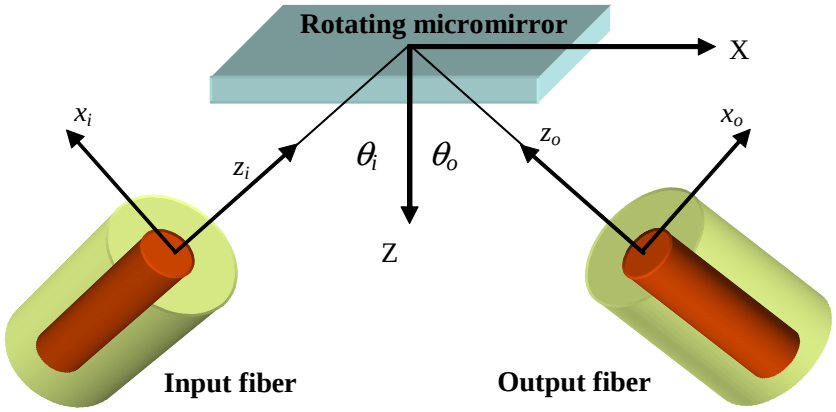

Figure B.1: A schematic diagram of optical MEMS switch. Fields are expressed by two local coordinate systems at the input and output fibers and one main coordinate system centered at the micromirror. θ_i and θ_o are the incident and reflected angles, respectively, from the micromirror.

$$\begin{aligned} x_i &= -X\cos\theta_i - Z\sin\theta_i \\ y_i &= Y \\ z_i &= d + X\sin\theta_i - Z\cos\theta_i \end{aligned} \tag{B.1}$$

and

$$\begin{aligned} x_o &= -X\cos\theta_0 + Z\sin\theta_0 \\ y_o &= Y \\ z_o &= d - X\sin\theta_0 - Z\cos\theta_0 \end{aligned} \tag{B.2}$$

where θ_i and θ_o are the input and output fibers incident and reflected angles, respectively and d is the distance from the input SMF to the micrror.

The the fundamental guided mode in a weakly guiding single mode fibers (SMF)is well modeled with a plane wave with a gaussian profile distribution inside the core of the input SMF. The transmitted field from the input SMF is well approximated by a Gaussian beam with its waist w_o at the endface of the input SMF [160].

$$\begin{aligned} E_{ax}^{inc} &= T_e \tfrac{w_o}{w(z_i)} \exp\left(\tfrac{-r^2}{w^2(z_i)}\right) \exp\left(-jkz_i - jk\tfrac{r^2}{2R(z_i)} + j\zeta(z_i)\right) \\ T_e &= \tfrac{2n_{Co}}{n_{air}+n_{Co}} \\ \xi_o &= \tfrac{w_o^2.\pi}{\lambda} \\ w(z_i) &= w_o.\left(1+\left(\tfrac{z_i}{\xi_o}\right)^2\right)^{1/2} \\ R(z_i) &= z_i.\left(1+\left(\tfrac{\xi_o}{z_i}\right)\right)^2 \\ \zeta(z_i) &= \tan^{-1}\left(\tfrac{z_i}{\xi_o}\right) \end{aligned} \tag{B.3}$$

where w_o is the waist radius of the Gaussian beam, ξ_o is the Rayleigh range.

B.0.1 Physical Optics Sources

The Gaussian beam at the end face of the input SMF propagates a distance d between the input SMF and the micromirror. The incident field on the surface of the micromirror in terms of the micromirror coordinate system take the form

$$\begin{aligned} E_{ax}^{inc} &= T\tfrac{w_o}{w_p} \exp\left(\tfrac{-r^2}{w_p^2}\right).\exp\left(-j\beta z_p - jk\tfrac{r^2}{2R_p} + j\zeta_p\right) \\ w_p &= w_o.\left(1+\left(\tfrac{z_p}{\xi_o}\right)^2\right)^{1/2} \\ R_p &= z_p.\left(1+\left(\tfrac{\xi_o}{z_p}\right)\right)^2 \\ \zeta_p &= \tan^{-1}\left(\tfrac{z_p}{\xi_o}\right) \\ r^2 &= X^2\cos^2\theta_i + Y^2 \\ z_p &= d + X\sin\theta_i \end{aligned} \tag{B.4}$$

To speed up the computation, at the present stage, we have used a simplified model based on plane wave approximation for the reflection from plane surface. Applying Snell's law to determine the reflected fields from the micromirror surface, the tangential electric and magnetic fields are

$$\begin{aligned}\mathbf{E}_{ax}^{rfl} &= R_m^{TM}(\theta_i)\, E_{ax}^{inc}(\hat{X}\cos\theta_i - \hat{Z}\sin\theta_i)\\ \mathbf{H}_{ay}^{rfl} &= \tfrac{R_m^{TM}(\theta_i)}{\eta_o} E_{ax}^{inc}\hat{Y}\end{aligned} \tag{B.5}$$

where $R_m^{TM}(\theta_i)$ is mirror reflection coefficient for TM-polarization. The total tangential fields on the micromirror surface are the sum of the incident and reflected fields:

$$\begin{aligned}\mathbf{E}_m^{\tan} &= \{(\mathbf{E}_{ax}^{inc} + \mathbf{E}_{ax}^{ref}).\hat{X}\}\hat{X}\\ \mathbf{H}_m^{\tan} &= \{(\mathbf{H}_{ay}^{inc} + \mathbf{H}_{ay}^{ref}).\hat{Y}\}\hat{Y}\end{aligned} \tag{B.6}$$

The equivalent sources on the micromirror surface or equivalently the physical optics sources are [158]

$$\begin{aligned}\mathbf{J}_m^{PO} &= \hat{n}\times\mathbf{H}_m^{\tan}\\ \mathbf{M}_m^{PO} &= \hat{n}\times\mathbf{E}_m^{\tan}\end{aligned} \tag{B.7}$$

where $\mathbf{J}_m^{PO}$ and $\mathbf{M}_m^{PO}$ are the electrical and magnetic equivalent sources on the micromirror surface, $\mathbf{E}_m^{\tan}$ and $\mathbf{H}_m^{\tan}$ are the total (incident plus scattered) fields on the micromirror surface and $\hat{n}$ is the unit normal to the mirror's surface point in out of the mirror. Substituting from (B.6)in (B.7)yields the *PO* sources in term of the incident field.

$$\begin{aligned}\mathbf{J}_m^{PO} &= -\hat{X}(1+R^{TM}(\theta_i))\tfrac{E_{ax}^{inc}}{\eta_o}\\ \mathbf{M}_m^{PO} &= \hat{Y}\cos\theta_i(1-R^{TM}(\theta_i)E_{ax}^{inc}\end{aligned} \tag{B.8}$$

B.0.2 Electromagnetic Reciprocity Theorem

In order to calculate the coupled field to the output fiber, we have to determine the radiated field from the *PO* sources on the surface of the micromirror. Then we have to determine the fields at the endface of the output fiber and after that we can use the coupling relations to get the coupled field in the output fiber. To efficiently calculate the fields coupled into the output fiber due to the *PO* sources on the micromirror surface, we have used the mathematical relation between our original problem and a reciprocal problem wherein the lightwave propagating in

reverse direction namely the incident lightwave is coming along the output fiber. This relation provides a numerically efficient algorithm for computing coupling coefficient. Considering the output fiber as an input that radiates in the presence of the PO sources on the surface of the mirror. The modal field in the output SMF is considered the same as in the input SMF and take the same form as in (B.3). The transmitted field will also take the same form with slight different that it will be expressed in terms of the output fiber coordinate system. The radiated field from the output fiber in terms of the mirror coordinate system.

$$\begin{aligned}
&E_{bx}^{inc} = T_e \tfrac{w_o}{w_n} exp\left(\tfrac{-r^2}{w_n^2}\right).exp\left(-j\beta z_n - jk\tfrac{r^2}{2R_n} + j\zeta_n\right)\\
&w_n = w_o.\left(1+\left(\tfrac{z_n}{\xi_o}\right)^2\right)^{1/2}\\
&R_n = z_n.\left(1+\left(\tfrac{\xi_o}{z_n}\right)\right)^2\\
&\zeta_n = tan^{-1}\left(\tfrac{z_n}{\xi_o}\right)\\
&r^2 = X^2 cos^2\theta_o + Y^2\\
&z_n = d + X sin\theta_o
\end{aligned} \tag{B.9}$$

Following [158], we applied the reciprocity relation between the field by the physical optics sources and coupled to the output fiber and the source-free modal field of the output fiber combined with the orthogonality relation [4], to derive the amplitude of the guided mode in the output fiber

$$C_m^{TM} = \frac{-1}{2N_m} \iint\limits_{micromirror} (\mathbf{E}_{bx}^{inc}.\mathbf{J}_m^{PO} - \mathbf{H}_{by}^{inc}.\mathbf{M}_m^{PO}) dX dY \tag{B.10}$$

$$N_m = \iint\limits_{fiber\ cross-section} \mathbf{e}_{bx} \times \mathbf{h}_{by}.(-\hat{z}_o) dx_o dy_o \tag{B.11}$$

where $\mathbf{e}_{bx}$ and $\mathbf{h}_{by}$ are the modal field of the output fiber. Substitute from equation (3.2) in (3.27) to find the value of the normalization factor N_m

$$N_m = \frac{-\pi}{2}\frac{n_{co} w_o^2}{\eta_o} \tag{B.12}$$

Combining equations (3.23), (3.25), and (3.26) to derive the amplitude C_m^{TM} of the guided mode in the output fiber

$$C_m^{TM} = \frac{-\left[R^{TM}\left(\cos\theta_o + \cos\theta_i\right) + \left(\cos\theta_o - \cos\theta_i\right)\right]}{2\eta_o N_m} \iint\limits_{micromirror} E_{ax}^{inc} E_{bx}^{inc} dX dY \tag{B.13}$$

As we notice, to determine the coupling between the input and output fibers, we should supply the same value of the incident and reflected angles i values o respectively. For a cross talk calculation, we only need to change the output angle to the fiber that we want to determine the cross-talk at it. The normalized coupled power will be C_m^2.

B.0.3 Mechanical Misalignments

Mechanical misalignments of micromirror, input, and output SMF are considered a significant source of loss in the optical MEMS switch that degrade the switch performance (Fig. B.2). Mechanical misalignments are either offset along x, y, and/or z-axes or angular around x and/or y-axes. The mechanical misalignments are add to the switch analysis using coordinate system transformation, translation or rotation. Using the following coordinate system transformation, mechanical missaligment are included in our analysis of the switch at any stage of the formulations.

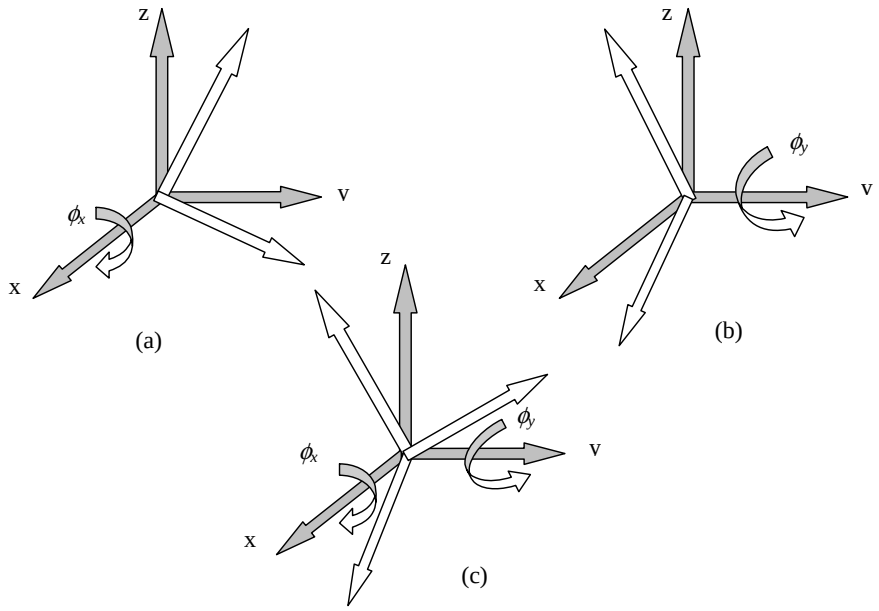

Figure B.2: Mechanical misalignment resulting from rotation around (a) x-axes. (b) y-axes. (c) both x-axes and y-axes.

$$\begin{bmatrix} x \\ y \\ z \end{bmatrix} \rightarrow \begin{bmatrix} 1 & 0 & 0 \\ 0 & \cos\varphi_x & \sin\varphi_x \\ 0 & -\sin\varphi_x & \cos\varphi_x \end{bmatrix} \begin{bmatrix} \cos\varphi_y & 0 & -\sin\varphi_y \\ 0 & 1 & 0 \\ \sin\varphi_y & 0 & \cos\varphi_y \end{bmatrix} \begin{bmatrix} x+s_x \\ y+s_y \\ z+s_y \end{bmatrix} \tag{B.14}$$

where ϕ_x and ϕ_y are te rotation around x and y-axes, respectively, and s_x, s_y, and s_z are offset translation along x, y, and z-axes, respectively.

Bibliography

[1] H. Toshiyoshi and H. Fujita, "Electrostatic micro torsion mirrors for an optical switch matrix," *J. Microelectromech. Syst.*, vol. 5, no. 4, pp. 231–237, Dec. 1996.

[2] L.-Y. Lin, E. L. Goldstein, and R. W. Tkach., "On the expandability of free-space micromachined optical cross connects," *J. Lightw. Technol.*, vol. 18, no. 4, pp. 482–489, Apr. 2000.

[3] C. Marxer, C. Thio, M. A. Gretillat, N. F. de Rooij, R. Battig, O. Anthamatten, B. Valk, and P. Vogel, "Vertical mirrors fabricated by deep reactive ion etching for fiber-optic switching applications," *J. Microelectromech. Syst.*, vol. 6, no. 3, pp. 277–285, Sep. 1997.

[4] C.-H. Ji, Y. Yee, J. Choi, S.-H. Kim, and J.-U. Bu, "Electromagnetic 2×2 mems optical switch," *IEEE J. Sel. Topics Quantum Electron.*, vol. 10, no. 3, pp. 545–550, May/June 2004.

[5] J.-N. Kuo, G.-B. Lee, and W.-F. Pan, "A high-speed low-voltage double switch optical crossconnect using stress-induced bending micromirrors," *IEEE Photon. Technol. Lett.*, vol. 16, no. 9, p. 2042, Sep. 2004.

[6] H.-T. Hsieh, C.-W. Chiu, T. Tsao, F. Jiang, and G.-D. J. Su, "Low-actuation-voltage mems for 2-d optical switches," *J. Lightw. Technol.*, vol. 24, no. 11, Nov. 2006.

[7] V. A. Aksyuk, F. Pardo, D. Carr, D. Greywall, H. B. Chan, M. E. Simon, A. Gasparyan, H. Shea, V. Lifton, C. Bolle, S. Arney, R. Frahm, M. Paczkowski, M. Haueis, R. Ryf, D. T. Neilson, J. Kim, C. R. Giles, and D. Bishop, "Beam-steering micromirrors for large optical crossconnects," *J. Lightw. Technol.*, vol. 21, no. 3, pp. 634–642, Mar. 2003.

[8] M. Yano, F. Yamagishi, and T. Tsuda, "Optical mems for photonic switching-compact and stable optical crossconnect switches for simple, fast, and flexible wavelength applications in recent photonic networks," *IEEE J. Sel. Topics Quantum Electron.*, vol. 11, no. 2, p. 383394, Mar./Apr. 2005.

[9] D. S. Greywall, P. A. Busch, F. Pardo, D. W. Carr, G. Bogart, and H. T. Soh, "Crystalline silicon tilting mirrors for optical cross-connect switches," *J. Microelectromech. Syst.*, vol. 12, no. 5, pp. 708–712, Oct. 2003.

[10] J. Jonathan, W. P. Taylor, J. D. Brazzle, C. J. Corcoran, G. Kirkos, J. E. Odhner, A. Pareek, M. Waelti, and M. Zai, "Electromagnetically actuated mirror arrays for use in 3-d optical switching applications," *J. Microelectromech. Syst.*, vol. 13, no. 3, June 2004.

[11] L. Fan and M. C. Wu, "Two-dimensional optical scanner with large angular rotation realized by self-assembled micro-elevator," *in Proc. IEEE/LEOS Summer Topical Meeting. Dig. Broadband Opt. Netw. and Technol.: An Emerging Reality. Opt. MEMS. Smart Pixels. Organic Opt. and Optoelectron.*, pp. 107–108, New York 1998.

[12] J.-C. Tsai and M. C. Wu, "Design, fabrication, and characterization of a high fill-factor, large scan-angle, two-axis scanner array driven by a leverage mechanism," *J. Microelectromech. Syst.*, vol. 15, no. 5, pp. 1209–1213, Oct. 2006.

[13] J. Singh, T. Gan, A. Agarwal, Mohanraj, and S. Liw, "3-d free space thermally actuated micromirror device," *Sens. Actuators, Phys. A*, vol. 123-124, pp. 468–475, 2005.

[14] S. T. Todd, A. Jain, H. Qu, and H. Xie, "Amulti-degree-of-freedom micromirror utilizing inverted-series-connected bimorph actuators," *J. Optics A: Pure and Appied Optics*, vol. 8, p. S352S359, 2006.

[15] J. Klemic, A. Yasseen, J. Mitchell, and D. Smith., "A rotary electrostatic micromirror 1×8 optical switches," *IEEE J. Sel. Topics Quantum Electron.*, vol. 5, no. 1, pp. 26–32, Jan./Feb. 1999.

[16] J. H. Comtois, M. A. Michalicek, , and C. C. Barron, "Electrothermal actuators fabricated in four-level planarized surface micromachined polycrystalline silicon," *Sens. Actuators, Phys. A*, vol. 70, pp. 23–32, 1998.

[17] J.-S. Park, L. L. Chu, A. D. Oliver, and Y. B. Gianchandani, "Bent-beam electrothermal actuators-part ii: Linear and rotarymicroengines," *J. Microelectromech. Syst.*, vol. 10, no. 2, pp. 255–263, June 2001.

[18] T. Akiyama and H. Fujita, "A quantitative analysis of scratch drive actuator using buckling motion," *in Proc. IEEE Inte. Conf. on Microelectromech. Syst. (MEMS '95)*, p. 310, Feb. 1995.

[19] T. Akiyama, D. Collard, and H. Fujita, "Scratch drive actuator with mechanical links for self-assembly of three-dimensional mems," *J. Microelectromech. Syst.*, vol. 6, no. 1, pp. 10–17, March 1997.

[20] J. A. Yeh, J.-Y. Huang, and C.-N. Chen, "Design of an electrostatic rotary comb actuator," *J. Microlith., Microfab., Microsyst.*, vol. 5, no. 2, pp. 1–13, Apr./June 2006.

[21] C.-C. Tu, K. Fanchiang, and C.-H. Liu, "Rotary electrostatic micromirror switches using wafer-scale processing and assembly," *Journal Microsystem Technologies*, vol. 12, no. 12, pp. 1099–1108, June 2006.

[22] L.-S. Fan, Y.-C. Tai, and R. Muller, "Ic-processed electrostatic micromotors," *Sens. Actuators, Phys. A*, vol. 20, pp. 41–48, November 1989.

[23] M. Mehregany and Y.-C. Tai, "Surafce micromachined michanisims and micromotor," *J. Micromech. Microeng.*, vol. 1, pp. 73–85, 1991.

[24] A. A. Yasseen, J. N. Mitchell, D. A. Smith, and M. Mehregany, "High-aspect-ratio rotary micromotor scanners," *Sens. Actuators, Phys. A*, vol. 77, pp. 73–79, 1996.

[25] J. Moher, P. Bley, M. Strohrmann, and U. Wallrabe, "Microactuators fabricationed by the liga process," *J. Micromech. Microeng.*, vol. 2, pp. 234–241, 1992.

[26] M. Baltzer, T. Kraus, and E. Obermeier, "Design and fabrication of surface micromachined micromotors with large dimensions." *J. Micromech. Microeng*, vol. 7, pp. 196–199, 1997.

[27] T. Ebefors, J. Ulfstedt-Mattsson, E. Kälvesten, and G. Stemme, "3d micromachined devices based on polyimide joint technology," *SPIE Symposium on Microelectronics and MEMS*, vol. 3892, no. Gold Coast, Queensland, Australia, pp. 118–132, Oct 1999.

[28] R. R. Syms, "Surface tension powered self-assembly of 3-d micro-optomechnical structures," *J. Microelectromech. Syst.*, vol. 8, no. 4, pp. 448–455, Dec. 1999.

[29] N. Sarkar, "Mems actuation and self-assembly applied to rf and optical devices," Master's thesis, Electrical & Compter Engineering, University of Waterloo, 2004.

[30] J. Zou, J. Chen, C. Liu, and J. E. Schutt-Ainé, "Plastic deformation magnetic assembly (pdma) of out-of-plane microstructures: technology and application," *J. Microelectromech. Syst.*, vol. 10, no. 2, pp. 302–309, June 2001.

[31] "Photo gallery, mems precision instruments, c. g. keller.http://www.memspi.com/gallery.html [online]."

[32] N. Dechev, W. L. Cleghorn, and J. K. Mills, "Microassembly of 3d microstructures using a compliant, passive microgripper," *J. Microelectromech. Syst.*, vol. 13, no. 2, pp. 176–189, April 2004.

[33] M. A. Basha, N. Dechev, S. Chaudhuri, and S. Safavi-Naeini, "Digital optical $1 \times n$ mems switch utilizing microassembled rotating micromirror," *in Proc. IEEE/LEOS Int. Conf. Optical MEMS (MOEMS06)*, August 21-24 2006.

[34] H. J. Eom, T. J. Park, K. Yoshitomi, and T. I. Choi, "Tm-scattering from a rectangular channel in a conducting plane," *Proceedings of IEEE AP-S*, vol. 1, pp. 400–403, 18-25 July 1992.

[35] Y.-L. Kok, "General solution to the multiple-metalic-grooves scattering: the fast-polarization case," *Applied Optics*, vol. 32, no. 14, pp. 2573–2581, JULY 1993.

[36] I. Dufour, E. Sarraute, and A. Abbas, "Optimization of the geometry of electrostatic micromotors using only analytical equations," *J. Micromech. Microeng.*, vol. 6, pp. 108–111, 1996.

[37] S.-S. Lee, L.-S. Huang, C.-J. Kim, and M. C. Wu, "Free-space fiber-optic switches based on mems vertical torsion mirrors," *J. Lightw. Technol.*, vol. 17, no. 1, Jan. 1999.

[38] R. A. Miller, Y. C. Tai, G. Xu, J. Bartha, and F. Lin, "An electromagnetic mems 2×2 fiber optic bypass switch," in *Proc. Int. Conf. Solid-State Sensors and Actuators (Transducers97)*, Chicago, IL, June 1997.

[39] B. Behin, K. Y. Lau, and R. S.Muller, "Magnetically actuated micromirrors for fiber-optic switching," *in Proc. Tech. Dig. Solid-State Sensor and Actuator Workshop*, pp. 273–276, Cleveland, OH 1998.

[40] L.-Y. Lin, E. L. Goldstein, J. M. Simmons, and R. W. Tkach, "High-density micromachined polygon optical crossconnects exploiting network connection-symmetry," *IEEE Photon. Technol. Lett.*, vol. 10, no. 10, pp. 1425–1427, Oct. 1998.

[41] R. T. Chen, H. Nguyen, and M. C. Wu, "A high-speed low-voltage stress induced micromachined 2 2 optical switch," *IEEE Photon. Technol. Lett.*, vol. 11, no. 11, pp. 1396–1398, Nov. 1999.

[42] A. Fernandez, B. P. Staker, W. E. Owens, L. P. Muray, J. P. Spallas, and W. C. Banyai, "Modular mems design and fabrication for an 80 80 transparent optical cross-connect switch," *Proc. SPIEInt. Soc. Opt. Eng*, vol. 5604, no. 1, p. 208217, 2004.

[43] T. Yamamoto, J. Yamaguchi, N. Takeuchi, A. Shimizu, E. Higurashi, R. Sawada, and Y. Uenishi, "A three-dimensional mems optical switching module having 100 input and 100 output ports," *IEEE Photon. Technol. Lett.*, vol. 15, no. 10, pp. 1360–1362, Oct 2003.

[44] X. Zheng, V. Kaman, Y. Shifu, X. Yuanjian, O. Jerphagnon, K. Adrian, R. C. Anderson, H. N. Poulsen, L. Bin, J. R. Sechrist, C. Pusarla, R. Helkey, D. J. Blumenthal, and J. E. Bowers, "Three-dimensional mems photonic cross-connect switch design and performance," *IEEE J. Sel. Topics Quantum Electron.*, vol. 9, no. 2, pp. 571–578, Mar./Apr. 2003.

[45] R. Sawada, J. Yamaguchi, E. Higurashi, A. Shimizu, T. Yamamoto, N. Takeuchi, , and Y. Uenishi, "Single si crystal 1024 ch. mems mirror based on terraced electrodes and a

high-aspect ratio torsion spring for 3-d cross-connect switch," *in Proc. IEEE/LEOS Int. Conf. Optical MEMS (MOEMS02)*, pp. 11–12, Piscataway, NJ 2002.

[46] M. Kozhevnikov, N. R. Basavanhally, J. D. Weld, Y. L. Low, P. Kolodner, C. A. Bolle, R. Ryf, A. R. Papazian, A. Olkhovets, F. Pardo, J. Kim, D. T. Neilson, V. A. Aksyuk, and J. V. Gates, "Compact 64 64 micromechanical optical cross connect," *IEEE Photon. Technol. Lett.*, vol. 15, no. 7, p. 993995, Jul. 15.

[47] V. A. Aksyuk, S. Arney, N. R. Basavanhally, D. J. Bishop, C. A. Bolle, C. C. Chang, R. Frahm, A. Gasparyan, J. V. Gates, R. George, C. R. Giles, J. Kim, P. R. Kolodner, T. M. Lee, D. T. Neilson, C. Nijander, C. J. Nuzman, M. Paczkowski, A. R. Papazian, F. Pardo, D. A. Ramsey, R. Ryf, R. E. Scotti, H. Shea, and M. E. Simon, "238 238 micromechanical optical cross connect," *IEEE Photon. Technol. Lett.*, vol. 15, no. 4, p. 587, Apr. 2003.

[48] D. T. Neilson, R. Frahm, P. Kolodner, C. A. Bolle, R. Ryf, J. Kim, A. R. Papazian, C. J. Nuzman, A. Gasparyan, N. R. Basavanhally, V. A. Aksyuk, and J. V. Gates, "256 256 port optical crossconnect subsystem," *J. Lightw. Technol.*, vol. 22, no. 6, pp. 1499–1509, Jun. 2004.

[49] J. Kim, C. J. Nuzman, B. Kumar, D. F. Lieuwen, J. S. Kraus, A. Weiss, C. P. Lichtenwalner, A. R. Papazian, R. E. Frahm, N. R. Basavanhally, D. A. Ramsey, V. A. Aksyuk, F. Pardo, M. E. Simon, V. Lifton, H. B. Chan, M. Haueis, A. Gasparyan, H. R. Shea, S. Arney, C. A. Bolle, P. R. Kolodner, R. Ryf, D. T. Neilson, and J. V. Gates, "1100 1100 port mems-based optical crossconnect with 4-db maximum loss," *IEEE Photon. Technol. Lett.*, vol. 15, no. 11, p. 15371539, Nov. 2003.

[50] R. Ryf, J. Kim, J. P. Hickey, A. Gnauck, D. Carr, F. Pardo, C. Bolle, R. Frahm, N. Basavanhally, C. Yoh, D. Ramsey, R. Boie, R. George, J. Kraus, C. Lichtenwalner, R. Papazian, J. Gates, H. R. Shea, A. Gasparyan, V. Muratov, J. E. Griffith, J. A. Prybyla, S. Goyal, C. D. White, M. T. Lin, R. Ruel, C. Nijander, S. Arney, D. T. Neilson, D. J. Bishop, P. Kolodner, S. Pau, C. J. Nuzman, A. Weis, B. Kumar, D. Lieuwen, V. Aksyuk, D. S. Greywall, T. C. Lee, H. T. Soh, W. M. Mansfield, S. Jin, W. Y. Lai, H. A. Huggins, D. L.

Barr, R. A. Cirelli, G. R. Bogart, K. Teffeau, R. Vella, H. Mavoori, A. Ramirez, N. A. Ciampa, F. P. Klemens, M. D. Morris, T. Boone, J. Q. Liu, J. M. Rosamilia, and C. R. Giles, "1296-port mems transparent optical crossconnect with 2.07 petabit/s switch capacity," *in Proc. OFC Tech. Dig. Postconference Edition. Postdeadline Papers*, vol. 4, pp. PD28–1–3, 2001.

[51] T. Tsuboi, H. Kurokawa, T. Nomura, H. Ueda, and H. Kasai, "Novel optical packet switched access network architecture," *Proceedings of the OFC 2006*, Anaheim, California. 2006.

[52] N. Dechev, M. A. Basha, S. Chaudhuri, and S. Safavi-Naeini, "Microassembly of 3d micromirrors as building elements for optical mems switching," *In Proc. SPIE Photonics East*, vol. 6374, Boston Oct, 2006.

[53] D. Koester, A. Cowen, R. Mahadevan, M. Stonefield, and B. Hardy, *PolyMUMPs Design Handbook Revision 9.0*, 9th ed., MEMSCAP, MEMS Business Unit (CRONOS), Research Triangle Park, N.C., USA, 2001.

[54] M. A. Basha and S. Safavi-Naeini, "Optimization of electrostatic side-drive micromotor torque using new rotor-pole-shaping technique," in *Proc. of SPIE Photonics East*, vol. 6374, Boston, Oct. 2006.

[55] M. A. Basha, S. Safavi-Naeinie, and S. Chaudhuri, "Design and fabrication of an electrostatic micromotor with a low operating voltage," *Int. Conf. Solid-State Sensors and Actuators (TRANSDUCERS'07)*, no. Lyon, France, June 2007.

[56] L.-Y. Lin, E. L. Goldstein, and R. W. Tkach, "Free-space micromachined optical switches with submillisecond switching time for large-scale optical crossconnects," *IEEE Photon. Technol. Lett.*, vol. 10, no. 4, pp. 525 – 527, April 1998.

[57] C. Marxer and N. F. de Rooij, "Micro-opto-mechanical 2×2 switch for single-mode fibers based on plasma-etched silicon mirror and electrostatic actuation,," *J. Lightw. Technol.*, vol. 17, no. 1, pp. 2–6, Jam. 199.

[58] T. Akiyama and K. Shono, "A new step motion of polysilicon microstructures," *in Proc. IEEE Inte. Conf. on Microelectromech. Syst. (MEMS '00)*, pp. 272–277, Feb. 1993.

[59] L.-Y. Lin, E. L. Goldstein, and L. M. Lunardi, "Integrated signal monitoring and connection verification in mems optical crossconnects," *IEEE Photon. Technol. Lett.*, vol. 12, no. 7, pp. 885 – 887, July 2000.

[60] K. S. Pister, M. W. Judy, S. R. Burgett, and R. S. Fearing, "Microfabricated hinges," *Sens. Actuators, Phys. A*, vol. 33, no. 3, pp. 249–256, June 1992.

[61] W. Noell, L. D. P. Clerc, B. Guldimann, H. Herzig, O. Manzardo, C. R. Marxer, K. J. Weible, R. Dändliker, and N. de Rooij, "Applications of soi-based optical mems," *IEEE J. Sel. Topics Quantum Electron.*, vol. 8, no. 1, pp. 148–154, Jan./Feb. 2002.

[62] M. Hoffmann, P. Kopka, and E. Voges, "Lowloss fiber-matched low temperature pecvd waveguides with small-core dimensions for optical communication systems," *IEEE Photon. Technol. Lett.*, vol. 8, no. 9, pp. 1238–1240, Sept. 1997.

[63] J. Kim, D. Christensen, and L. Lin, "Monolithic 2-d scanning mirror using self-aligned, angular vertical comb drives," *IEEE Photon. Technol. Lett.*, vol. 17, no. 11, pp. 2307–2309, Nov. 2005.

[64] N. Kouma, O. Tsuboi, Y. Mizuno, H. Okuda, X. Mi, M. Iwaki, H. Soneda, S. Ueda, and I. Sawaki, "A multi-step drie process for a 128 × 128 micromirror array," *in Proc. IEEE/LEOS Int. Conf. Opt. MEMS*, pp. 53–54, Piscataway, NJ 2003.

[65] T. D. Kudrle, C. C. Wang, M. G. Bancu, J. C. Hsiao, A. Pareek, M. Waelti, G. A. Kirkos, T. Shone, C. D. Fung, and C. H. Mastrangelo, "Single-crystal silicon micromirror array with polysilicon flexures," *Sens. Actuators A, Phys.*, vol. 119, no. 2, pp. 559–566, Apr. 2005.

[66] J.-C. Tsai and M. C. Wu, "Gimbal-less mems two-axis optical scanner array with high fill-factor," *J. Microelectromech. Syst.*, vol. 14, no. 6, Dec. 2005.

[67] I. W. Jung, U. Krishnamoorthy, and O. Solgaard, "High fill-factor two-axis gimbaled tip-tilt-piston micromirror array actuated by self-aligned vertical electrostatic combdrives," *J. Microelectromech. Syst.*, vol. 15, no. 3, pp. 563–571, June 2006.

[68] "http://www.sandia.gov/mstc/technologies/micromachines/tech-info/technologies/summit5.html."

[69] J. Chen, W. Weingartner, A. Azarov, and R. C. Giles, "Tilt-angle stabilization of electrostatically actuated micromechanical mirrors beyond the pull-in point," *J. Microelectromech. Syst.*, vol. 13, no. 6, pp. 988–997, Dec. 2005.

[70] P. B. Chu, I. Brener, C. Pu, S. Lee, J. I. Dadap, S. Park, K. Bergman, N. H. Bonadeo, T. Chau, M. Chou, R. A. Doran, R. Gibson, R. Harel, J. J. Johnson, C. D. Lee, D. R. Peale, B. Tang, D. T. Tong, M. Tsai, Q. Wu, W. Zhong, E. L. Goldstein, L.-Y. Lin, and J. A. Walker, "Design and nonlinear servo control of mems mirrors and their performance in a large port-count optical switch," *J. Microelectromech. Syst.*, vol. 14, no. 2, pp. 261–272, Apr. 2005.

[71] "http://www.diconfiberoptics.com. [online]."

[72] L. A. Fiel, D. L. Burriesci, P. R. Robrish, and R. C. Ruby, "Micromachined 1×2 optical-fiber switch," *Sens. Actuators, Phys. A*, vol. 53, no. 1, pp. 311–315, May 1996.

[73] M. Hoffmann, P. Kopka, D. Nusse, and E. Voges, "Fibre-optical mems switches based on bulk silicon micromachining," *J. Microsystem Technologies*, vol. 9, no. 5, pp. 299–303, May 2003.

[74] H.-W. Lee, W.-Y. Wu, Z.-C. Shi, W.-Z. Guo, and Y.-H. Lee, "Low-loss 1×2 mems optical switch with three degrees-of-freedom actuation," *in Proc. IEEE/LEOS Int. Conf. Optical MEMS (MOEMS03)*, pp. 131–132, 18-21 August 2003.

[75] K. Fan, W. Lin, T. Chung, H. Wang, and L. Wu, "A miniature low cost and high reliability 1×2 mechanical optical switch." *J. Micromech. Microeng.*, vol. 15, no. 8, pp. 1565–1570, 2005.

[76] L. A. Field, D. L. Burriesci, P. R. Robrish, and R. C. Ruby, "Micromachinied 1×2 optical-fiber switch," *Sens. Actuators, Phys. A*, vol. 53, pp. 311–315, 1996.

[77] W. Lin, K. Fan, L. Chiang, Y. Yang, W. Kuo, and T. Chung, "A novel micro/nano 1×4 mechanical optical switch," . *Micromech. Microeng.*, vol. 16, no. 1408, p. 1415, 2006.

[78] S. Dong, S. P. Lim, K. H. Lee, J. Zhang, L. C. Lim, , and K. Uchino, "Piezoelectric ultrasonic micromotor with 1.0 mm diameter," *IEEE Trans. Ultrasonic, Ferroelectric, And Frequency Control*, vol. 50, no. 4, April 2003.

[79] V. J. Snitka and V. Mizariene, "State-of-the-art ultrasonic micromotors and their future applications," *Proceedings of SPIE*, vol. 4236, pp. 330–338, March 2001.

[80] B. Wagner, M. Kreutzer, and W. Benecke, "Permanent magnet micromotors on silicon substrates," *J. Microelectromech. Syst.*, vol. 2, no. 1, March 1993.

[81] H. Gucckel, K. J. Skrobis, T. R. Christenson, J. Klein, S. Han, B. Choi, E. G. Lovell, and T. W. Chapman, "Fabrication and testing of the planar magnetic micromotors," *J. Micromech. Microeng.*, vol. 1, pp. 135–138, 1991.

[82] M. Mehregany, P. Nagarkar, S. D. Senturia, and J. H. Lang, "Micromotor fabrication," *IEEE Trans. Electron. Devices*, vol. 39, pp. 2060–1069, Sept 1992.

[83] W. Xinli, C. Shumei, and C. Shukang, "Advantages of electrostatic micromotor and its application to medical instruments," *Industry Applications Conference*, vol. 4, pp. 2466–2468, 2002.

[84] D. Polla, A. Erdman, D. Peichel, R. Rizq, Y. Gao, and D. Markus, "Precision micromotor for surgery," *1st Annual International, Conference On Microtechnologies in Medicine and Biology*, pp. 180–183, 2000.

[85] A. A. Yasseen, S. W. Smith, F. L. Merat, and M. Mehregany, "Diffraction grating scanners using polysilicon micromotors," *IEEE J. Selected Topics Quantum Elec.*, vol. 5, no. 1, p. Jan./Feb., 1999 1999.

[86] M. Simard, Z. Khalid, and A. Kirk, "Digital optical space switch based on micromotor grating scanners," pp. 313–315, Jan. 2006.

[87] L. Fan, "Design and fabrication of micromotors for high density data storage," *IEEE Trans. Magnetics*, vol. 32, no. 3, May 1996.

[88] P. Dario, M. C. Carrozza, C. Stefanini, and S. D'Attanasio, "A mobile microrobot actuated by a new electromagnetic wobble micromotor," *IEEE/ASME Transction on Mechatronics*, vol. 3, no. 1, March 1998.

[89] H. Lu, J. Zhu, and Y. Guo, "Development of a slot-less tubular linear interior permanent magnet micromotor for robotic applications," *IEEE Transaction on Magnetics*, vol. 41, no. 10, Oct. 2005.

[90] j. H. Comtois, V. Bright, and M. W. Phipps, "Thermal microactuators for surface-micromachining process," *SPIE*, vol. 2642, pp. 10–21, 1995.

[91] L. Que, J.-S. Park, and Y. B. Gianchandani, "Bent-beam electro-thermal actuators for high force applications," *Twelfth IEEE International Conference on Micro Electro Mechanical Systems (MEMS '99)*, pp. 31–36, Jan 1999.

[92] M. J. Sinclair, "A high force low area mems thermal actuator," *The Seventh Intersociety Conference on Thermal and Thermomechanical Phenomena in Electronic Systems*, vol. 1, pp. 127–132, may 2000.

[93] L. Que, J.-S. Park, and Y. B. Gianchandani, "Bent-beam electrothermal actuators- part i: single beam and cascaded devices," *J. Microelectromech. Syst.*, vol. 10, no. 2, pp. 247–254, June 2001.

[94] W. D. Cowan and V. Bright, "Vertical thermal actuators for micro-opto-electro-mechanical systems," *SPIE*, vol. 3226, pp. 137–146, 1997.

[95] W. Riethmüller and W. Benecke, "Thermally excited silicon microactuators," *IEEE Trans. Electron Devices*, vol. 35, no. 6, pp. 758–761, June 1988.

[96] D. M. Burns and V. Bright, "Design and performance of a double hot arm polysilicon thermal actuator," *SPIE*, vol. 3224, pp. 296–306, 1997.

[97] J. D. Grade and H. Jerman, "Mems electrostatic actuators for optical swithcing applications," *Optical Fiber Communication Conference and Exhibit(OFC2001)*, vol. 3, pp. wx21–wx21, 2001.

[98] J. D. Grade, K. Y. Yasumura, and H. Jerman, "Micromachined actuators with braking mechanisms," *Sens. Actuators, Phys. A*, vol. 122, pp. 1–8, 2005.

[99] J. A. Yeh, C.-N. Chen, and Y.-S. Lui, "Large rotation actuated by in-plane rotary comb-drives with serpentine spring suspension," *J. Micromech. Microeng.*, vol. 15, pp. 201–206, 205.

[100] M. Wu, Y.-L. Lin, and S. L. K. Pister, "Micromachined free-space integrated micro-optics," *Sens. Actuators, Phys. A*, vol. 50, pp. 127–134, 1995.

[101] L. Fan, M. Wu, and K. C. amd M. Crawford, "Self-assembled microactuated xyz stages for optical scanning and alignment," *Int. Conf. Solid-State Sensors and Actuators (Transducers97)*, vol. 1, pp. 319–322, Chicago, IL 1997.

[102] K. F. Harsh, V. M. Bright, and Y. C. Lee, "Solder self-assembly for threedimensional microelectromechanical systems," *Sens. Actuators, Phys. A*, vol. 77, pp. 237–244, 1999.

[103] P. W. Green, R. R. Syms, and E. M. Yeatman, "Demonstration of three-dimentional microstructure self-assembly," *J. Microelectromech. Syst.*, vol. 4, no. 4, pp. 170–176, Dec. 1995.

[104] E. Shimada, J. A. Thompson, J. Yan, R.Wood, and R. S. Fearing, "Prototyping millirobots using dextrous microassembly and folding," in *Proc. ASME IMECE/DSCD*, Orlando, Florida, Nov. 5-10 2000, pp. 993–940.

[105] J. A. G. G. Yang and B. J. Nelson, "A flexible experimental workcell for efficient and reliable wafer-level 3d microassemblyg," in *Proc. IEEE International Conference on Robotics and Automation (ICRA 2001)D*, Seoul, South Korea, 2001, pp. 133–138.

[106] C. G.Keller and M. Ferrari, "Milli-scale polysilicon structures," in *Proc. Solid-State Sensor and ActuatorWorkshop*, Hilton Head, SC, June 1994, pp. 132–137.

[107] J. Feddema and R. Simon, "Visual servoing and cad-driven microassembly," *PIEEE Robotics and Automation Magazine*, vol. 5, no. 4, pp. 17–24, Dec 1998.

[108] C. J. Kim, A. P. Pisano, and R. S. Muller, "Silicon-processed overhanging microgripper," *J. Microelectromech. Syst.*, vol. 1, pp. 31–36, Mar 1992.

[109] S. Yuan and N. A. Riza, "General formulation for coupling-loss characterization of a single -mode fiber collimators by use of gradient-index rod lenses," *Applied Optics*, vol. 38, no. 15, pp. 3214–3222, May 1999.

[110] "http://www.mellesgriot.com/."

[111] M. A. Basha, A. Rohani, and S. Safavi-Naeini, "A fast method for analysis and modeling of optical mems switches," in *in Proc. Microelectromech. Syst. Conf.*, Berkely, CA, 24-26 Aug 2001, pp. 54–57.

[112] M. A. Basha, "Analysis and design of optical mems switch," Master's thesis, Electrical & Compter Engineering, University of Waterloo, Waterloo, On, Canada, 2002.

[113] S. F. Bart, M. Mehregany, L. S. Tavrow, J. H. Lang, and S. D. Senturia, "Electric micromotor dynamics," *IEEE Trans. Electron Devices*, vol. 39, no. 3, pp. 566–575, March 1992.

[114] Z. Ren and A. Razek, "Force caclulcation by maxwell stress tensor in a 3d hybrid finite element-boundary integral formulation," *IEEE Trans. magnetics*, vol. 26, no. 5, pp. 2774–2776, Sept. 1990.

[115] F. Paschen, *Wiedemann Ann. Phys. Chem.*, vol. 37, pp. 69–96, 1889.

[116] M. P. Omar, M. Mehregany, and R. L. Mullen, "Electric and fluid field analysis of side-drive micromotors," *J. Microelectromech. Syst.*, vol. 1, no. 3, pp. 130–140, Sept. 1992.

[117] W.-H. Chut, M. Mehreganyt, and R. L. Mullen, "Analysis of tip deflection and force of a bi-metallic cantilever microactuator," *J. Micromech. Microeng.*, vol. 3, pp. 4–7, 1993.

[118] M. A. Basha, N. Dechev, S. Safavi-Naeini, and S. Chaudhuri, "A scalable $1 \times n$ optical mems switcharchitecture utilzing a microassembled rotating mirror," *IEEE J. Sel. Topics Quantum Electron.,*, vol. 13, no. 2, March/April 2007.

[119] M. A. Basha, N. Dechev, S. Safavi-Naeini, , and S. Chaudhuri, "Improved design og large 3d micro-mirror for microassembly into an optical mems cross-connect," *SPIE*, Lussan, Switsland Oct. 2007.

[120] N. Dechev, W. L. Cleghorn, and J. K. Mills, "Mechanical fastener designs for use in the microassembly of 3d microstructures," *Proc. ASME International Mechanical Engineering Congress and RD&D Expo 2004*, Anaheim, California Nov13-19, 2004.

[121] N. Dechev, L. Ren, W. Liu, W. L. Cleghorn, and J. K. Mills, "Development of a 6 degrees of freedom robotic micromanipulator for the use in 3d mems microassembly," *Proceedings of the IEEE International Conference on Robotics and Automation (ICRA2006)*, Orlando, Florida May 15-19, 2006.

[122] J. W. Yu, W. J. Byun, , and N. H. Myung, "Tm scattering from hollow and dielectric-filled semielliptic channels with arbitrary eccentricity in a perfectly conducting plane," *IEEE Trans. Microwave Theory Tech.*, vol. 46, no. 9, pp. 1336–1339, Sept. 1998.

[123] M. S. Mirotznik, D. W. Parther, and J. N. Mait, ""boundary integral methods applied to the analysis of diffractive optical elements," *J. Opt. Soc. Am. A.*, vol. 14, pp. 34–43, 1997.

[124] E. N. Glytsis, K. Hirayama, and T. K. Gaylord, "Rigorous electromagnetic analysis of diffraction by finite-number-of-periods gratings," *J. Opt. Soc. Am. A*, vol. 14, pp. 907–917, 1997.

[125] L. Rayleigh, "On the dynamical theory of grating," *Proc. Roy. Soc.*, vol. A79, pp. 399–416, 1907.

[126] N. R. Hill and V. Celli, "Limits of convergence of thr rayleigh method for surface scattering," *Physical Review B*, vol. 17, no. 6, pp. 2478–2481, March 1978.

[127] P. M. V. D. Berg and J. T. Fokkema, "The rayleigh hypothesis in the theory of reflection by a grating," *J. Opt. Soc. Am.*, vol. 69, no. 1, pp. 27–31, January 1979.

[128] J. A. DeSanto, "Scattering from a sinusoid: derivation of linear equation for the field amplitudes," *L. Acoust. Soc. Am A*, vol. 57, no. 5, pp. 1195–1197, May 1975.

[129] ——, "Scattering from perfectly reflecting arbitrary periodic surface: An exact theory," *Radio Science*, vol. 16, no. 6, pp. 1315–1326, November-December 1981.

[130] R. Petit, Ed., *Electromagnetic Theory of gratings*, ser. Topics in Current Physics. Springer-Verlag, 1980.

[131] J. Chandezon, M. T. Dupuis, G. Gornet, and D. Maystre, "Mutlicoated gratings: a differential formalism applicable in the entire optical region," *L. Opt. Soc. Am. A*, vol. 72, no. 7, pp. 839–846, July 1982.

[132] D. M. Pai and K. Awada, "Analysis of dielectric gratings of arbitrary profiles and thickness," *J. Opt. Soc. Am. A*, vol. 8, no. 5, pp. 755–762, May 1991.

[133] T. K. Gaylord and M. G. Moharam, "Planar dielectric grating diffraction theories," *Applied Physics B*, vol. 28, pp. 1–14, 1982.

[134] S. T. Peng, "Rigorous formulation of scattering and guidance by dielectric grating waveguides: general case of oblique icidence," *J. Opt. Soc. Am. A*, vol. 6, no. 12, pp. 1869–1880, Dec. 1989.

[135] S. T. Peng, T. Tamir, and H. L. Bertoni, "Theory of periodic dielectric grating," *IEEE Trans.Microwave Theory Tech*, vol. 23, pp. 123–133, 1975.

[136] T. K. Gaylord and M. G. Moharam, "Analysis and application of optical diffraction by grating," *Proceedings of the IEEE*, vol. 73, no. 5, pp. 894–937, MAy 1985.

[137] G. S. White and J. F. Marchiando, "Scattering from a v-shaped groove in the resonance domain," *Applied Optics*, vol. 22, no. 15, 1983.

[138] K. Toshitomi, "Scattering of an electromagnetic beam wave of rectangular grooves on a perfect conductor," *Tans. IECE Jpn.*, vol. E67, pp. 447–448, 1984.

[139] Y.-L. Kok, "Boundary-value solution to electromagnetic scattering by a rectangular groove in a ground plane," *J. Opt. Soc. Am.A*, vol. 9, pp. 302–311, 1992.

[140] H. Eom, T. J. Park, and K. Yoshitomi, "An analysis of transverse electric scattering from rectangular channel in a conducting plane," *Radio. Sci.*, vol. 28, pp. 663–673, 1993.

[141] K. Barkeshli and J. L. Volakis, "Te scattering by a two-dimensional groove in a ground plane using higher order boundary conditions," *IEEE Trans. Antennas Propag.*, vol. 38, no. 9, pp. 1421–1428, Sept. 1990.

[142] M. K. Hinders and A. D. Yaghjian, "Dual-series solution to scattering from a semicircular channel in a ground plane," *IEEE- Microwave Guided Wave Lett.*, vol. 1, no. 9, pp. 239–242, Sept. 1991.

[143] T. J. Park, H. J. Eom, M.-W. Boerner, and Y. Yamaguchi, "Tm scattering from a dielectric-loaded semi-circular tough in a conducting plane," *Trans. IEICE Commun.*, vol. E57-B, pp. 87–91, 1992.

[144] H. A. Ragheb, "Electromagnetic scattering from a coaxial dielectric circular cylinder loading a semicircular gap in a ground plane," *IEEE Microwave Theory Tech.*, vol. 43, pp. 1303–1309, June 1995.

[145] T. Shen, Z. Sun, and W. Dou, "Gaussian beam scattering from a semicircular channel in a ground plane," *IEE-APS conference*, pp. 1018–1–21, 1996.

[146] T. J. Park, H. Eom, and K. Yoshitomi, "Analysis of tm scattering from finite rectangular grooves in a conducting plane," *J. Opt. Soc. Am. A.*, vol. 10, no. 5, pp. 905–911, May 1993.

[147] J. W. Yu, W. J. Byun, and N. H. Myung, "Multiple scattering from two dielectric-filled semi-circular channels in a conducting plane: Tm case," *IEEE Microwave Theory Tech.*, vol. 50, no. 9, pp. 125–1253, Sept 2002.

[148] M. G. Moharam, E. Bran, D. A. Pommet, and T. K. Gaylord, "Formulation for stable and efficient implementation of the rigorous coupled-wave analysis of binary gratings," ,.

[149] P. M. Morse and H. Feshbach, *Method of theoretical Physics.* McGraw-Hill Book Company, 1953, vol. I, no. CHAP(4).

[150] H. J. Eom, *Electromagnetic Wave Theory for Boundary-Value Problems.* Springer-Verlag, 2004.

[151] M. A. Basha, S. Chaudhuri, S. Safavi-Naeini, and H. J. Eom, "Rigorous formulation for electromagnetic plane wave scattering from a general shaped-groove in a perfectly conducting plane," *J. Opt. Soc. Am.A*, vol. 6, June 2006.

[152] A. Corporation, "Ansoft hfss," 2002.

[153] T. J. Park, H. Eom, and K. Yoshitomi, "Analysis of tm scattering from finite rectangular grooves in a conducting plane," *J. Opt. Soc. Am. A.*, vol. 10, no. 5, pp. 905–911, May 1993.

[154] D. M. Pai and K. Awada, "Analysis of dielectric gratings of arbitrary profiles and thickness," *J. Opt. Soc. Am. A*, vol. 8, no. 5, pp. 755–762, May 1991.

[155] M. G. Moharam, D. A. Pommet, and E. B. Grann, "Stable implementation of the rigorous coupled-wave analysis for surface-relief gratings: enhanced transmittance matrix approach," *J. Opt. Soc. Am. A*, vol. 12, no. 5, pp. 1077–1086, May 1995.

[156] C. L. Xu and W. P. Huang, "finite-difference beam propagation method for guided-wave optics," *Progress In Electromagnetic Waves, PIERS 11, EMW Piblishing*, pp. 1–49, 1995.

[157] A. Rohani, A. A. Shishegar, and S. Safavi-Naeini, "A fast gaussian beam tracing method for reflection and refraction of general vectorial astigmatic gassuain beams from general curved surfaces," *Optics Communications*, vol. 232, pp. 1–10, 2004.

[158] S. Safavi-Naeini and Y. L. Chow, "A physical optics methid for analysis of jucntions in dielectric waveguides," *Progress In Electromagnetic Waves, PIERS 11, EMW Piblishing*, pp. 199–254, 1995.

[159] R. E. Collin, *Field theory of guided waves.* IEEE Press, 1991.

[160] B. E. A. Saleh and M. C. Teich, *Fundamentals of photonics.* IEEE Press, 1991.